MICROCOPY RESOLUTION TEST CHART
NATIONAL BUREAU OF STANDARDS 1963 A

ACTIVE VIBRATION CONTROL OF A CANTILEVERED

BEAM WITH THREE ELASTIC COORDINATES

THESIS

Thomas A. Cristler
Captain, USAF

AFIT/GA/AA/87D-1

DEPARTMENT OF THE AIR FORCE
AIR UNIVERSITY

AIR FORCE INSTITUTE OF TECHNOLOGY

Wright-Patterson Air Force Base, Ohio

88 2 03 064

AFIT/GA/AA/87D-1

ACTIVE VIBRATION CONTROL OF A CANTILEVERED

BEAM WITH THREE ELASTIC COORDINATES

THESIS

Thomas A. Cristler
Captain, USAF

AFIT/GA/AA/87D-1

DTIC
SELECTED
FEB 0 8 1988

H

AFIT/GA/AA/87D-1
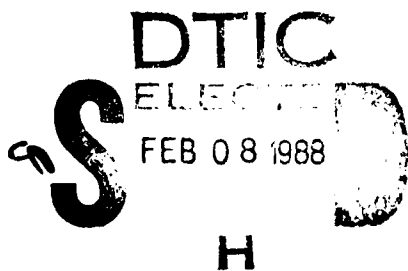
ACTIVE VIBRATION CONTROL OF A CANTILEVERED BEAM WITH THREE ELASTIC

COORDINATES

THESIS

Presented to the Faculty of the School of Engineering

of the Air Force Institute of Technology

Air University

In Partial Fulfillment of the

Requirements for the Degree of

Master of Science in Astronautical Engineering

Thomas A. Cristler, B.S.

Captain, USAF

December 1987

Approved for public release; distribution unlimited

Preface

This experiment was developed and run in conjuction with the Flight Dynamics Laboratory, Vibration and Acoustics Branch, Wright Patterson AFB. Ohio, as a part of their in-house Large Space Structures Technology Program. The experiment was conceived and constructed in Building 24C. Area B, Wright Patterson AFB. Project Manager for the experiment is Mr. Robert Gordon (AV785-5236), and the Lead Engineer is Mr. Wayne Yuen.

The purpose here is not only to document the work done to develop and test the system, but to provide those future researchers interested in conducting experiments with this aparatus with a working level knowledge of the system, its development, and some of its idiosyncracies. While the text may seem to get bogged down with incredible detail on actuator development and structural modelling, there are some issues raised about these subjects that even the reader interested only in Large Space Structure Control applications should find useful. However, unless one is planning on using the experiment for future investigations, studying Chapters 2 and 3 in great detail is not necessary for understanding the subsequent material. Familiarization with the system configuration and problems encountered in developing it are probably the most important points to be gleaned from those sections of this report.

While a number of people made significant contributions to this project, I would like to thank several individuals in particular for their help, understanding, and sympathetic listening when things weren't working as planned. First, my advisor, Dr. Robert Calico for guiding me through this often frustrating project. Bob Gordon and Wayne Yuen provided me not only with sound technical advice, but did most of the dirty work of procuring hardware and lining up technical services and

Table of Contents

iv

List of Figures

ix

List of Tables

Abstract

Many control methods have been proposed for dealing with the large space structure vibration control problem. To experimentally evaluate these various approaches in a way which will allow consistent comparison of results requires a baseline experiment in which all variables are understood and controlled. From this baseline, the various aspects of each control scheme can be implemented, and their relative merits compared on a consistent basis. This experiment was implemented using a vertically suspended cantilever beam with rectangular cross section. Proof mass actuators were developed to provide control force inputs to the structure. Closed loop control was formulated using linear quadratic regulator theory and results are compared with simulation and eigenvalue predictions to establish baseline performance. Modal suppression techniques were implemented to demonstrate control of selected modes while maintaining overall system stability. Results applicable to future testing and development in the large space structure control area are identified.

ACTIVE VIBRATION CONTROL OF A CANTILEVERED BEAM WITH THREE ELASTIC COORDINATES

I. Introduction

As man's presence in space grows, so does the size of the vehicles he deems necessary to put there. Programs such as the Space Defense Initiative and NASA's space station are generating requirements for very large vehicles which must point with arc-second accuracies, hold the shape of optics surfaces to within a few tenths of the electromagnetic wavelength being used, or maintain a vibration free environment for experimentation while docking and cargo transfer occurs elsewhere on the vehicle. While these operations are readily, and in some cases commonly accomplished on earth, they present a challenging problem when attempted in the space environment.

As platforms grow in size, economics dictate a reduction in weight. The result is a large flexible structure which tends to have many closely spaced, lightly damped vibration modes that are easily excited. Mechanisms for inducing vibration in the structure range from the attitude control system and active power generation, to cargo transfer, or personnel moving about the vehicle. If the amplitude or duration of the vibration will degrade the performance of the system, then some means of controlling it must be introduced. Adding passive damping (shock absorbers, visco-elastic materials, etc.) would most likely be the first attempt at a solution. However, there are cases where passive

damping will still not achieve the desired performance and an active means of control must be introduced.

Many approaches have been proposed for dealing with the active vibration control problem, and there is considerable ongoing work in the field. Two examples of current work include Lockheed's demonstration of a high authority control/low authority control (HAC/LAC) scheme on a suspended plate, and static and dynamic shape control of a fixed-free beam, which was accomplished at the Jet Propulsion Laboratory using Kalman and adaptive control techniques (1:3). Many of the experiments conducted to date have used ground referenced sensors or actuators, which is not representative of the problem. While this simplifies the implementation of the experiment, it seems to be oriented more toward control law evaluation than being a complete emulation of the large space structure control problem.

To provide a more realistic test bed for research in this area, Air Force Wright Aeronautical Laboratory, Wright-Patterson AFB, initiated an in house program under its vibrations branch (AFWAL/FIBG) to investigate large space structures technologies. An advanced beam experiment was devised to demonstrate active vibration control of a cantilevered beam in two orthogonal bending axes as well as torsion about its long axis. This configuration has closely spaced and coupled modes and features inertial sensors and actuators. The experiment was designed to emulated as many large space structure problems as possible. AFIT was invited to participate in the implementation and testing of this experiment, which is depicted in Figure 1.1.

Two related methods of structural control which have received attention in recent years are reduced order and decoupled controllers. The importance of these controllers lies in the fact that a large space structure will in general present many more modes than can reasonably be
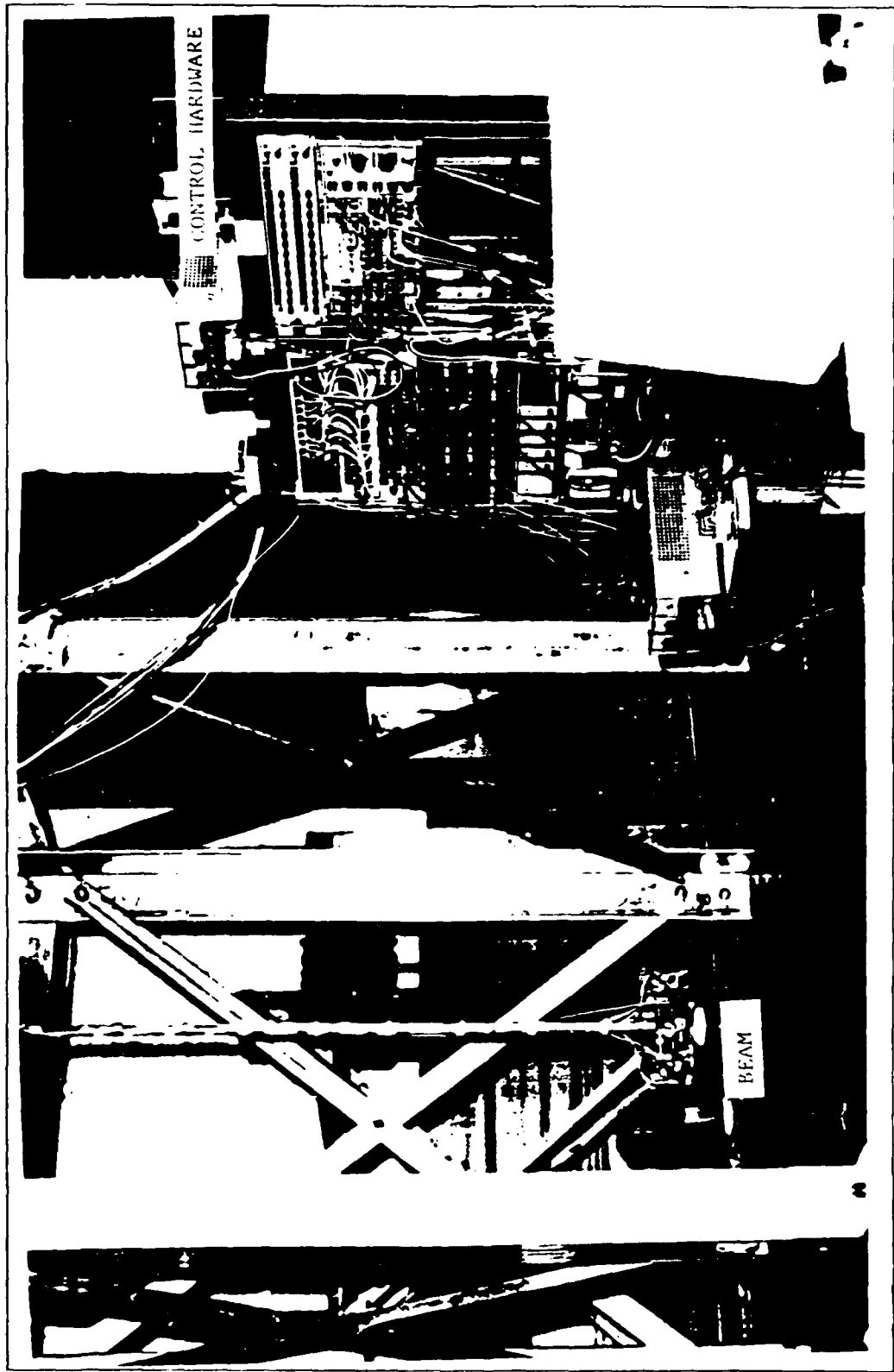
Figure 1.1. Advanced Beam Experiment

controlled by a single system. Weight and hardware capability become serious issues when the modes to be controlled can number in the hundreds. If the system can be subdivided and a subset of the modes to be controlled assigned to separate controllers, the implementation of the structural control can be greatly simplified. Indeed, not all of the modes may require active control to meet the vehicle performance requirements. In such cases, reducing the order of the control model can greatly reduce the size and weight of the requisite control system.

The difficulty with implementing this reduced order model is that the sensors may still contain information about the modes which have been omitted from the model. Also, since the actuators operate on a continuous structure they will excite, and potentially destabilize these ignored modes. These effects have been classified as observation and control spillover respectively (Ref 2). Work by Coradetti (Ref 3) showed that spillover could be eliminated by finding a transformation matrix which is applied to the feedback gains, thus "suppressing" the omitted modes. Calico and Janiszewski (Ref 4) showed that eliminating either observation or control spillover was sufficient to ensure stability of the suppressed modes and demonstrated a procedure for calculating the appropriate transformation matrix. Wright (Ref 5) implemented this modal suppression technique on a single bending axis of a cantilevered beam. While being able to show increased stablility in the second bending mode of the beam without destabilizing the first or third modes, direct correlation between predicted and measured performance was not achieved.

The goals of the research presented here are to conduct the system identification of the experiment, to include the actuators, sensors, and structure, and demonstrate predictable closed loop control response using state space control techniques. Once this has been accomplished,

implementation and demonstration of reduced order controllers will be attempted, leading up to a demonstration of a decoupled control algorithm.

II. Actuators

Actuator System Description

The actuators chosen by AFWAL for use on this system are proof
mass linear motors which provide control force using momentum exchange
between the base and the moving mass. The specific actuators being used
in this experiment are based on a TRW design used in the AFWAL sponsored
VCOSS program. System drawings and descriptions were provided to AFWAL,
who purchased and fabricated the necessary components to assemble the
devices.

The actuators consist of a linear motor coil mounted on two support
brackets (see Figure 2.1). A cylindrical proof mass of 0.9 kg contains
the motor magnets and is driven by the motor coil. This mass travels on
linear bearings along a center shaft with a nominal travel of ±0.5
inches. The nominal motor parameters published by the manufacturer,
Kaiser Electroprecision, are listed in Appendix A. The actuator is
instrumented with a Linear Variable Differential Transformer (LVDT),
manufactured by Schaevitz Engineering, which provides feedback of
relative position between the proof mass and the motor base. The proof
mass itself is instrumented with an Endevco piezoresistive accelerometer
to provide feedback control of the proof mass acceleration. LVDT and
accelerometer specifications and calibrations are listed in Appendix A.
The motor coil is driven by a power amplifier circuit (see Appendix A)
which transforms a voltage command into a drive current. The power
amplifier has a current limiter to prevent burning out the motor coil
which has a steady state current limit is 2 amps. This limits the force
output of the actuators to 4 lbf.
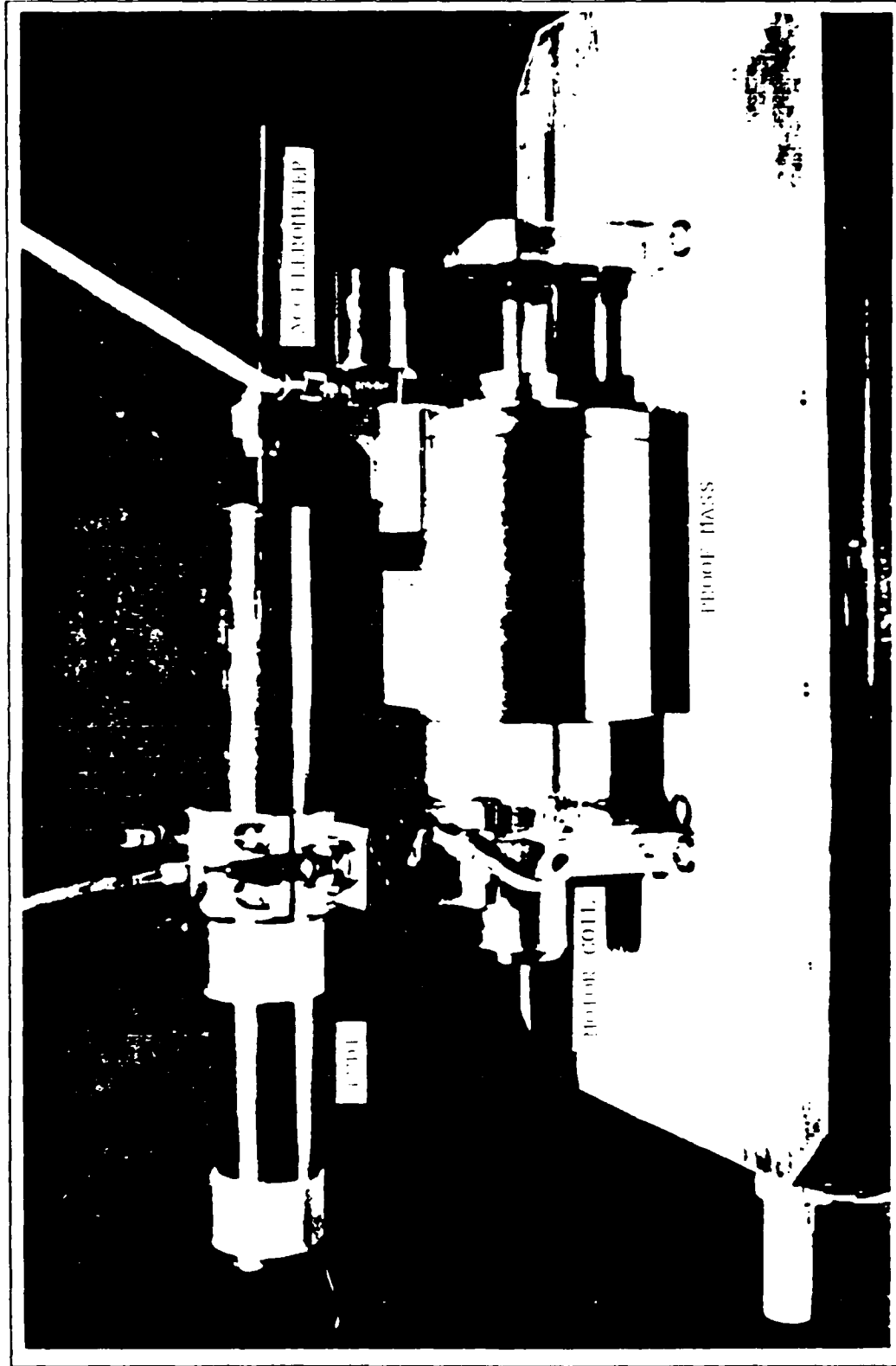
Figure 2.1. Proof Mass Actuator

Initial open loop testing of the actuators found them to have several undesirable characteristics:

1) The low frequency output was very non-linear. The bearing friction and hysteresis in the system caused the proof mass to wander away from the center of travel when commanded at low frequencies. Since the actuator stroke is limited, the amplitude of low frequency commands must be kept small to prevent driving the proof mass into the support brackets. However, when the input is kept low, friction can overcome the proof mass motion and cause it to stick, or at least significantly lag the sinusoidal input command. This leaves the proof mass off center, and after a few cycles the mass is driven into the end stop.

2) The zero reference potentiometer in the power amplifer, which provides centering adjustment for the proof mass, required continual adjustment during the initial testing of the actuators. Changes in input gain and changes in frequency would cause a shift in the zero reference (the center point of the actuator travel). This problem was evident at higher frequencies (greater than 3 Hz), and is a separate condition from the "wander" previously described.

3) The actuator frequency response has a low frequency roll-off and phase shift in the vicinity of the fundamental bending modes of the structure.

To modify the frequency response of the actuators and maintain proof mass centering, a feedback control system using classical analog control techniques was implemented around each actuator.

Feedback Compensation Design Goals

The actuator control was developed around accomplishing the following objectives:

1) Actuator frequency response should be "flat" over the structure control bandwidth, i.e. constant magnitude and zero phase. The control bandwidth for this experiment has been limited to 0 to 50 Hz.

2) The actuator proof mass should maintain an inertial position when the actuator is not being commanded, which prevents the actuator proof masses from contributing to the structure inertia.

3) The proof mass should maintain its centering when commanded at different frequencies and amplitudes.

4) The proof mass travel should be limited to the actuator stroke of ±0.5 inches.

Open Loop Testing

Each actuator was tested in the original configuration to determine its frequency response characteristics. These tests were performed by driving the actuator power amplifier with a random input signal and measuring the acceleration of the proof mass with the actuator base fixed to a clamped plate. The frequency response was calculated using Fast Fourier Transforms (FFTs) on the measured data and dividing the output spectrum by the input spectrum to determine the transfer function. The data collection, FFT and transfer function calculation were all automatically performed by an Ono Sokki CF-910 Dual Channel FFT Analyzer. The output signal measured was the voltage out of the proof mass accelerometer. This output, and consequently the transfer function, can easily be transformed to force by adding 4.9 dB to the magnitude response function (accelerometer scale factor time mass of the proof mass).

The transfer functions measured for each actuator are shown in Figures 2.2 to 2.5. The response is consistent between the four actuators, with the exception of the phase response of actuator #4. The 180° phase shift was found to be due to the motor coil leads being wired opposite of the other three actuators. When corrected, the phase response of actuator #4 was consistent with actuators #1 through #3.

System Model

Initially the actuators were modelled using standard linear motor equations of motion. This approach did not prove fruitful, primarily because the power amplifier circuit was constructed so that it significantly reduced the back-emf of the motor. Because of this the basic model was developed by fitting the measured transfer function with the circuit dynamics of the power amplifier plus any additional dynamics necessary to match the response. From the power amplifier circuit diagram in Appendix A, the power amplifier frequency domain dynamics are found to be

$$\frac{I(s)}{E(s)} = \frac{500}{S + 2500} \tag{1}$$

where I(s) is the current signal to the motor coil, and E(s) is the voltage signal to the power amplifier.

The resulting analytic transfer function that gives the best fit to the data is
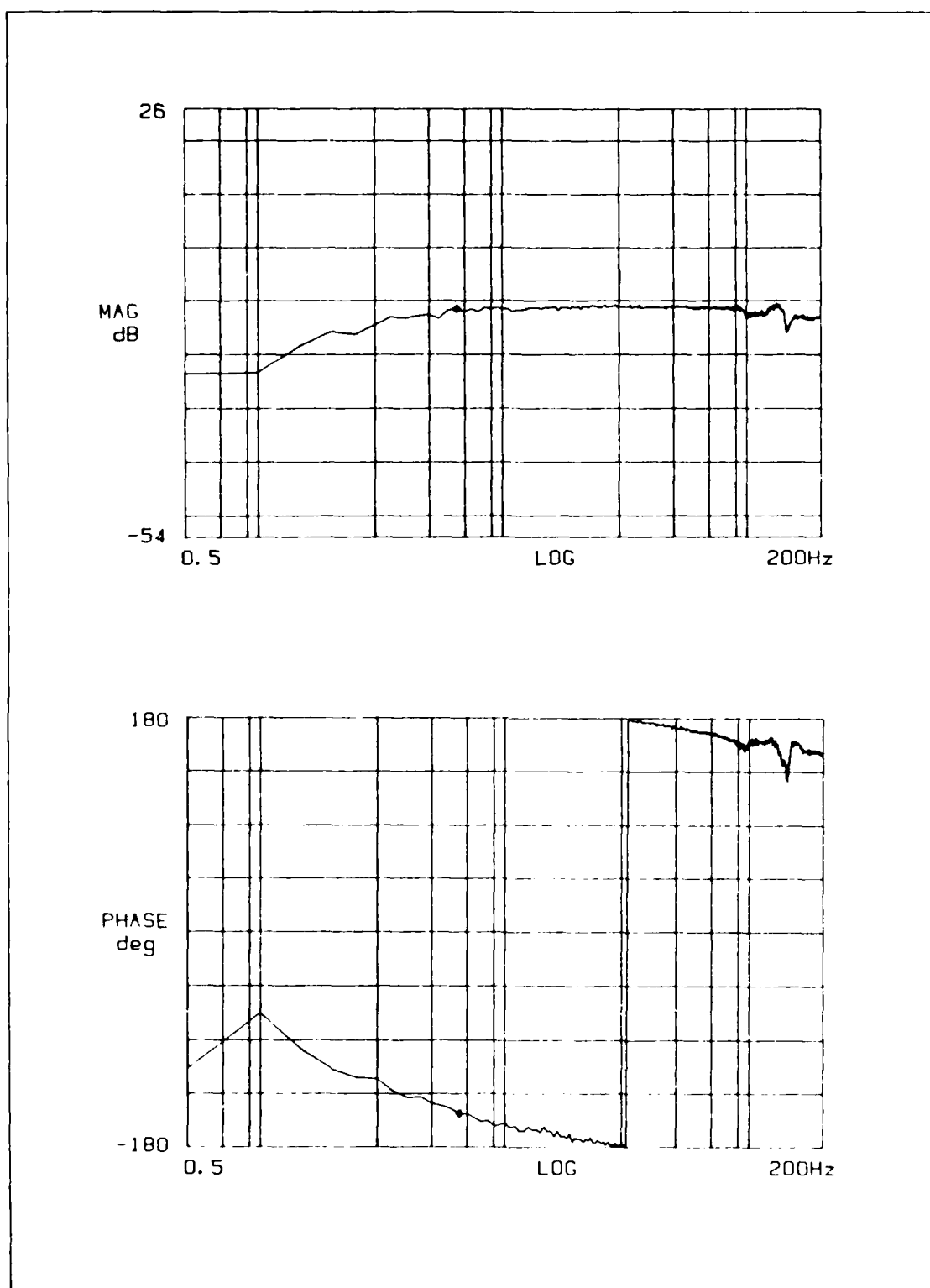
Figure 2.2. Actuator #1 Open Loop Transfer Function
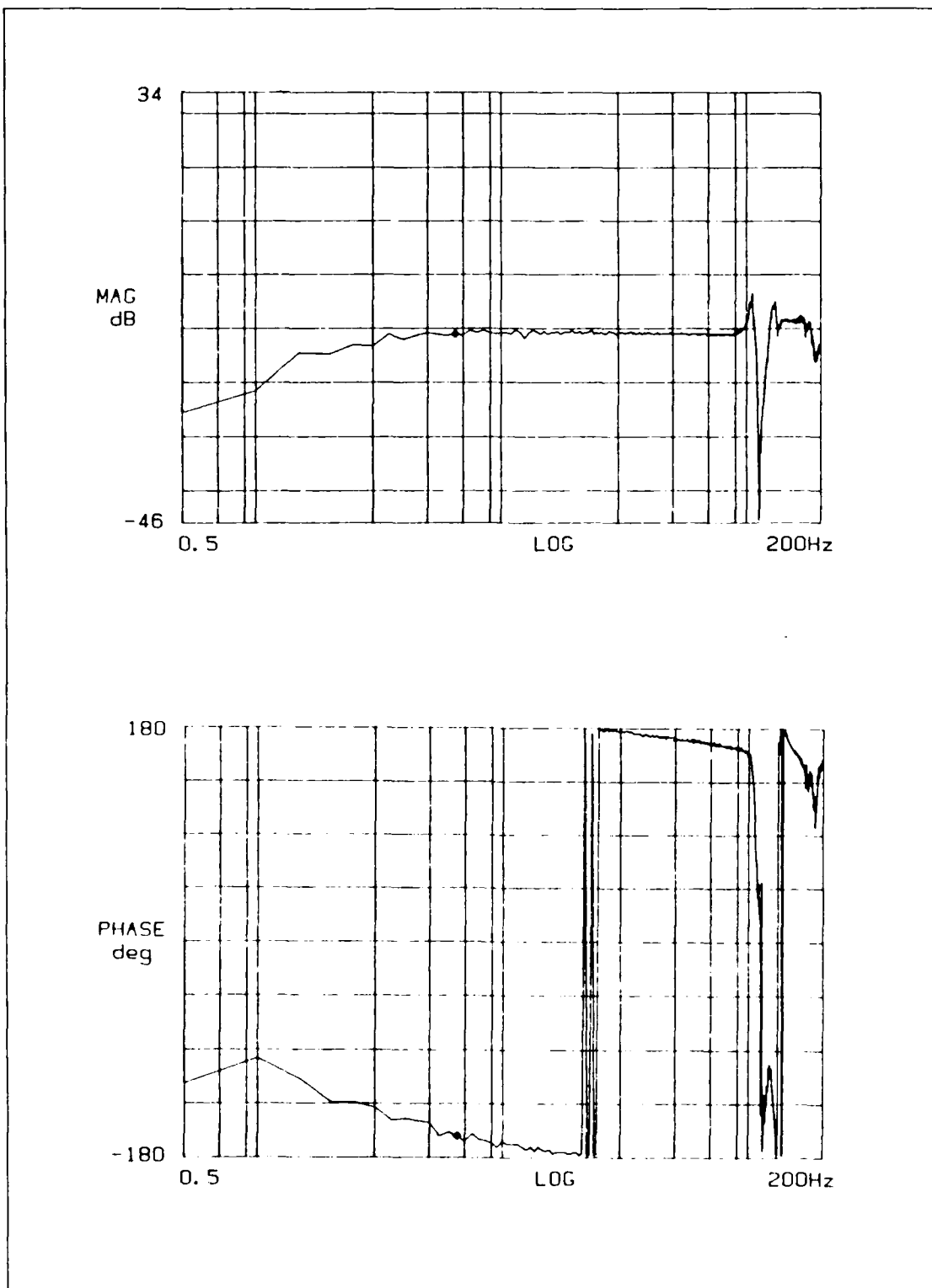
Figure 2.3. Actuator #2 Open Loop Transfer Function
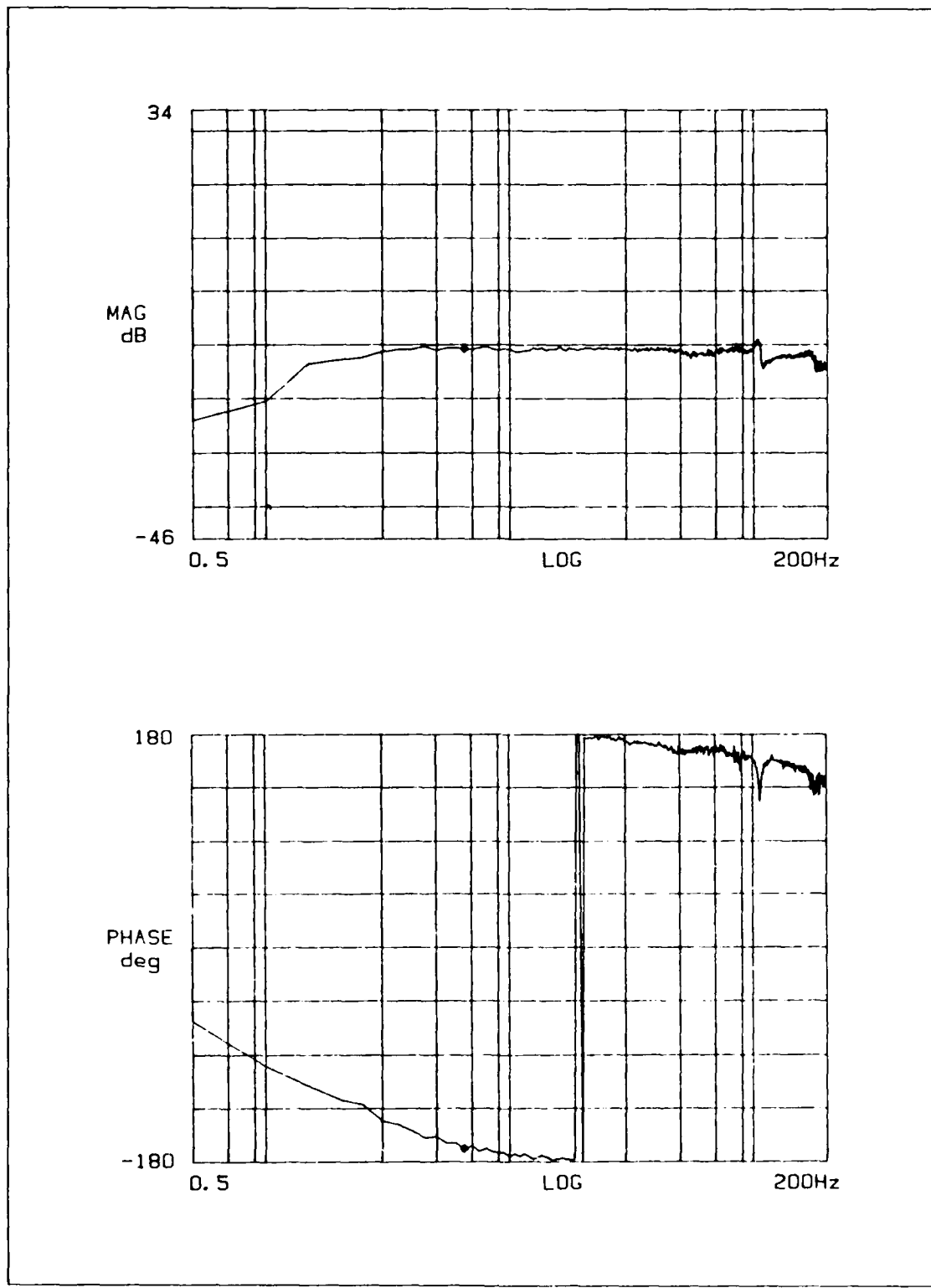
Figure 2.4. Actuator #3 Open Loop Transfer Function
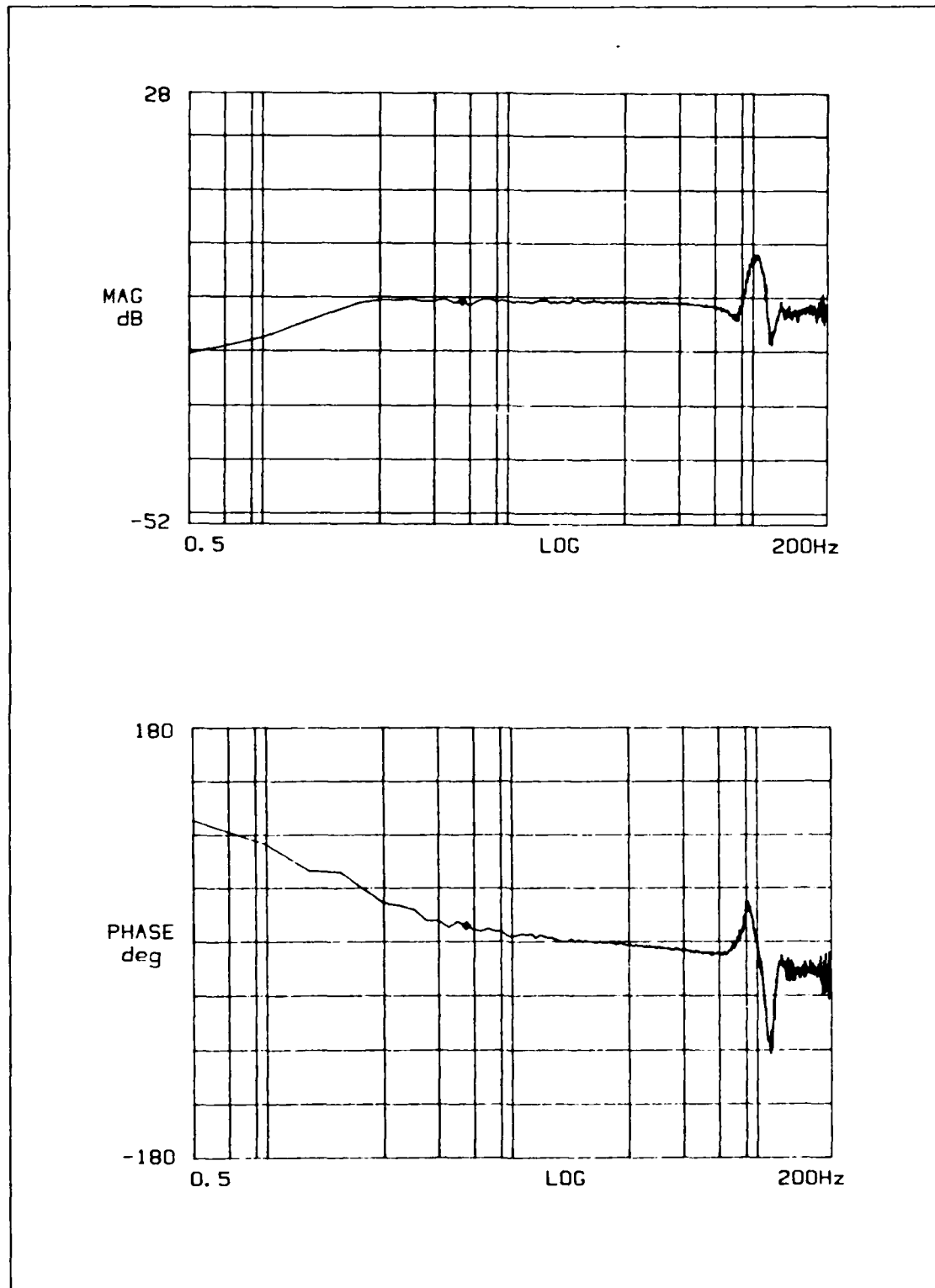
Figure 2.5. Actuator #4 Open Loop Transfer Function

$$\frac{\overset{..}{X}(s)}{E(s)} = \frac{500\ S}{(S + 35)(S + 2500)} \qquad (2)$$

Figures 2.6 and 2.7 show comparisons of the magnitude and phase response of this transfer function with the frequency response measured for actuator #1. The model matches the data very closely except in the very low frequencies (below 1 Hz). The low frequency data is somewhat suspect due to the short sample times and low input amplitude required to complete a test on the uncompenstated actuator without driving the proof mass into the end bracket. Figure 2.8 shows the coherence for the actuator #1 frequency response, which is a measure of the correlation between the input and output. A coherence of 1.0 indicates perfect correlation between input and output, while 0.0 indicates no correlation at all. The coherence measured for low frequencies is very poor, indicating the data is suspect.

The model also does not include the dynamics which are obviously present in the measured data around 150 Hz. This effect appears to be a mechanical response in the actuator, however the frequency is much too low to match either the first bending mode of the end bracket or the first axial vibration mode of the motor shaft. To isolate the effect the mounting bracket was instrumented with an accelerometer and the response measured while driving the actuator with a random input signal. Figure 2.10 shows the transfer function between the voltage command input and the bracket acceleration. Comparing this response with the actuator transfer function indicates the energy is indeed being transfered to the mounting brackets and not the proof mass in the 150 Hz range. Since this effect is outside the desired control bandwidth for the structure, the command signals should not have any spectral content
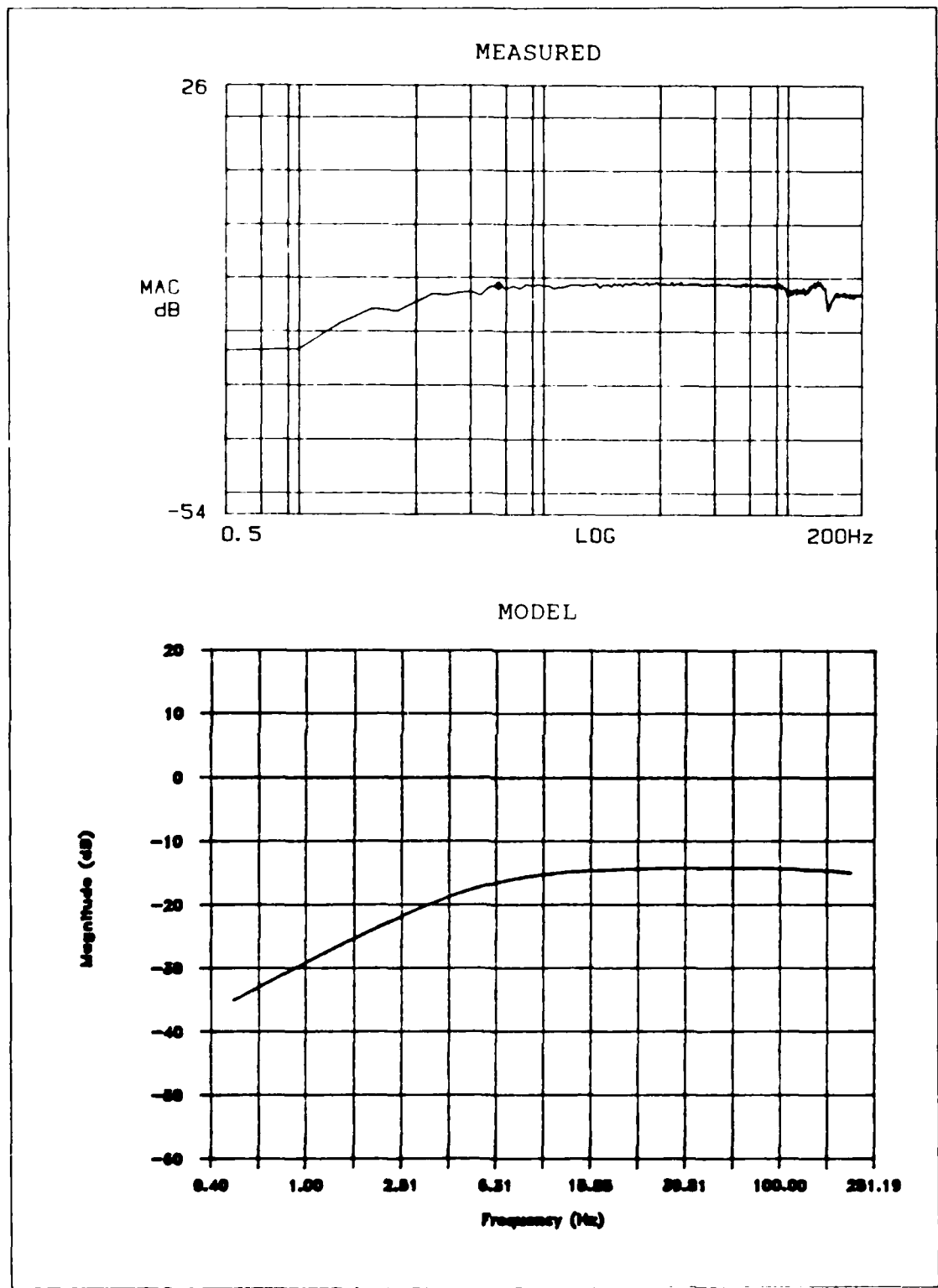
MEASURED

MODEL

Figure 2.6. Actuator #1 Magnitude Response - Measured vs Model
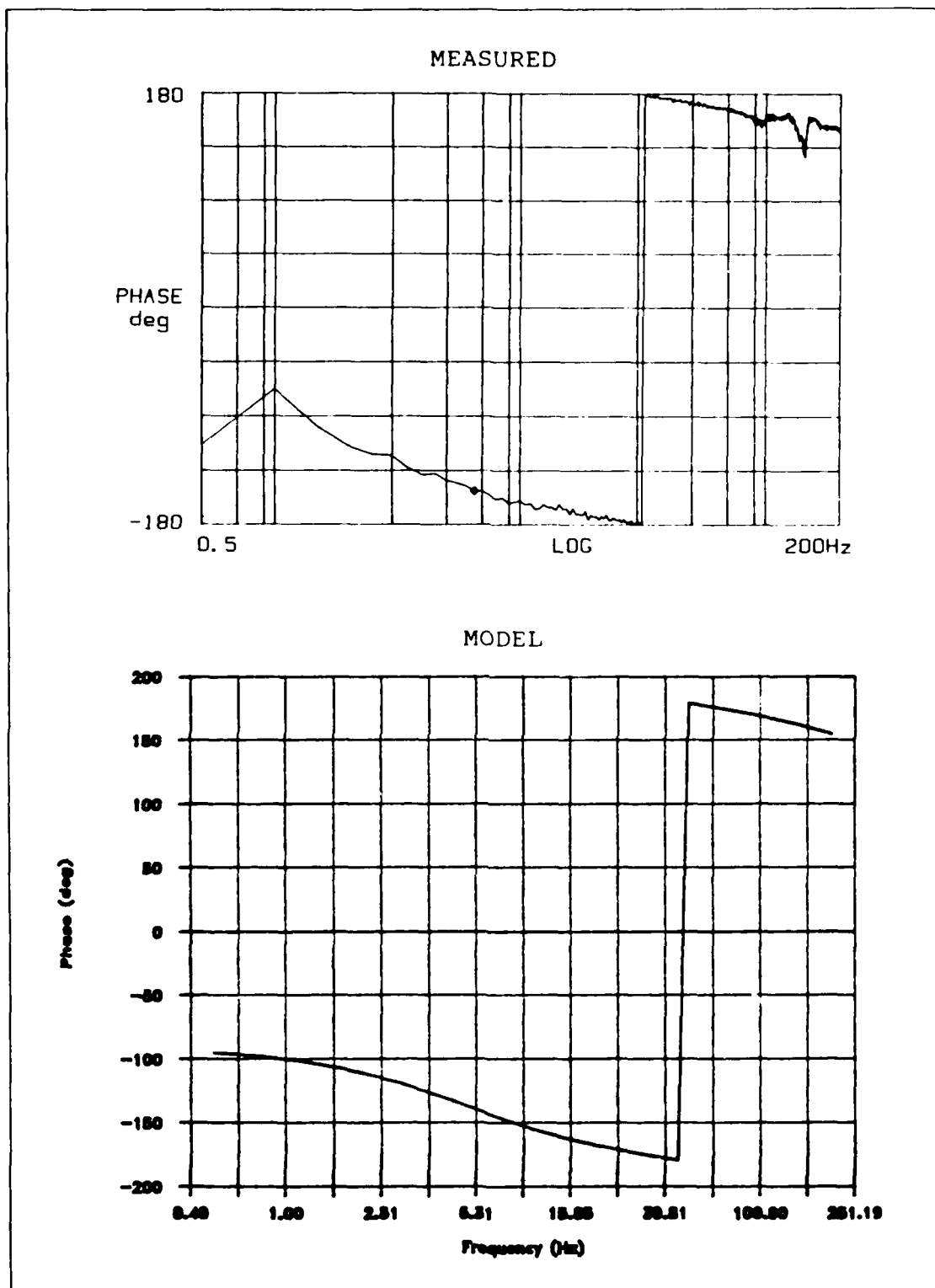
Figure 2.7. Actuator #1 Phase Response - Measured vs Model
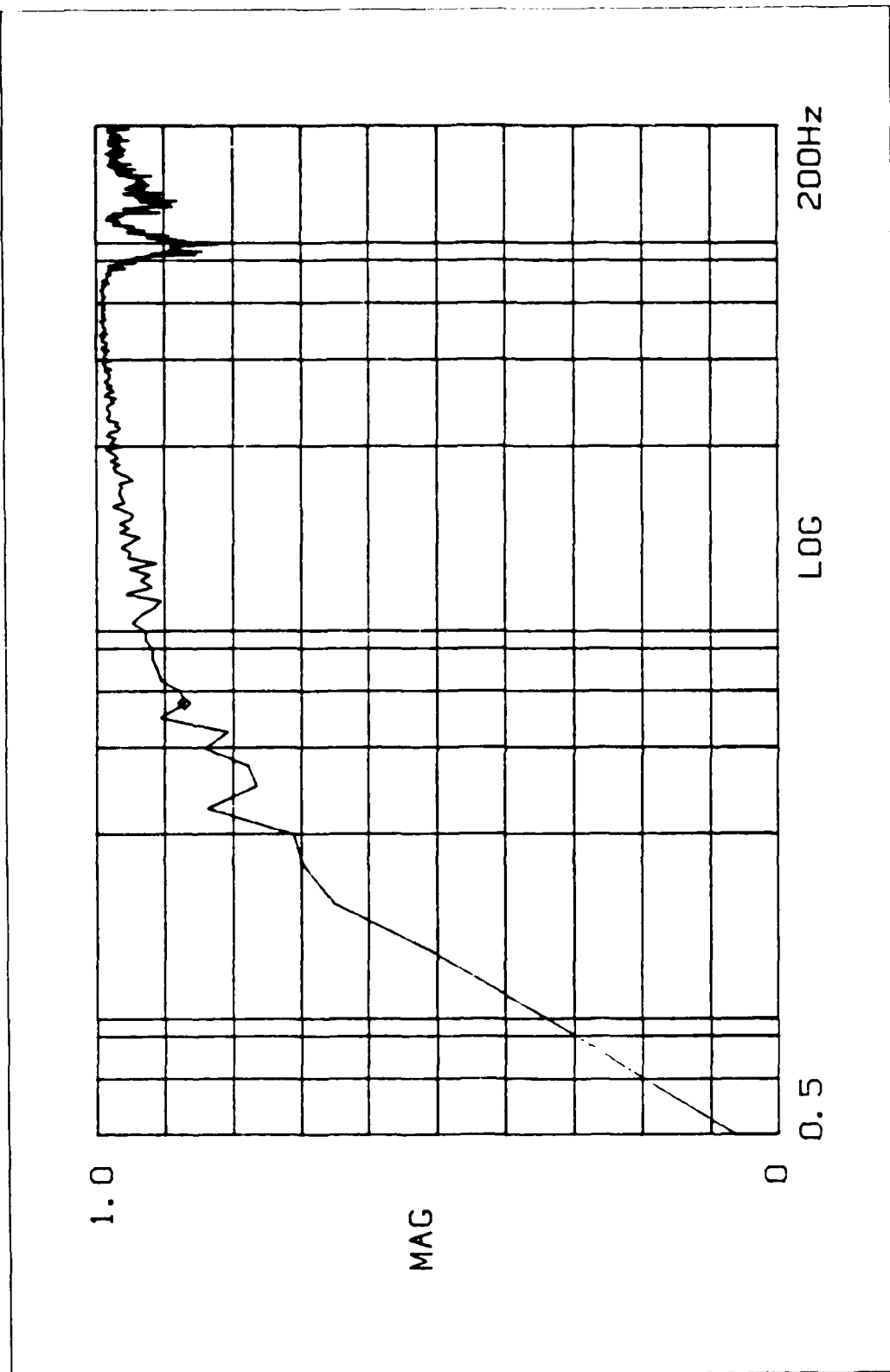
Figure 2.8. Actuator #1 Transfer Function Coherence
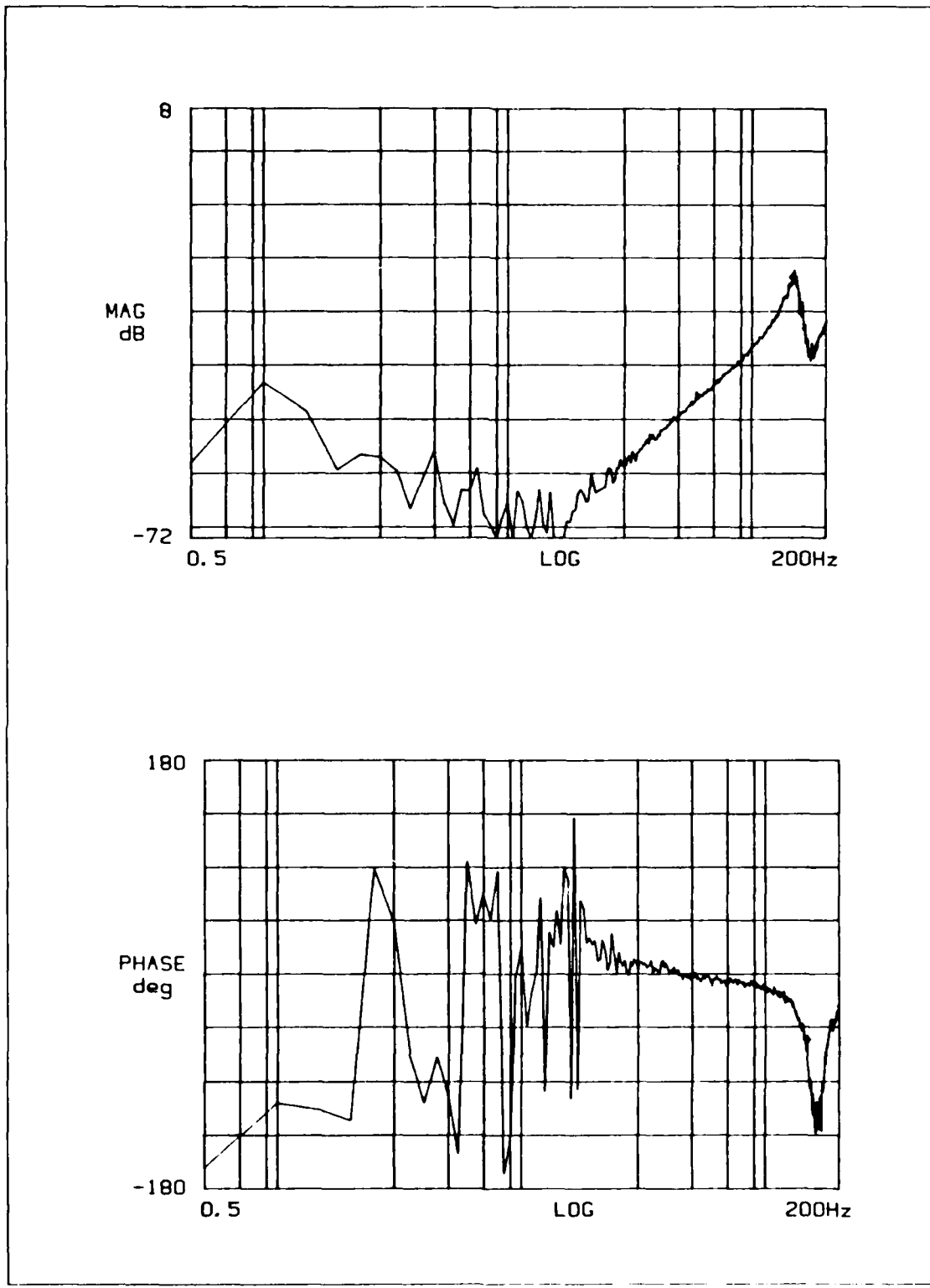
Figure 2.9. Actuator Mounting Bracket Response Function

in this frequency range. Ignoring it should not cause a problem other than perhaps adding some noise in the acceleration feedback.

To further evaluate this model, and determine that the high frequency response is not aggrevated by changing the system dynamics, a position feedback loop was implemented using the LVDT output signal. The LVDT is modelled as a double integrator of the proof mass acceleration and a gain. The gain is calculated by applying the nominal motor parameters and the nominal LVDT scale factor (see Appendix A). The resulting closed loop model is represented by the block diagram in Figure 2.10.
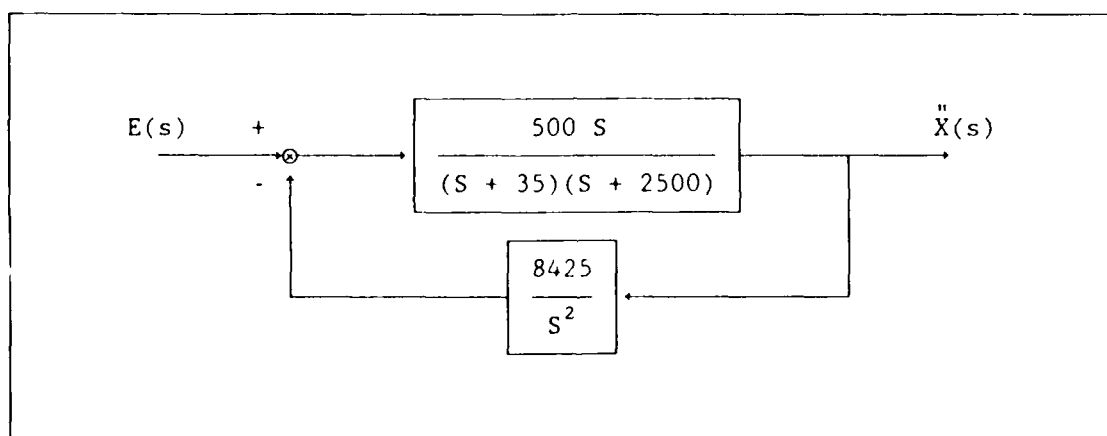
Figure 2.10. Position Feedback Block Diagram

Figures 2.11 and 2.12 compare the transfer function derived from this analytic model and the transfer function measured for actuator #1. Agreement between the model and measured data is good and the high frequency response has not been aggrevated.
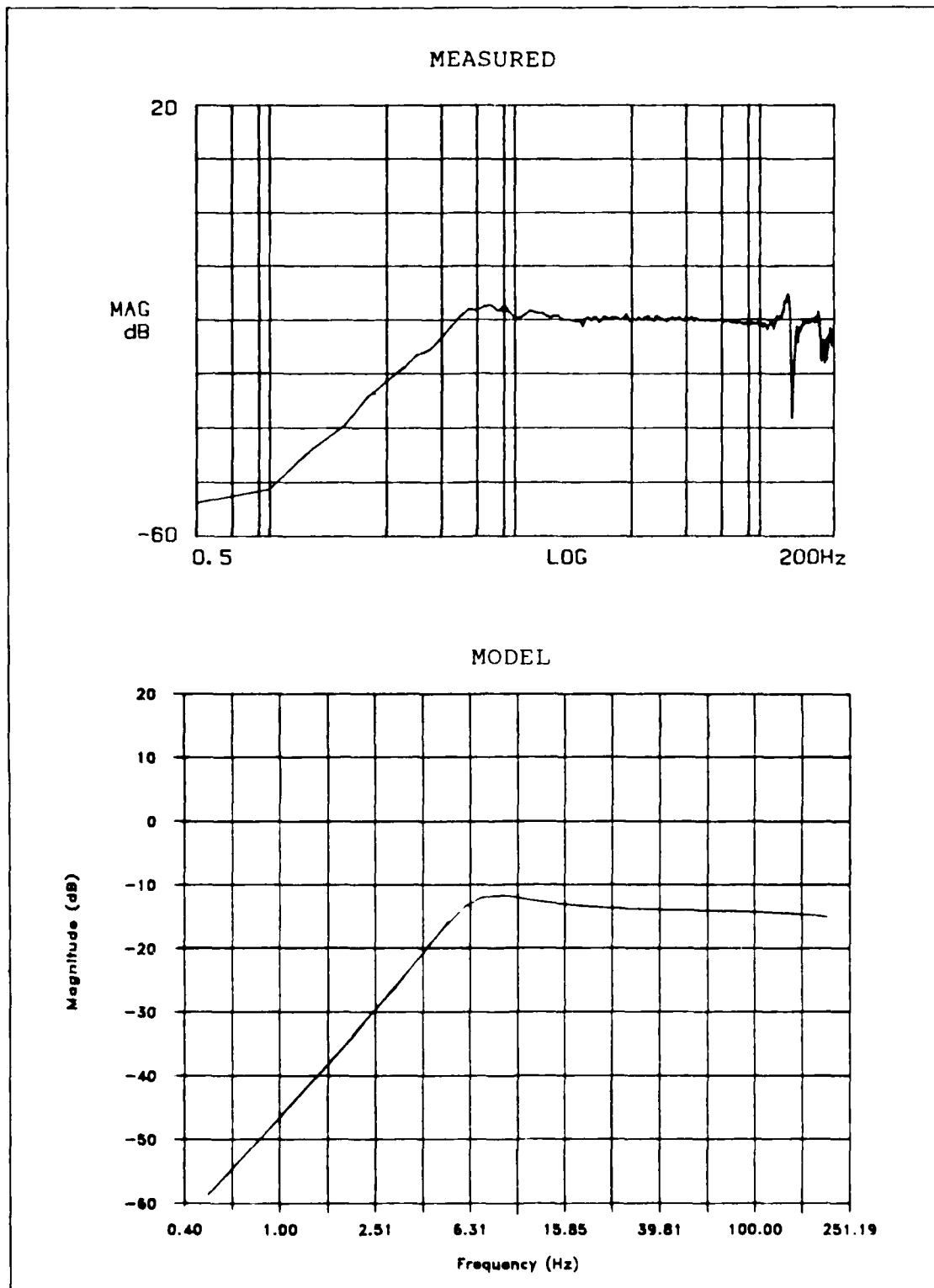
Figure 2.11. Position Feedback Magnitude Response Comparison

MEASURED

MODEL
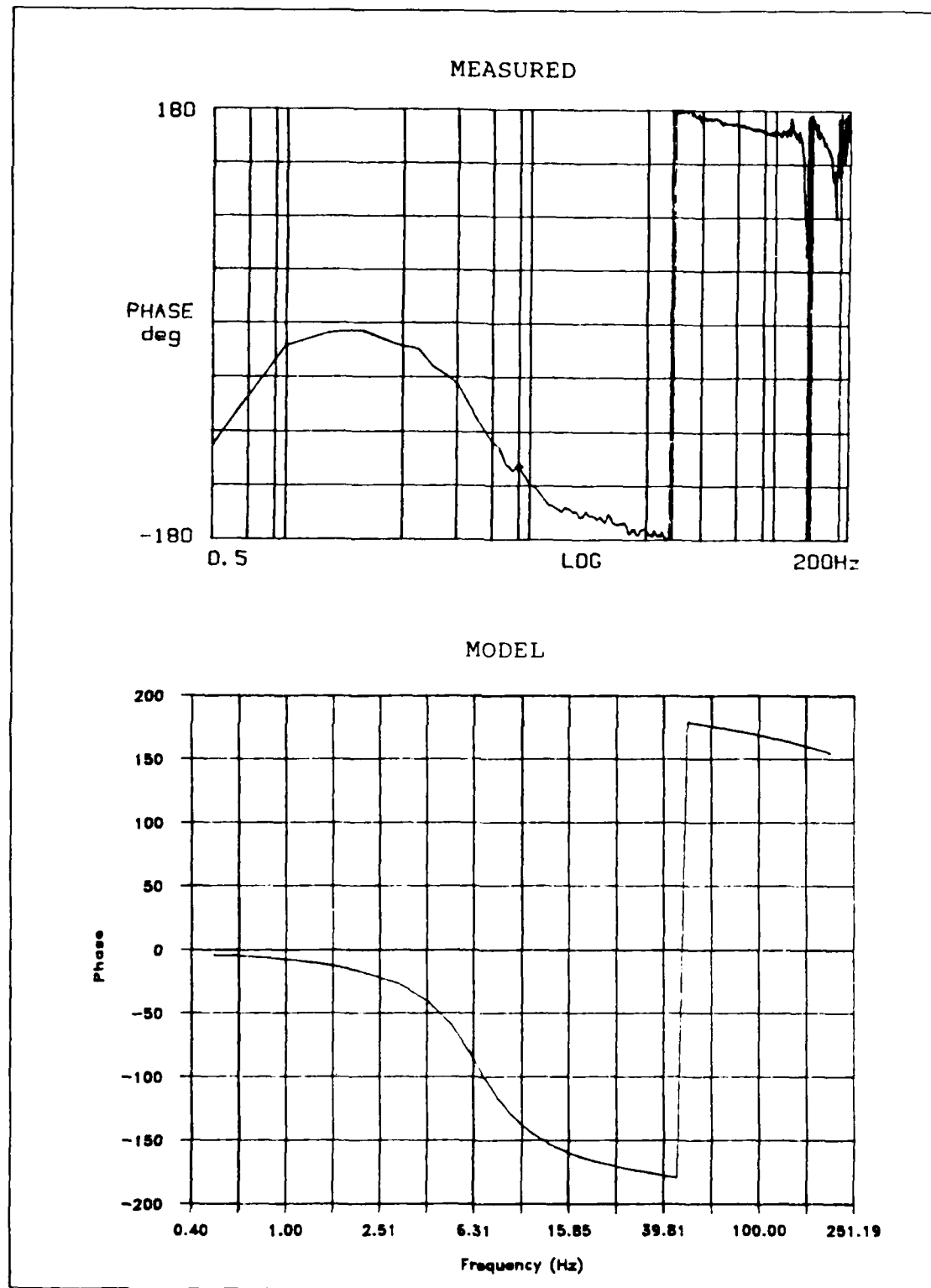
Figure 2.12. Position Feedback Phase Response Comparison

Control Design

The parameters accessible in this system are the current command
from the power amplifier to the motor coil, the proof mass acceleration,
and the relative position between the end bracket and proof mass as
measured by the LVDT. Evaluating the affect of these parameters as
feedback signals on a heuristic level, one notes that position feedback
has the same effect as adding a spring between the end bracket and proof
mass. This would help in accomplishing the design goals of maintaining
the centering of the proof mass, as well as helping to limit its travel.
Since proof mass acceleration varies from the force by only a constant,
it would have the effect of feeding back the desired output. This
should provide not only a more accurate response, but also an error
signal which will accomplish the goal of maintaining an inertial proof
mass position when the actuator is uncommanded. A current feedback loop
around the power amplifier may help improve the accuracy of the current
command, but since the power amplifier dynamics are already outside of
the control bandwidth, it should not be necessary to modify its
response.

To move the actuator dynamics outside the control bandwidth, a root
locus analysis was used to determine the effects of closing the feedback
loops discussed above. Closing the position feedback loop adds a low
order pole to the system, which with increasing gain combines with the
(S + 35) root and forms a complex pair. The break frequency for this
pair occurs at approximately 6.5 Hz. If the acceleration loop is closed
around the position feedback, the order of the system remains the same
and the break frequency of the complex pole pair is lowered as the gain
is increased. To have all effects of these roots out of the control
bandwidth requires placing them below 0.2 Hz.

Figure 2.13 shows a block diagram of this preliminary configuration. While it is theoretically possible to move the complex pole pair as close to the origin as desired, the gain required to move the poles below 0.2 Hz is approximately 100. Since nominal gain for the operational amplifiers intended to be used in this control circuit is 10, this would require more than one amplification stage, and would most likely saturate the amplifiers. An alternative to this is to boost the acceleration gain as much as the circuit will handle, and then adjust the overall response by prefiltering the input signal. Applying a gain of 10 to the acceleration feedback would move the poles below 1 Hz. Increasing the position feedback gain will drive the damping ratio down and reduce the frequency range over which the phase contribution of these poles acts. A predicted frequency response for this configuration is shown in Figure 2.14. This configuration has a prefilter (lag compensation), position feedback gain of 0.1, and an acceleration feedback gain of 10. This provides not only a fairly flat response over the bandwidth, but also the centering and inertial position control desired.

Closed Loop Testing

Many technical problems were discovered while implementing the control design. A discussion of each of the major problems encountered and their resolution, if any, is in Appendix B. There were two important problems which led to changing the control design. First, the acceleration gain could not be increased beyond a factor of 6 without high frequency noise dominating the feedback signal. Figure 2.15 shows the frequency response measured for the baseline configuration with the
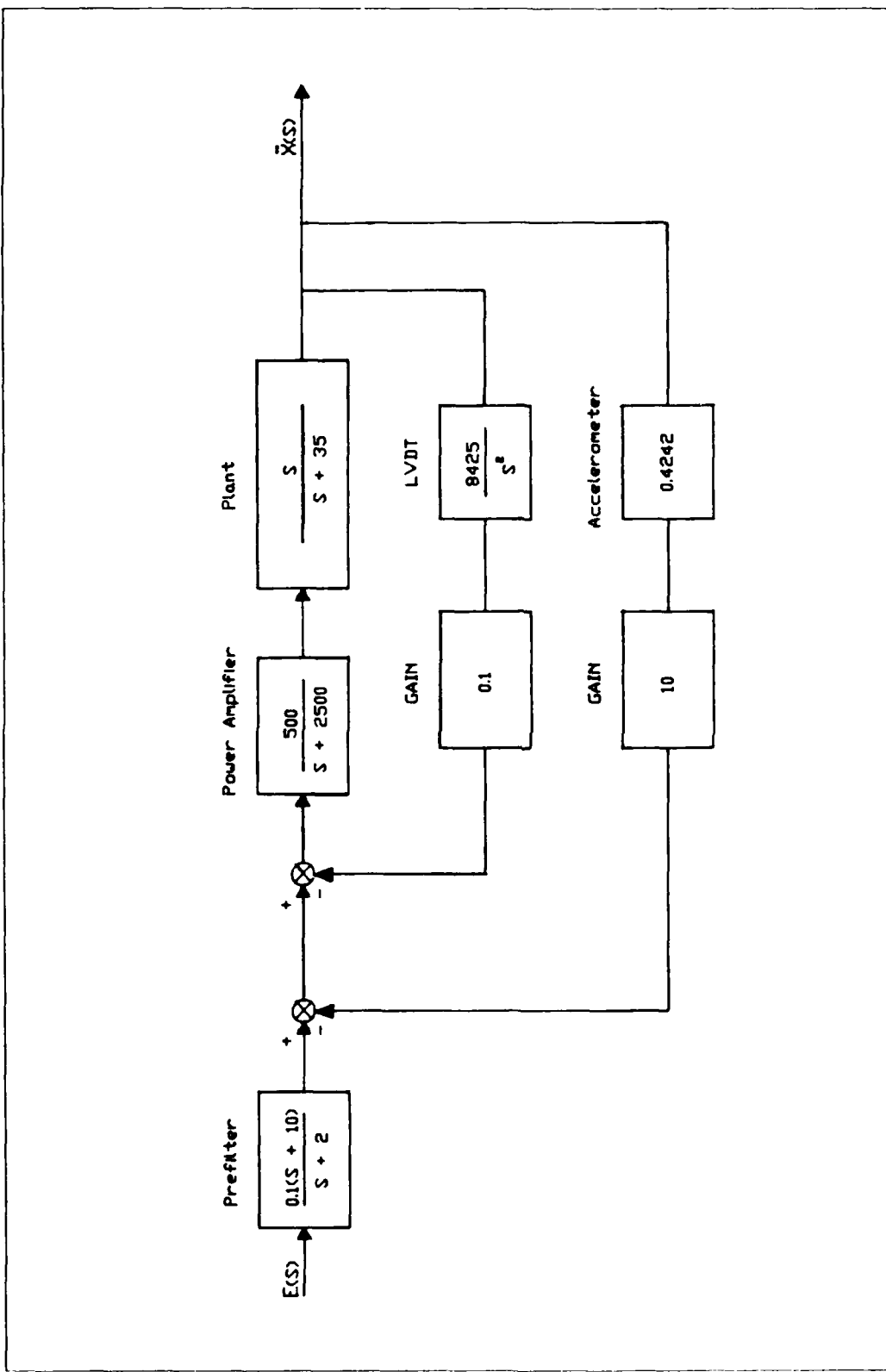
Figure 2.13. Preliminary Control Design Block Diagram
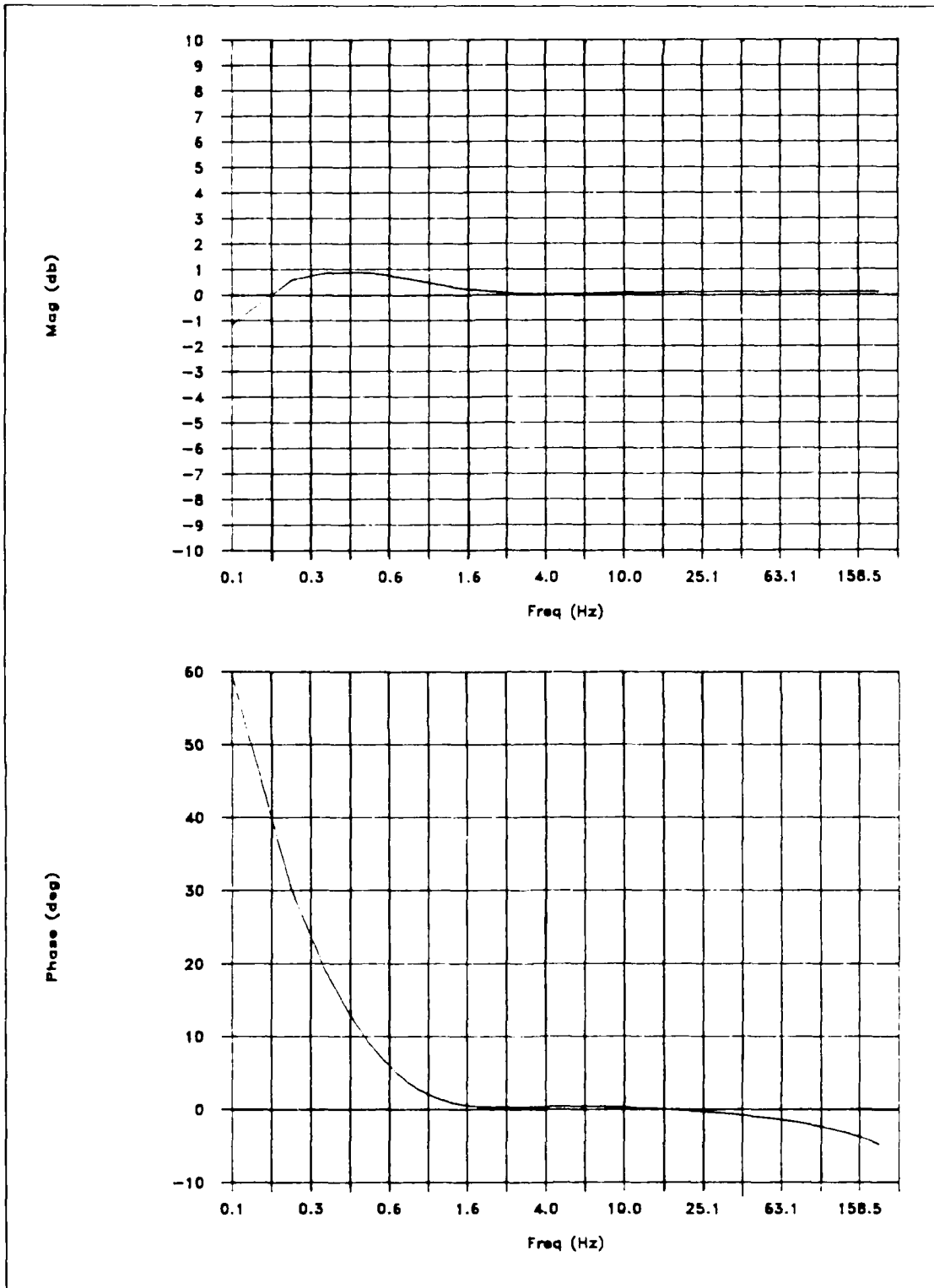
Figure 2.14. Preliminary Control Design Predicted Frequency Response
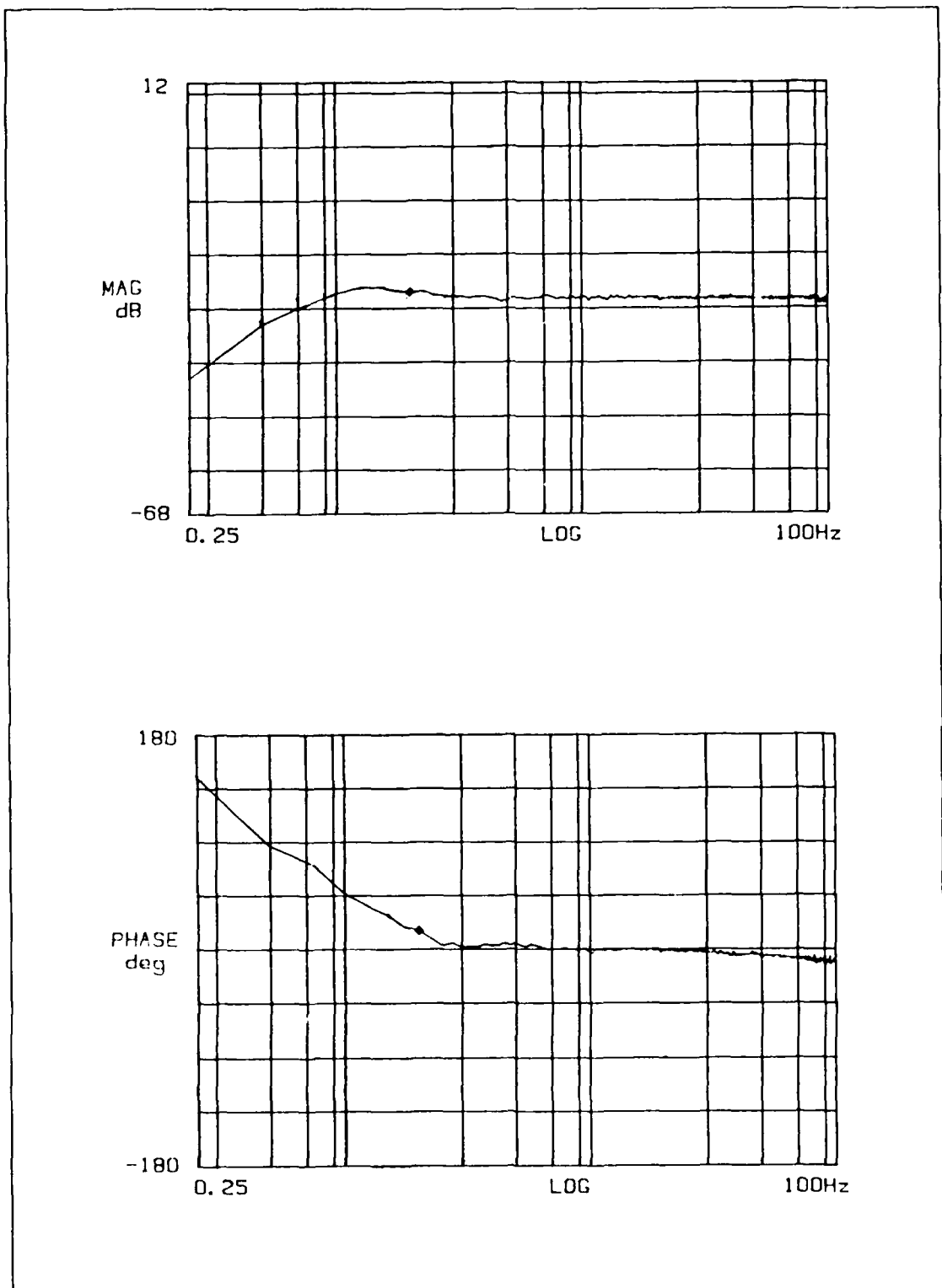
Figure 2.15. Preliminary Control Design Measured Frequency Response

acceleration feedback gain at 5 and the position feedback gain at 0.05.
While the magnitude response is fairly flat, there is too much low
frequency phase shift. The input prefilter can be adjusted to further
reduce the phase, but it then has the undesireable side effect of
increasing the magnitude over the same range. Since noise was the
limiting factor a low-pass filter with a break frequency of 100 Hz was
placed in the acceleration feedback loop.

The second problem was that the centering of the proof mass shifted
as the amplitude of the input signal was increased, even with the
position feedback loop. In an attempt to correct the centering problem,
a feedback loop was placed around the power amplifier. Initially, this
loop was also plagued by high frequency noise problems. By changing the
inverter in the feedback path to a low-pass filter with a break
frequency of 50 Hz, the noise problem was significantly reduced. This
modification did not help the centering problem, however it did reduce
the overall noise in the system and improve the "quality" of the
response data (measured transfer functions were much smoother and more
repeatable). The solution to the centering problem was later found to
be associated with unstable, very high frequency oscillations (kilohertz
range) in the power amplifier. Details of this problem are discussed in
Appendix B.

Making the modifications discussed above and several adjustments to
gains results in the configuration shown in Figure 2.16. Figure 2.17 is
the circuit implementation of this block diagram. Since the low-pass
filters in the feedback loops add zeros in the closed loop system, an
additional pole was added as a prefilter to reduce the phase. The
desired response for each actuator was set by adjusting the various
potentiometers in the circuit, which accounted for variations in gain
and sensitivity of the various elements in the system.
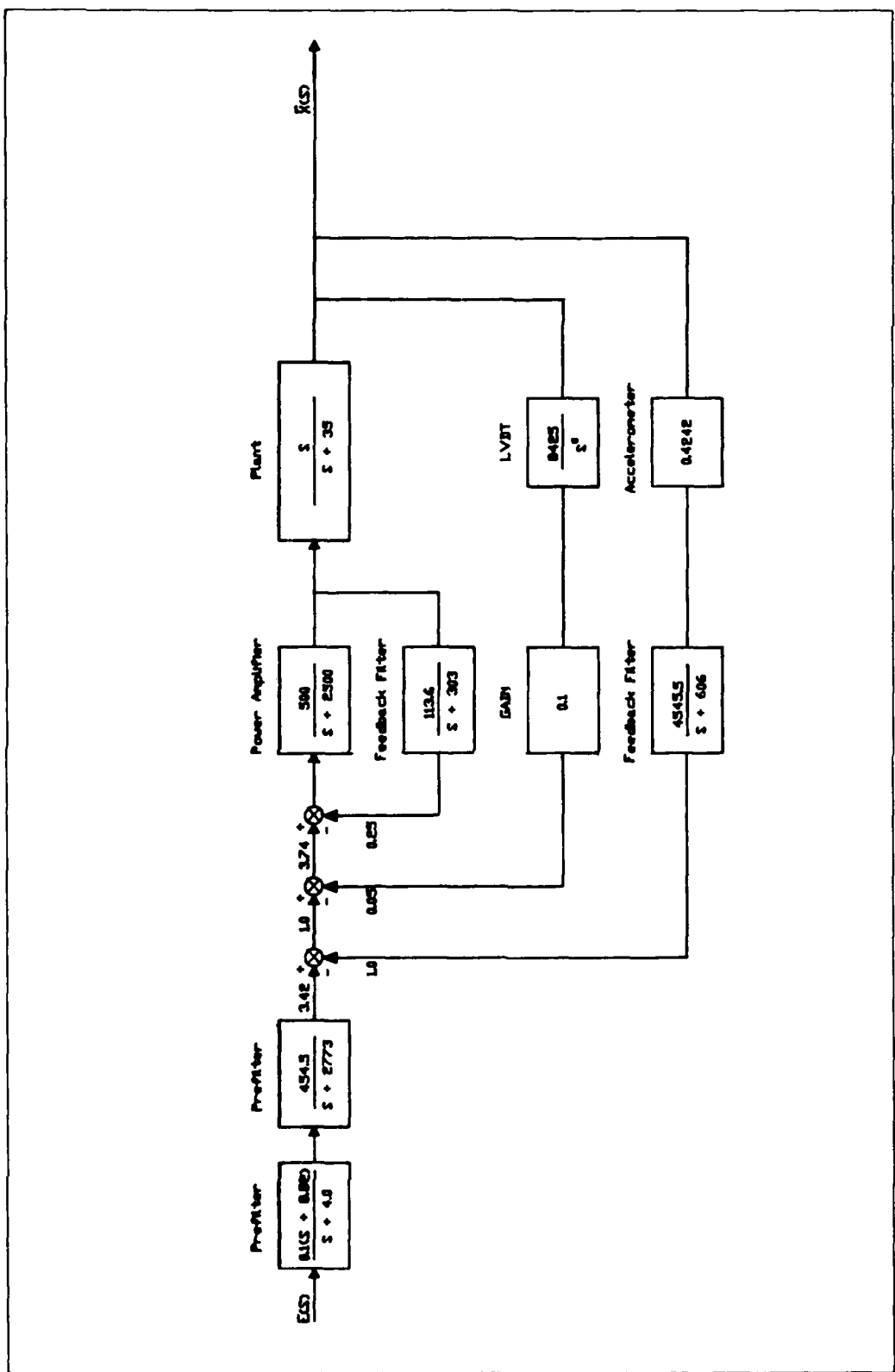
Figure 2.16. Final Control Configuration Block Diagram
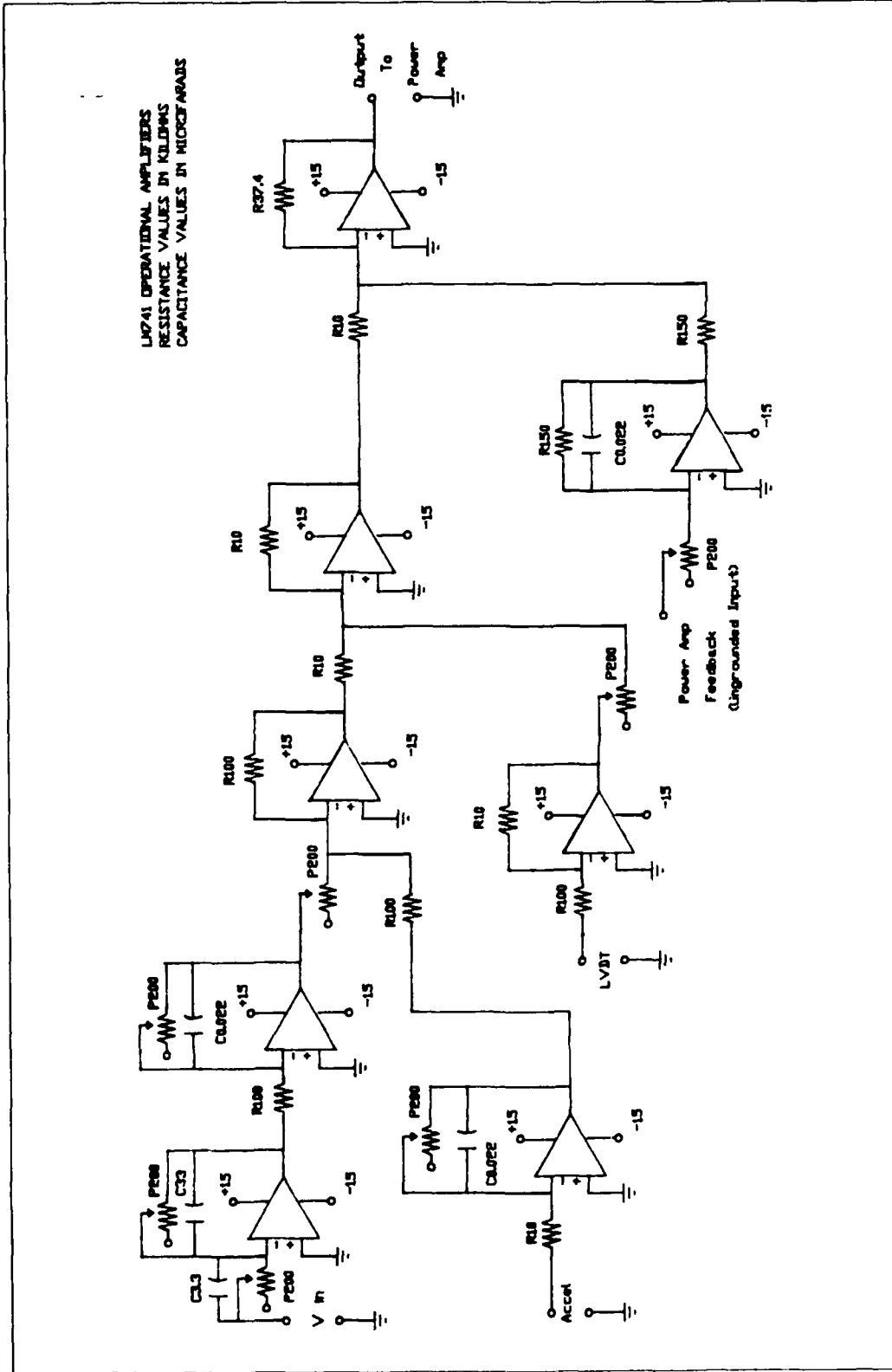
Figure 2.17. Actuator Compensator Circuit Diagram

The predicted frequency response of this configuration is shown in Figure 2.18. The measured response of the four actuators is overlaid on the prediction in Figures 2.19 and 2.20, and show excellent agreement with the prediction. The frequency response was measured using a sine sweep rather than the random input tests. This test drives the actuator at a single frequency, measures the response, and then increments to the next frequency. The method gives more consistent results and is a much better approximation to the actual commands the actuator will receive when mounted on the structure.

Characterization of Final Actuator Configuration

To fully evaluate the actuator performance, a series of tests were performed that simulated the operating environment an actuator will experience when mounted on the beam. These tests measured the actuator frequency response with the base free to move, the maximum force output of the actuators at each modal frequency, the uncommanded actuator response to base motion (how well the proof masses "float"), and the variation of the transfer function while forces are applied orthogonal to the direction of proof mass motion.

A better estimate of the actual performance the actuators will deliver when fixed to a moving beam can be made by testing each actuator on a slip table. The slip table is a plate which rides on bearings and is free to move in a single direction. The test configuration is depicted in Figure 2.21. The force output of the actuator was derived by measuring the acceleration of the base plate and multiplying by the combined mass of the plate and actuator base (all components except the proof mass). Figures 2.22 to 2.25 show the transfer functions measured
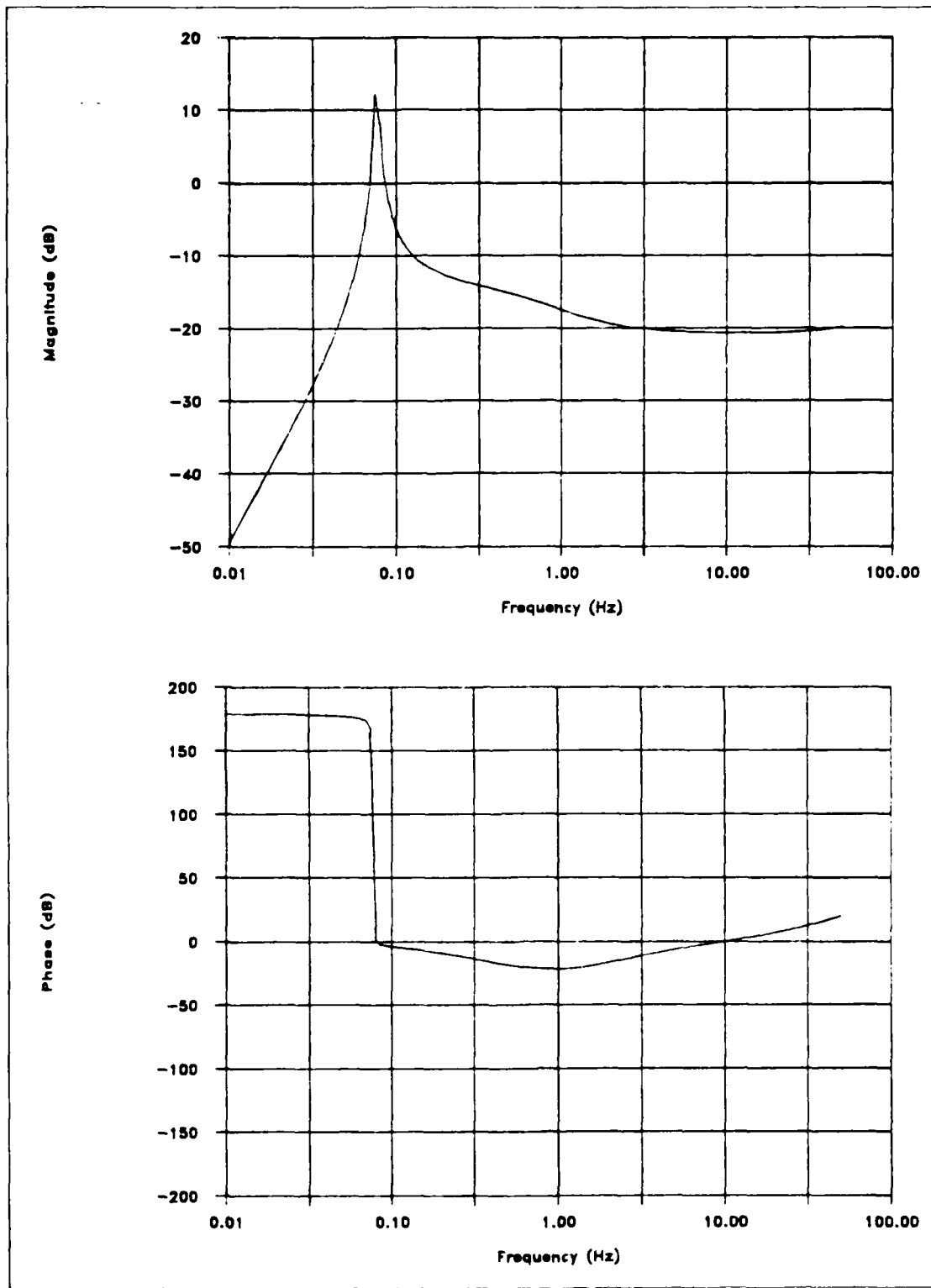
Figure 2.18. Predicted Frequency Response of Final Configuration
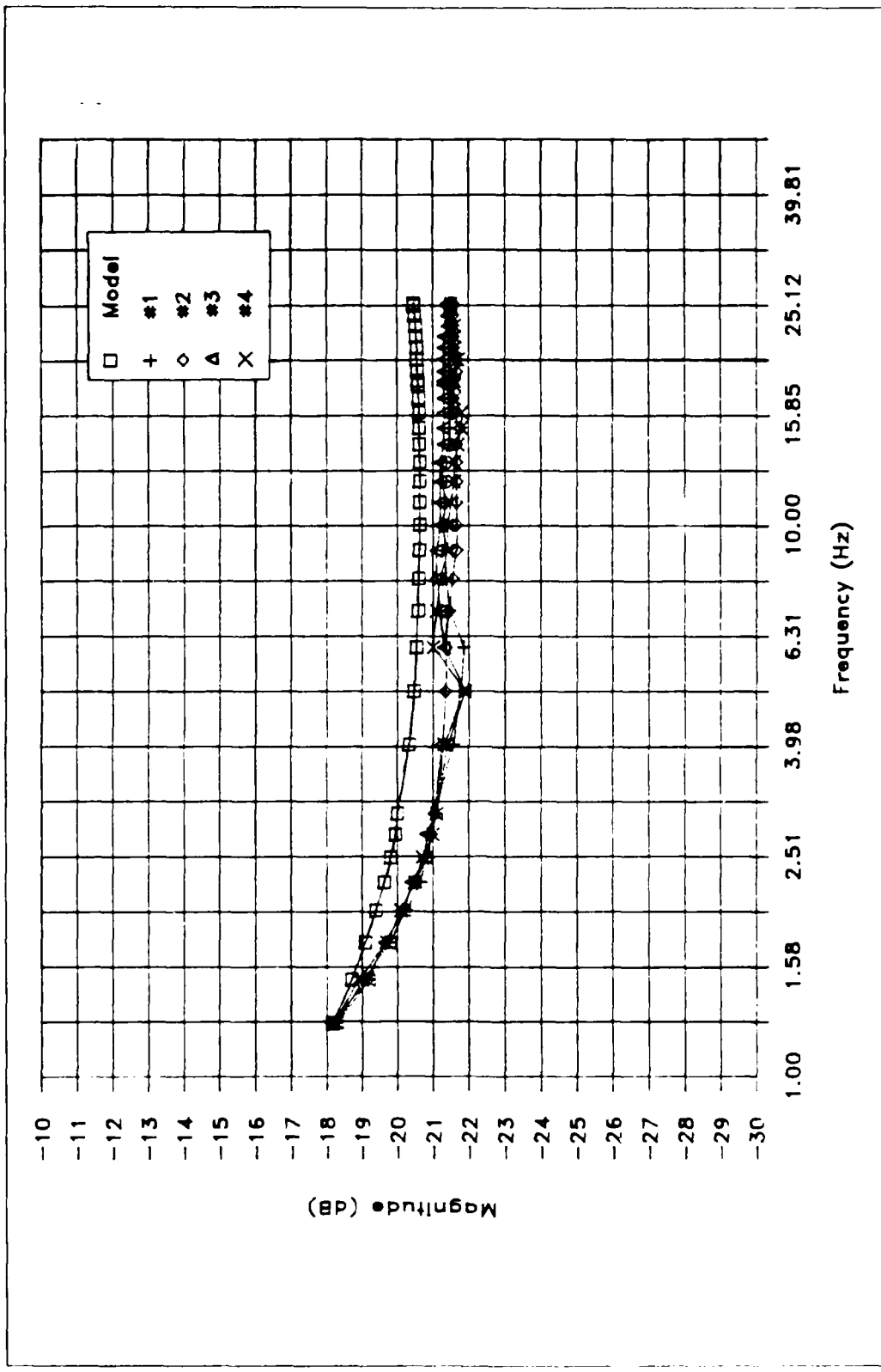
Figure 2.19. Compensated Actuator Transfer Function - Predicted vs Measured Magnitude
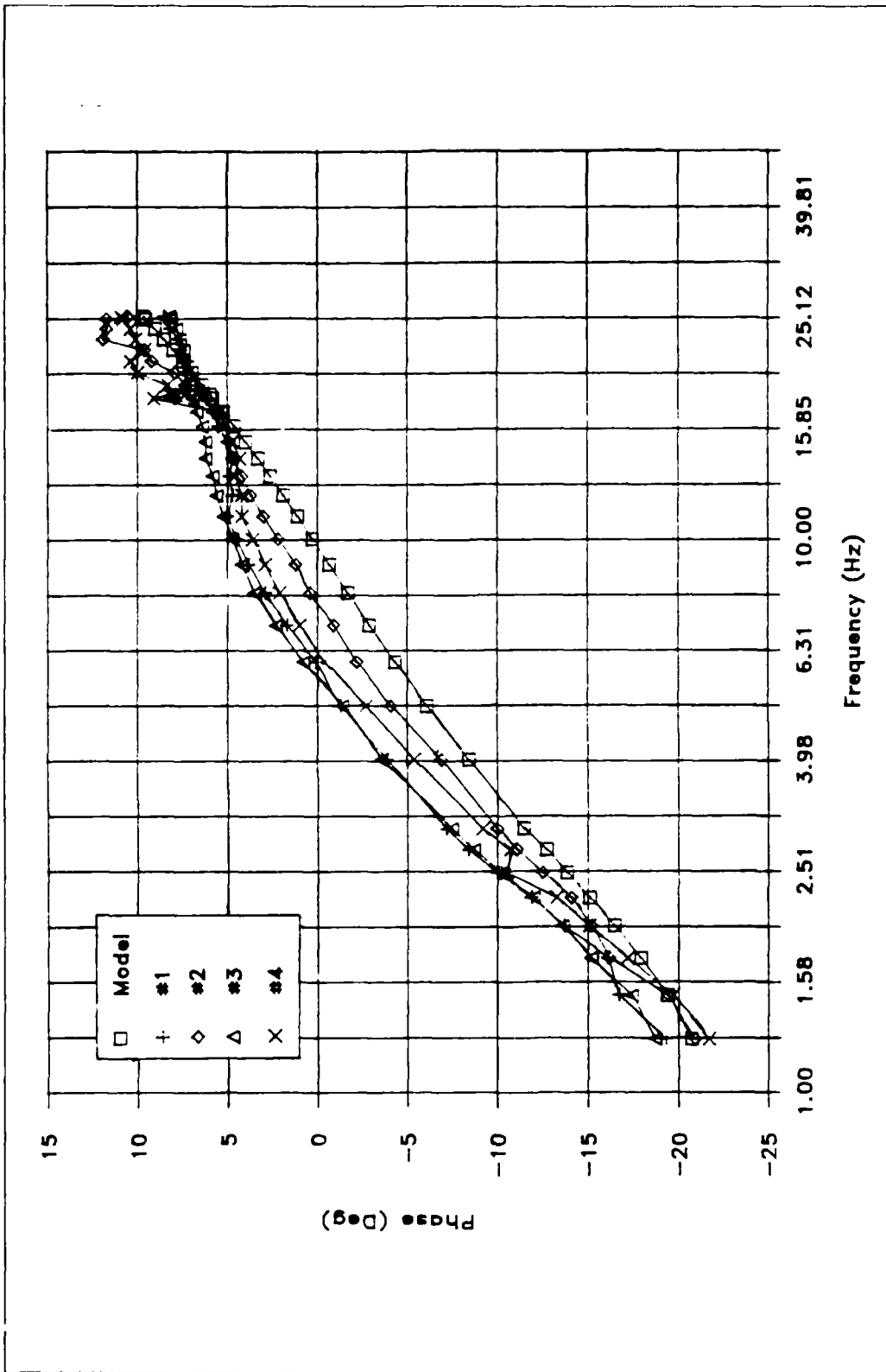
Figure 2.20. Compensated Actuator Transfer Function - Predicted vs Measured Phase
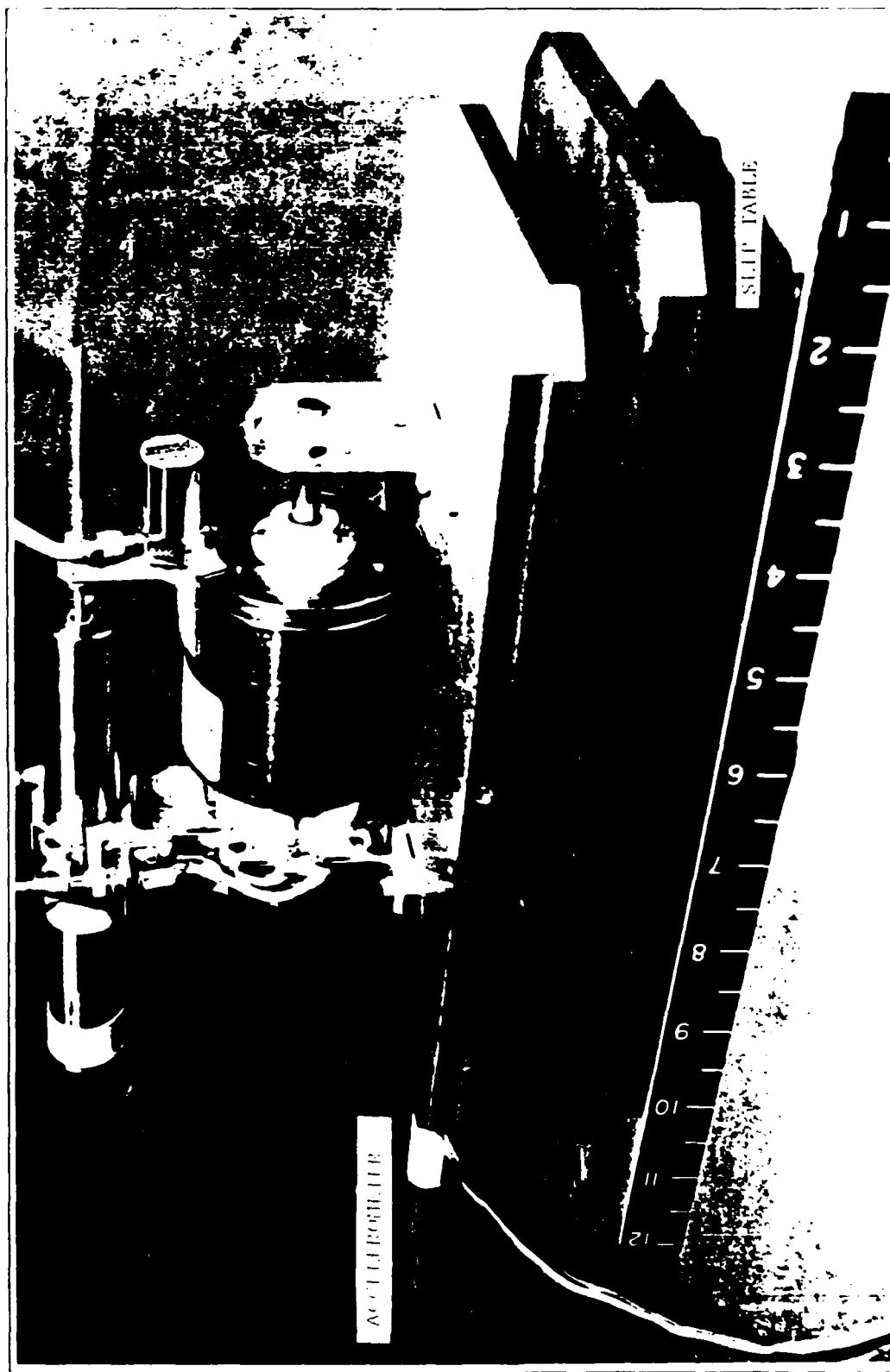
Figure 2.21. Actuator Slip Table Test Configuration
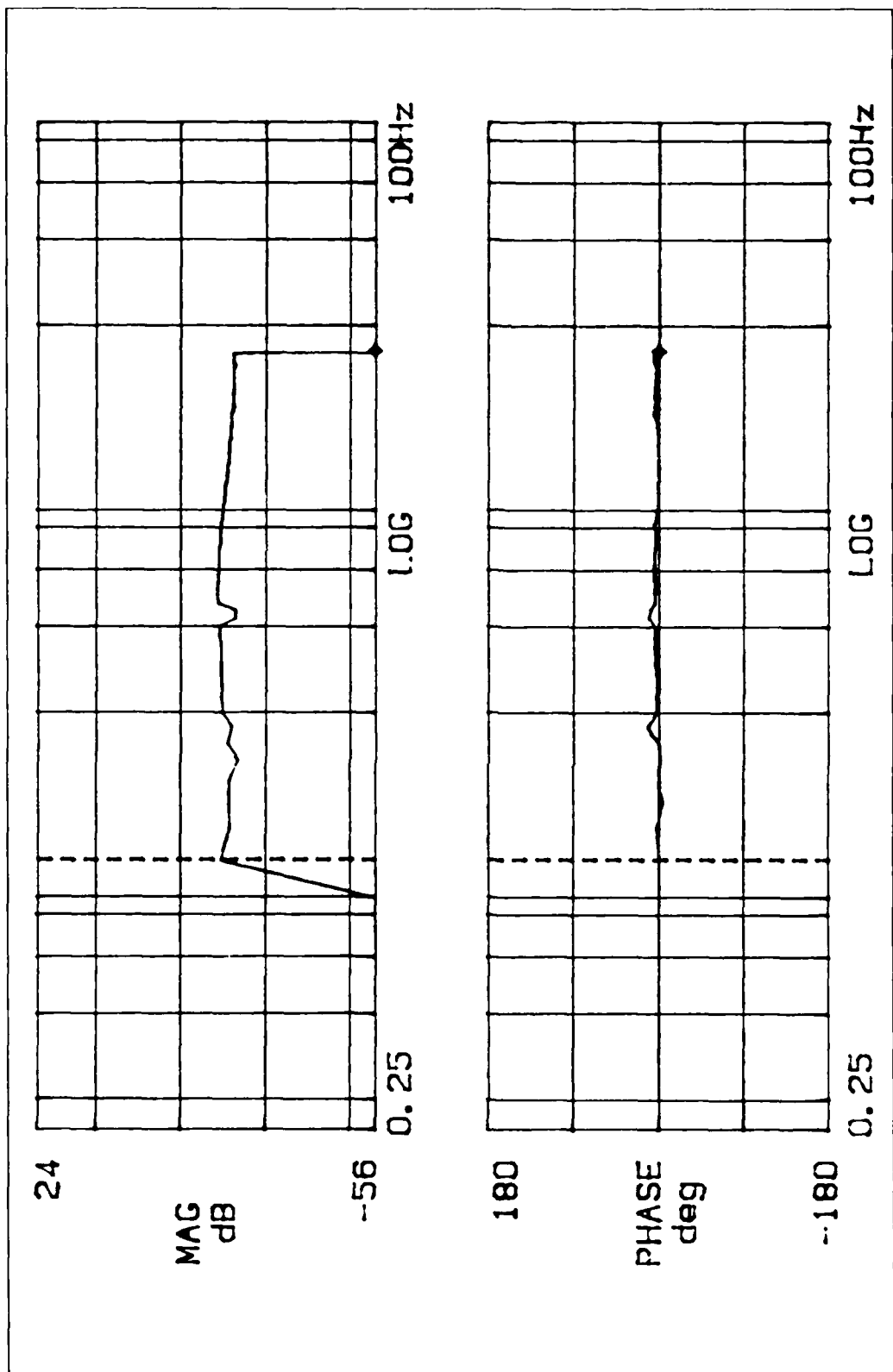
Figure 2.22. Actuator #1 Slip Table Transfer Function
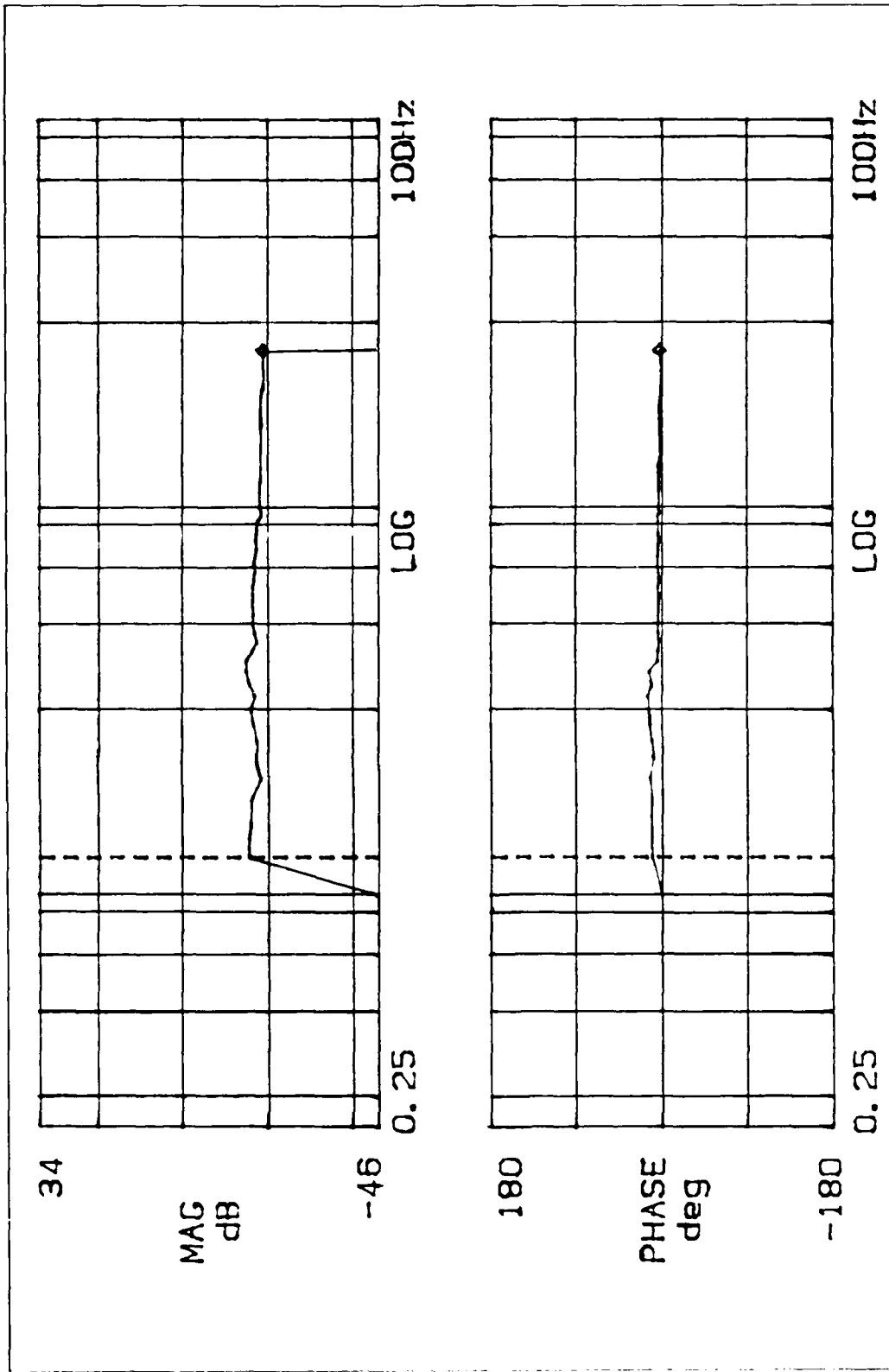
Figure 2.23. Actuator #2 Slip Table Transfer Function
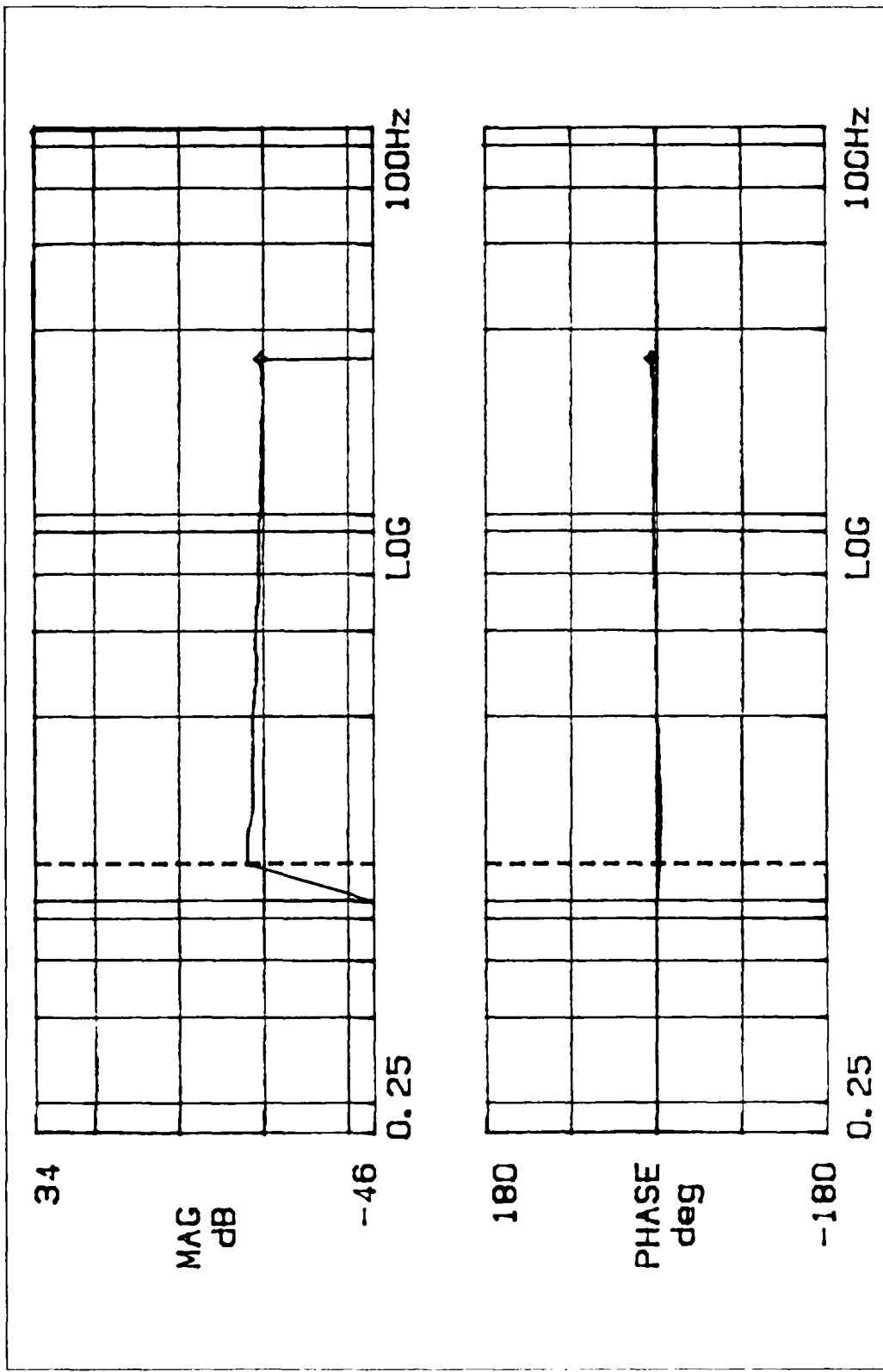
Figure 2.24. Actuator #3 Slip Table Transfer Function
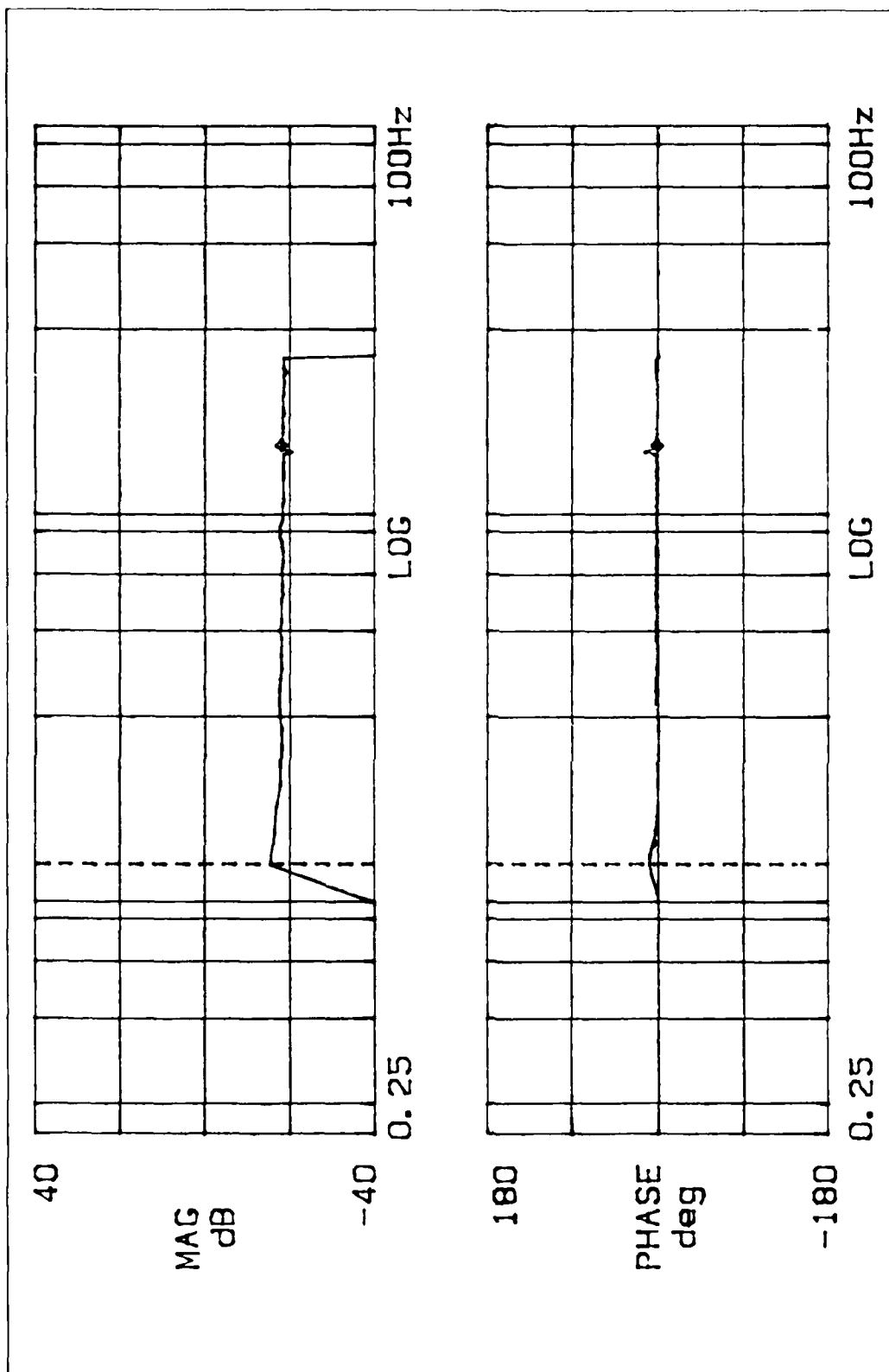
Figure 2.25. Actuator #4 Slip Table Transfer Function

2 - 34

for each actuator. For most of the tests there was very little change from the fixed base tests, mainly a phase shift of a few degrees. However, for very low amplitude tests the response sometimes changed noticably, especially in magnitude. This seemed to be due to the wires attached to the actuator preventing free motion of the slip table. The motor power lead is a relatively stiff cable, and even though it was suspended vertically from the actuator, it often had more effect on slip table motion than the actuator itself.

The maximum force output of a proof mass actuator is limited in the low frequencies by the distance the mass can travel, and in the high frequencies by the maximum current the motor coil can handle. The maximum peak force for the actuator can be calculated using equation 3.

$$F_{OUT} = m_{PF} \, \omega_n^2 \, d \qquad (3)$$

where m_{PF} is the mass of the proof mass, ω_n is the frequency of the signal driving the proof mass, and d is the maximum proof mass displacement.

Using the maximum displacement of ±0.42 inches (0.16 inches of the nominal stroke is lost to the rubber grommets which buffer the proof mass from the mounting brackets). This results in a maximum actuator output of 0.15 lbf for the fundamental z-axis bending mode (1.33 Hz), and 0.26 lbf for the fundamental y-axis bending mode (1.75 Hz). The maximum output for the first torsion mode is 13.3 lbf, far beyond the motor coil capability of 4.2 lbf. To verify this capability, the actuator was driven near the modal frequency with the base fixed. The input amplitude was set so that the proof mass used the entire range of travel without hitting the end brackets. Table 2.1 shows the maximum force outputs and efficiency measured for each actuator.

Table 2.1. Actuator Maximum Force Outputs

Actuator	Frequency (Hz)	Measured Maximum (lbf)	Efficiency
#1	1.25	0.114	85.7%
	1.75	0.214	82.3%
#2	1.25	0.110	82.7%
	1.75	0.224	85.2%
#3	1.25	0.102	76.7%
	1.75	0.242	93.1%
#4	1.25	0.108	81.2%
	1.75	0.212	81.5%

Applying the efficiency for actuators #2 and #4 to the z-axis fundamental bending frequency and summing the maximum forces results in a maximum control force of 0.246 lbf. Similarly, actuators #1 and #3 should provide 0.462 lbf for the fundamental y-axis bending frequency

To determine the ability of the control circuit to maintain the inertial position of the proof mass when the actuator is uncommanded, the the slip table was driven by a shaker while the compensation circuit was operated without an input signal. This test configuration is shown in Figure 2.26. The acceleration of the proof mass should be zero if it is perfectly floating. If not, it will be applying a force to the beam, the effect of which is determined by the phase of the response. A 90° phase lead could drive the beam unstable if the force is large enough to overcome the inherent damping in the beam. An out of phase signal would act as a resonance, leaving the structure unaffected. A 90° phase lag acts as a viscous damper, and an in phase response would effectively add inertia to the system, as if the proof mass were fixed to the base.
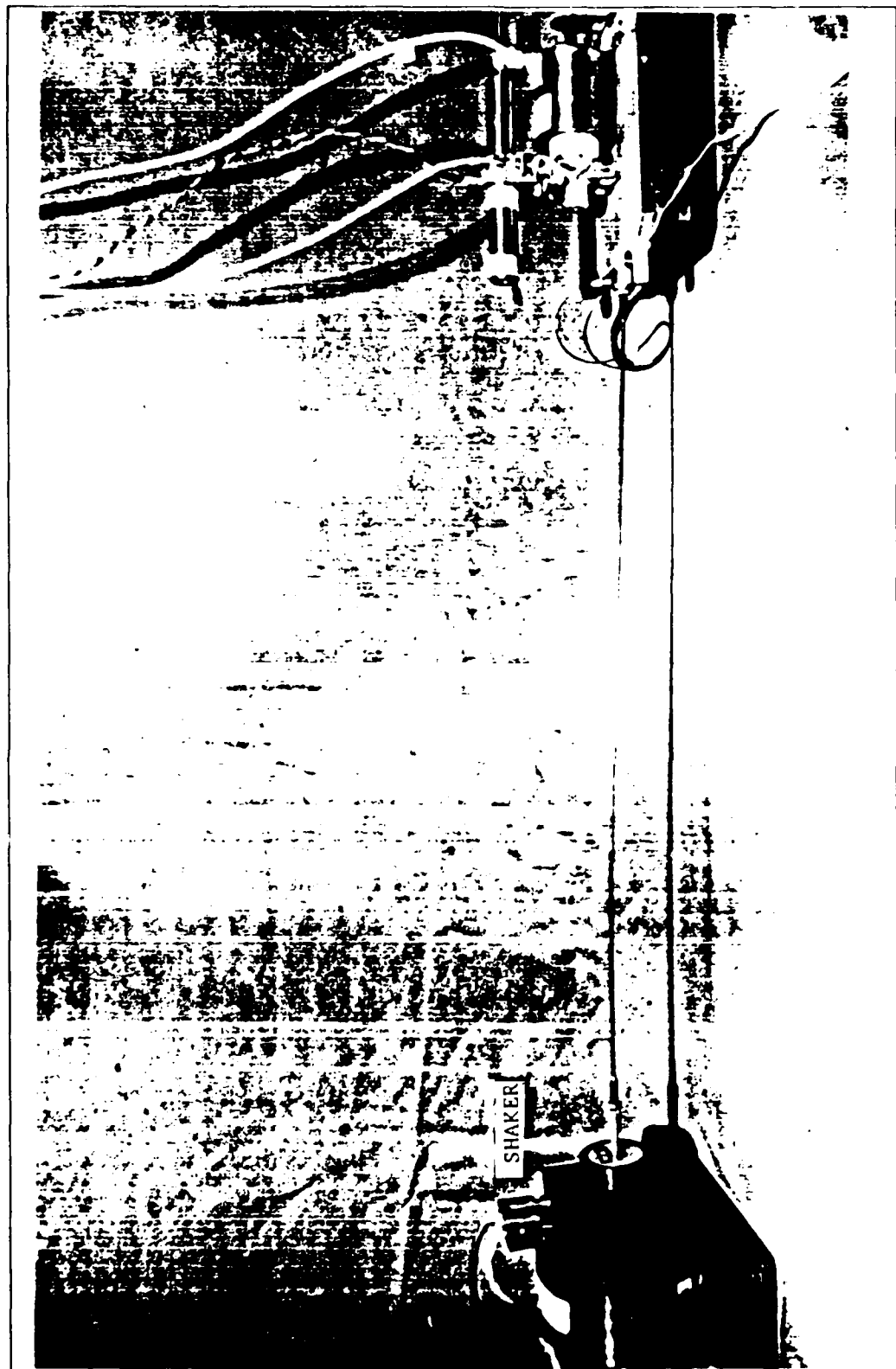
Figure 2.26. Base Motion Test Configuration

The base motion transfer functions measure the accleration response of the proof mass to the force applied to the slip table by the shaker. A force gauge was mounted between the slip table and shaker armature to determine the force applied to the base and a sine sweep was used to drive the shaker over the desired frequency range. The frequency response functions measured for each actuator are shown in Figures 2.27 through 2.30. A force ratio can be derived from the magnitude response by adding -6.1 dB. Note the phase of the response is approximately -90°, which indicates the uncommanded actuators should act essentially as viscous dampers on the structure.

To estimate the damping the uncommanded actuators will impart to the fundamental bending modes, the slip table was driven at the modal frequency and the proof mass acceleration measured. Several different force levels were applied to the slip table to determine the variation of proof mass acceleration with base displacement and velocity. The peak base velocities were calculated using equation 4, and peak displacements were derived by dividing the velocities by the natural frequency.

$$\text{Base Velocity} = \frac{F_{IN}}{W_B} * \frac{386.4 \text{ in/sec}^2}{1 \text{ g}} * \frac{1}{\omega_n} \qquad (4)$$

where F_{IN} is the force driving the slip table base, W_B is the weight of slip table base, and ω_n is the modal frequency in rad/sec. Results of these tests for the fundamental bending frequencies are in Tables 2.2 through 2.5.

The force out of the uncommanded actuators is not a constant with respect to velocity, which would have represented a standard viscous damper. However, a first order approximation can be made to the damping by assuming an average value for each actuator, adding the averages for
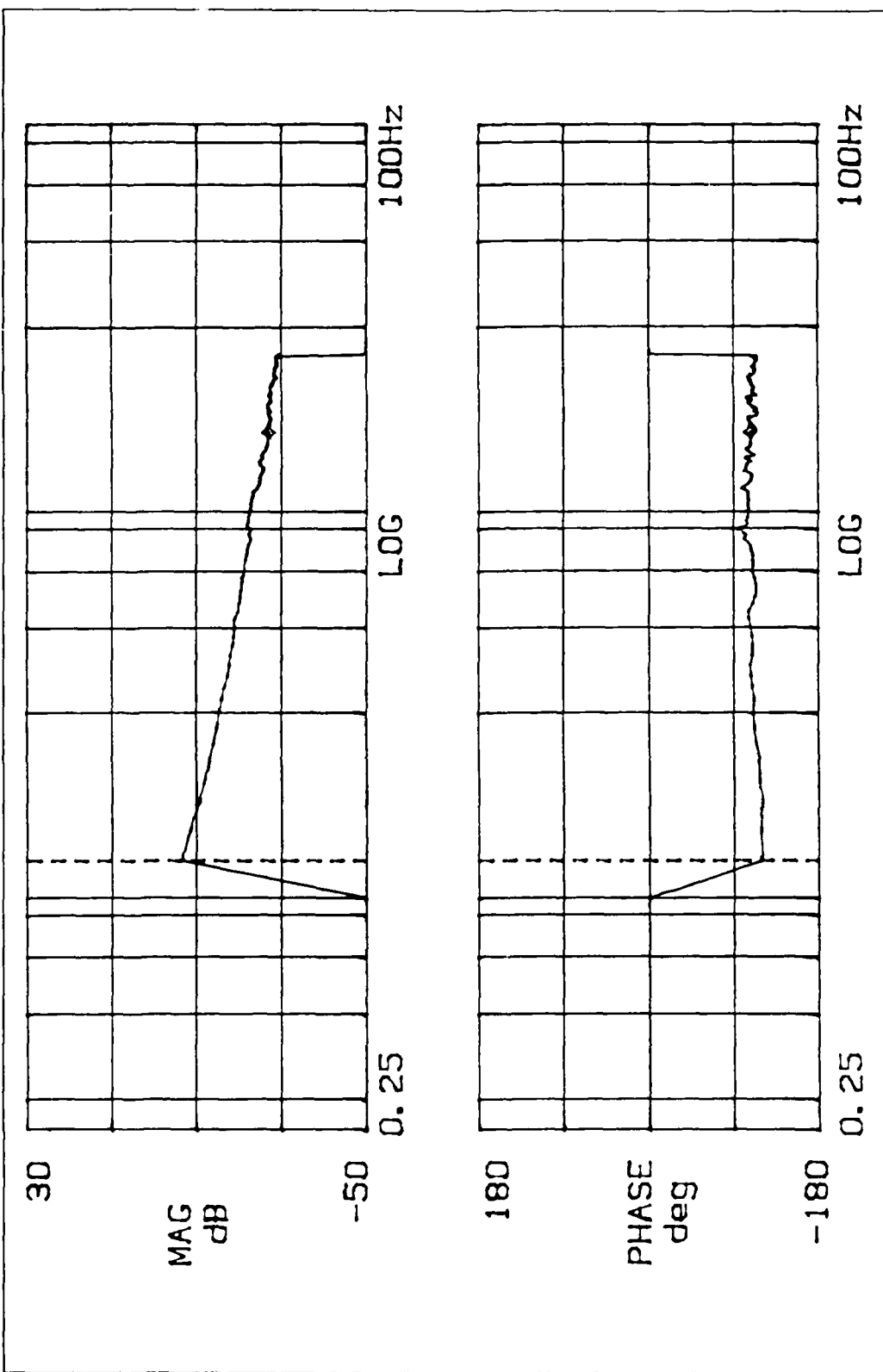
Figure 2.27. Actuator #1 Base Motion Transfer Function

2 - 39
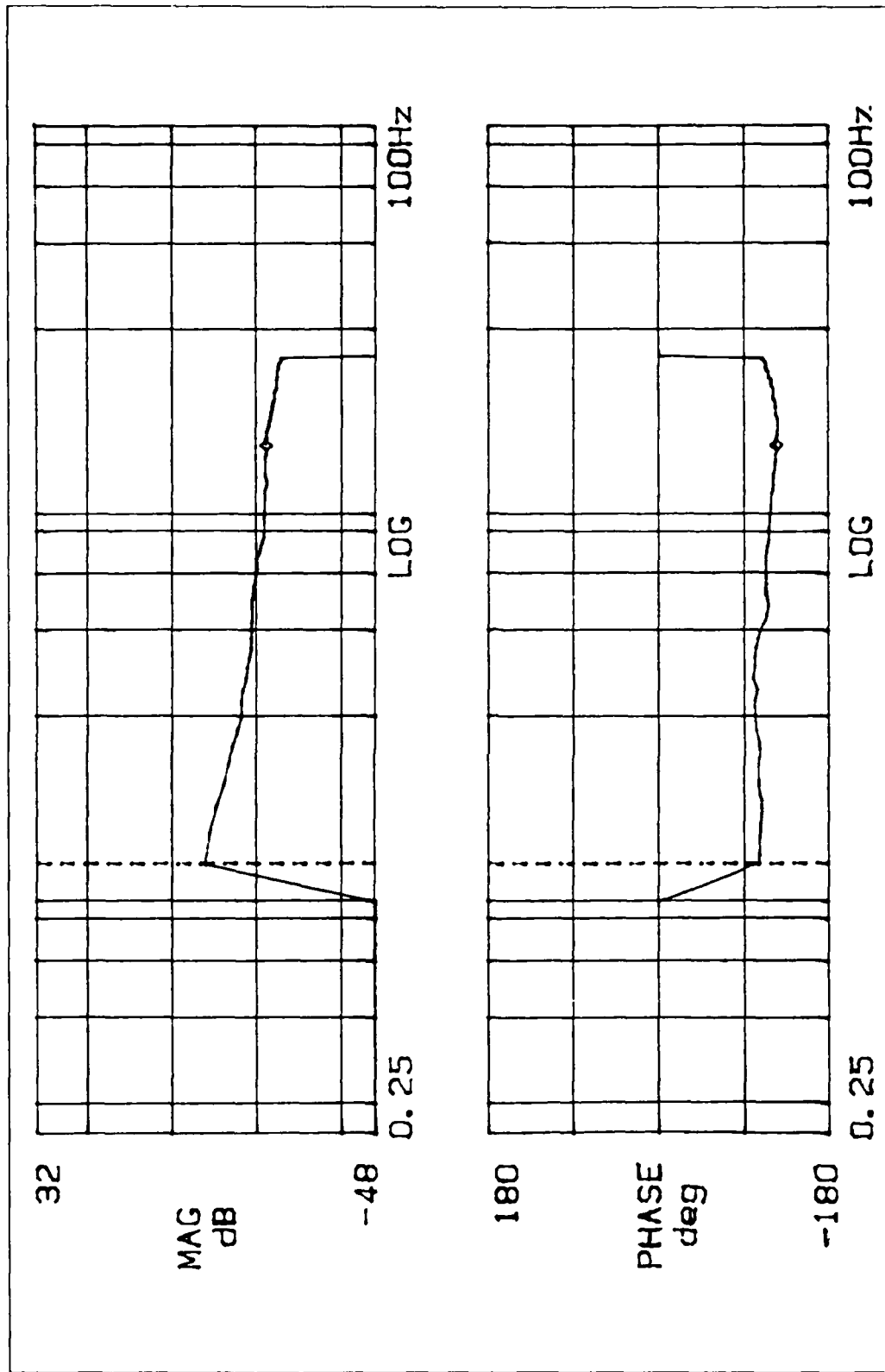
Figure 2.28. Actuator #2 Base Motion Transfer Function
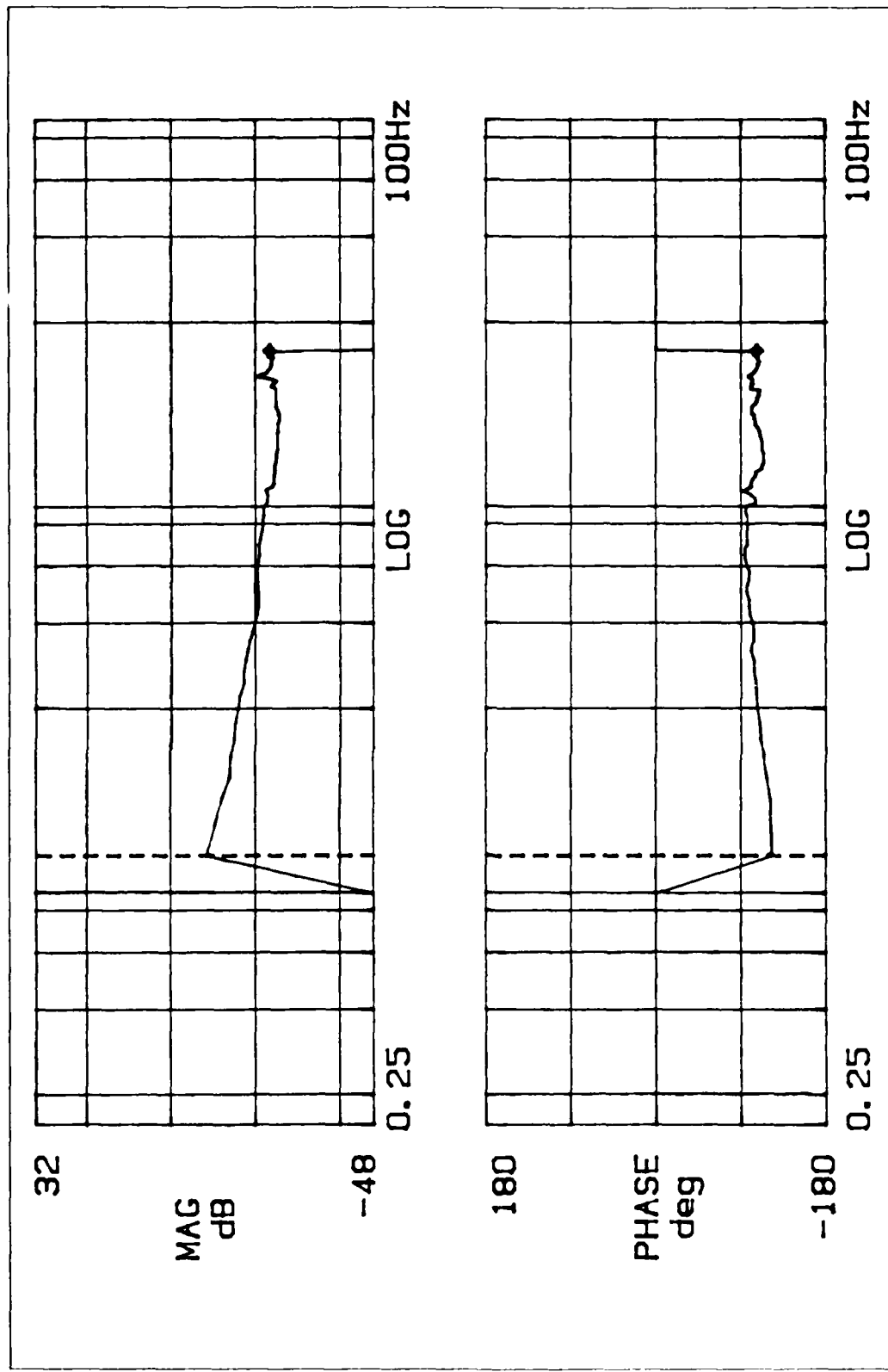
Figure 2.29. Actuator #3 Base Motion Transfer Function
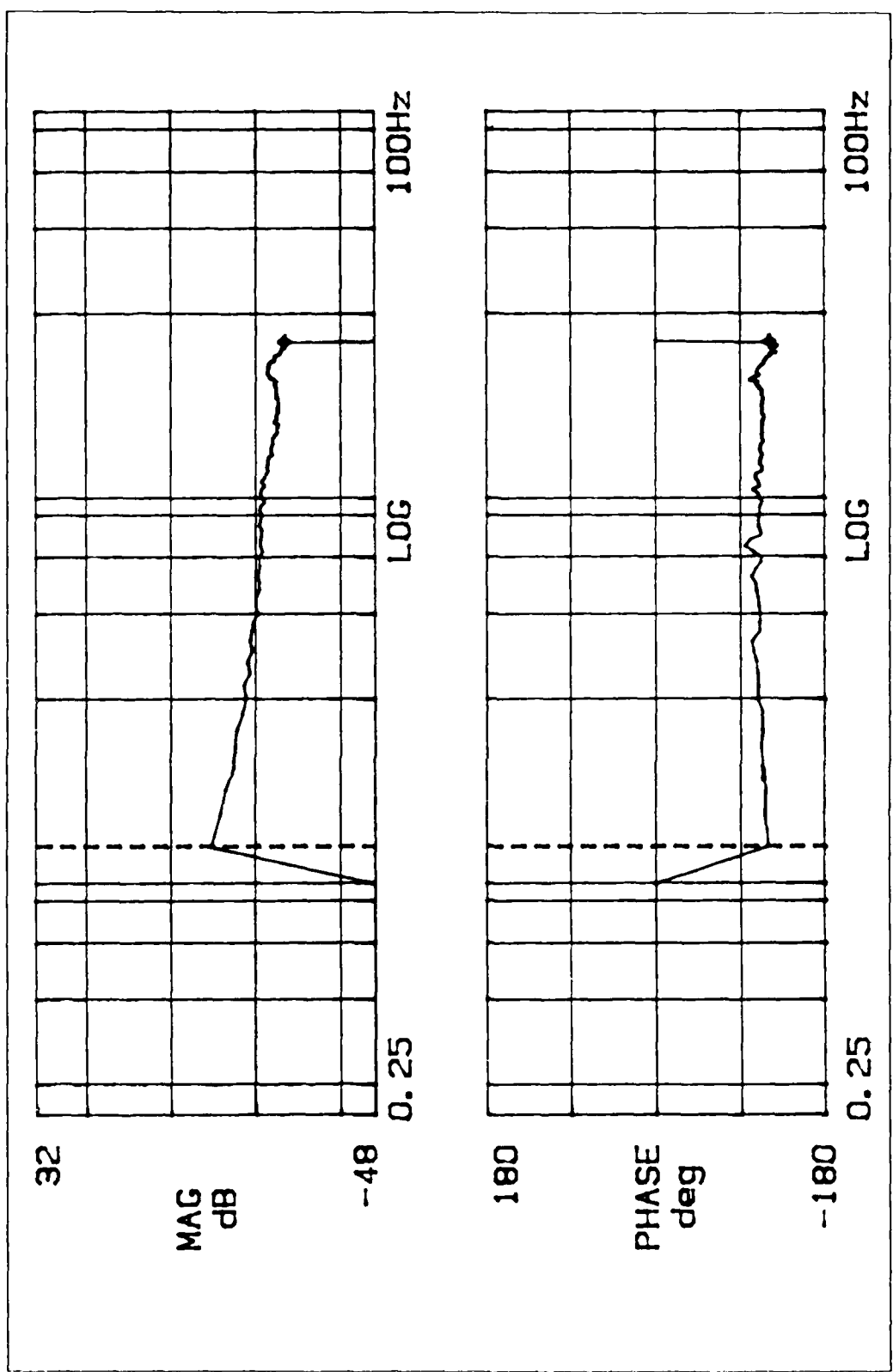
Figure 2.30. Actuator #4 Base Motion Transfer Function

Table 2.2. Base Motion Actuator Response - Actuator #1

ω_n (Hz)	Base Weight (lbf)	F_{IN} (lbf)	V_B (in/sec)	D_B (in)	F_{PM} (lbf)	C $\left(\dfrac{lbf}{in/sec}\right)$
1.25	5.223	0.0841	0.793	0.101	0.0204	0.0257
		0.1413	1.331	0.169	0.0302	0.0227
		0.2213	2.085	0.265	0.0427	0.0205
	10.921	0.2399	1.081	0.138	0.0255	0.0238
		0.3589	1.616	0.206	0.0347	0.0215
		0.3936	1.773	0.226	0.0368	0.0207
1.75	5.223	0.1035	0.696	0.063	0.0174	0.0250
		0.2188	1.472	0.134	0.0277	0.0187
		0.3458	2.387	0.217	0.0403	0.0169
	10.921	0.3631	1.167	0.106	0.0237	0.0203
		0.5188	1.669	0.152	0.0299	0.0179
		0.5957	1.917	0.174	0.0332	0.0173

F_{IN} =   Peak force driving the base

V_B =   Peak base velocity

D_B =   Peak base displacement

F_{PM} =   Force applied by the proof mass to the base

Table 2.3. Base Motion Actuator Response - Actuator #2

ω_n (Hz)	Base Weight (lbf)	F_{IN} (lbf)	V_B (in/sec)	D_B (in)	F_{PM} (lbf)	C $\left(\dfrac{lbf}{in/sec}\right)$
1.25	5.223	0.0462	0.436	0.055	0.0153	0.0298
		0.0708	0.667	0.085	0.0195	0.0248
		0.1585	1.493	0.190	0.0324	0.0184
	10.921	0.1622	0.731	0.093	0.0221	0.0257
		0.2754	1.241	0.158	0.0292	0.0199
		0.3350	1.509	0.192	0.0347	0.0195
1.75	5.223	0.0955	0.643	0.058	0.0197	0.0260
		0.1429	0.961	0.087	0.0240	0.0212
		0.2958	1.986	0.181	0.0347	0.0163
	10.921	0.1641	0.528	0.048	0.0148	0.0238
		0.3589	1.155	0.105	0.0257	0.0208
		0.5129	1.650	0.150	0.0292	0.0165

F_{IN} = Peak force driving the base

V_B = Peak base velocity

D_B = Peak base displacement

F_{PM} = Force applied by the proof mass to the base

Table 2.4. Base Motion Actuator Response - Actuator #3

ω_n (Hz)	Base Weight (lbf)	F_{IN} (lbf)	V_B (in/sec)	D_B (in)	F_{PM} (lbf)	$C\left(\frac{lbf}{in/sec}\right)$
1.25	5.223	0.0412	0.388	0.049	0.0114	0.0295
		0.0989	0.931	0.119	0.0206	0.0221
		0.1445	1.362	0.173	0.0281	0.0206
	10.921	0.0617	0.278	0.035	0.0134	0.0484
		0.1059	0.477	0.061	0.0149	0.0312
		0.3467	1.562	0.199	0.0294	0.0188
1.75	5.223	0.0484	0.326	0.030	0.0103	0.0317
		0.1365	0.918	0.083	0.0175	0.0191
		0.2344	1.577	0.143	0.0256	0.0179
	10.921	0.0794	0.256	0.023	0.0103	0.0404
		0.3467	1.116	0.101	0.0197	0.0176
		0.4955	1.594	0.145	0.0242	0.0152

F_{IN} = Peak force driving the base

V_B = Peak base velocity

D_B = Peak base displacement

F_{PM} = Force applied by the proof mass to the base

Table 2.5. Base Motion Actuator Response - Actuator #4

ω_n (Hz)	Base Weight (lbf)	F_{IN} (lbf)	V_B (in/sec)	D_B (in)	F_{PM} (lbf)	C $\left(\dfrac{lbf}{in/sec}\right)$
1.25	5.223	0.0531	0.500	0.064	0.0149	0.0298
		0.1161	1.094	0.139	0.0253	0.0231
		0.1862	1.754	0.223	0.0365	0.0208
	10.921	0.0933	0.420	0.054	0.0141	0.0334
		0.1622	0.731	0.093	0.0208	0.0285
		0.3020	1.360	0.173	0.0315	0.0231
1.75	5.223	0.0617	0.415	0.038	0.0136	0.0327
		0.1718	1.156	0.105	0.0247	0.0214
		0.2541	1.710	0.155	0.0322	0.0188
	10.921	0.1334	0.429	0.039	0.0134	0.0313
		0.2661	0.856	0.078	0.0205	0.0240
		0.3631	1.168	0.106	0.0250	0.0214

F_{IN} =   Peak force driving the base

V_B =   Peak base velocity

D_B =   Peak base displacement

F_{PM} =   Force applied by the proof mass to the base

the actuator pair controlling the axis being analyzed, and applying the resulting coefficient as a damping element between the end node of the structure and a fixed node. The element is oriented in the plane of the axis being evaluated. This procedure was implemented using the finite element model for the beam with floating proof masses configuration (see Chapter 3, Table 3.4).

The finite element code forms the system of equations for the model in the form of (6:2-26,2-27)

$$M \ddot{\underline{x}}(f) + C \dot{\underline{x}}(f) + K \underline{x}(f) = F(f) \tag{5}$$

where $\underline{x}(f)$ are the nodal displacements, $F(f)$ is a periodic forcing function applied at given nodes, and f is a discrete frequency value. This system is assumed to be in a steady state condition at the given frequency, thus the velocities and displacements are

$$\ddot{\underline{x}}(f) = -(2\pi f)^2 \underline{x}$$

$$\dot{\underline{x}}(f) = i(2\pi f) \underline{x} \tag{6}$$

where $i \equiv (-1)^{1/2}$. The system of equations now becomes

$$\left[-(2\pi f)^2 M + i(2\pi f)C + K \right] \underline{x}(f) = F(f) \tag{7}$$

which is solved for each designated frequency to generate a frequency response function. The damping can be estimated from the frequency response data using the half power point method (7:96) which has the form

$$\zeta = \frac{\omega_1 - \omega_2}{2\,\omega_n} \qquad\qquad (8)$$

where ω_1 and ω_2 are the frequencies at which the response is 3 dB below the resonant peak, ω_n.

Actuators #2 and #4 have been designated to control the z-axis of the beam, and #1 and #3 will control the y-axis (see Figure 5.3). Averaging the damping coefficients measured from the base motion data and summing the coefficients for the two actuators results in a z-axis damping coefficient of 0.0495 lbf/in/sec, and a y-axis coefficient of 0.0431 lbf/in/sec. These coefficients were applied to the appropriate finite element beam models and the structural frequency response calculated for each axis. Results are shown in Figures 2.31 and 2.32 for the z and y axes respectively. The damping ratios predicted by this model for the fundamental bending modes are in Table 2.6.

Table 2.6. Predicted Modal Damping Due to Actuators

Axis	Predicted Damping Coefficient
z	0.0644 ± 0.0038
y	0.0410 ± 0.0014

While this is substantially more damping than would normally be encountered in an uncontrolled structure, there will still be enough margin between the residual damping and the maximum actuator capability to demonstrate the controller is affecting the structure.

Finally, since the actuators will operate in orthogonal pairs, they will experience side force loading as the orthogonal axis vibrates. To
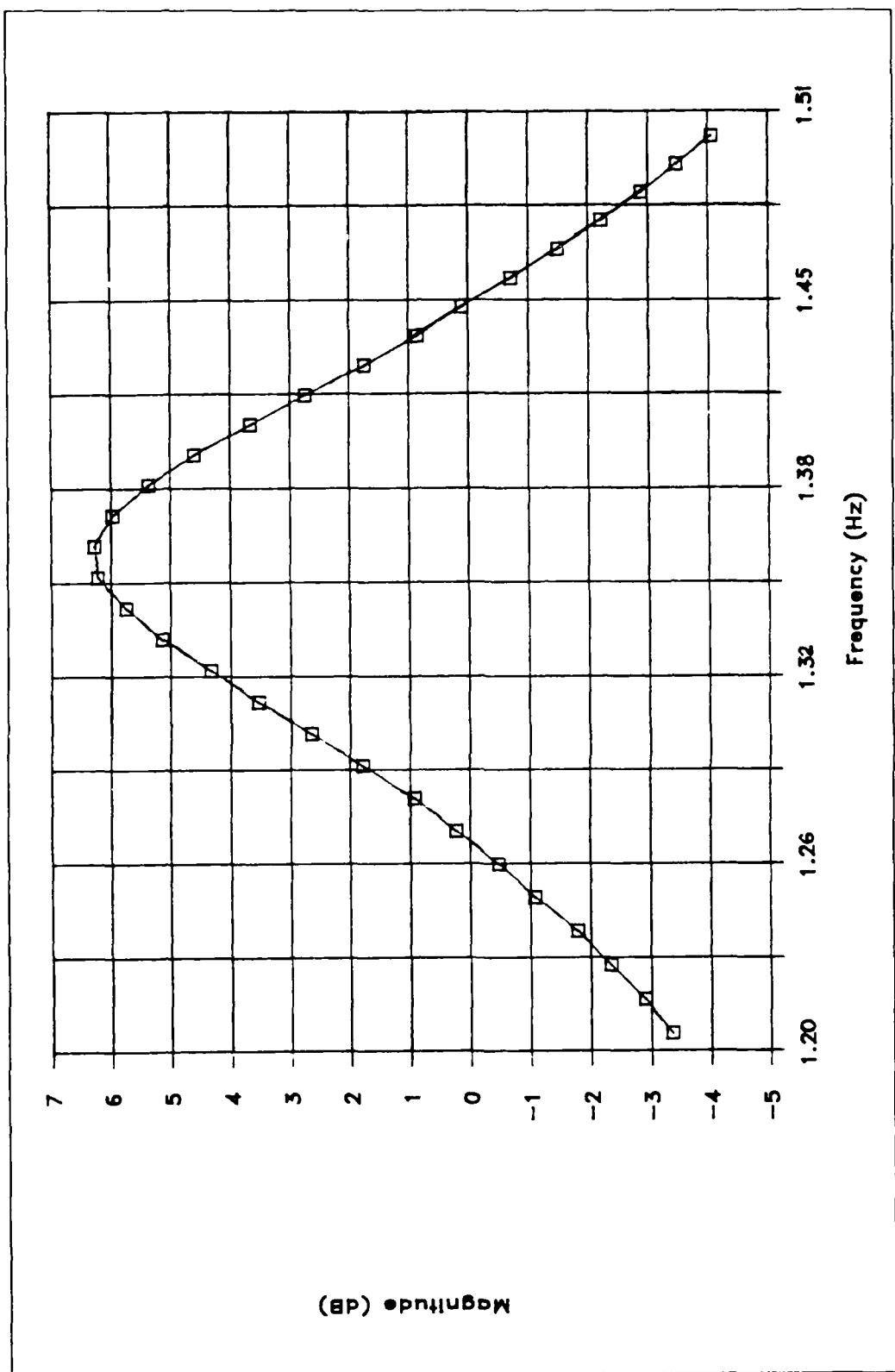
Figure 2.31. Predicted Z-Axis Structural Frequency Response With Uncommanded Actuators
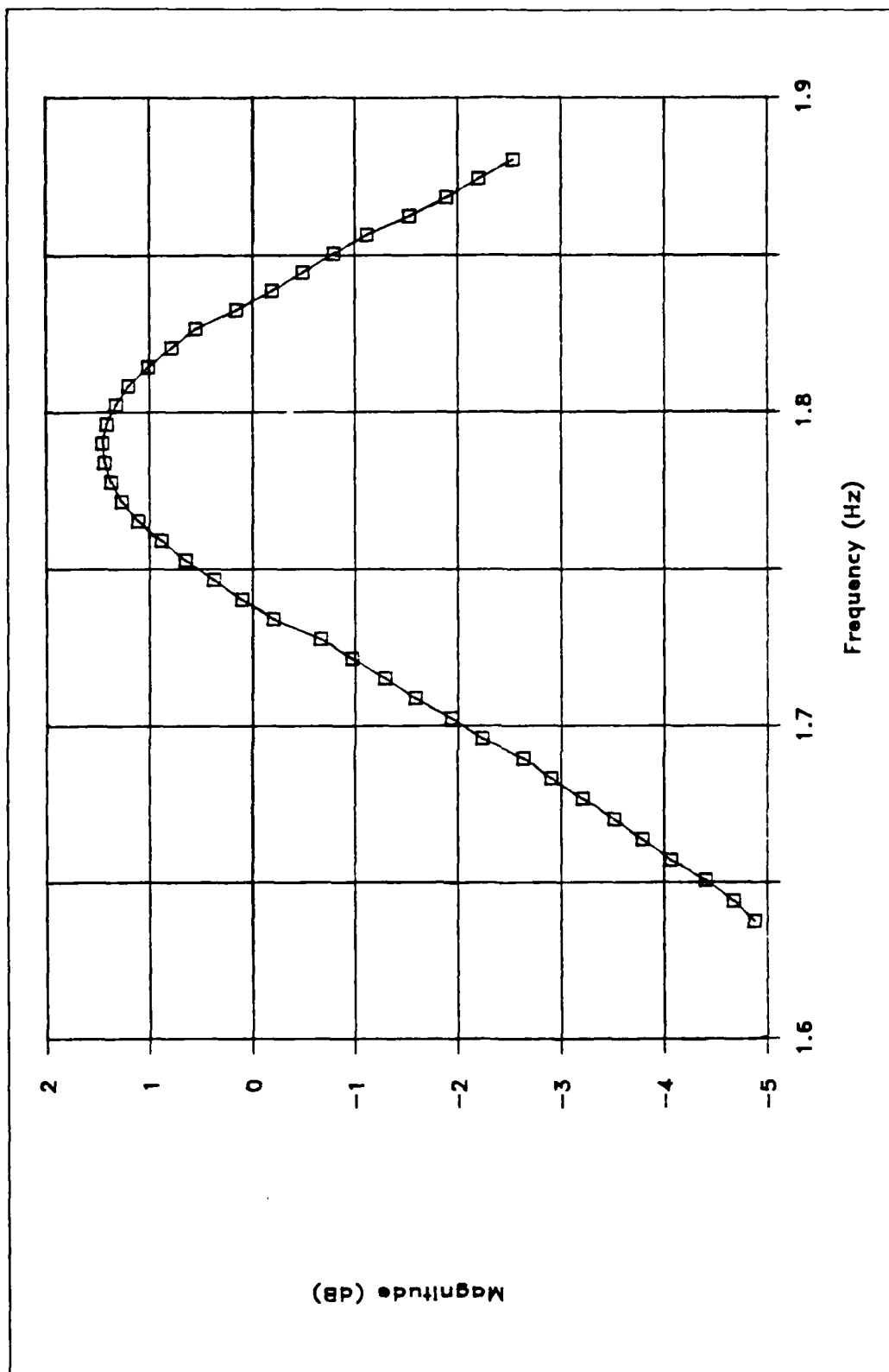
Figure 2.32. Predicted Y-Axis Structural Frequency Response With Uncommanded Actuators

ensure this loading does not adversely affect the actuator operation, actuator transfer functions were measured while driving the slip table with the actuator mounted perpendicular to the direction of slip table motion. Tests were conducted by using the shaker to drive the slip table at two different amplitudes for each of the first five modal frequencies. A sine sweep was used to generate an actuator transfer function over the control bandwidth while the slip table was in motion. Variation of the actuator response with off axis force and frequency was minimal and no trends were observed in the response variation. The standard deviation from the nominal transfer function of all the tests appears in Figure 2.33, and the variation seems to be mainly measurement error. The stability of the response under these conditions indicates that the actuators should not be affected by off-axis forces.

Comparison of Response with Design Goals

Table 2.7 lists the final transfer function for each actuator at each modal frequency. The response still has some magnitude and phase variation, however it was decided the magnitude variation could be accounted for in the state space model and the phase variation would be ignored. While ignoring 20° of phase at the fundamental bending frequency may seem excessive, this was the maximum observed for all input amplitude levels. A problem which remains unresolved is the phase response variation with command signal amplitude. The phase was observed to increase as much as 15° when the input amplitude was reduced by half. The data presented in the table 2.7 is for an input amplitude that gives the maximum force output from the actuator near the z-axis fundamental bending frequency. Any reduction in force command will
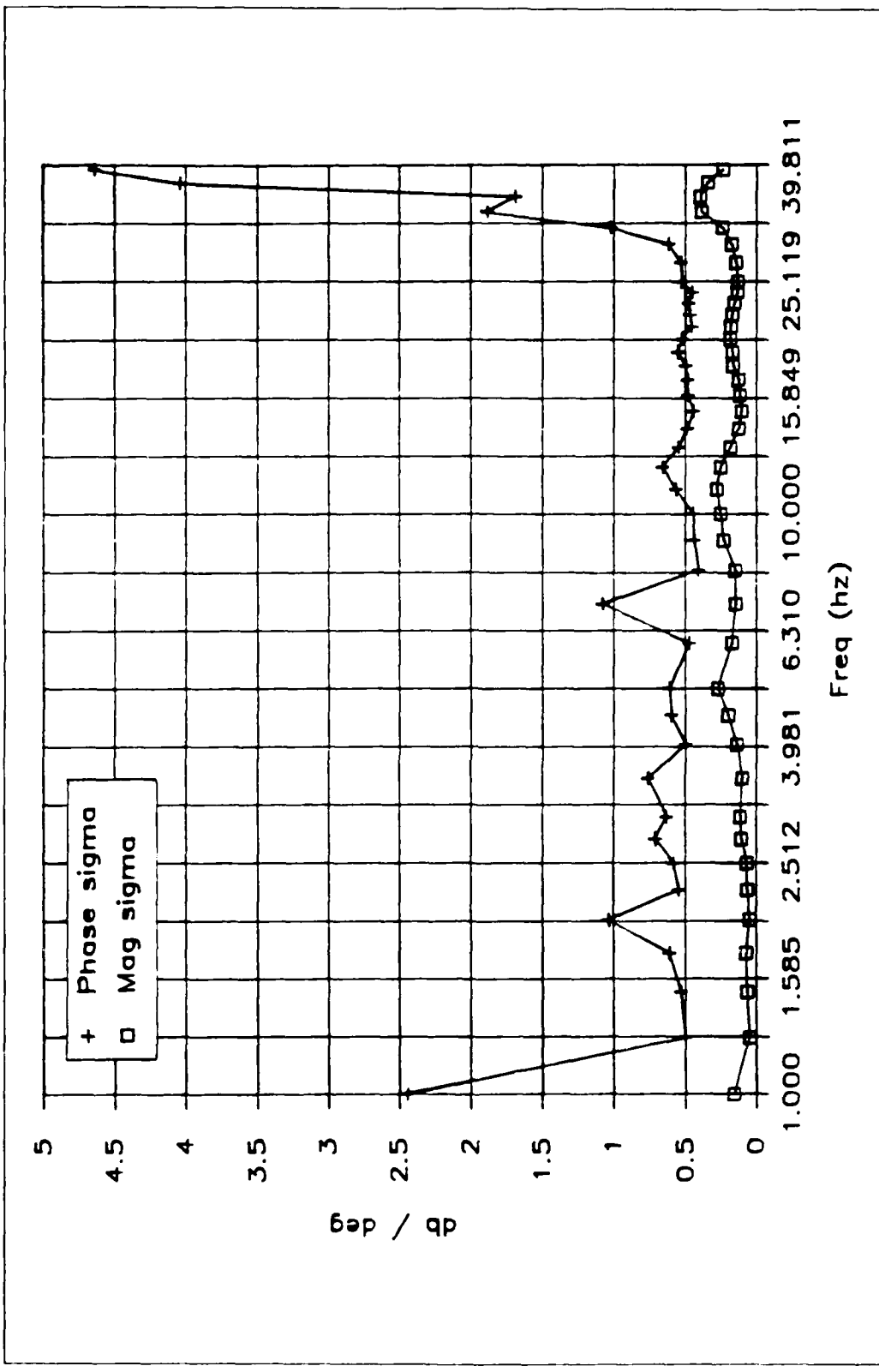
Figure 2.33. Standard Deviation of the Variation in Actuator Frequency Response with Side Force Loading

Table 2.7. Final Actuator Transfer Functions

Actuator		Frequency (Hz)				
		1.25	1.75	13.0	19.0	25.25
#1	Mag *	0.5828	0.4904	0.4126	0.4032	0.4032
	Phase #	-19.3	-16.1	4.9	6.6	8.5
#2	Mag	0.5893	0.4959	0.3939	0.3939	0.3984
	Phase	-20.9	-16.2	4.2	7.3	10.5
#3	Mag	0.5800	0.4880	0.4153	0.4106	0.4059
	Phase	-18.7	-15.2	5.8	7.1	8.2
#4	Mag	0.5858	0.4929	0.3961	0.3961	0.4007
	Phase	-21.7	-17.2	4.6	8.3	10.9

*   Magnitude in lbf/V   #   Phase in degrees

increase the phase response, thus moving it closer to zero. A

discussion and characterization of this problem is in Appendix B.

The actuators do add some damping to the structure, thus the proof

masses are not perfectly floating, however the level is low enough that

showing significance between residual and commanded damping levels

should not present a problem. The greater concern is the point at which

the proof masses come to rest and suddenly contribute to the system

inertia. While this amplitude level is small, and may be reduced even

more when the actuators are commanded, it makes testing with the modal

analyzer difficult, since the response appears as two separate modes

which are present and different times.

The proof masses do maintain a centered position when commanded,

though some change in center still was observed with input amplitude.

With the sensitivity to bias shifts that these actuators exhibit, the

shift could easily be in the frequency generator of the Ono Sokki. A
3 mV bias shift in a 2 V signal is a very small percentage error and
would be difficult to detect.

No specific measures were taken to limit the proof mass travel.
The structural deflections will be limited to prevent the actuators from
saturating.

Unresolved Problems, Conclusions, and Recommendations

The variation in the final actuator transfer function will induce
some errors if it is ignored in the overall system model. To minimize
this error, the response magnitude can be accounted for in the state
space model, however the error induced by the phase variation is
probably best ignored since it will vary with input amplitude and would
significantly increase the complexity of the model. Future work to
eliminate this problem is recommended to increase the accuaracy of the
actuator response and the overall experiment. Another problem which
remains unresolved is noise in the system, especially at 60 Hz.
Filtering of noise this close to the control bandwidth is difficult
since the filter dynamics will affect the response of the system.
Filtering the power inputs to the compensation circuit may provide some
isolation and reduce the noise amplitude.

Several concerns about linear proof mass actuators as viable
control mechanisms for this experiment and for large space structures in
general have arisen from the development for this experiment. First is
the limited force output at very low frequencies. Since the force
output is derived from accelerating a mass, large low frequency force
outputs require either a very long travel for the mass or a large mass.

Both approaches have problems when considered for space structure control. If the proof mass is given a long travel, linearity of the motor output becomes a problem. Perhaps this nonlinearity could be modeled and accounted for, but the cost would be a significant increase in the computational requirements on the control system. Large masses present two disadvantages. First, unless the moving mass is designed to consist at least partially of hardware that would normally be a part of the vehicle the increased mass is merely dead weight which must be boosted into orbit. Second, and more significant to the control problem, is adding large masses to a light, flexible structure tends to create nodal points at or very close to the actuators. The significantly reduced modal amplitude at the control mechanism requires the actuator to deliver more force to maintain the same level of control. This problem is not as significant if the proof mass is controlled such that it is not contributing to the structural mass (as is the case for this experiment), but if the actuators are mounted on the structure in colocated, orthogonal pairs, the orthogonal actuator does create a node. Future experiments and actual structures which use linear proof mass actuators should avoid colocating the actuators if their mass is large in relation to the structure being controlled.

III. Structure

Description

The structure to be controlled in this experiment is a cantilevered beam with rectangular cross section. A circular plate is mounted on the free end of the beam to provide a surface to mount the actuators (see Figure 3.1). The configuration and dimensions are shown in Figure 3.2 and Table 3.1 lists the physical charcteristic of the structure. This configuration was selected by the Flight Dynamics Laboratory to exhibit the large space structure charcteristics of low frequency, closely spaced vibration modes. It also allowed for ungrounded sensing and actuation which, with vertical suspension of the beam, provides an approximation to the zero gravity free vibration environment of a large space structure.

Modelling

There are many modelling methods available to find the natural vibration frequencies and mode shapes for structures. The cantilevered beam with a tip mass is a simple enough structure to permit analytical solution of the free vibration equations of motion. Other techniques which form approximations to this exact solution include, but are not limited to, Rayliegh-Ritz, Assumed Modes, Collocation, Galerkin, and Finite Element methods. Because the Finite Element Method is highly automated and easily applied it was used as the primary modelling tool for this structure. To verify the validity of the solution, the
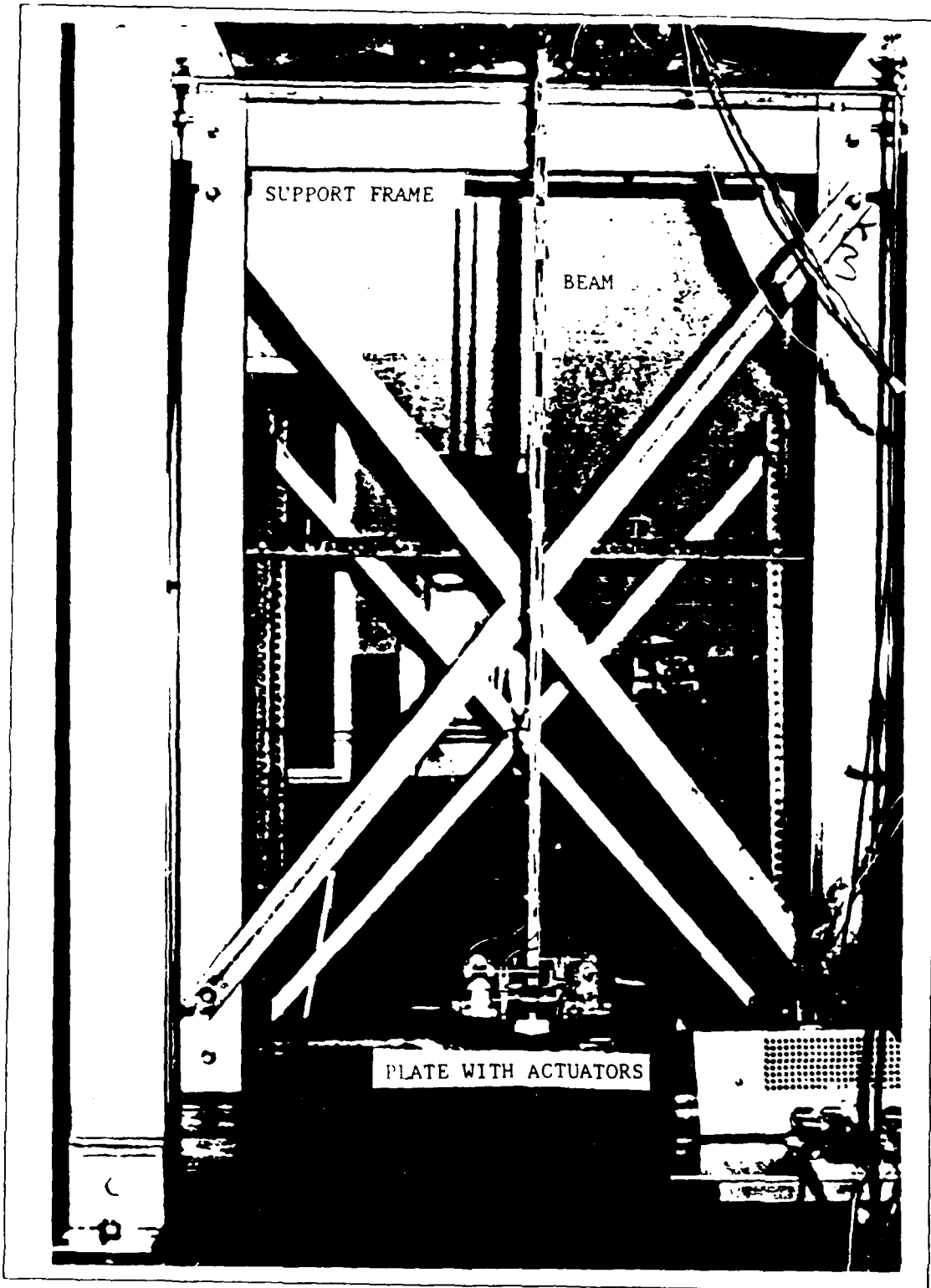
Figure 3.1. Beam With End Plate and Actuators

Node #	(x,y,z)
1	(0,0,0)
2	(7,0,0)
3	(14,0,0)
4	(21,0,0)
5	(28,0,0)
6	(35,0,0)
7	(42,0,0)
8	(49,0,0)
9	(56,0,0)
10	(63,0,0)
11	(70.75,0,0)
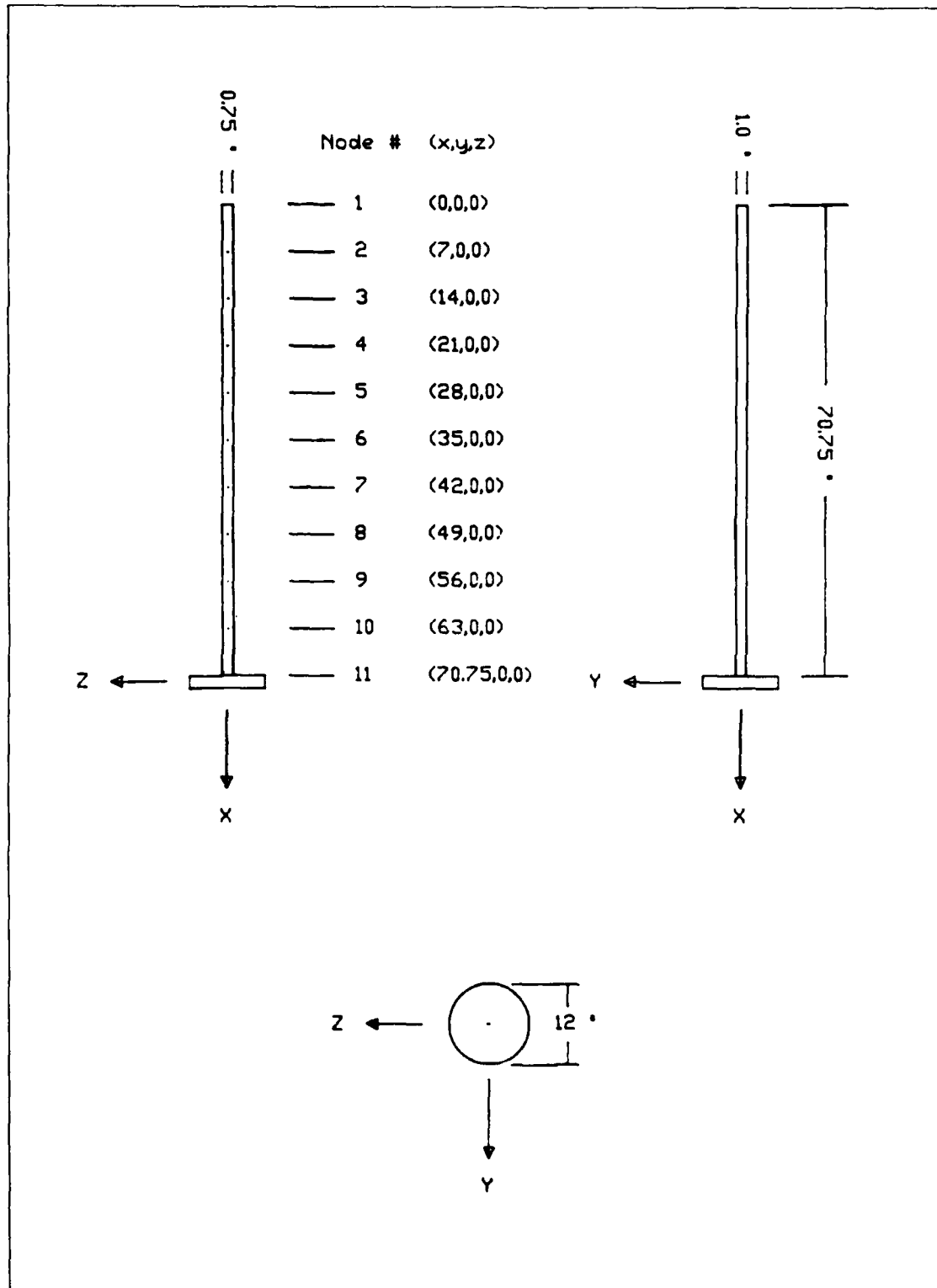
Figure 3.2. Structure Configuration

Table 3.1. Structure Physical Properties

Property Description	Value	Units
Beam Length (L)	70.75	in
Y Cross-Section Width (a)	1.01	in
Z Cross-Section Width (b)	0.758	in
Cross-Section Area (A)	0.7656	in^2
Young's Modulus (E)	10.8×10^6	psi
Shear Modulus (G)	4.1×10^6	psi
Beam Density (ρ_B)	2.591×10^{-4}	$lbf \cdot sec^2/in^4$
Beam Mass (M_B)	1.403×10^{-2}	$lbf \cdot sec^2/in$
Y Moment of Inertia (I_y)	3.667×10^{-2}	in^4
Z Moment of Inertia (I_z)	6.508×10^{-2}	in^4
Torsional Moment of Inertia $(K)^*$	7.913×10^{-2}	in^4
Polar Mass Moment of Inetia (I_{mx})	1.865×10^{-3}	$lbf \cdot sec^2/in$
Plate Diameter (d)	12.0	in
Plate Thickness (t)	1.0	in
Plate Mass (M_P) (measured)	2.847×10^{-2}	$lbf \cdot sec^2/in$
X Mass Moment of Inertia (I_{Dmx})	0.5125	$lbf \cdot sec^2 \cdot in$
Y-Z Mass Moment of Inertia (I_{Dm})	0.2562	$lbf \cdot sec^2 \cdot in$

* Adjusts for the rectangular cross-section

$$M_B = \rho_B AL \qquad\qquad I_{mx} = M_B(a^2 + b^2)/12$$

$$I_y = ab^3/12 \qquad\qquad I_{Dmx} = M_P d^2/8$$

$$I_z = ba^3/12 \qquad\qquad I_{Dm} = M_P d^2/16$$

$$K = ab^3[16/3 - 3.36(b/a)(1-b^4/12a^4)]/8 \quad (8:290)$$

equations of motion were solved for a cantilevered beam with tip mass and compared with the finite element results. The finite element model was implemented using the MSC·PAL software package availible at the Flight Dynamics Laboratory. MSC·PAL is a finite element code which runs on an IBM-PC or compatible micro-computer.

The structure was modelled in two steps. First, the finite element and exact solutions were formulated and compared for the beam without the actuators mounted. The finite element solution was modified by adding elements to the model until the solution converged and matched the solution to the equations of motion. Using this finite element model the mass model for each actuator was added to determine the natural frequencies and mode shapes for the controlled configuration. Since an ideal actuator will have a floating proof mass, this mass will not contribute to the tip mass in the actuator control axis. Thus, the final model is actually a composite of three different models, one for the tip mass configuration of each bending direction and torsion.

The classical solution for bending vibration of beams can be found in many textbooks. The equations of motion are formulated using Hamilton's Principal, and after applying separation of variables, the resulting boundary value problem can be solved for the natural frequencies and mode shape of the structure (9:161) In general, shear and rotatory inertia effects are ignored for beams with cross-sectional areas that are small compared with the length, thus the equations of motion for bending vibration of this structure are

$$\frac{\partial^2}{\partial x^2}\left[EI(x)\ \frac{\partial^2 \psi(x,t)}{\partial x^2}\right] \ = \ - \ m(x)\psi(x,t) \qquad (9)$$

and the boundary conditions are represented by

$$\psi(x,t)\big|_{x=0} = 0 \tag{10a}$$

$$\frac{\partial \psi(x,t)}{\partial x}\Bigg|_{x=0} = 0 \tag{10b}$$

$$\frac{\partial}{\partial x}\left[EI(x)\frac{\partial^2\psi(x,t)}{\partial x^2}\right]\Bigg|_{x=L} = M_p\frac{\partial^2\psi(x,t)}{\partial t^2}\Bigg|_{x=L} \tag{10c}$$

$$EI(x)\frac{\partial^2\psi(x,t)}{\partial x^2}\Bigg|_{x=L} = -I_{Dm}\frac{\partial}{\partial x}\left(\frac{\partial^2\psi(x,t)}{\partial t^2}\right)\Bigg|_{x=L} \tag{10d}$$

where E = Young's Modulus for the beam

   I = Moment of inertia of the beam in the bending axis

   ψ = Displacement function of the beam

   x = Distance along the beam

   m = Mass per unit length of the beam

Separating variables and applying boundary conditions results in a characteristic equation that is solved numerically for it roots, which are the natural vibrations frequencies of the beam. Through a similar procedure the torsional equation of motion is formulated (9:156) and is found to be

$$\frac{\partial}{\partial x}\left[GJ(x)\frac{\partial\theta(x,t)}{\partial x}\right] = I(x)\frac{\partial^2\theta(x,t)}{\partial t^2} \tag{11}$$

with the boundary conditions

$$\theta(x,t)\big|_{x=0} = 0 \tag{12a}$$

$$GJ(x) \left. \frac{\partial \theta(x,t)}{\partial x} \right|_{x=L} = - I_{Dm} \left. \frac{\partial^2 \theta(x,t)}{\partial t^2} \right|_{x=L} \tag{12b}$$

where   GJ = Torsional rigidity of the beam

       I = Polar mass moment of inertia of the beam

       θ = Angular displacement of the beam

Again, separating variables and applying boundary conditions results in a charcteristic equation which can be solved numerically for the natural frequencies.

The Finite Element Method formulates the problem by breaking the structure into discrete elements and assuming a form of the displacement function over each element. The elements are connected at nodal points and thus form a piecewise approximation to the structure (10:2). Each element has a mass and stiffness matix associated with it, which is defined by the beam properties and the specific displacement function assumed for the element. Combining these elemental matrices results in a system of equations of the form

$$M \, \overset{..}{\underset{\sim}{x}} \; + \; K \, \underset{\sim}{x} \; = \; \underset{\sim}{f} \tag{13}$$

where   M = Mass matrix

       K = Stiffness matrix

       $\underset{\sim}{x}$ = Nodal displacement vector

       $\underset{\sim}{f}$ = Vector of forces applied at the nodes

The homogeneous solution to this coupled system of equations represents the free vibration of the structure from which the natural frequencies and mode shapes are found by solving for the eigenvalues and

eigenvectors. The accuracy of this method when applied to a simple beam depends primarily on the number of elements chosen to model the structure. For this case, a 10 element model was found to match the exact solution for the lower modes to reasonable accuracy. The higher modes will show increasingly more error as the mode number approaches the number of elements in the model. Table 3.2 compares the natural frequencies for the structure that were derived from the two solutions.

Using the finite element model for the basic beam, the actuator mass models were added to predict the natural frequencies and mode shapes for the structure in the control configuration. The actuator mass models were developed by breaking them into six components which could be approximated by simple figures. The mass, center of gravity, and mass moments of inertia for each of these figures were then used in the finite element model. The MSC·PAL software supports adding a lumped mass at some point on the structure and assigning the effects of that mass to a specific node point. All actuator mass elements were assigned to the end node of the beam (#11), along with the plate. The software automatically uses the parallel axis therom to calculate the moments of inertia for each mass element about the assigned node. The detailed model for each actuator can be found in Appendix C. To approximate a floating proof mass, the mass elements representing the proof masses were omitted for the actuators controlling the modelled axis. For torsion, all proof masses were omitted since for small displacements they should not contribute to the structure mass properties. Natural frequencies from the beam/actuator finite element model are shown in Table 3.3.

Table 3.2. Exact and Finite Element Modal Frequencies

Mode	Axis	Modal Frequencies (Hz)		FEM error (%)
		Exact	Finite Element	
1	Z	1.611	1.608	0.19
2	Y	2.146	2.136	0.47
3	T	14.401	14.401	0.00
4	Z	20.968	20.749	1.04
5	Y	27.938	27.642	1.06
6	Z	56.974	57.115	0.25
7	Y	75.911	76.092	0.24
8	Z	103.382	104.656	1.23
9	Y	137.744	139.414	1.21
10	Z	180.088	181.375	0.71

Table 3.3. Beam/Actuator Modal Frequencies

Mode	Axis	Modal Frequency
1	Z	1.325
2	Y	1.773
3	T	12.796
4	Z	19.431
5	Y	25.883
6	Z	47.896
7	Y	63.817
8	Z	86.451

Modal Tests

The most accurate method for determining the frequencies and mode shapes of a structure is almost always modal testing. While models give insight into the phenomena being observed in a system, they are still only mathematical representations of reality. Unfortunately, modal testing may be impractical for many large space structures. Due to their size and flexibility, they may not even be able to be assembled until they are on orbit. Even if they can be assembled, simulating a zero gravity environment for a large structure may prove extremely difficult. While actual space structures do present these problems, maintaining the accuracy of the experiment is a paramount consideration and the structure model for the control design will use modal test data whenever possible.

Modal tests were conducted using the impact method which excites the structure by tapping it with a force hammer. The hammer has a piezoelectric crystal in the tip which registers a voltage signal when stressed. The structural response to this force is measured using accelerometers located at various points on the structure. The force and accelerometer signals are recorded by a GenRad Modal Analyzer, which Fast Fourier Transforms the time response data and generates a frequency response function for the structure. Natural modes of vibration for the structure show up as peaks in this frequency response. Mode shapes can be determined by measuring the response at several different points along the beam. The amplitude and direction of the mode at each point is defined by the amplitude and phase of the frequency response measured there.

The first modal test was conducted on the basic beam configuration without the actuators. Results of this test and the difference between

the measured response and finite element model are shown in Table 3.4. While the fundamental frequencies match fairly well with the model, the errors grow unexpectedly large for the second bending modes and beyond. The modelling of a cantilevered beam is a straight forward process and should generate accurate predictions well beyond the second mode. To evaluate this problem, Mr. Bob Gordon of AFWAL/FIBG developed a series of models which varied both the beam parameters and the boundary

Table 3.4. Measured vs Finite Element Modal Frequencies - No Actuators

Mode	Axis	Modal Frequencies (Hz)		FEM error (%)
		Measured	Finite Element	
1	Z	1.617	1.608	0.56
2	Y	2.129	2.136	0.33
3	T	14.436	14.401	0.24
4	Z	20.160	20.749	2.92
5	Y	26.847	27.642	2.96
6	Z	54.828	57.115	4.17
7	Y	72.985	76.092	4.26
8	Z	98.932	104.656	5.79

conditions of the model. Results of this effort were inconclusive. While a more accurate prediction of the high frequency modes could be achieved, it was always at the cost of adding error to the fundamental modes. Neither changing beam parameters, nor changing the boundary condition from a perfect cantilever to a pinned joint with a rotational spring had the effect of maintaining the fundamental frequencies while lowering the higher mode predicted frequencies. Mr. Gordon also found that a model of the entire support frame and beam resulted in a very

ill-conditioned system of equations which induced substantial numerical errors into the solution. The ill-conditioning results from the support plate to which the beam is attached (see Figure 3.1). This plate is the most massive and stiffest element in the frame/beam structure, while the least massive and stiff element is the attached beam. While the difference between the model and modal test data probably lies in some coupling between beam and support structure, it could not be demonstrated in the model.

The model was considered acceptable for the first five modes, consisting of the first two bending modes in each direction and the first torsion mode, since the prediction of the fundamental modes is fairly accurate and the errors in the second bending modes were less than 3%. While the remaining modes exhibited larger errors, they are outside the control bandwidth for the experiment and as such will not be incorporated in the controller.

A second modal test was performed with the actuators mounted on the beam. This test was performed prior to completion of the actuator compensators; therefore, to simulate the ideal actuator, the proof masses were removed from the actuators controlling the axis under test. For torsion, all proof masses were removed. Results of this modal test are in Table 3.5. The data shows the finite element model for this configuration to have errors similar to the basic beam tests for the first five modes. Errors are more substantial in the higher modes.

Several problems were encountered in conducting the modal tests which relate to low frequency testing of lightly damped structures. First, the lighter the damping, the more difficult it is to accurately estimate a damping coefficient for the mode. The software in the GenRad system estimates damping by fitting a complex exponential curve to the frequency response data. To accurately fit the data for a lightly

damped structure requires very small frequency steps in the transformed data. If the frequency step is too large, the true resonant peak will be aliased out of the data. In addition, the peak that is captured may be so sharp that a single frequency step may drop below the half power

Table 3.5. Measured vs Finite Element Modal Frequencies - With Actuators

| Mode | Axis | Modal Frequencies (Hz) | | FEM error (%) |
		Measured	Finite Element	
1	Z	1.346	1.325	1.56
2	Y	1.761	1.773	0.68
3	T	12.963	12.796	1.29
4	Z	18.877	19.431	2.93
5	Y	25.141	25.883	2.95
6	Z	44.567	47.896	7.47
7	Y	59.861	63.817	6.81
8	Z	86.451	94.875	9.74

points. Without these data points, the accuracy of the damping estimate becomes very suspect. This situation existed for both of the modal tests. Even with the GenRad's smallest frequency step the true resonant peaks and half power points were rarely captured. Damping ratio estimates for most modes were below 0.0005 and were in actuality probably less.

The second problem this caused was to make accurate measurement of the mode shapes almost impossible. Missing the true resonant peak of the mode corrupts the estimate of the modal amplitude. In addition, the change in the phase of the response occurs so quickly that one frequency step shifts the phase $180°$, effectively missing the $\pm 90°$ phasing of the

mode. This problem is illustrated in Figure 3.3. The resonant peak of

the second z-axis bending mode is seen at 18.9 Hz. The true resonant

peak has been aliased on this mode. Note how the phase of the response

shifts so rapidly that instead of passing through the -90° phase point

it jumps in one frequency step all the way through -180°.
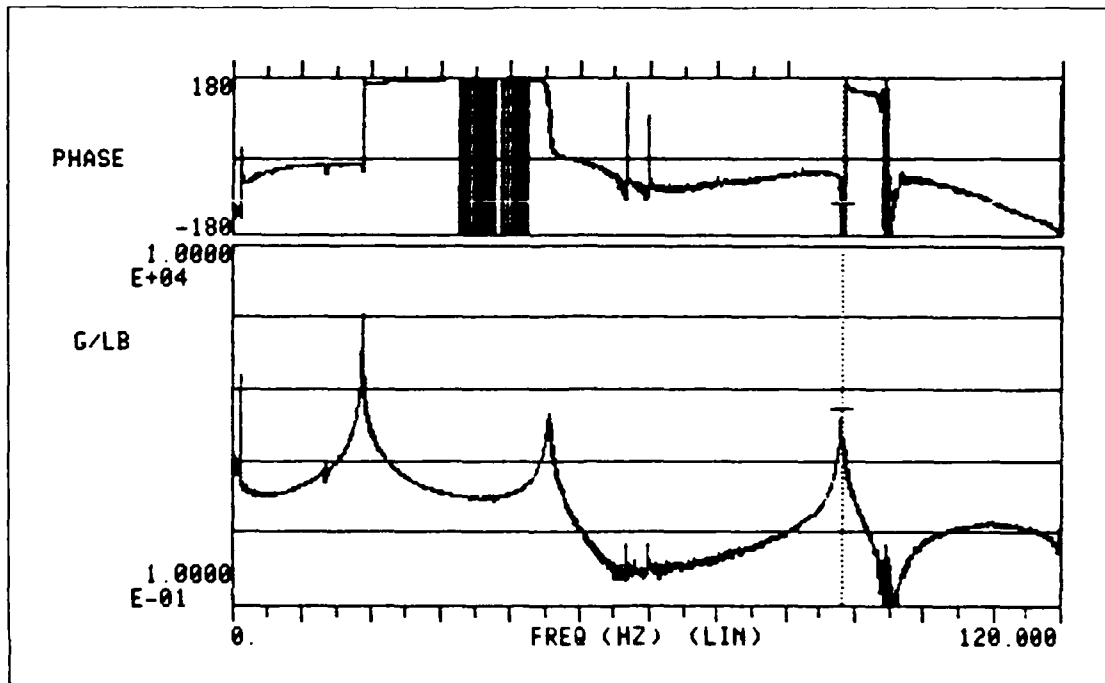
Figure 3.3. Z-Axis Frequency Response - With Actuators

When fitting a mode shape to this response the software incorrectly

interprets the phase at this point to be +90°. Since this effect occurs

at almost every node point tested, the estimated mode shapes have widely

varying amplitudes and often many more nodes than are possible (as an

example the first estimate of the second bending mode had three nodes

and bore no resemblance to the second bending mode expected for a beam).

As a result of these problems the modes shapes and damping estimates

for these two modal tests were not used for comparison with the models.

The final modal test was accomplished with the structure and actuators in the final configuration for control testing. All wiring for sensors and actuators was attached to the beam and the compensated actuators were mounted and operating without command inputs. Data collection and analysis was again accomplished with the GenRad system, with the exception of the fundamental bending modes. One of the problems with the actuators was the tendancy of the proof masses to stick when the amplitude of the oscillation in the fundamental modes became small. The result is the structure effectively has two closely spaced modes, one when the proof masses are floating and a second when they become fixed. Because of this, the GenRad proved incapable of providing good estimates of the fundamental bending modes. To test these modes, a sine dwell was conducted by fixing small magnets to the base plate in the axis to be tested and forcing the beam at a single frequency using magnetic induction coils. A frequency response function was generated by incrementally increasing the frequency of the forcing function, allowing the motion to become steady state, and measuring the magnitude and phase of the beam acceleration with respect to the forcing signal. The resonant peak of this response function was used to define the modal frequency and the modal damping was estimated using the half power points of resonant peak (see equation 8). The mode shape was estimated by forcing the structure at the resonant freqeuency and measuring the acceleration at several points along the beam. The stations used for this test coincide with the node points of the finite element model, which allows for consistent comparison of results with the finite element model. This data and the data for the higher modes obtained using the GenRad can be found in Appendix D.

A summary of the natural frequencies is presented in Table 3.5 and the mode shapes, normalized with respect to the mass matrix, are shown

Table 3.6. Modal Frequencies and Damping for Control Configuration

Mode	Axis	Modal Frequencies (Hz)		FEM error (%)	Damping
		Measured	Finite Element		
1	Z	1.33	1.329	0.08	0.0377
2	Y	1.75	1.775	1.43	0.0350
3	T	12.580	12.655	0.60	0.0127
4	Z	18.094	19.394	7.21	0.0029
5	Y	23.897	25.839	8.11	0.0032
6	Z	43.454	47.734	9.86	0.0022
7	Y	57.624	63.608	10.39	0.0014

in Table 3.7. Since the generalized mass was not derived from the modal test data the value calculated in the finite element model was used to appropriately scale the measured mode shapes. The error induced should be small since the model closely matched the first five modes. The actuators have added enough damping to the structure to alleviate the problem previously encountered with estimating damping and mode shapes. The finite element modal was found to give a slightly better approximation to the modal test data if the inertia of the proof masses was included without their mass. The correction mainly affected the fundamental modes and slightly improved the higher modes.

The normalized bending mode shapes measured for the first two bending modes in each axis are compared with the finite element model mode shapes in Figures 3.4 through 3.7. The mode shape for the torsional vibration mode was not measured in the modal test because the beam was not instrumented to measure torsion at any location other than the base plate. Since the finite element fundamental bending modes showed good agreement with the modal tests, and the torsion frequency

matched very closely with finite element prediction, the finite element model was used to define the torsion mode shape, which is shown in Figure 3.8.

Table 3.7. Structure Modal Amplitudes

FEM Node	Z-1 Bending	Y-1 Bending	First Torsion	Z-2 Bending	Y-2 Bending
1	0.00000	0.00000	0.00000	0.00000	0.00000
2	0.05146	0.02259	-	0.75459	1.06325
3	0.11494	0.20693	-	2.92907	3.24512
4	0.30783	0.56328	-	5.64428	5.84183
5	0.62817	0.97277	-	8.23860	8.42785
6	1.11862	1.38610	-	10.2239	10.1976
7	1.78287	1.89519	-	10.8717	10.6843
8	2.15374	2.39399	-	8.67409	8.60025
9	3.26069	3.10030	-	8.33159	8.22494
10	3.98271	3.67899	-	4.78725	4.71435
11	4.90482	4.94348	1.24048	-0.5734	-0.6087
Generalized Modal Mass $(lbf/in/sec^2)$	0.01663	0.01664	0.17525	0.00201	0.00201
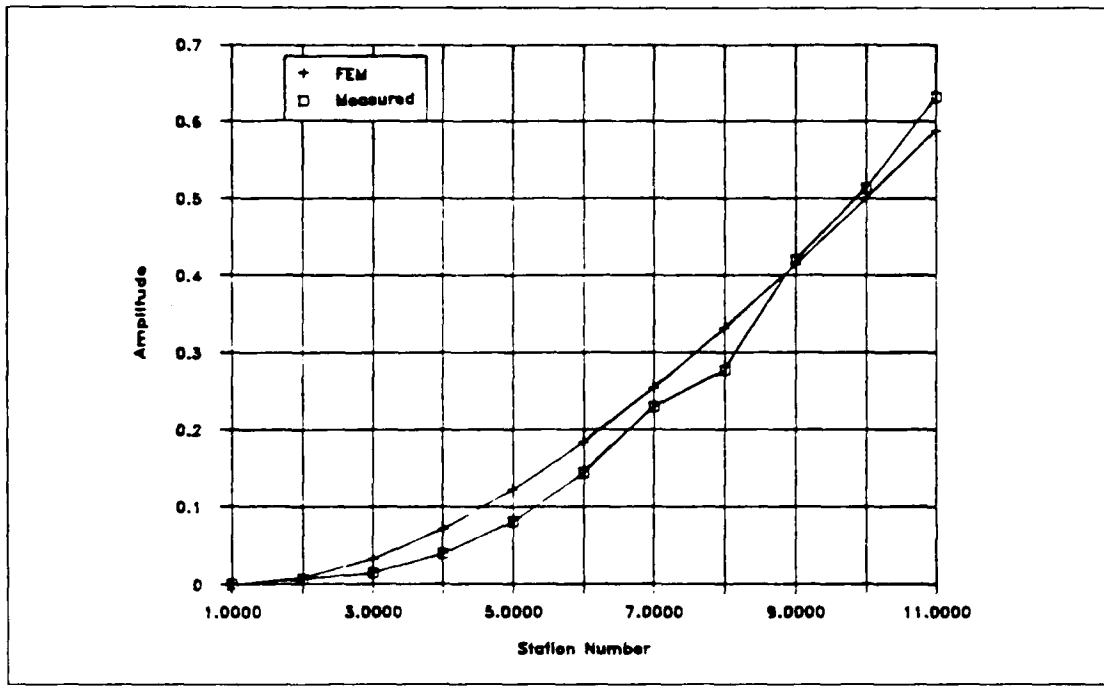
Figure 3.4. Z-Axis Fundamental Bending Mode
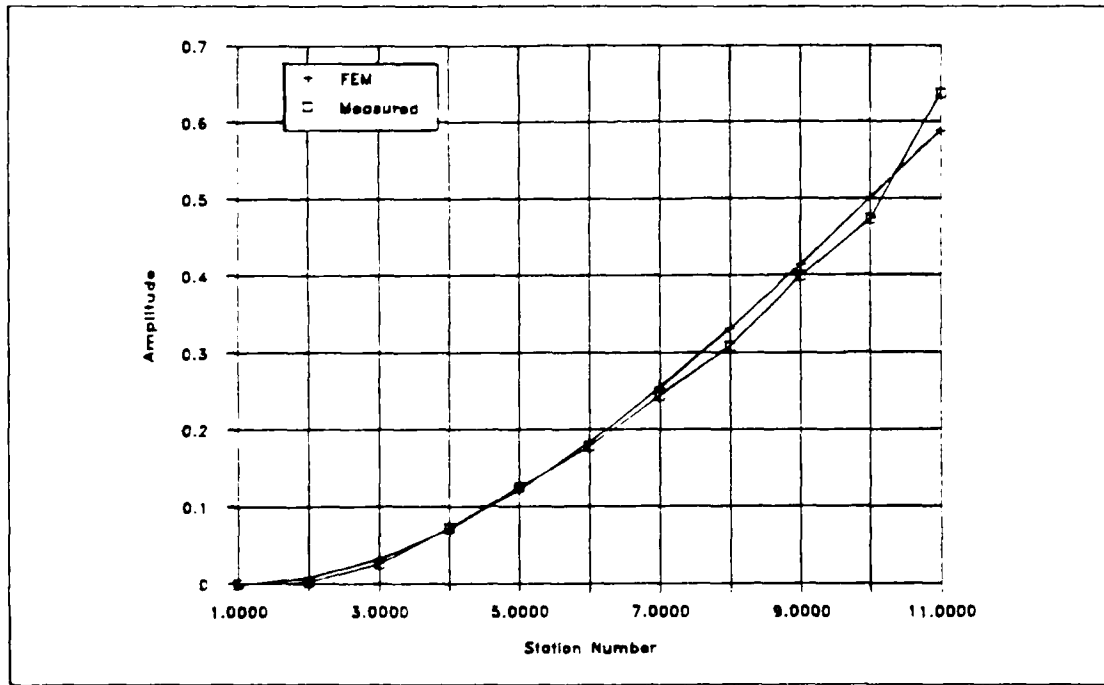
Figure 3.5. Y-Axis Fundamental Bending Mode

3 - 18
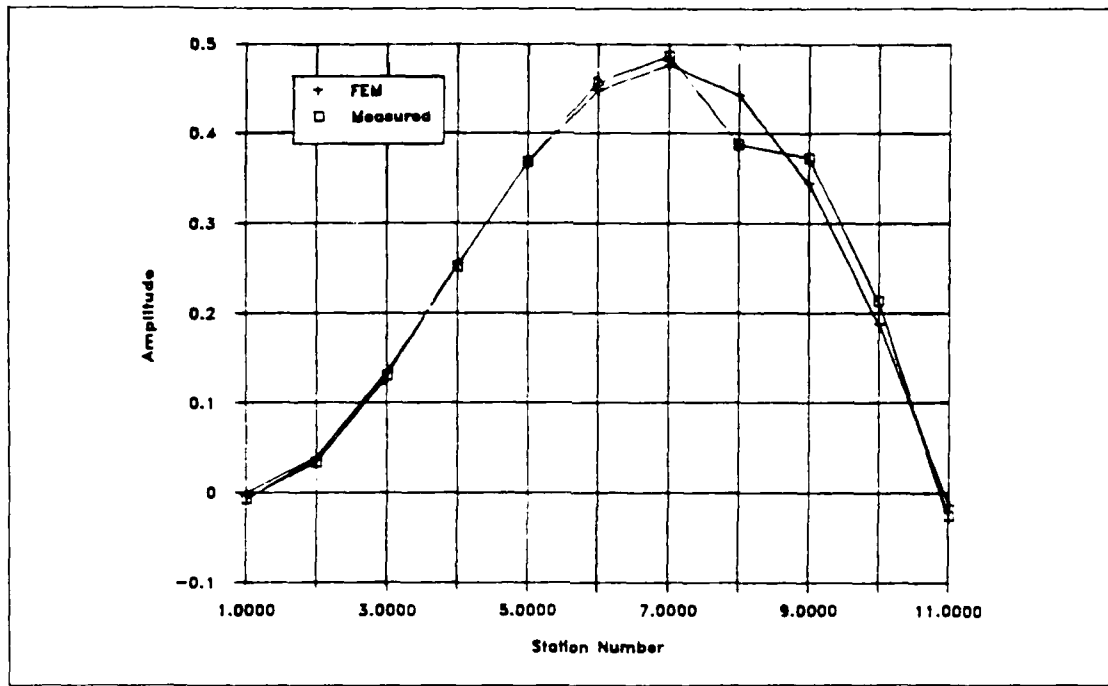
Figure 3.6. Z-Axis Second Bending Mode
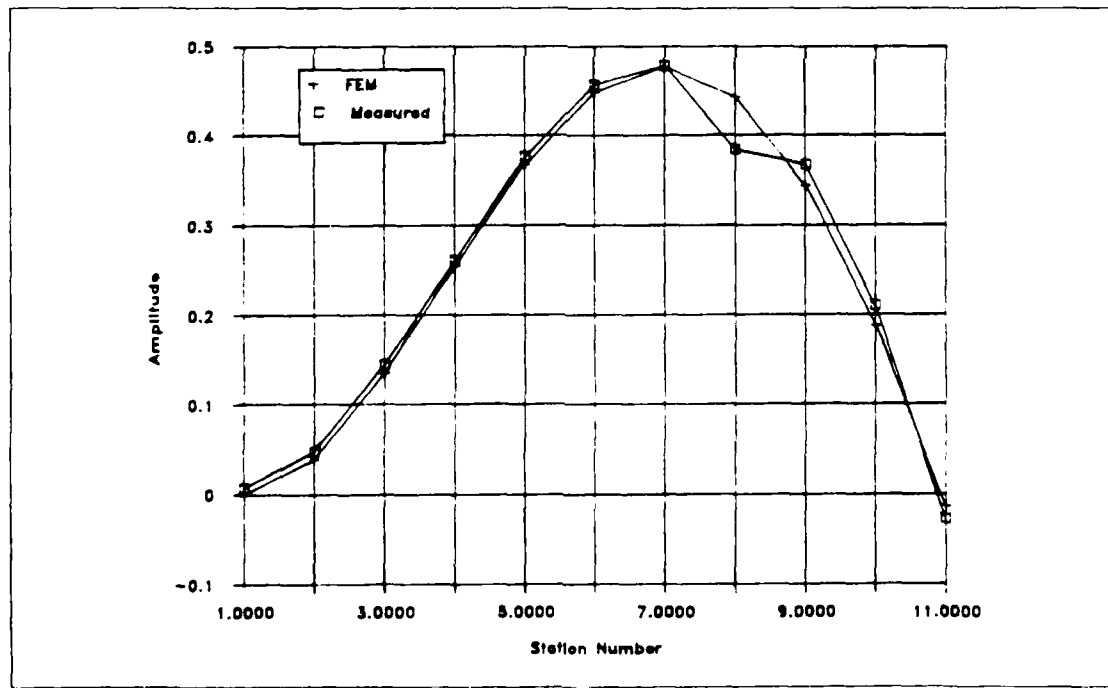
Figure 3.7. Y-Axis Second Bending Mode

3 - 19
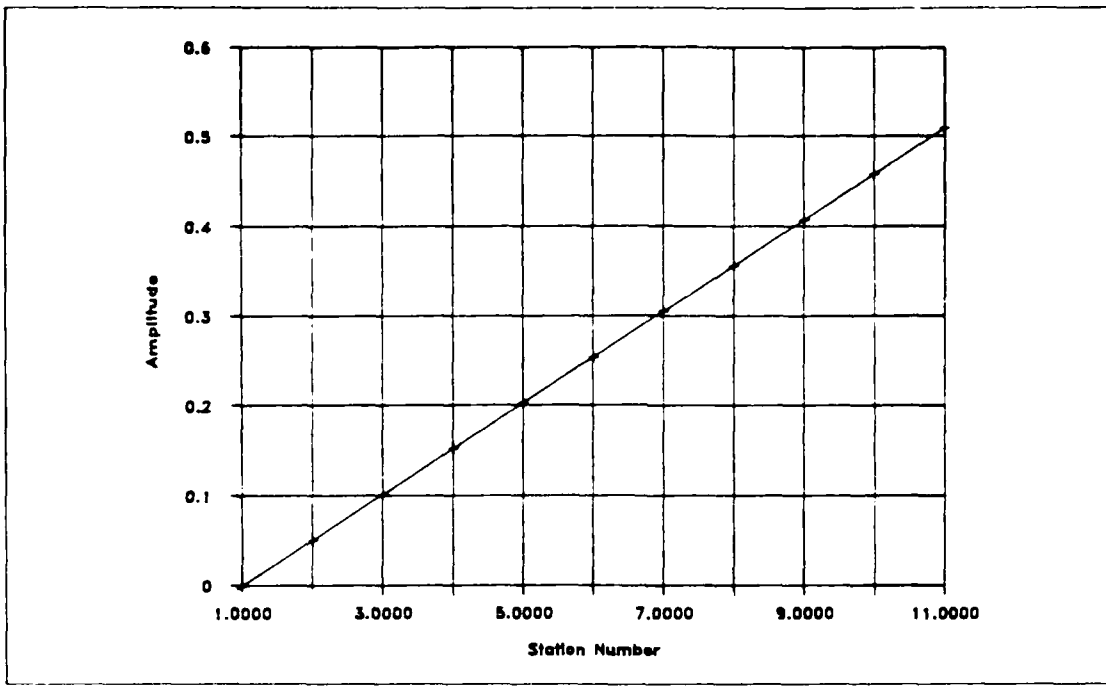
Figure 3.8. First Torsion Mode - Finite Element Model Only

IV. Sensors

In keeping with the goal of constructing an experiment with as much in common with large space structures as possible, the sensors selected for use in controlling the beam were piezoelectric accelerometers. Accelerometers provide an inertial sensing capability which is required in space. The primary disadvantages of using accelerometers are that the output must be integrated to generate a velocity measurement for the control algorithm, and that most accelerometers of this type have not been designed for an accurate response below 1 Hz. While integration does tend to smooth some high frequency noise, it also aggrevates very low frequency drift and bias signals. An example of the drift seen in one accelerometer is shown in Figure 4.1.

The specific accelerometers selected for sensors on the beam were manufactured by Kistler Instrument Corporation. Specifications for these devices are listed in Appendix E. These instruments had the best low frequency response characteristics and the least drift of the accelerometers available at the Flight Dynamics Laboratory for this experiment. Even so, the output was found to have so much low frequency drift the actuators would not remain centered when a control loop was closed. Because the complex pole pair in the actuator dynamics has been moved below 1 Hz, they are very responsive to these low frequency signals. As was noted earlier, a 5 mV drift in the input signal has been observed to drive the proof mass to the end of its stroke.
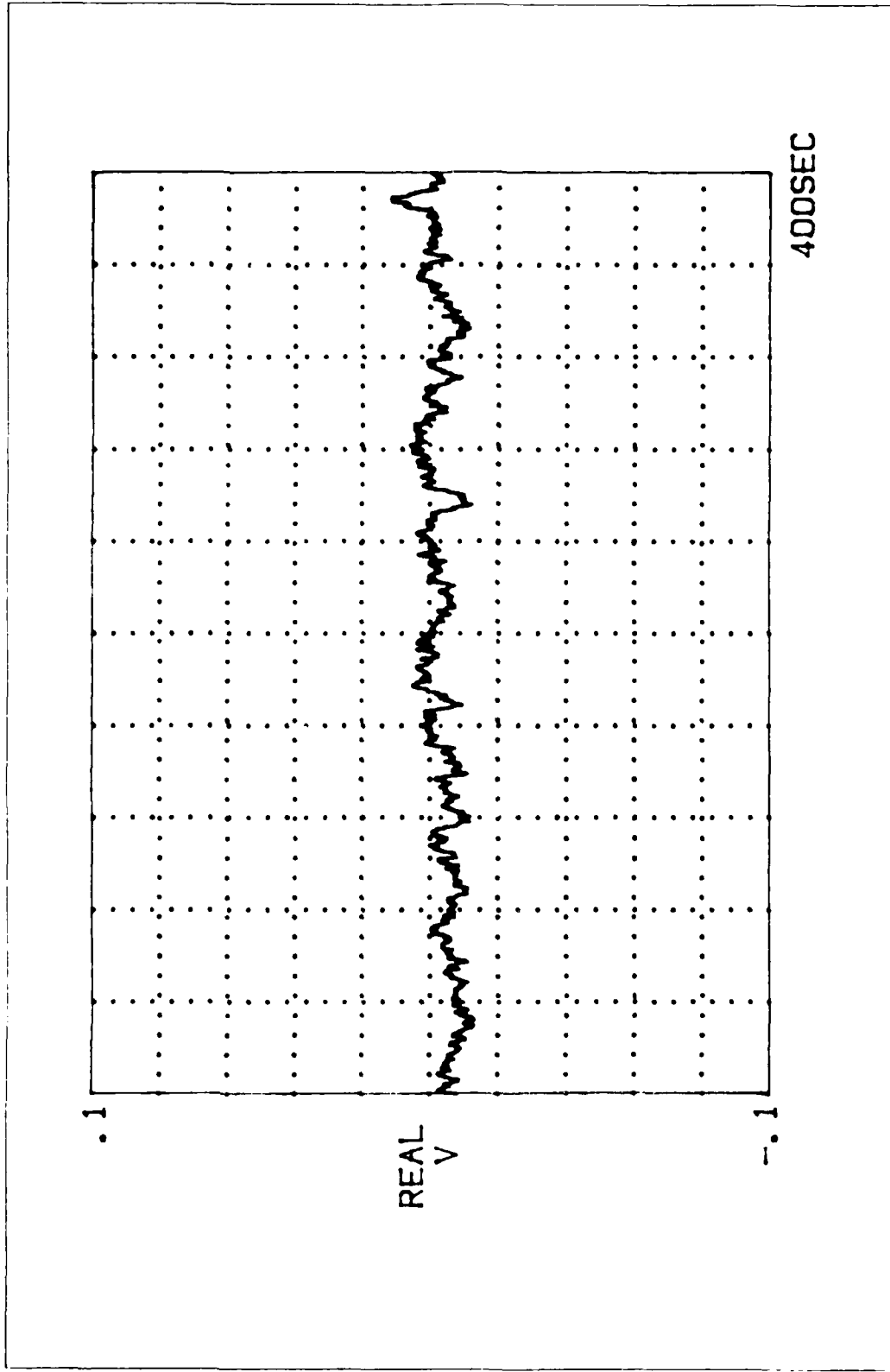
Figure 4.1. Accelerometer Long-Term Drift

AD-A189 824   ACTIVE VIBRATION CONTROL OF A CANTILEVERED BEAM WITH   2/3
THREE ELASTIC COORDINATES(U) AIR FORCE INST OF TECH
WRIGHT-PATTERSON AFB OH SCHOOL OF ENGI.. T A CRISTLER
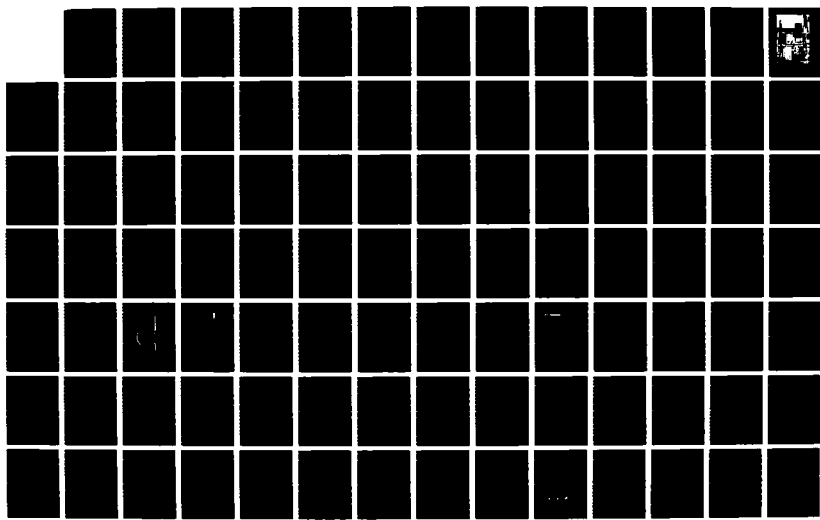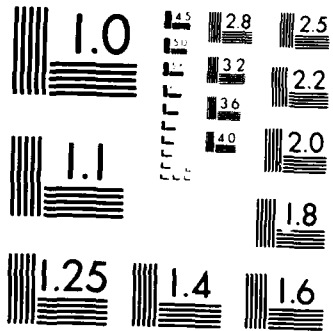
MICROCOPY RESOLUTION TEST CHART

NATIONAL BUREAU OF STANDARDS 1963 A

Signal Conditioning

To remove this drift from the velocity measurements the
accelerometer output was passed through a signal conditioning circuit
prior to integration. Ideal signal conditioning for this experiment
would reject all signals below 1 Hz and not affect the rest of the
frequency spectrum. Unfortunately, filters which reduce the magnitude
of the signal affect the phase for a decade beyond the break frequency.
Therefore, to ensure that the phase of the signal is unaffected at the
fundamental bending frequency of the beam requires placing the break
frequency at or below 0.15 Hz. The problem again arises that noise in
the system is so close in frequency to the control bandwidth that
filtering dynamics contaminate the measurement response in this
bandwidth.

The approach taken to filter some of the low frequency input was to
split the signal and on one side, low-pass filter it to remove
frequencies above 1 Hz, invert the filtered signal and then sum it with
the original, unfiltered signal. This should have the effect of
subtracting out the drift. The filter and integrator were implemented
using the circuit in Figure 4.2. The resulting transfer function from
acceleration to velocity is

$$\frac{\dot{X}(s)}{\ddot{X}(s)} = \frac{3.5081 \ (S_{1,2} + 7.814 \pm 10.76j)(S_{3,4} + 20.46 \pm 6.628j)}{(S + 11.31)^5 \ (S + 0.6378)} \quad (14)$$

The predicted frequency response for this circuit is in Figure 4.3.
This filtering has reduced the response magnitude of the 0.1 to 1 Hz
frequency range when compared with a simple integrator. The transfer

4 - 3
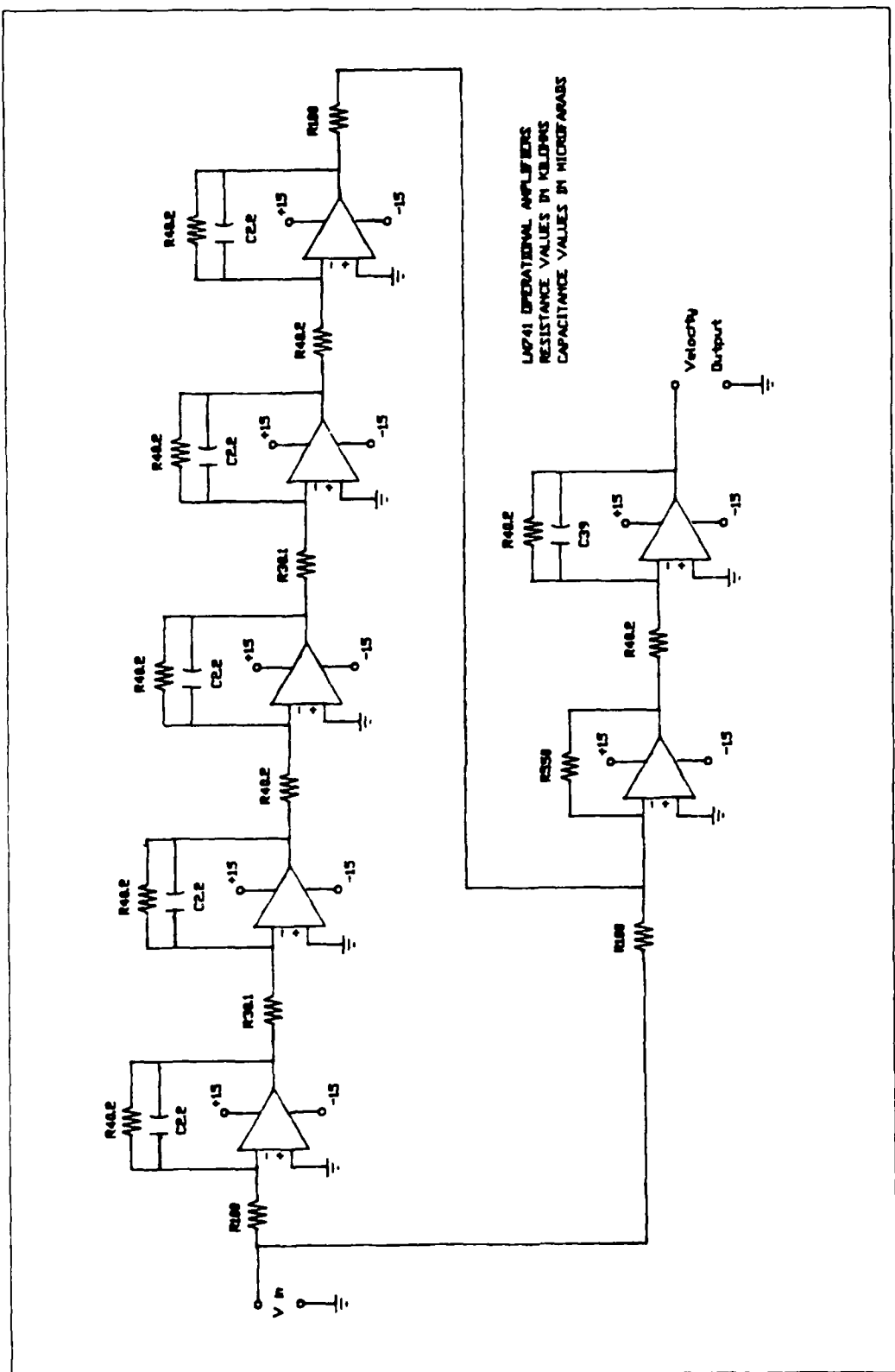
Figure 4.2. Accelerometer Signal Conditioning and Integration Circuit
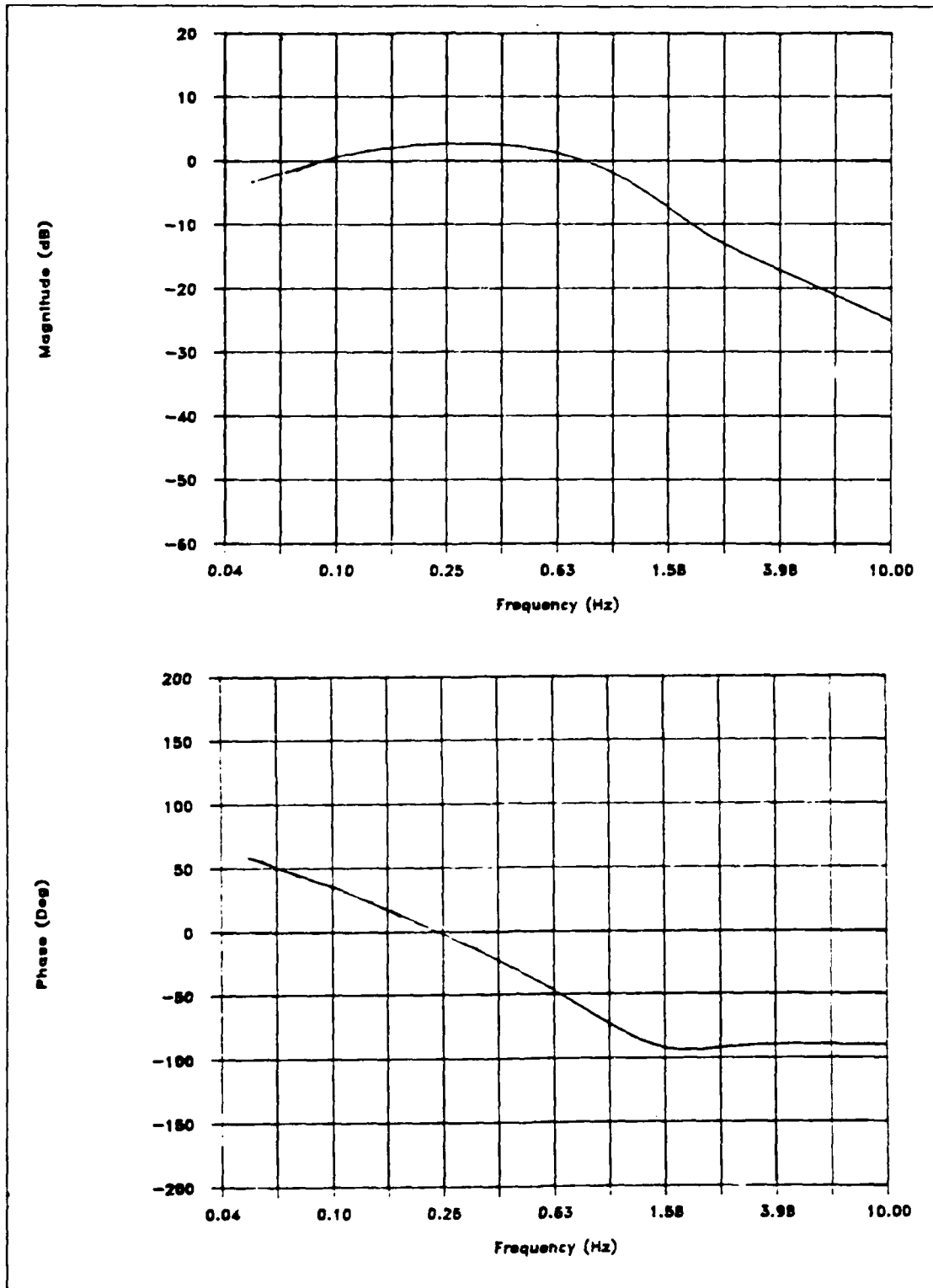
Figure 4.3. Predicted Signal Conditioning/Integration Frequency Response

function for an integrator has a 15 dB drop in magnitude from 0.2 Hz to 1.3 Hz. The peak magnitude for the filter occurs at 0.4 Hz and is only 7 dB above the 1.3 Hz response magnitude. While it would be desireable to move the low frequency cutoff even higher, the phase response shows that the phase has just settled at $-90°$, so moving the filter higher would begin to shift the phase of the output away from a velocity signal. The frequency response of the actual circuit comes very close to the prediction, as can be seen in Figures 4.4 through 4.7. As a final step in the signal conditioning process the output from the integrator was passed through an A/C coupled Intek Variable Gain Amplifier to remove any bias that may still be present in the signal. The break frequency of this A/C coupling is at 0.16 Hz, which accounts for the extra phase shift seen in the measured frequency response verses prediction.

Sensor Calibration and Scale Factors

The accelerometers were calibrated using a 1 g peak shaker which operates at 80 Hz. Ideally a frequency response function would have been generated for each sensor over the control bandwidth. Unfortunately, the only shakers available of high enough quality response to be used as a calibration instrument had a low frequency cutoff of 10 Hz. As a result, each sensor was calibrated at a single frequency and the manufacturer specification of a flat response function over the operating range of the sensor was relied upon. The calibration measured for each accelerometer is listed in Table 4.1.
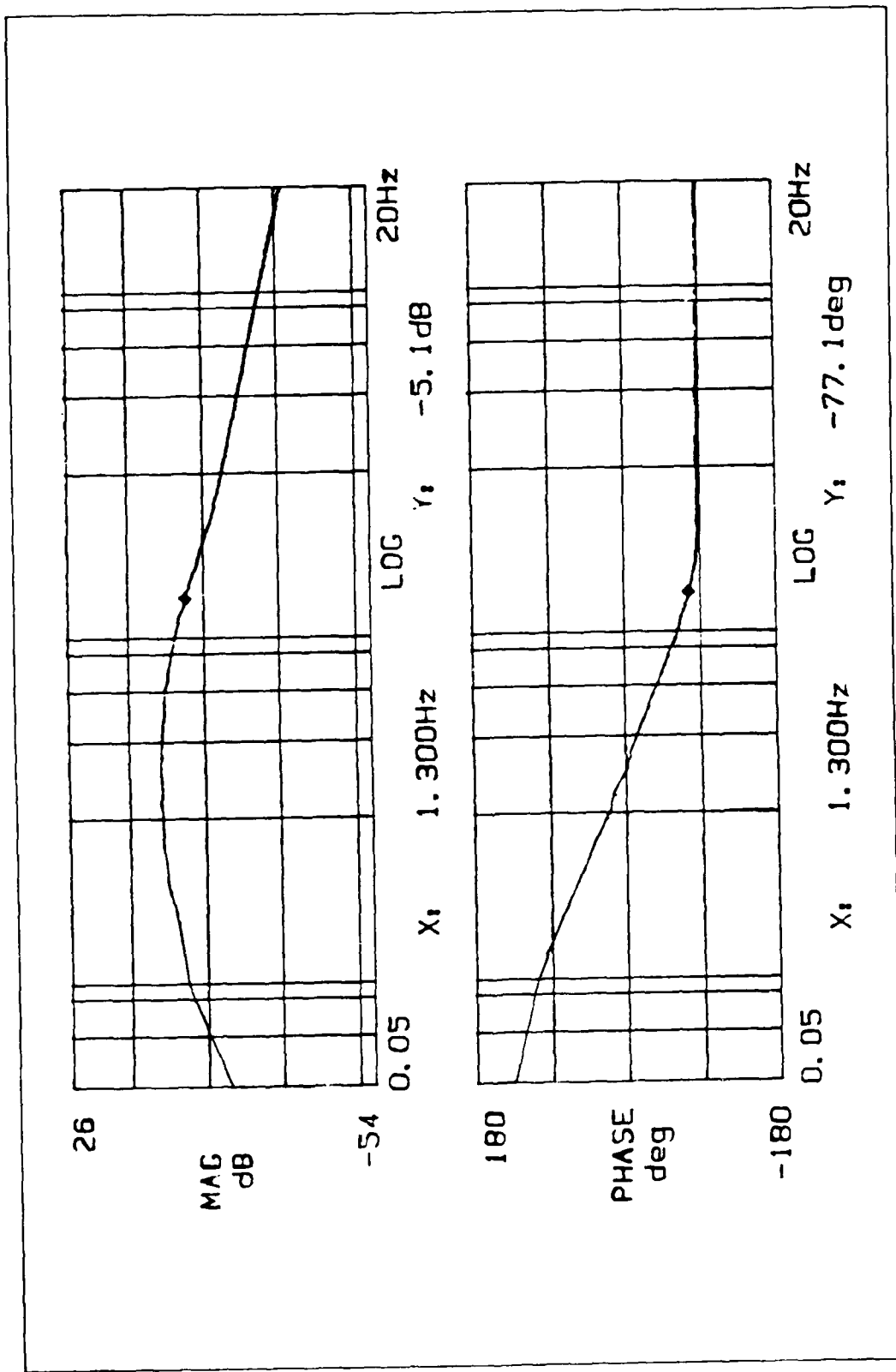
Figure 4.4. Sensor Channel #1 Frequency Response
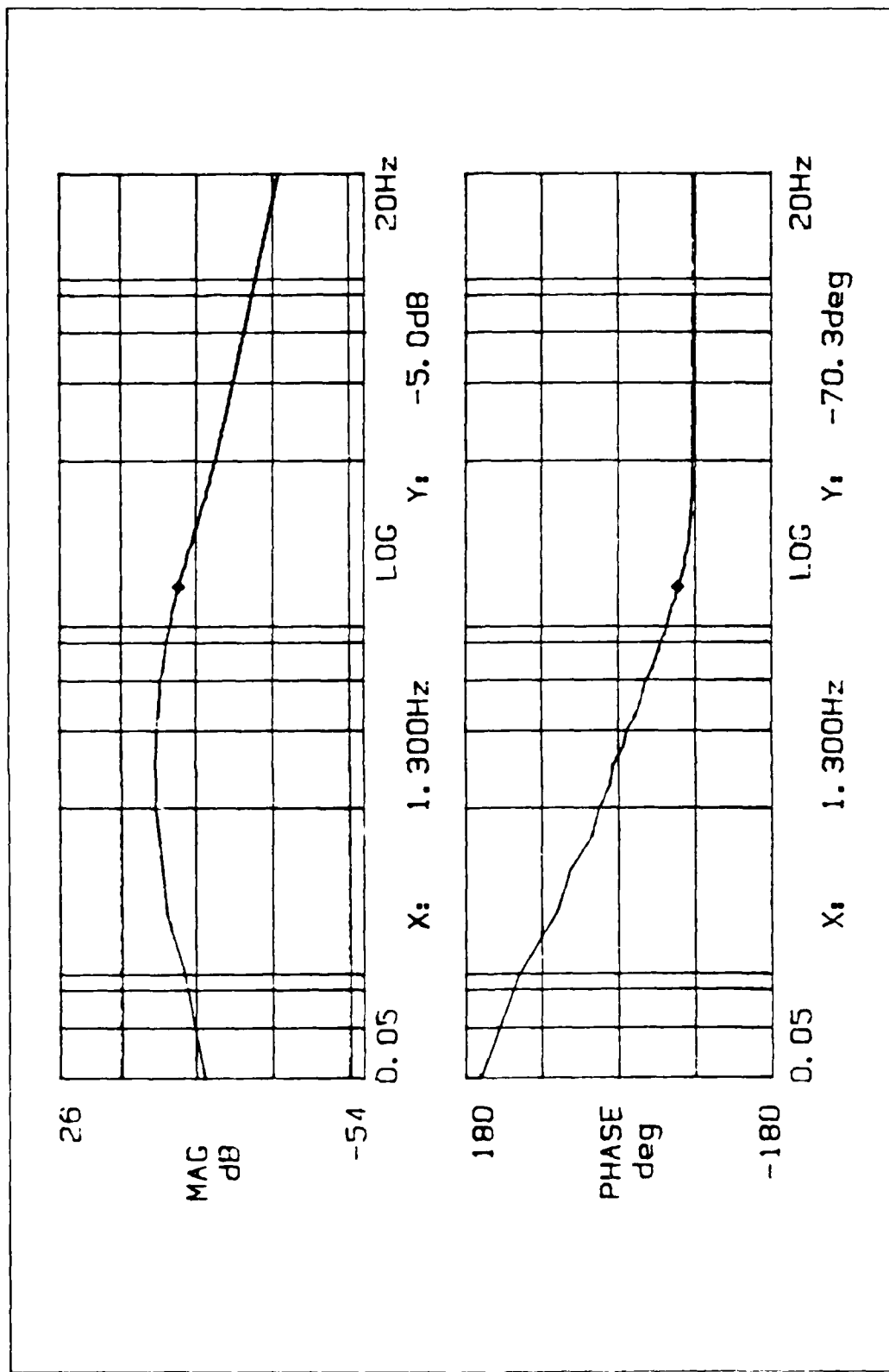
Figure 4.5. Sensor Channel #2 Frequency Response
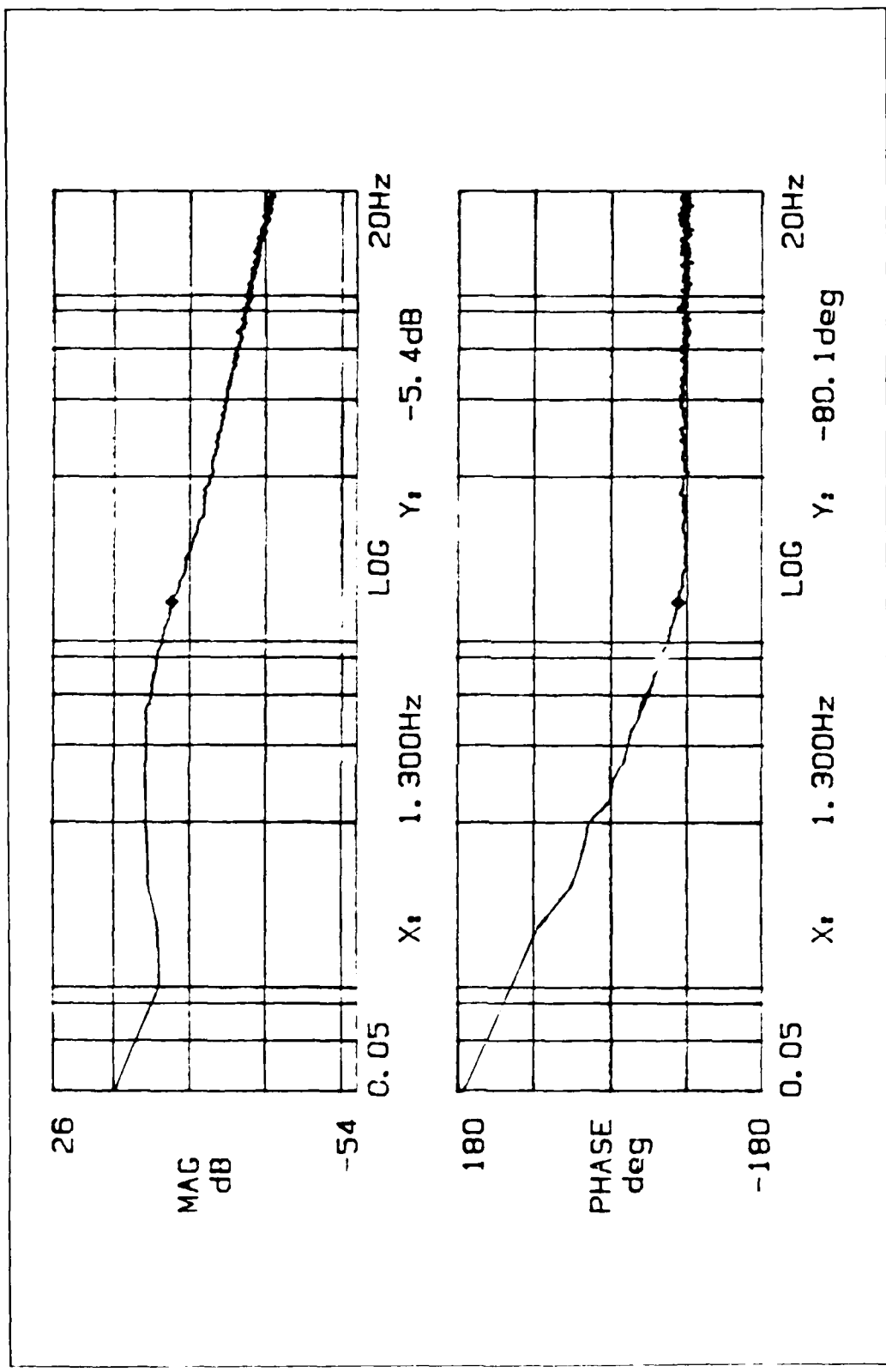
Figure 4.6.. Sensor Channel #3 Frequency Response
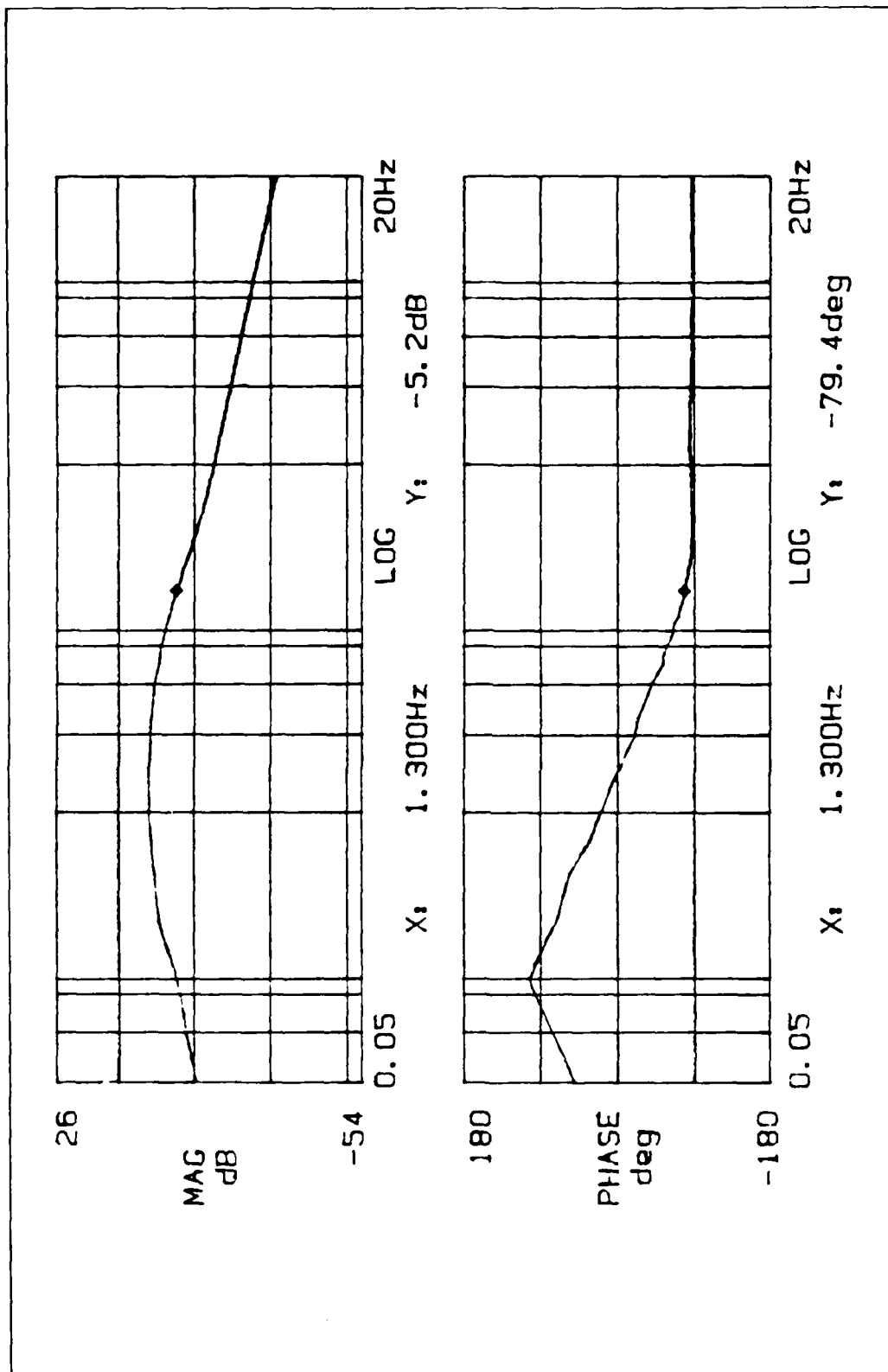
Figure 4.7. Sensor Channel #4 Frequency Response

Table 4.1. Sensor Calibration Data

Serial #	Sensor #	Sensitivity (V/g)
C82629	1	0.881
C82753	2	0.881
C82736	3	0.891
C82702	4	0.871

To achieve the best accuracy possible for the sensor measurements the response functions measured for the signal conditioning and integrator (Figures 4.4 to 4.7) were adjusted to match the predicted response magnitude at 1.3 Hz by adding or subtracting the required gain. The nominal and adjusted gains for each sensor channel are listed in Table 4.2. Combining these gains with the accelerometer sensitivities results in the sensor scale factors shown in Table 4.3.

Table 4.2. Integration and Signal Conditioning Gain

Sensor #	Nominal Gain	Measured Gain
1		3.369
2	3.508	3.408
3		3.255
4		3.331

Table 4.3. Sensor Scale Factors

Sensor #	mV/ft/sec	mV/in/sec
-	92.19	7.68
2	93.26	7.77
3	90.10	7.51
4	90.10	7.51

System Configuration and Gain Verification

Configuration

The hardware used in the experiment consists of the beam and four proof mass actuators, four accelerometers as sensors, several stages of signal conditioning on inputs and outputs, and the PC-1000 Systolic Array Processor and its host computer, a Compaq Portable Computer. Data collection was accomplished using the Ono Sokki Freqeuncy Spectrum Analyzer with an HP-7874 Plotter, and the GenRad Modal Analyzer (see Figures 5.1 and 5.2).

The actuators were mounted on the base plate in orthogonal pairs parallel to the y and z beam axes (see Figure 5.3). This configuration provides symmetric forces from each pair for bending control and asymmetric forces from all four for torsion control. The actuator located along the minus z direction was arbitrarily selected as #1, and remaining actuators were numbered from there in a counterclockwise directon. Positive force outputs act in the directions indicated in Figure 5.3. The accelerometers to be used as sensors were mounted colocated with the actuators with the same numbering and output sign (see Figure 5.3). Accelerometer measurements were input to the signal conditioning and integration circuit to estimate beam velocity. This velocity measurement was then filtered using an A/C coupled amplifier to remove any bias in the integration circuit. Finally, the measurements were input to the PC-1000, which is a high speed digital array processor used for real-time data collection, estimation, and control applications. Analog inputs are converted to 12-bit digital data and internal calculations are performed using 32-bit floating point
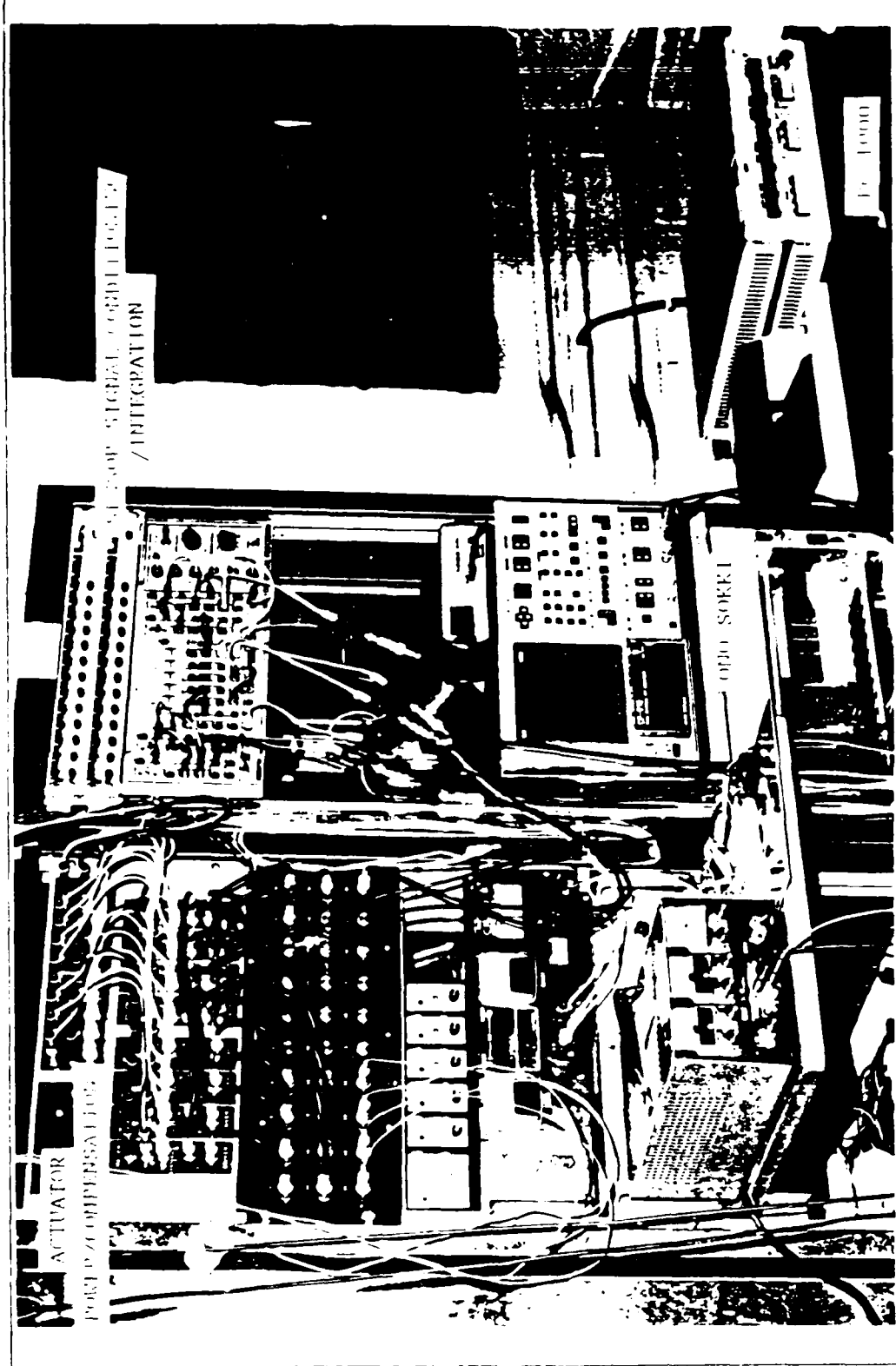
Figure 5.1. Experiment Signal Conditioning and Control Hardware

5 - 2
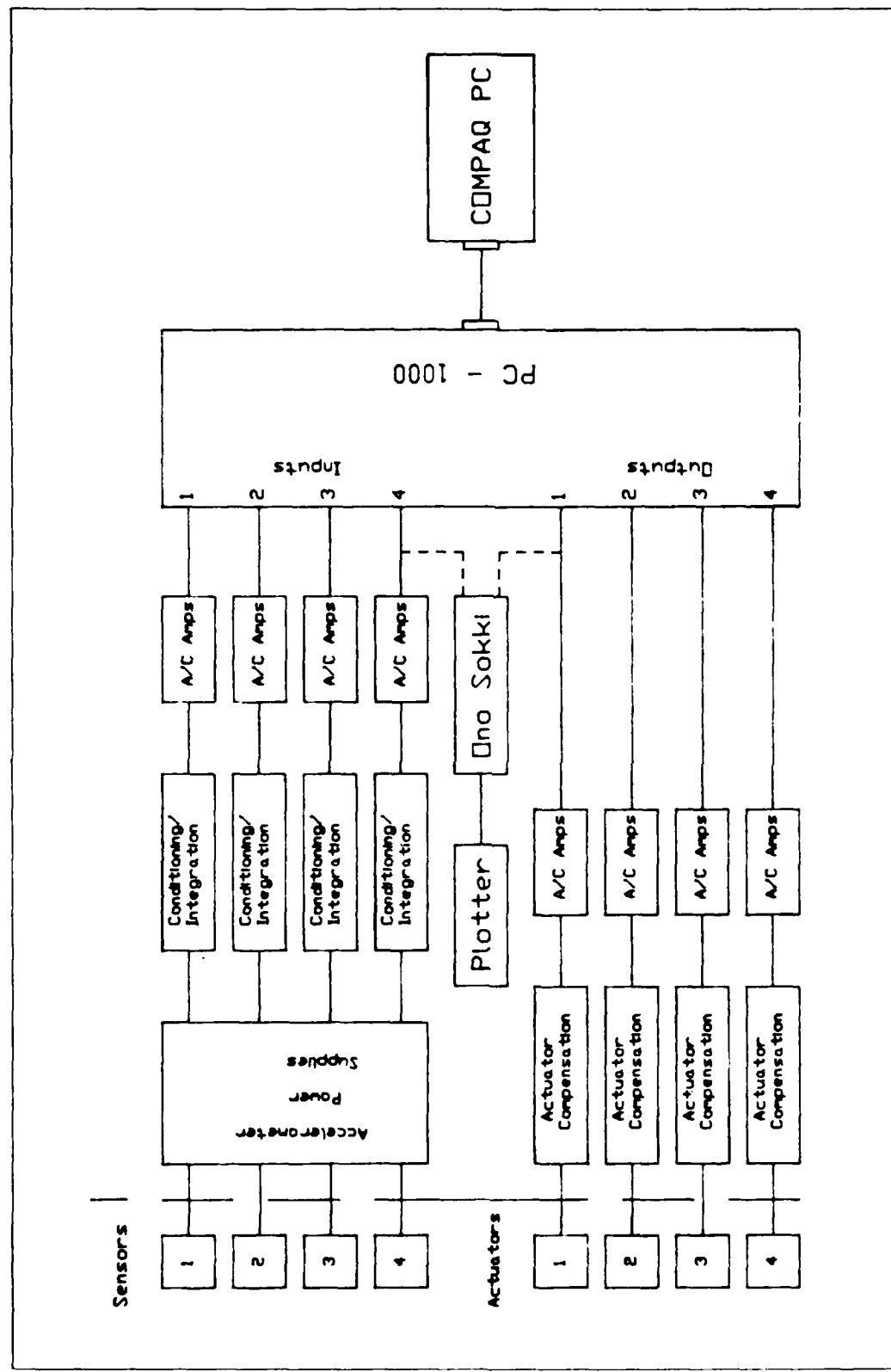
Figure 5.2. Experiment Functional Configuration Diagram
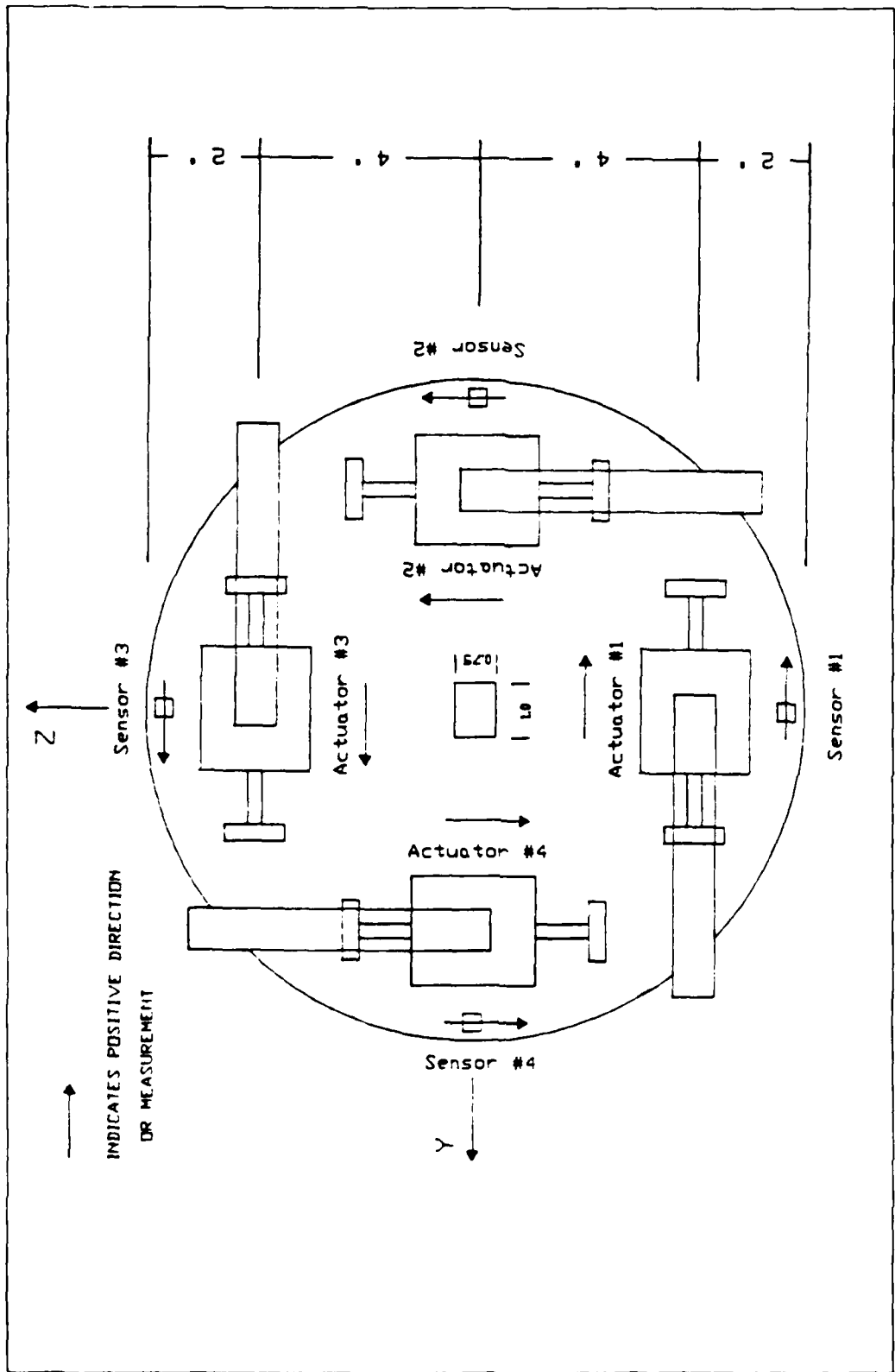
Figure 5.3. Base Plate Configuration

arithmetic. Calculated outputs are converted back to analog signals to command the actuators. The processor can be programmed for various sample rates (in Hz), input and output signal ranges (in volts),and input/output channel gains. Further information about the PC-1000, its operation and capabilities, can be found in Reference 12. The PC-1000 was programmed with the estimation and control algorithm to be tested, and the control commands it generated were input to the actuators. In operating the PC-1000, a small bias was found on the input channels, probably residing in the analog-to-digital (A/D) converter. This bias would pass through the estimator/controller and saturate the actuators. To remove it, the control commands were filtered using a set of A/C coupled amplifiers identical to those used in filtering the sensor measurements. The conditioned control commands were then provided to the actuators.

System Gain Verification

Prior to attempting to control the structure with the PC-1000, an analog velocity feedback loop was implemented to verify the gains through the system. Using the sensor scale factors calculated in Chapter 4 and the actuator transfer functions from Chapter 2, Table 2.7, a viscous damping coefficient in lbf/in/sec can be calculated. The coefficient can be changed using the Intek amplifiers in the sensor signal conditioning path, which could be adjusted in 10 dB increments.

Before closing the feedback loop, the open loop damping due to the actuators was characterized by finding a damping coefficient which would generate a structure frequency response that matched the damping measured in the final modal test. This was done using the same method

discussed in Chapter 2 for estimating the acutator residual damping (see equation 5 - 7). This residual damping coefficient was then added to the commanded feedback coefficient for each actuator controlling the axis under test resulting in a total coefficient applied to the structure. Two tests were conducted in each bending axis, one with the nominal sensor gains calculated in Chapter 4, and a second with the sensor scale factor increased by 10 dB. Table 5.1 summarizes the damping coefficients calculated for the closed loop response for these tests.

Table 5.1. Closed Loop Viscous Damping Coefficients (lbf/in/sec)

Axis	Test #	Actuator	Commanded Coefficient	Residual Coefficient	Total Coefficient
Z	1	2	0.0046	0.029	0.0377
		4	0.0041		
	2	2	0.0145		0.0565
		4	0.0130		
Y	3	1	0.0037	0.038	0.0452
		3	0.0036		
	4	1	0.0117		0.0611
		3	0.0114		

These damping coefficients were used in the finite element model to generate a frequency response for the structure. The damping ratio predicted for the structure was estimated from the frequency response using the half power method (equation 8). Tests were conducted on the structure by displacing the base plate and recording the free decay time response of the beam on the Ono Sokki FFT Analyzer. Since the Ono Sokki

records the data digitally, the peaks of the response could be listed
and the damping ratio estimated using the log decrement method (7:61)

$$\zeta = \frac{1}{2\pi} \ln\left(\frac{M_{P1}}{M_{P2}}\right) \qquad (15)$$

where M_{P1} = Magnitude of the first peak

M_{P2} = Magnitude of the next peak in the response

To obtain an accurate estimate, ζ was calculated for each pair of peaks
in the response. The damping ratio and uncertainty is listed for each
test in terms of the mean and standard deviation of all damping ratios
calculated for a single free decay of the structure.

Table 5.2 summarizes the predicted and measured damping ratios for
the experiment. Figures 5.4 and 5.5 show the predicted frequency
response and the measured time response for the z axis tests, and
Figures 5.6 and 5.7 are the same data for the y axis tests. Agreement
between predicted and measured damping ratios is excellent for these
tests. The slight differences are most likely due to the damping added
by the sensor and actuator wiring, not accounted for in the model.

Table 5.2. Predicted vs Measured Damping Ratios

Test #	Predicted ζ	Measured ζ
1	0.0590	0.059
2	0.0722	0.074
3	0.0424	0.044
4	0.0579	0.061

PREDICTED FREQUENCY RESPONSE

MEASURED TIME RESPONSE
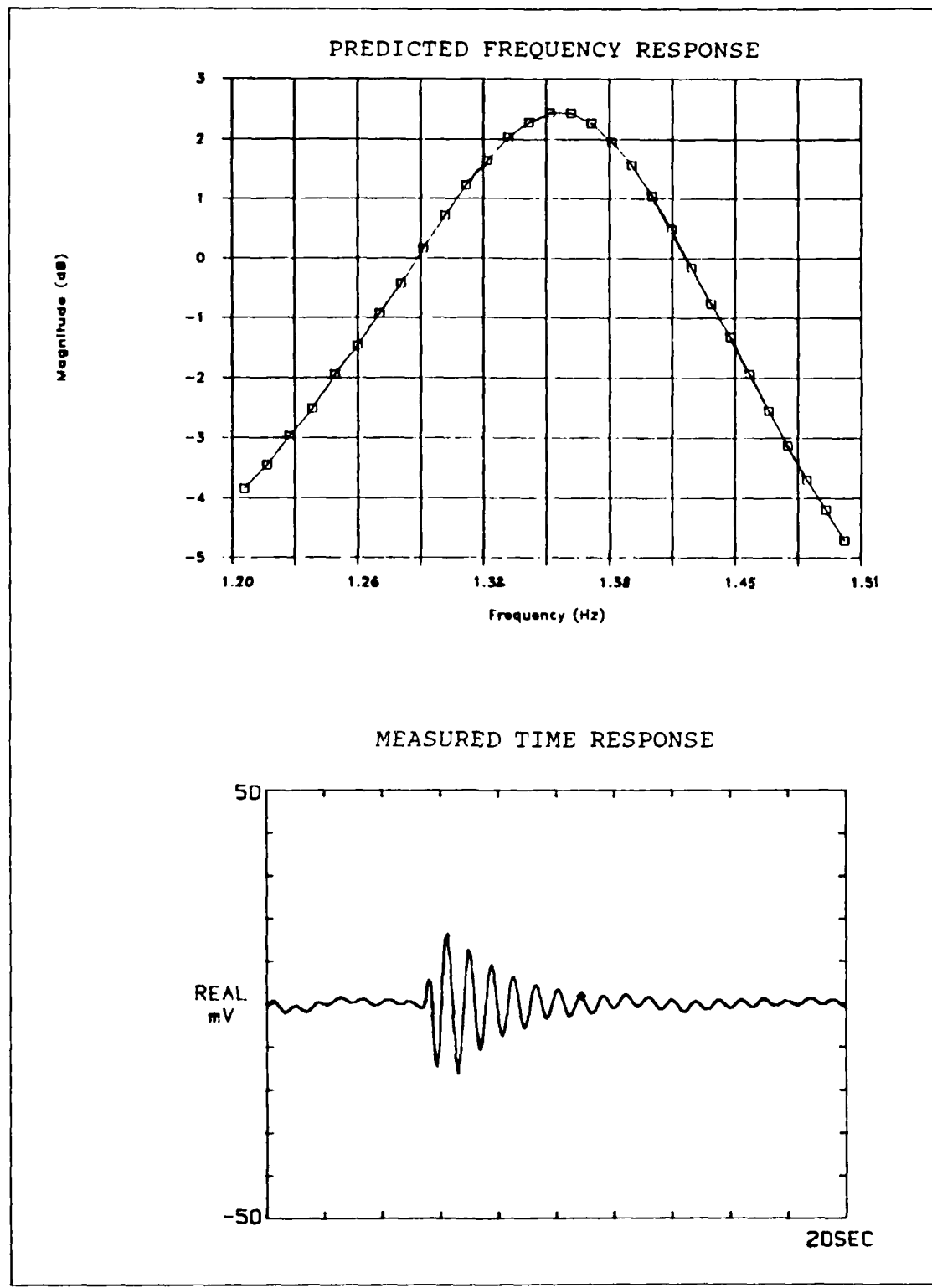
Figure 5.4. Predicted and Measured Z-Axis Response (C = 0.0377)

PREDICTED FREQUENCY RESPONSE
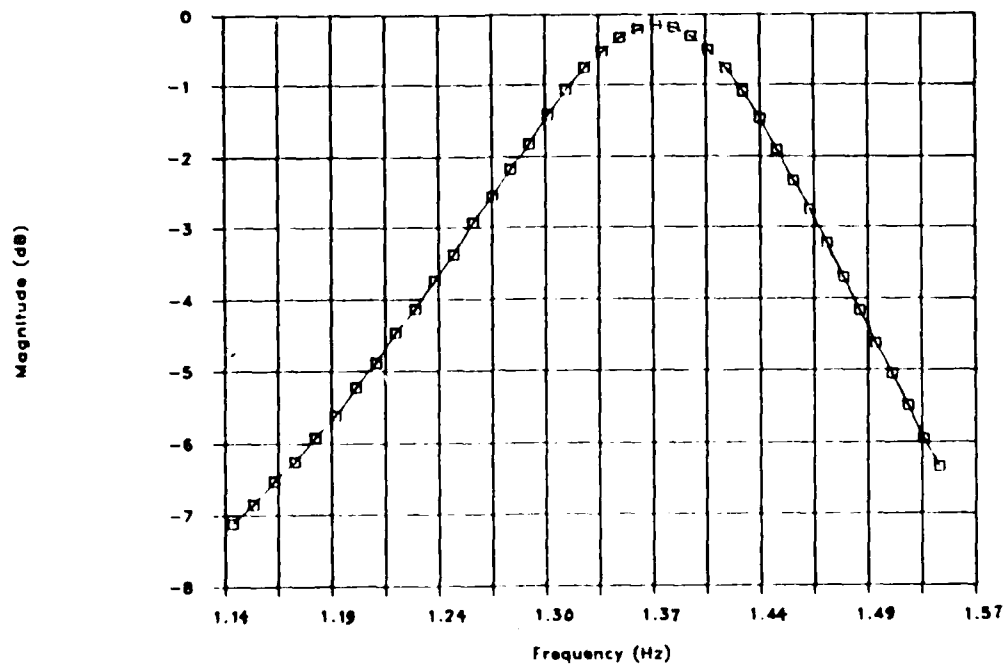
MEASURED TIME RESPONSE
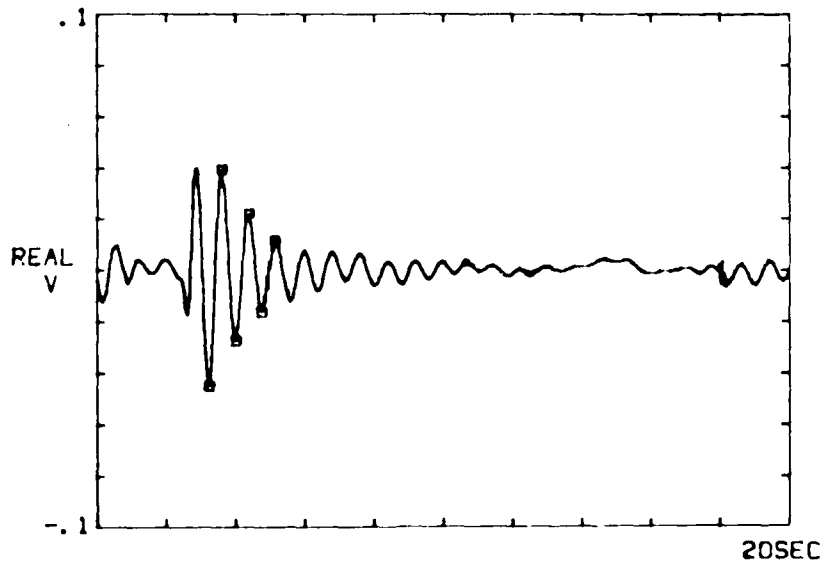
Figure 5.5. Predicted and Measured Z-Axis Response (C = 0.0565)

5 - 9
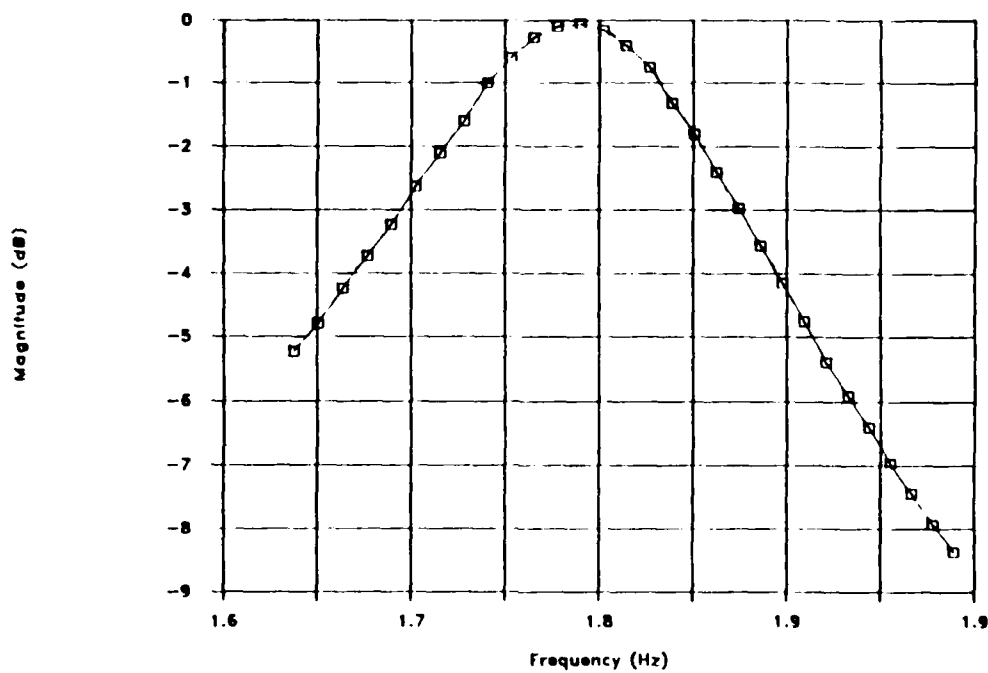
PREDICTED FREQUENCY RESPONSE
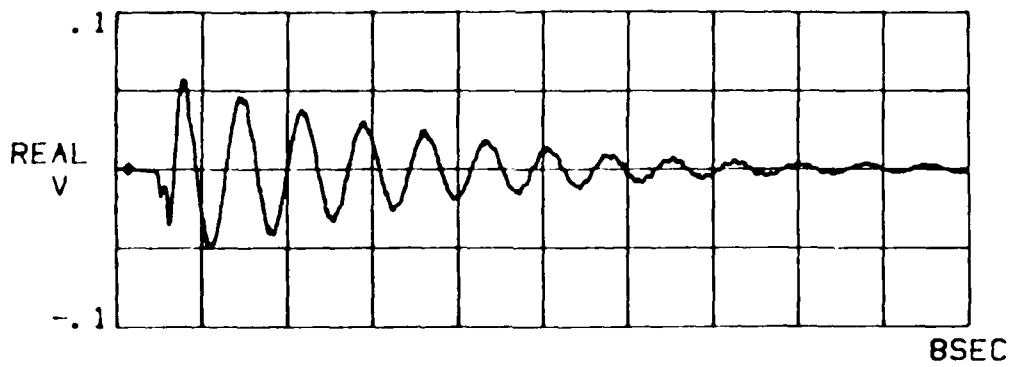
Figure 5.6. Predicted and Measured Y-Axis Response (C = 0.0452)

MEASURED TIME RESPONSE

PREDICTED FREQUENCY RESPONSE

(graph: Magnitude (dB) vs Frequency (Hz), ranging from 1.6 to 1.9 Hz)

MEASURED TIME RESPONSE

(graph: REAL V vs BSEC)
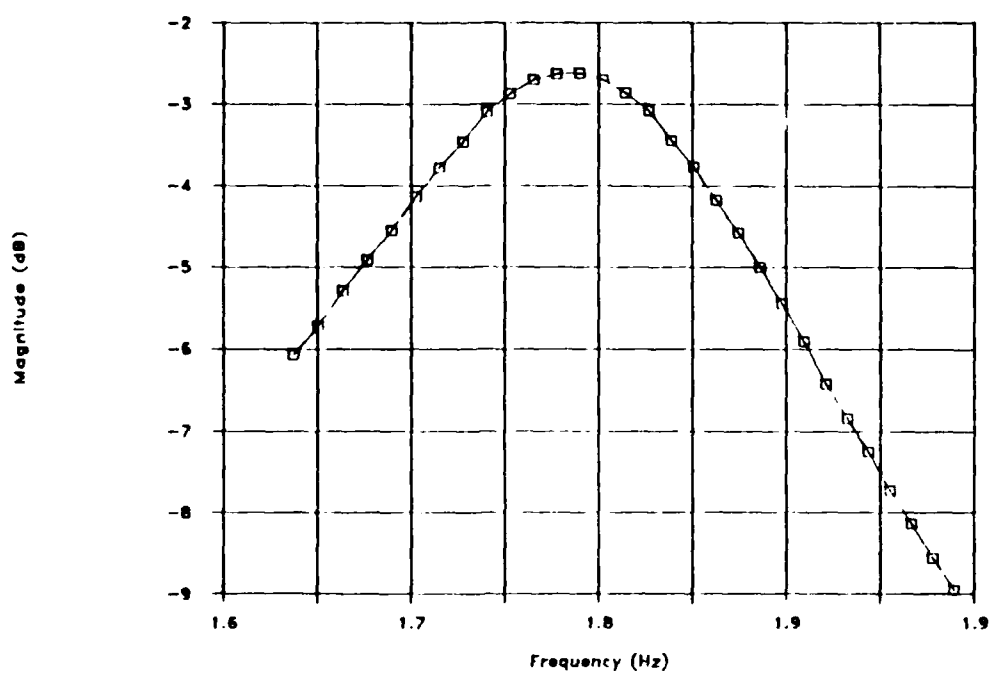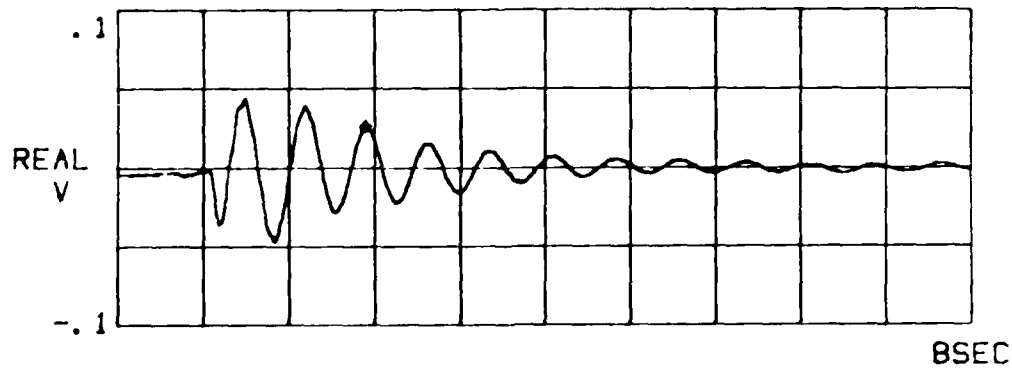
Figure 5.7. Predicted and Measured Y-Axis Response (C = 0.0611)

With the results of the analog closed loop tests indicating the sensor and actuator scale factors are correct, the PC-1000 input gains were calculated using the accelerometer scale factors. These gains are programmed into the PC-1000 and boost the sensor scale factors to unity prior to the signal going to the estimator/controller. Gains for each channel are listed in Table 5.3.

Table 5.3. PC-1000 Sensor Input Gains

Sensor Channel	Gain (lbf/ft/sec)	Gain (lbf/in/sec)
1	10.847	130.208
2	10.723	128.700
3	11.099	133.156
4	11.099	133.156

VI. Closed Loop Digital Control

Theory and Implementation

In general, the equations of motions for a vibrating structure which is being controlled can be written in the form

$$M\ddot{q} + C\dot{q} + Kq = D\underline{u} \tag{16}$$

where q is an n-vector of generalized coordinates, M is an nxn symmetric mass matrix, C is and nxn damping matrix, K is an nxn stiffness matrix, u is an m-vector of control inputs to the structure, and D is a nxm matrix of actuator coefficients (Ref 4). Equation 16 can be decoupled using the modal coordinates η and the modal matrix of right eigenvectors Φ, to define a transformation such that

$$\underline{q} = \Phi \underline{\eta} \tag{17}$$

which, after substituting for q and its higher time derivatives, and premultiplying by Φ^T, transforms equation 16 to the form

$$\ddot{\eta} + [2\zeta\omega]\dot{\eta} + [\omega^2]\underline{\eta} = \Phi^T D\underline{u} \tag{18}$$

where Φ has been normalized to meet the criteria $\Phi^T M\Phi = I$, an nxn identity matrix, $[2\zeta\omega]$ is an nxn diagonal damping matrix and $[\omega^2]$ is an nxn diagonal matrix of the eigenvalues of equation 16. Equation 18 can be formulated in the standard state space form of

$$\dot{\underline{x}} = A\underline{x} + B\underline{u} \qquad (19)$$

where $\underline{x}$ is defined as a 2n-vector composed of $\underline{\eta}$ and $\dot{\underline{\eta}}$, and A and B have the form

$$A = \left[\begin{array}{c|c} 0 & I \\ \hline -\omega^2 & -2\zeta\omega \end{array} \right]$$

$$B = \left[\begin{array}{c} 0 \\ \hline \Phi^T D \end{array} \right] \qquad (20)$$

In general, the states of a structure cannot be directly measured, but are some linear combination of the generalized coordinates $\underline{q}$ which can be measured, thus equation 19 is supplemented with the measurement equation

$$\underline{y} = C \underline{q} \qquad (21)$$

where $\underline{y}$ is an s-vector, s being the number of sensors used in the system, and C is an sxn matrix which can be partitioned into

$$C = \left[\begin{array}{c|c} C_p & C_v \end{array} \right] \qquad (22)$$

where the partitions C_p and C_v are coefficients for position and velocity sensors respectively. Using the modal matrix to write equation 21 in terms of the states gives the form

$$\underline{y} = \left[\begin{array}{c|c} C_p\Phi & C_v\Phi \end{array} \right] \underline{x} \qquad (23)$$

The state space model for the system is represented by equations 19 and 23. For this experimental configuration, C_p will be a zero matrix since only velocity is being derived from the accelerometer measurements. Closing the control loop using state space techniques simply requires feeding back the states through a gain matrix G (11:327). Thus the control input is defined by

$$\underline{u} = -G \underline{x} \qquad (24)$$

Unfortunately, since the controlled states cannot be measured directly, an estimator is required to generate the states to be used with the control matrix. One method of constructing this observer is to use the system model to estimate the states based on the sensor measurements. For this formulation, the estimator has the form

$$\dot{\hat{x}} = A\hat{x} + B\underline{u} + K(\underline{y} - \dot{y}) \qquad (25)$$

$$\dot{y} = C\hat{x} \qquad (26)$$

where $\bar{x}$ is the estimated state and $\bar{y}$ is the estimated output. The observer gain matrix K is chosen such that the error in the state estimate, defined by

$$e = \dot{x} - \underline{x} \qquad (27)$$

is stable. Since control must be based on the estimated states, the control input $\underline{u}$ must have the form

$$\underline{u} = -G \dot{x} \qquad (28)$$

6 - 3

Substituting for $\dot{y}$ and $\underline{u}$ in equation 25 and collecting like terms results in

$$\dot{x} = (A - BG - KC)\hat{x} + K\underline{y} \qquad (29)$$

which with equation 28 defines the estimator/controller to be used in the feedback loop.

There are many methods for selecting the K and G matrices to give the plant the desired characteristics. The one that will be used for this experiment is the optimal linear quadratic regulator. This method determines G by minimizing the performance index

$$J = \int_{0}^{\infty} (\underline{x}^T Q\ \underline{x} + \underline{u}^T R\ \underline{u})\ dt \qquad (30)$$

where Q and R are weighting matrices chosen such that the eigenvalues of (A - BG), the controlled plant, exhibit the desired stablity. K is similarly determined by minimizing the performance index

$$J_{ob} = \int_{0}^{\infty} (\underline{x}^T Q_{ob}\underline{x} + \underline{y}^T R_{ob}\underline{y})\ dt \qquad (31)$$

where Q_{ob} and R_{ob} are again weighting matrices selected such that the eigenvalues of (A - KC) define an observer with the desired stability. For this experiment, R and R_{ob} were selected as identity matrices and Q and Q_{ob} were selected independently to give the desired estimator and controller eigenvalues.

To implement the estimator/controller on the PC-1000, the solution to equation 25 is discretized into time steps. Defining

$$A_{oc} = A - BG - KC \tag{32}$$

the solution for a discrete time step δt becomes (5:25)

$$\hat{x}_{k+1} = \exp(A_{oc}\delta t)\,\hat{x}_k + A_{oc}^{-1}[\exp(A_{oc}\delta t) - I]K\,\underline{y}_k \tag{33}$$

$$\underline{u}_{k+1} = -G\,\hat{x}_k$$

where δt is defined by the inverse of the sample rate used in the array processor. The computational format of the PC-1000 is (Ref 12)

$$\left\{ \frac{\underline{u}_{k+1}}{\hat{x}_{k+1}} \right\} = \left[\begin{array}{c|c} F_{11} & F_{12} \\ \hline F_{21} & F_{22} \end{array} \right] \left\{ \frac{\underline{y}_k}{\hat{x}_k} \right\} \tag{34}$$

where the dimensions of the partitions are F_{11}:16x16, F_{12}:16x32, F_{21}:32x16, and F_{22}:32x32. Putting equations 33 into this form defines the partitions of the F matrix to be

$$F_{11} = 0$$

$$F_{12} = -G \tag{35}$$

$$F_{21} = A_{oc}^{-1}[\exp(A_{oc}\delta t) - I]K$$

$$F_{22} = \exp(A_{oc}\delta t)$$

The specific A, B, and C, matrices used to define the plant are listed in Appendix F. Calculation of the estimator/controller gain matrices and the system eigenvalues was accomplished using software based on work previously accomplished by Aldridge (Ref 13) and operating on one of the Vax 11/785 computers resident at AFIT. The gain and

system matrices were input to Matlab, a matrix manipulation software package residing on the Vax, which was used to calculate the F_{21} and F_{22} matrices.

Closed Loop Simulation

A closed loop simulation was implemented on the PC-1000 to verify the time response of the closed loop system is an accurate indicator of the predicted closed loop plant eigenvalues, and to evaluate the processor's abliity to perform the estimator/controller function. The estimator/controller configurations formed for the simulation incorporated the first three natural modes for the structure. In formulating the controller gain matrix the second and third modes were deweighted in the cost function, thus control was applied only to the first z-axis bending mode. Observer gains were weighted approximately equally. Two controllers were generated with identical control gains and different observer stablities to predict the effect of estimator errors on the closed loop system. Slave processor #2 of the array processor was loaded with the open loop plant model ($\dot{x} = A\underline{x} + B\underline{u}$) while slave processor #1 remained as the estimator/controller. An initial condition of $x_1 = 0.01$ was placed in the plant model which approximates an initial displacement of the base plate in the z direction. The time response of various parameters in the closed loop system was used to estimate the actual damping expected in the first z axis bending mode when control is applied to the beam. Data was recorded on the Ono Sokki spectrum analyzer and damping was estimated using the log decrement method (equation 15) on the time response data. Comparisons of the actual and estimated states and the sensor output and actuator commands

are shown in Figures 6.1 through 6.6. A summary of the system damping estimated from the various parameters in the system is presented in Table 6.1. Estimator damping and modal damping values are obtained from the eigenvalues of $(A - KC)$ and $(A - BG)$ respectively.

Table 6.1. Simulation Damping Results for First Z Bending Mode

Estimator Damping	Modal Damping	Plant States		Sensor	Estimated States	
		ζ_{x_1}	$\zeta_{\dot{x}_1}$	ζ_{s_2}	$\zeta_{\hat{x}_1}$	$\zeta_{\dot{\hat{x}}_1}$
0.155	0.101	0.093	0.111	0.113	0.068	0.091
0.548	0.101	0.091	0.101	0.101	0.081	0.099

Comparing the plant damping with the predicted modal damping indicates the less damped estimator should overcontrol the plant slightly. This is probably due to the error dynamics in the estimated states increasing the modal amplitude. As estimator damping increases, the error has less time to contribute to the estimated state and the plant damping approaches the predicted modal damping. This is readily seen in Figures 6.7 and 6.8 which show the estimator response to an initial condition with the sensor input removed from the PC-1000. Another observation is that the sensor data is a more accurate measurement of the actual plant damping than the estimated states, even for a highly damped estimator.
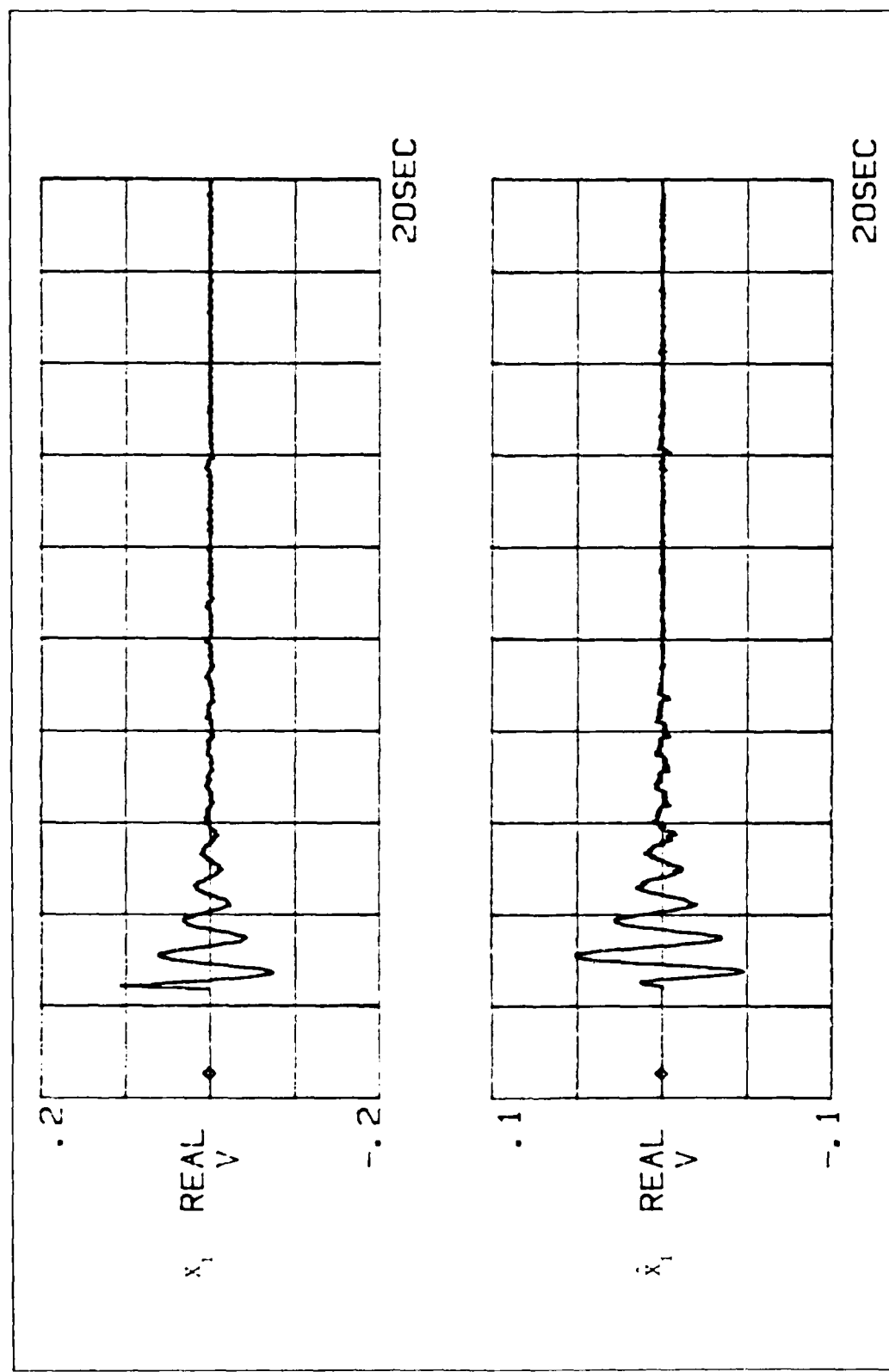
Figure 6.1. X_1 vs $\hat{X}_1$ - Estimator $\zeta = 0.548$
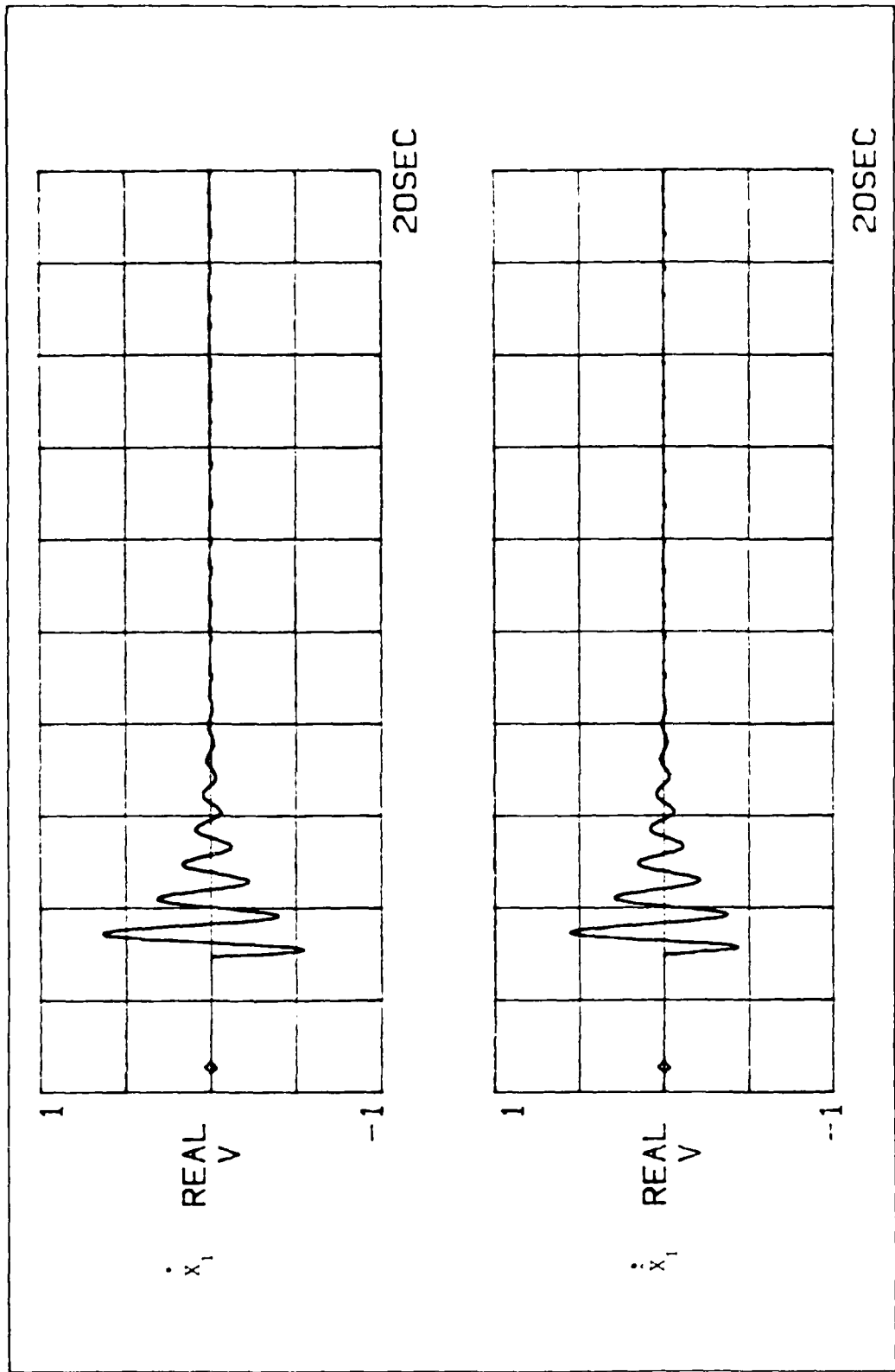
Figure 6.2. $\dot{X}_1$ vs $\dot{\hat{X}}_1$ - Estimator $\zeta = 0.548$
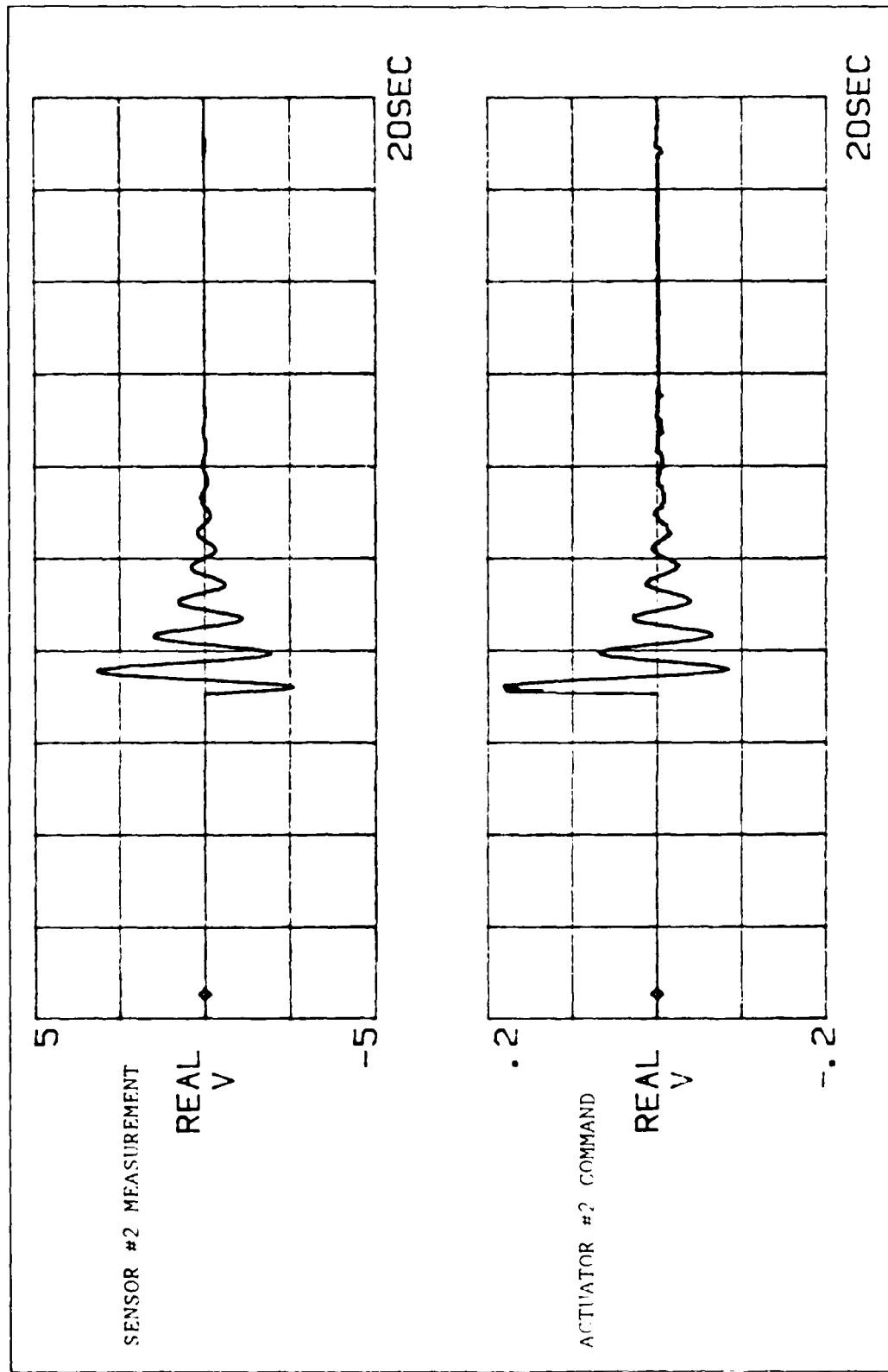
Figure 6.3. Sensor Input vs Command Output - Estimator ζ - 0.548

20SEC

20SEC

SENSOR #2 MEASUREMENT

REAL V

5

-5

ACTUATOR #2 COMMAND

REAL V

.2

-.2
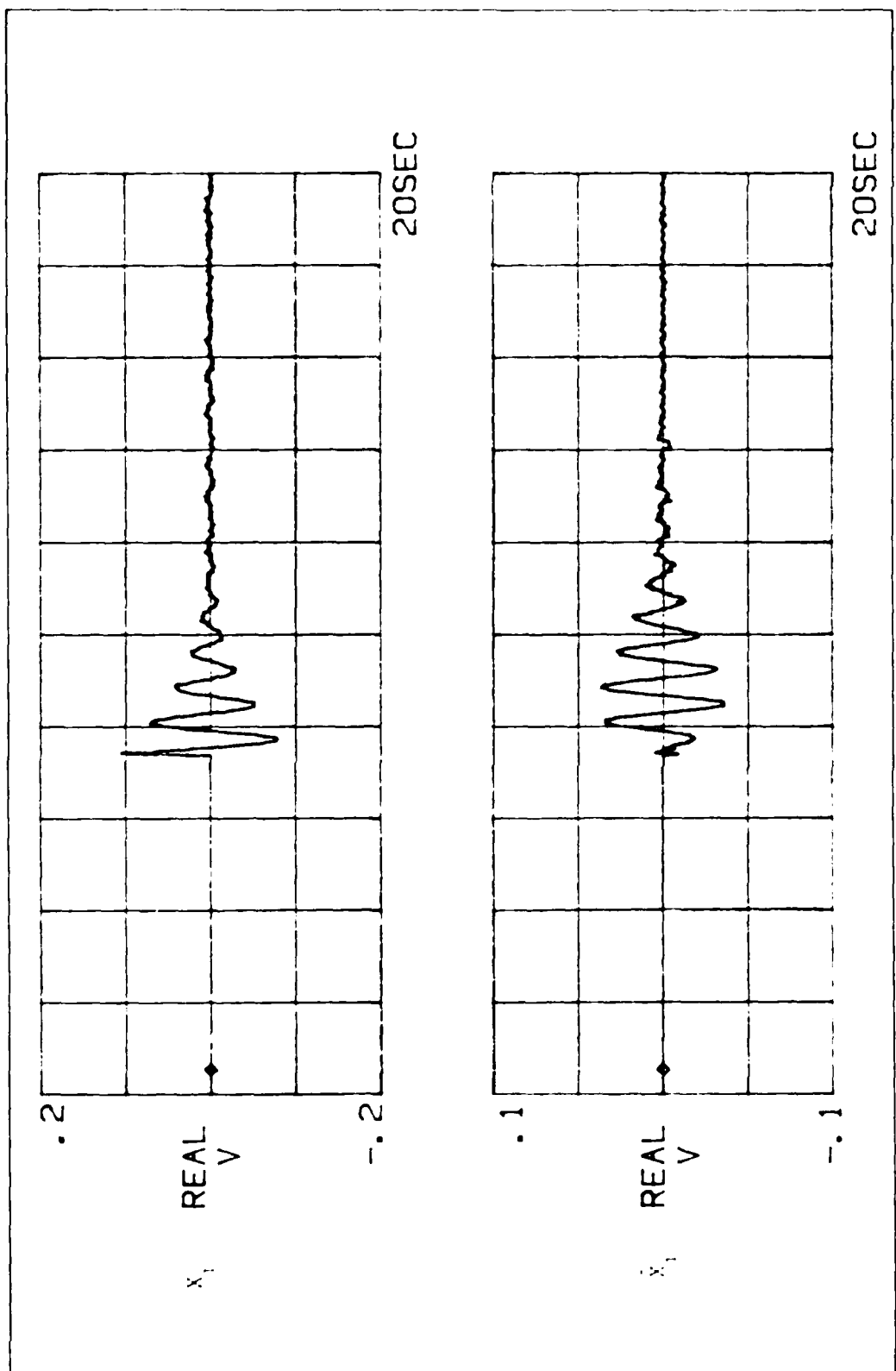
Figure 6.4. X_1 vs $\dot{X}_1$ - Estimator $\zeta = 0.155$
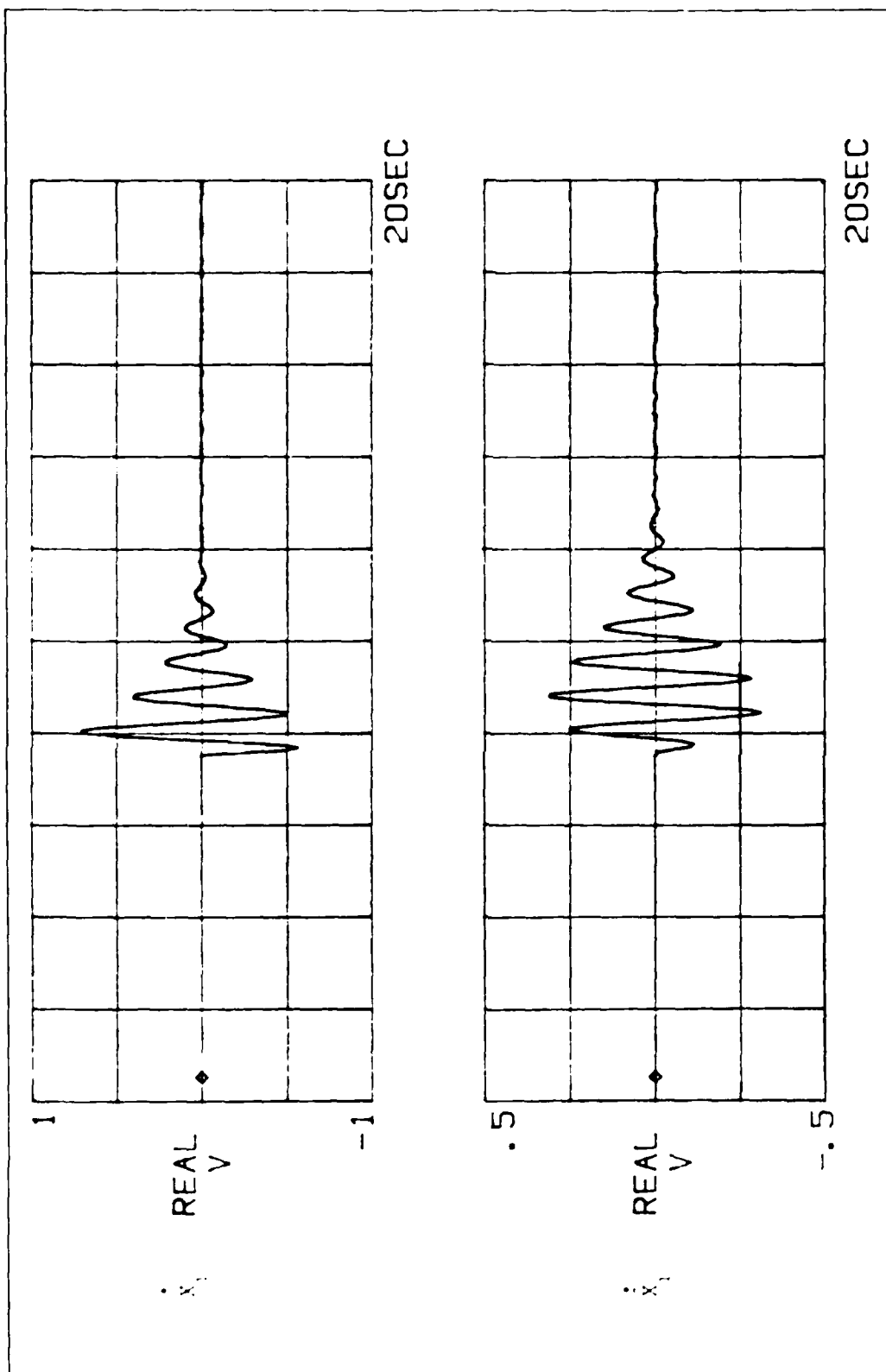
Figure 6.5. $\dot{X}_1$ vs $\dot{\hat{X}}_1$ - Estimator $\zeta = 0.155$
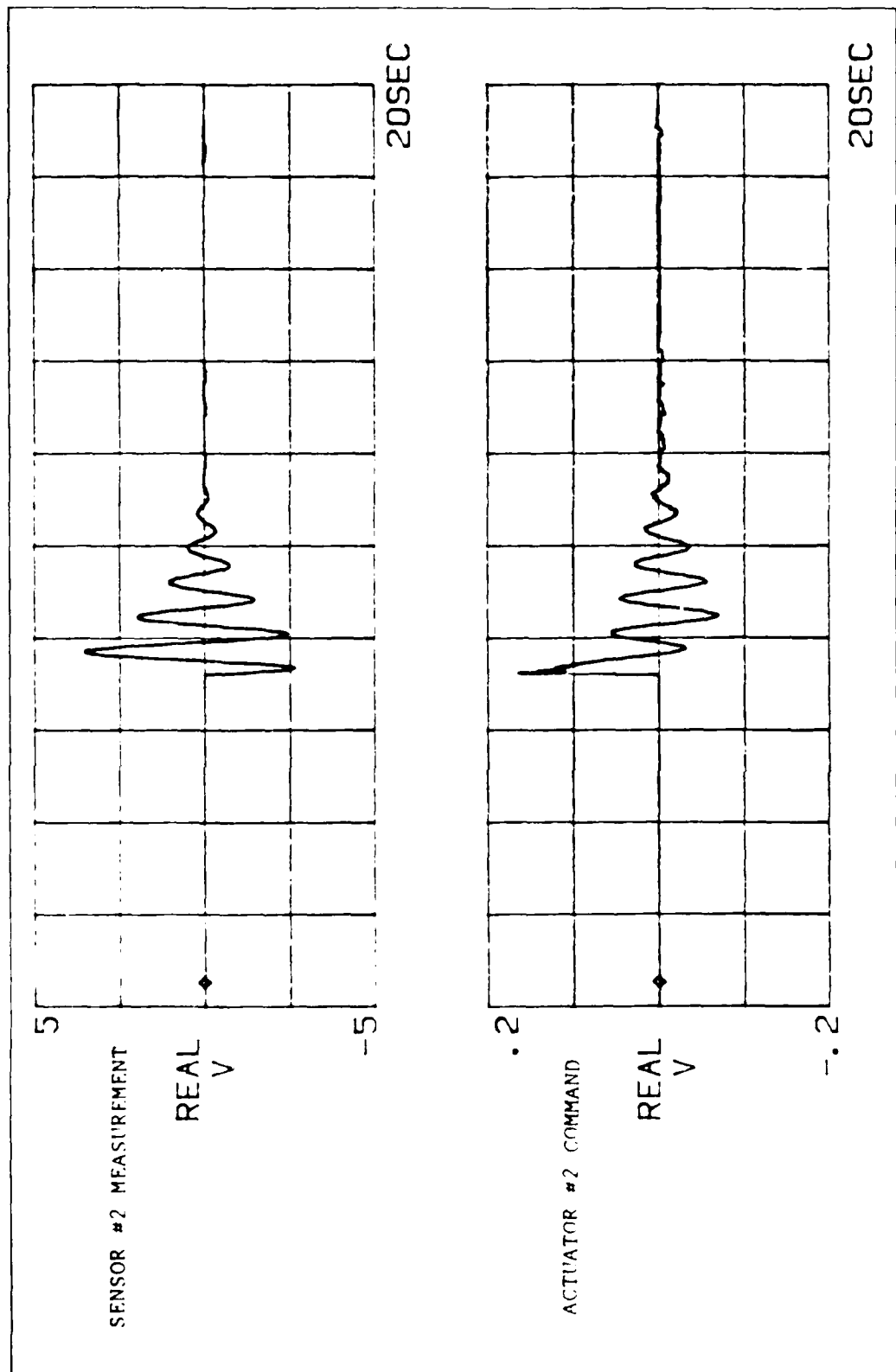
Figure 6.6. Sensor Input vs Command Output - Estimator ζ = 0.155
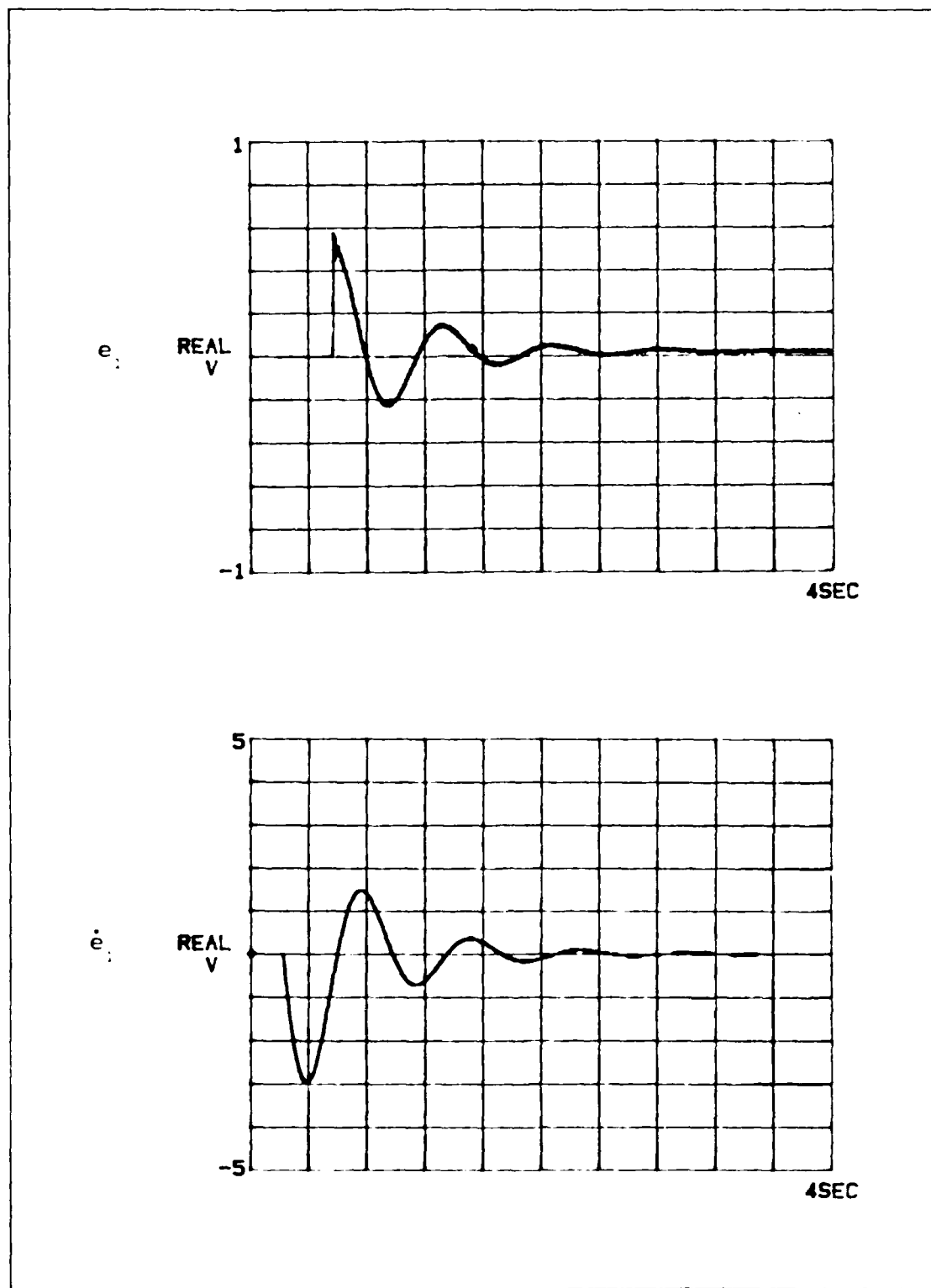
Figure 6.7. Estimator Error States ($\zeta = 0.155$)
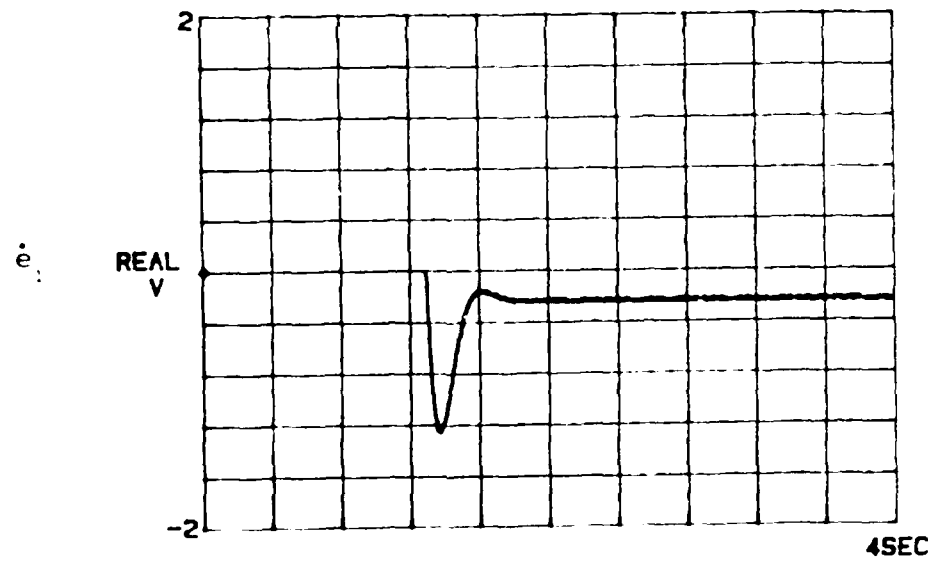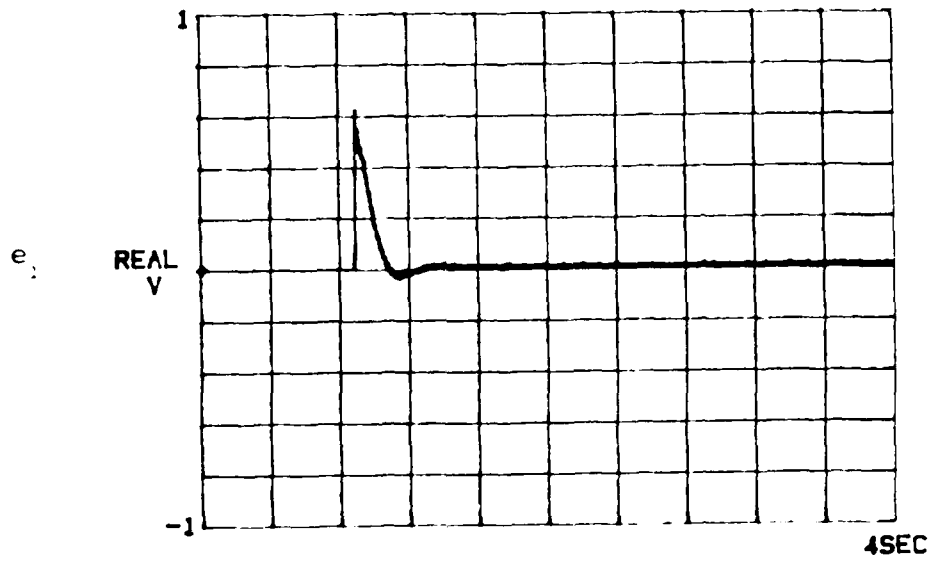
Figure 6.8. Estimator Error States ($\zeta = 0.548$)

Optimal Time Invariant Linear Regulator Control

Closed loop testing used the integrated accelerometer measurements from the beam as velocity inputs to the estimator and the control commands from the PC-1000 were input to the proof mass actuators. The estimator was started with zero initial conditions and the beam quiescent. Even so, transients proved to be a problem. The PC-1000 was found to have a small bias voltage on the input channels (approximately 60 mV), probably in the A/D converter. This bias was sufficient to cause high gain controllers to produce transients large enough to saturate the actuator stroke. To prevent overdriving and possibly damaging the actuators, power was removed until all transients settled.

Controllers were designed for the fundamental bending mode in each direction, and the first torsion mode. Estimator/controller states included all three modes, however control weightings were used which applied control to only one mode at a time and left the remaining modes essentially unchanged. Structural response for the fundamental modes was measured by giving the beam an initial displacement or velocity in the controlled axis and measuring the time response of sensors on that axis. Damping ratios were calculated for each test using the log decrement method. Results from several estimator/controller configurations are shown in Table 6.2.

The measured damping coefficients in Table 6.2 indicate a trend opposite to that seen in the simulation. As the ratio between the estimator and controller decreases, the measured damping also decreases. The simulation predicted higher damping in the case where the estimator damping closely approached the modal damping.

To determine if the log decrement data was accurate, the GenRad modal analyzer was also used to measure the modal damping for the first

Table 6.2. Closed Loop Modal Damping Coefficients

Axis	Estimator Damping	Predicted Damping	Ratio	Measured Damping	Error (%)
	0.3576	0.0716	4.994	0.080 ± 0.020	11.1
	0.2798	0.0716	3.908	0.069 ± 0.018	4.2
	0.2149	0.0716	3.001	0.070 ± 0.009	2.8
Z	0.1214	0.0716	1.696	0.066 ± 0.013	8.3
	0.1015	0.0716	1.418	0.066 ± 0.020	8.3
	0.0793	0.0716	1.112	0.041 ± 0.016	43.1
	0.1523	0.0715	2.130	0.059 ± 0.011	17.5
Y	0.1252	0.0715	1.751	0.058 ± 0.015	18.9
	0.0980	0.0715	1.371	0.056 ± 0.007	21.7
T	0.0865	0.0324	2.670	0.030 ± 0.010	7.4

two bending modes. The beam was excited in the controlled axis using a force hammer and damping estimates were obtained using a complex exponential curve fit to the resulting frequency response function measured by the GenRad. A comparison of these results to the log decrement data is shown in Table 6.3. While the curve fit data appears to be more accurate and shows the trend more clearly, the damping estimate was highly dependent upon the frequency range the software was allowed to fit. For the z-axis test with the estimator at 0.155, damping estimates ranging from 0.088 to 0.056 were observed. The data presented represents a "best fit" to the frequency response function based on minimizing the residuals between the measured and fit data. Since the log decrement data is reasonably accurate, testing of the fundamental bending and first torsion modes continued using this method.

Table 6.3. Damping Estimation Method Comparison - Log Decrement vs
Complex Exponential Curve Fit

Axis	Estimator Damping	Modal Damping (predicted)	Modal Damping (log dec)	Modal Damping (curve fit)
z	0.1214	0.0716	0.066	0.077
z	0.1015	0.0716	0.066	0.063
z	0.0793	0.0716	0.041	0.043
y	0.1252	0.0715	0.058	0.059

In an attempt to determine a cause of the lower than expected modal damping several more tests were run with the simulation to measure gains through the controller/estimator. Table 6.4 shows the gains between various system parameters.

Table 6.4. System Gains (dB)

Estimator ζ *	$\hat{x}_1/x_1$	$\dot{\hat{x}}_1/\dot{x}_1$	$\hat{x}_1/s_2$	$\dot{\hat{x}}_1/s_2$	u_2/s_2
0.155	-3.0	-2.8	-34.9	-16.5	-29.2
0.548	-2.2	-0.8	-34.9	-14.7	-27.5

* Predicted modal damping of 0.101 for both controllers

The simulation shows that the sensor to acutator command gain was smaller for the less damped estimator. This result is consistent with the trend in the experimental data of less modal damping for the less damped estimators, and is also consistent with the fact that the higher damped estimators have larger gains in the estimator gain matrix K. The discrepancy which remains unresolved is that the simulation still maintains the predicted level of modal damping even though it is

providing less control input to the plant. Further investigation of the simulation would be required to fully evaluate this difference.

A tabulation of additional single axis control tests conducted is in Table 6.5. From this data, to have the actual modal damping be close to the predicted eigenvalue, the estimator damping should be at least twice the modal damping for z-axis control, and three times the modal damping or higher for y-axis and torsion control.

While keeping the estimator damping high relative to the modal damping is desirable, this was found to limit the modal damping level that could be used in the experiment. The estimators operating with a damping coefficient greater than 0.2 were found to pass low frequency signals through the controller. When the control gains are large, the low frequency drift in the sensor signal caused the actuators to wander. For some controllers the drift was so bad that the actuators would not remain centered long enough to run even a single decay test. Figures 6.9 through 6.12 show the actuator command versus the sensor input for different estimator damping ratios. A z-axis controller with an estimator damping coefficient of 0.358 was the highest that could be tested. Estimators operating with damping coefficients less than about 0.2 had very little problem with drift. While some was still present, the magnitude was either below the actuator response threshold or slow enough to allow adjustment of the actuator centering before a test.

Table 6.5. Additional Closed Loop Control Test Results

	Predicted			Experimental	
Axis	Estimator Damping	Modal Damping	Ratio $\varsigma_x^-/\varsigma_x$	Measured Modal Damping	% of Predicted
z	0.1015	0.0716	1.4176	0.066 ± 0.020	0.922 ± 0.279
z	0.1268	0.0994	1.2757	0.085 ± 0.013	0.855 ± 0.131
z	0.1540	0.1245	1.2369	0.105 ± 0.022	0.843 ± 0.177
z	0.1863	0.1507	1.2369	0.128 ± 0.031	0.849 ± 0.206
z	0.2149	0.1790	1.2006	0.154 ± 0.065	0.860 ± 0.363
z	0.1268	0.0716	1.7709	0.065 ± 0.025	0.908 ± 0.349
z	0.1540	0.0994	1.5493	0.081 ± 0.013	0.815 ± 0.131
z	0.1863	0.1245	1.4964	0.115 ± 0.030	0.924 ± 0.241
z	0.2149	0.1507	1.4260	0.138 ± 0.043	0.916 ± 0.285
y	0.0980	0.0715	1.3706	0.056 ± 0.007	0.783 ± 0.098
y	0.1252	0.0965	1.2974	0.076 ± 0.017	0.786 ± 0.176
y	0.1523	0.1253	1.2155	0.099 ± 0.019	0.790 ± 0.152
y	0.1866	0.1492	1.2507	0.114 ± 0.004	0.764 ± 0.027
y	0.2136	0.1782	1.1987	0.143 ± 0.004	0.802 ± 0.022
y	0.1252	0.0715	1.7510	0.058 ± 0.015	0.811 ± 0.208
y	0.1523	0.0965	1.5782	0.081 ± 0.015	0.839 ± 0.155
y	0.1866	0.1238	1.5073	0.102 ± 0.010	0.824 ± 0.081
y	0.2136	0.1492	1.4316	0.125 ± 0.006	0.838 ± 0.040
y	0.2458	0.1782	1.3793	0.153 ± 0.035	0.859 ± 0.196
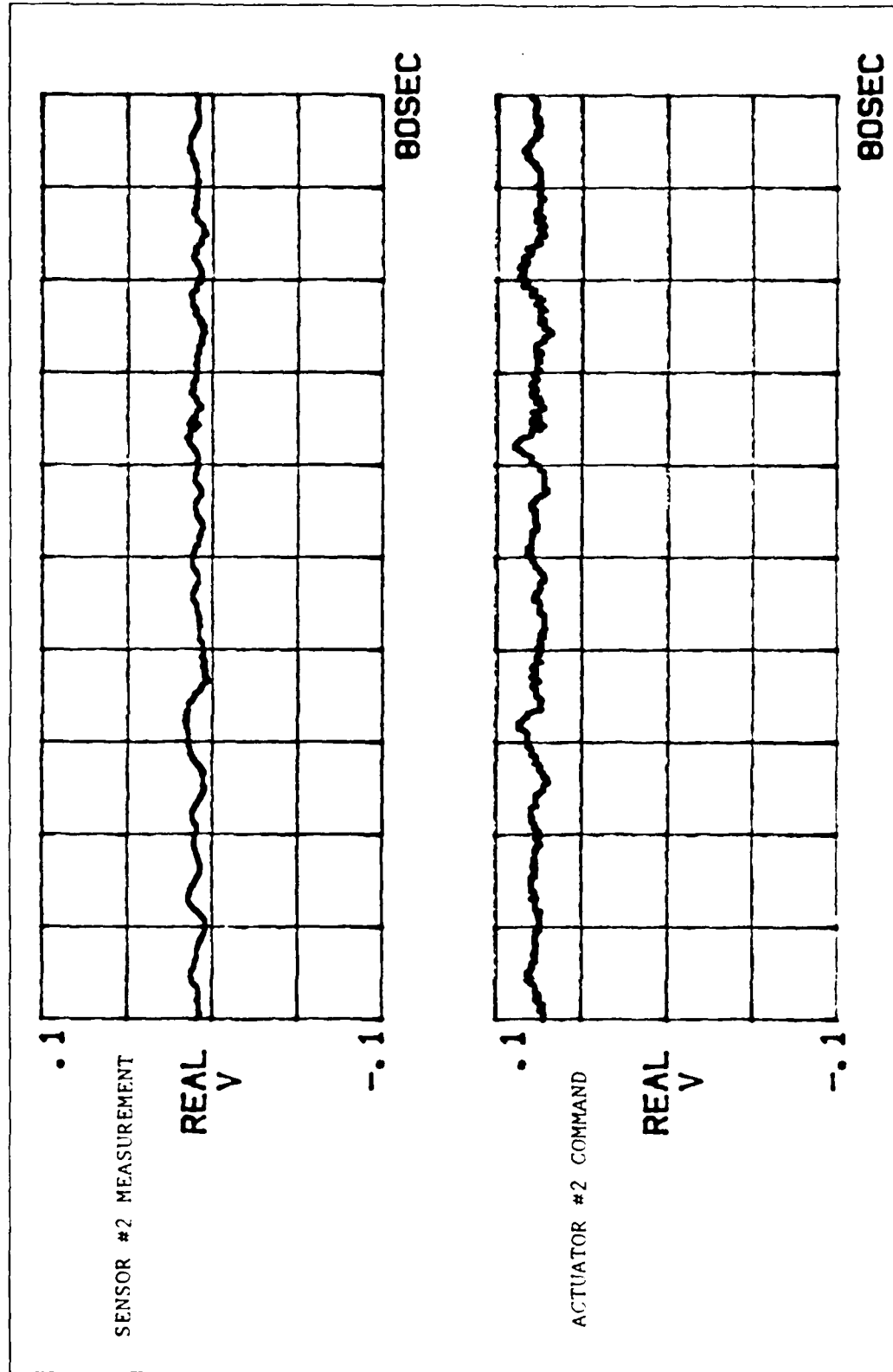
Figure 6.9. Estimator Output Drift - Sensor Input vs Command Output ($\zeta = 0.3576$)
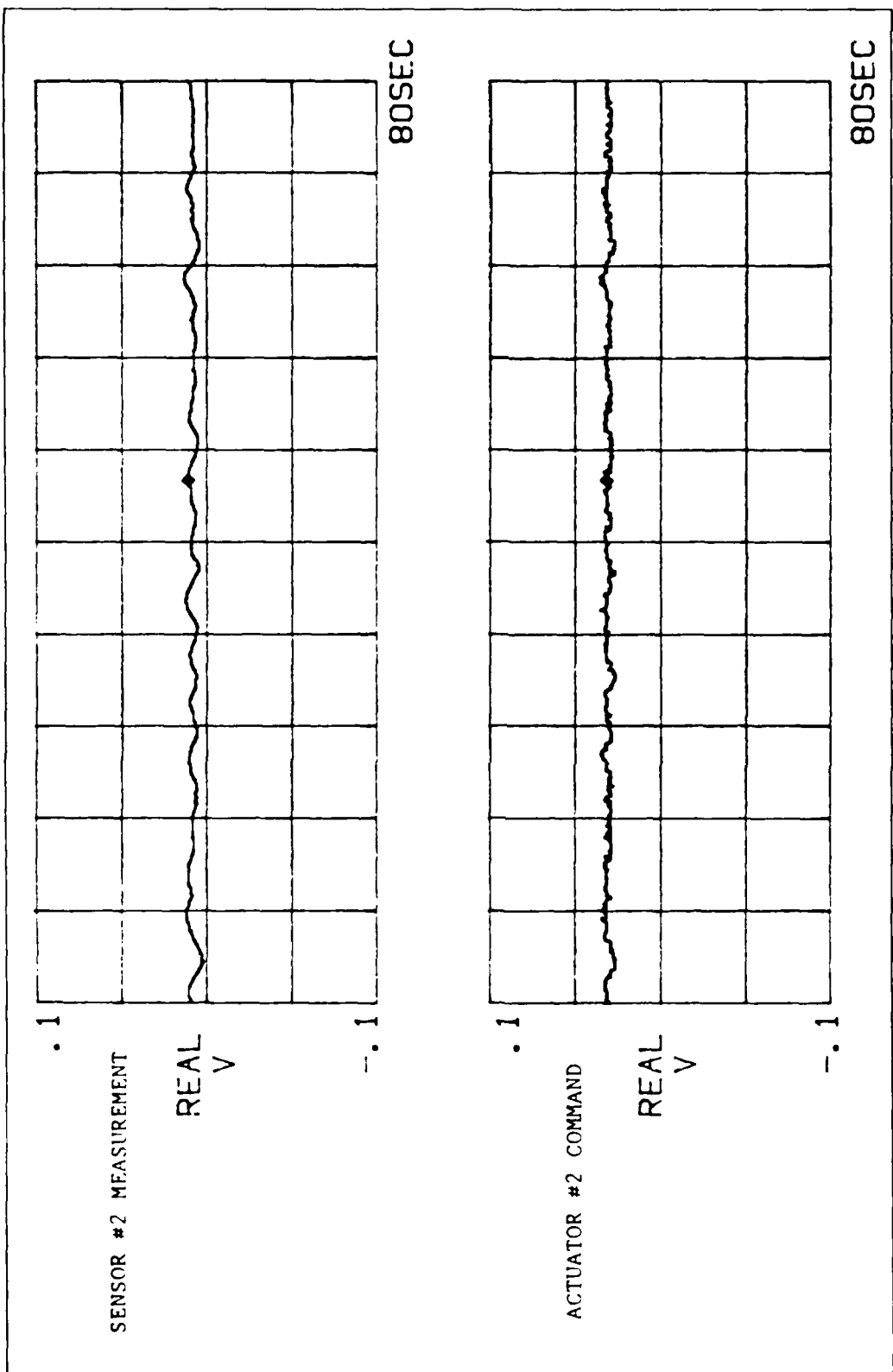
Figure 6.10. Estimator Output Drift - Sensor Input vs Command Output ($\zeta = 0.2798$)
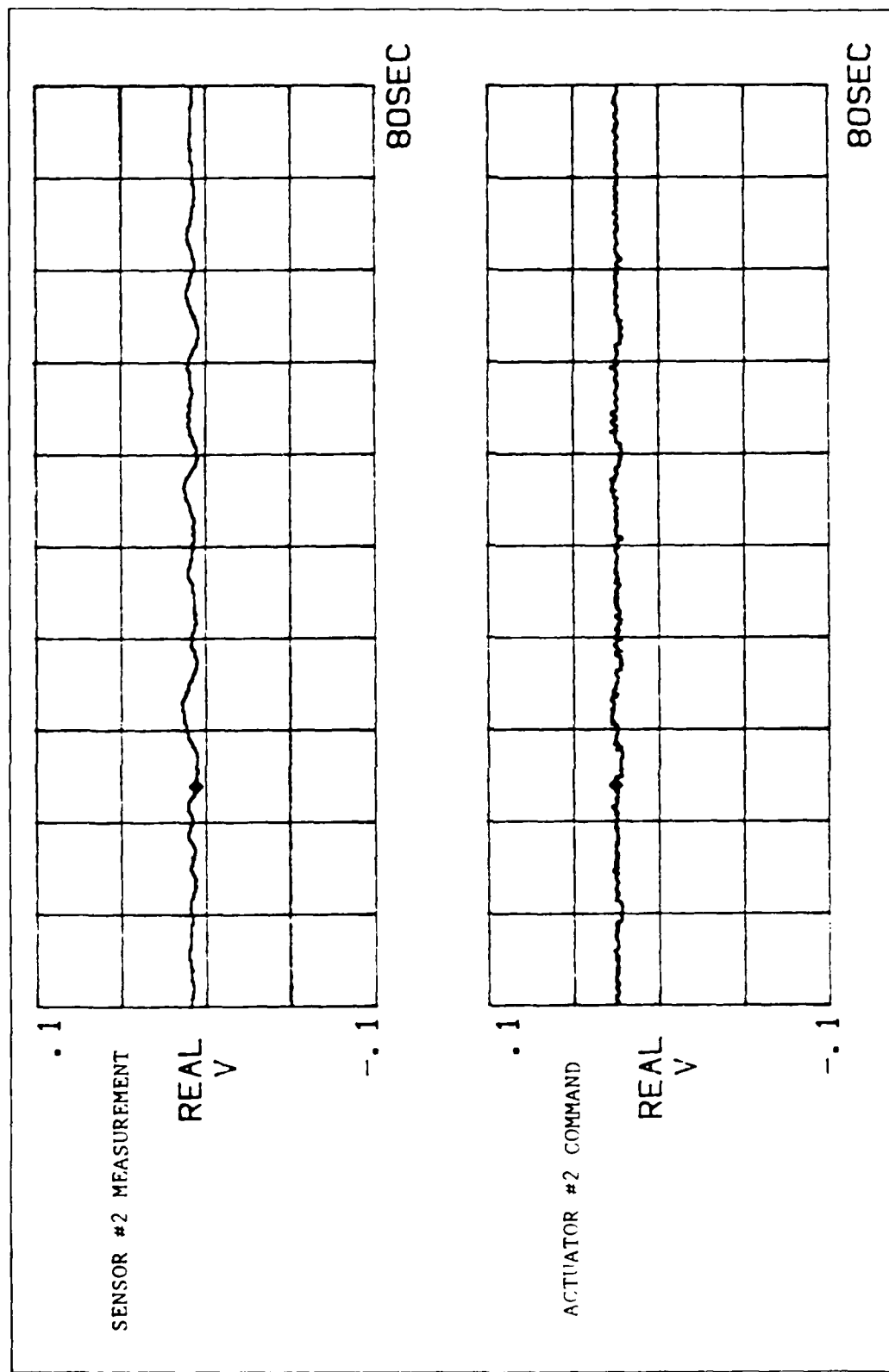
Figure 6.11. Estimator Output Drift - Sensor Input vs Command Output ($\zeta = 0.2149$)
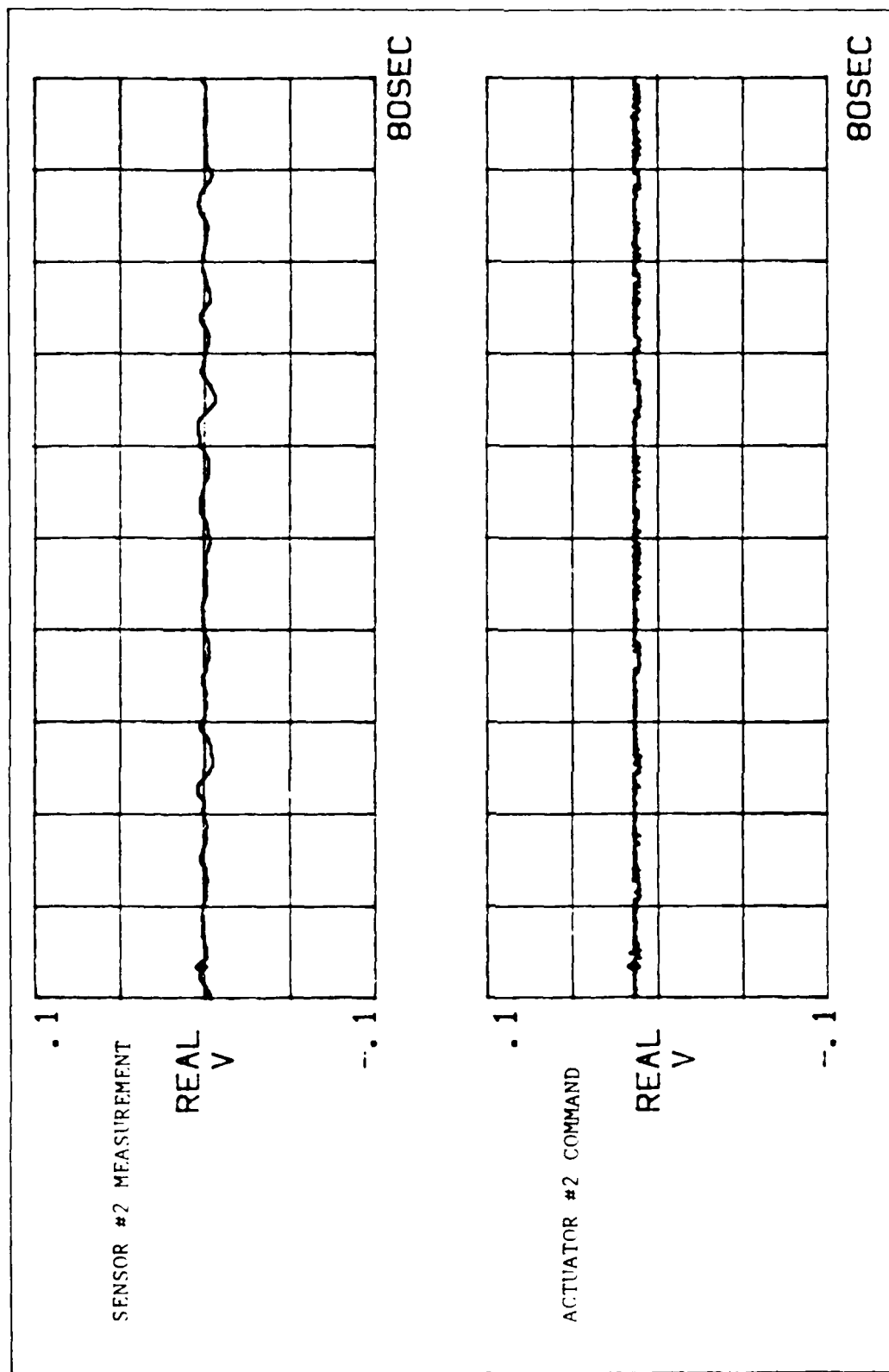
Figure 6.12. Estimator Output Drift - Sensor Input vs Command Output   ($\zeta = 0.1214$)

VII. Modal Suppression

Theory

Using a reduced order dynamic model reduces the order of the controller, and thus the computational requirements can be significantly reduced in a very large system. If the reduction is accomplished by just deleting modes, the uncontrolled modes can be driven unstable. This occurs because the sensor outputs and control commands still contain information about the deleted modes. These effects have become commonly refered to as observation and control spillover. A method for eliminating spillover and maintaining a stable system was developed by Calico and Janiszewski (Ref 4), and is used in this experiment to construct the reduced order controllers.

To accomplish this, the modes of a system are classified as controlled, suppressed, and residual. The state vector for the system now takes the form of

$$\underline{x} = (\underline{x}_c, \ \underline{x}_s, \ \underline{x}_r)^T \tag{36}$$

where $\underline{x}_c$ is an n_c-vector of controlled states, $\underline{x}_s$ is an n_s-vector of suppressed states, and $\underline{x}_r$ is an n_r-vector of residual states. The modes included in $\underline{x}_c$ are only those necessary to establish satisfactory system performance and do not necessarily include the lowest order modes.

Using this partitioning, the state space model can be written as

$$\dot{\underline{x}}_c = A_c \underline{x}_c + B_c \underline{u} \tag{37}$$

$$\dot{\underline{x}}_s = A_s \underline{x}_s + B_s \underline{u} \tag{38}$$

7 - 1

$$\dot{\underline{x}}_r - A_r \underline{x}_r + B_r \underline{u} \qquad (39)$$

$$\underline{y} - C_c \underline{x}_c + C_s \underline{x}_s + C_r \underline{x}_r \qquad (40)$$

The control input is still defined by equation 24, but with $\underline{x}$ replaced by $\underline{x}_c$. The coupling of the control $\underline{u}$ into the suppressed and residual equations could excite and destabilize these modes, and as such the problem is known as control spillover.

A similar situation exits for the the observer. The estimator still has the form of equations 25 and 26,

$$\dot{\hat{x}}_c - A_c \hat{x}_c + B_c \hat{x}_c + K(\underline{y} - \hat{y})$$

$$\hat{y} - C_c \hat{x}_c \qquad (41)$$

and as such, $\underline{y}$ still includes information about the suppressed and residual states. This coupling can induce errors into the estimated states and thus generate inappropriate control commands, possibly driving the system unstable. This is the effect known a observation spillover.

To maintain system stability, it is sufficient to eliminate either type of spillover (Ref 4). For this experiment it was decided to eliminate observation spillover, which can be accomplished by constraining the estimator gain and output matrices such that

$$KC_c \neq 0 \qquad (42a)$$

$$KC_s - 0 \qquad (42b)$$

For a reduced order controller the residual modes are ignored and the solution to equation 42b can be found by singular value decomposition of

C_s. If C_s is of full rank, a solution exists only if the number of sensors is greater than the number of suppressed modes. This is necessary because eliminating the observation requires constructing a new measurement set $\underline{w}$, which is a linear combination of sensor outputs such that the suppressed mode has in effect been subtracted out of the measurement, thus suppressed. This in effect "costs" a sensor for a mode to be suppressed. The results of the singular value decomposition of C_s are an orthogonal set of left singular vectors which can be partitioned into a set associated with the non-zero singluar values of C_s, and a set associated with the zero singular values of C_S. Defining the set associated with the zero singular values as Γ, equation 42b becomes

$$\Gamma C_s = 0 \tag{43}$$

Defining a new relation to represent the output after the suppressed modes are removed

$$\underline{w} = \Gamma \underline{y} \tag{44}$$

equation 40 becomes

$$\underline{w} = \Gamma C_c \, \underline{x}_c + \Gamma C_s \, \underline{x}_s + \Gamma C_r \, \underline{x}_r \tag{45}$$

which, by ignoring residuals reduces to

$$\underline{w} = \Gamma C_c \, \underline{x}_c \tag{46}$$

using this new measurement in the estimator equation results in

$$\dot{\hat{x}} = A_c\hat{x}_c - B_c\underline{u} - K(\underline{w} - \hat{w})$$

$$\hat{w} = \Gamma C_c\hat{x}_c \qquad\qquad (47)$$

$$\underline{u} = -G\hat{x}_c$$

which, when put in terms of $\underline{y}$, defines a state estimator of the form

$$\dot{\hat{x}}_c = (A_c - B_cG_c - K\Gamma C_c)\hat{x}_c + K\Gamma\underline{y} \qquad\qquad (48)$$

The time domain solution of equation 48 and its formulation for use in the PC-1000 is identical to equations 32 through 35, when the full state matrices are replaced with their reduced order counterparts, and the estimator gain matrix K is replaced with $K\Gamma$.

Results

Since the first two modes of the system are the first bending modes in two orthogonal directions, they are already physically decoupled and it is not necessary to apply modal suppression before eliminating the orthogonal axis from the controller. Therefore, suppressed mode controllers were designed and implemented for the z axis of the beam which dealt with the first and second z bending modes and torsion. Initially, to determine the effect of spillover on the system, a two mode controller using only torsion and second z bending was constructed, with the first z bending included in the model as a residual mode to predict its stability. The predicted eigenvalues for the estimator and

controller without incorporating the residual mode are listed in
Table 7.1. The eigenvalues for the system with the residual mode
incorporated are shown in Table 7.2.

Table 7.1. Predicted System Eigenvalues Without Residual Modes

Mode	Estimator		Controller	
	ζ	ω	ζ	ω
T1	0.1029	79.8805	0.0126	79.0245
Z2	0.1055	114.974	0.0301	113.688

Table 7.2. Predicted System Eigenvalues With Residual Modes

Mode	Estimator		Controller		Residual	
	ζ	ω	ζ	ω	ζ	ω
T1	0.1029	79.8805	0.0126	79.0245		
Z2	0.4701	65.6812	0.0048	114.387		
Z1					-1.0 -1.0	21.0709 10.0318

While the system appears well behaved when the residual mode is
ignored, the overall system is obviously unstable when the omitted mode
is accounted for. To verify this prediction, the estimator/controller
was implemented on the PC-1000. The resulting control response would
immediately saturate the actuators when initiated, and eventually drove
the z-axis unstable.

The first problem encountered in attempting to suppress the first z bending mode was maintaining observability of the second z bending mode. The problem lies in the large difference in modal amplitudes between the first and second bending modes at the base plate. Table 3.7 indicates the difference to be almost an order of magnitude. Thus, when suppressing the first bending mode, the small amplitude of the second mode was completely swamped. Tables 7.3 and 7.4 show the system eigenvalues before and after suppression of the first z bending mode. This problem was also manifested in requiring very high control gains to produce a significant increase in predicted damping. These high gains aggrevated the noise and low frequency drift problems already present in the system and made the configuration very difficult to test.

Table 7.3. Predicted System Eigenvalues Before Suppression

Mode	Estimator		Controller	
	ζ	ω	ζ	ω
T1	0.1005	79.8412	0.0127	79.0425
Z2	0.1592	116.683	0.0100	113.688

Table 7.4. Predicted System Eigenvalues After Suppression

Mode	Estimator		Controller	
	ζ	ω	ζ	ω
T1	0.1005	79.8412	0.0126	79.0245
Z2	0.0029	113.688	0.0100	113.688

To overcome the loss of observability, the sensors on the y axis were changed to stations 9 and 10 on the z axis. Modal amplitudes listed in Table 3.7 indicate the response at these stations is the same order of magnitude as the first bending mode at the base plate. Therefore, the second z bending signal should be substantial enough to not be subtracted out when the first mode is suppressed.

The new sensor stations were already instrumented with PCB Structural Accelerometers used in the modal tests. Rather than reinstrument, the PCB accelerometers were used in place of the Kistlers. The new accelerometer calibrations and scale factors after signal conditioning are shown is Table 7.5.

Table 7.5 PCB Accelerometer Calibrations and Scale Factors

Station	Serial #	Calibration (V/g)	Scale Factor (mV/ft/sec)
9	1223	0.8902	93.10
10	1216	0.9321	94.20

The results of the new sensor configuration are shown in Tables 7.6 and 7.7. The observability of the second mode returned and the suppression of the first bending had minimal effect on the controlled system eigenvalues.

Table 7.6. Predicted System Eigenvalues Before Suppression - Adjusted Sensor Locations

Mode	Estimator		Controller	
	ζ	ω	ζ	ω
T1	0.0876	79.6438	0.0127	79.0425
Z2	0.0827	114.473	0.0151	113.688

Table 7.7. Predicted System Eigenvalues After Suppression - Adjusted
Sensor Locations

Mode	Estimator		Controller	
	ζ	ω	ζ	ω
T1	0.0876	79.8412	0.0126	79.0425
Z2	0.0824	114.467	0.0151	113.688

Implementation of this controller proved to be only partially
successful. The first z bending mode was not driven unstable, however
is was slightly destablized. Figure 7.1 shows the time response for the
first z bending. The damping ratio calculated for the test was 0.0267,
a reduction of 0.01 over the normal residual damping in the structure.
The damping on the second z bending was estimated using the impact
method and the modal analyzer. The transfer function was then curve fit
to determine the damping, the result being shown in Figure 7.2. As is
readily apparent from the estimated roots, the damping has only been
marginally increased from its residual value of 0.00291 to 0.00493.
With a predicted controlled damping of 0.0151, this is by far the
largest deviation from prediction. The most likely explanation is the
low modal amplitude of the second mode at the base plate. The sensor
input and actuator command for this controller are shown in Figure 7.3.

A problem which can be seen in Figure 7.3 was a low frequency
transient in the PCB response when the beam was excited. The controller
output followed this signal very closely and almost invariably saturated
the actuator stroke unless the force input was kept extremely small.

Finally, to determine how well the suppression of the first bending
mode is operating the frequency spectra of the sensor input and the
suppressed measurement $\underline{w}$ were measured while exciting the suppressed
mode (see Figure 7.4). The sensor input magnitude of -44.8 dBV should
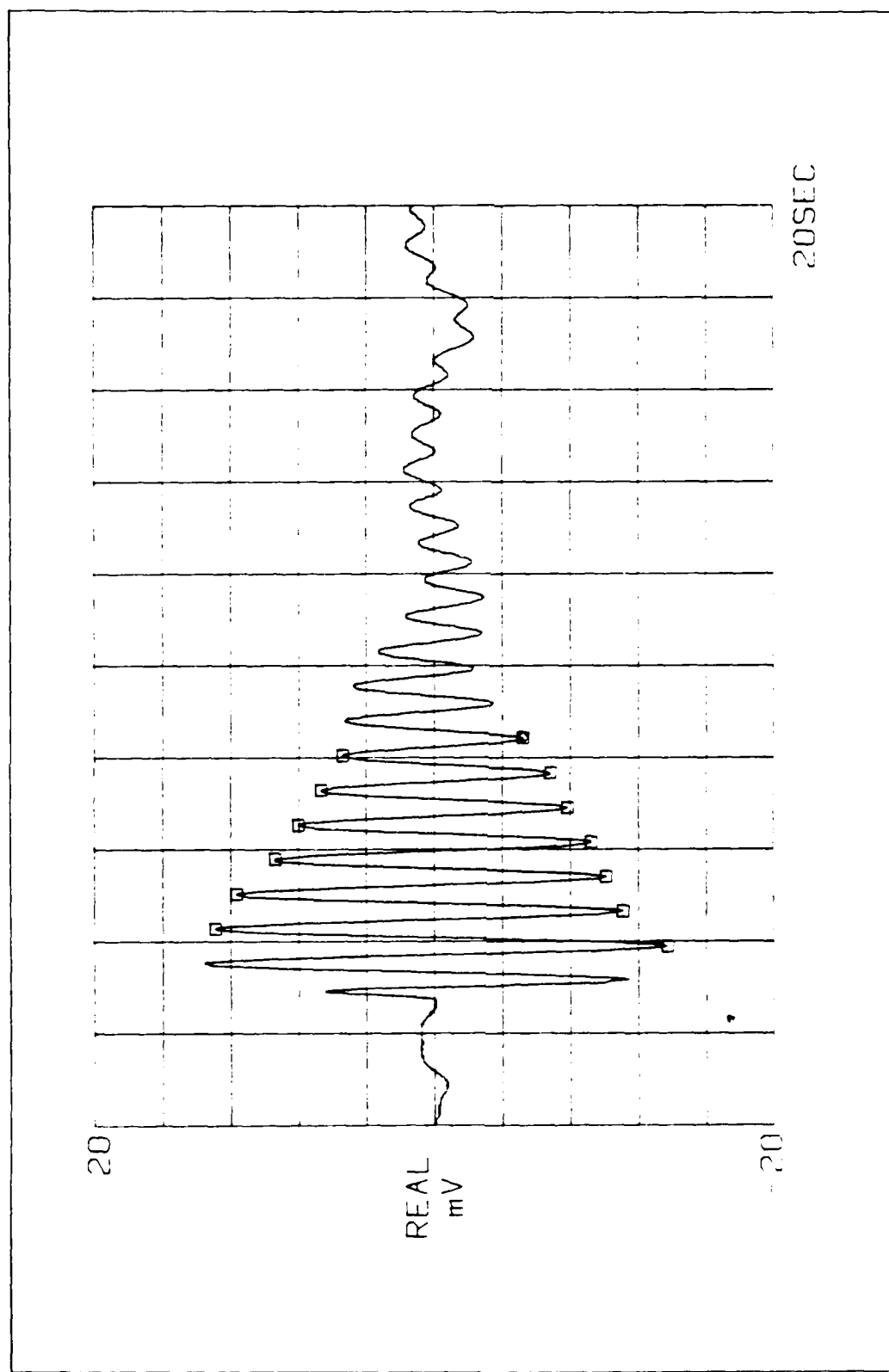
Figure 7.1. First Z Bending Mode Response - Suppressed
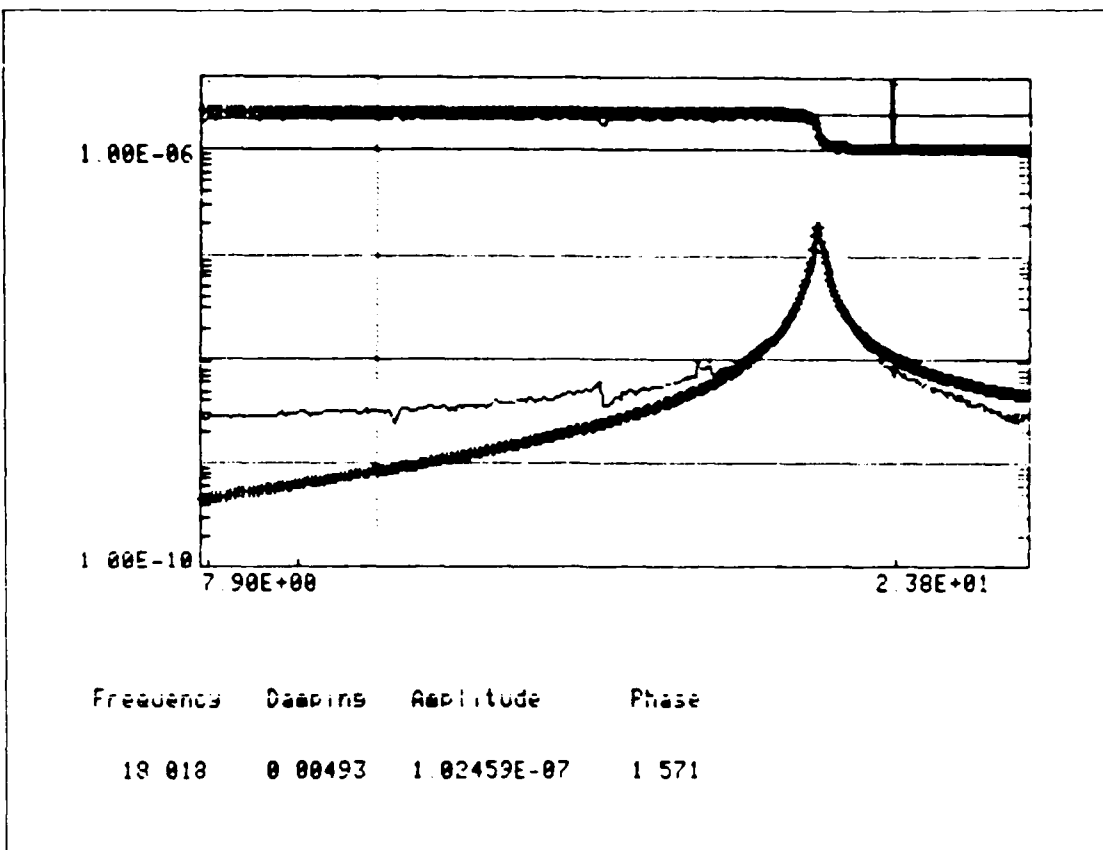
Figure 7.2. Second Z Bending Frequency Response Curve Fit

be corrected by adding 42.1 dB gain to account for the input scale factor in the PC-1000. Making this adjustment and comparing the result with the magnitude of the response in $\underline{w}$, the suppression has reduced the the first mode measurement amplitude by 15.4 dB (83.1%).
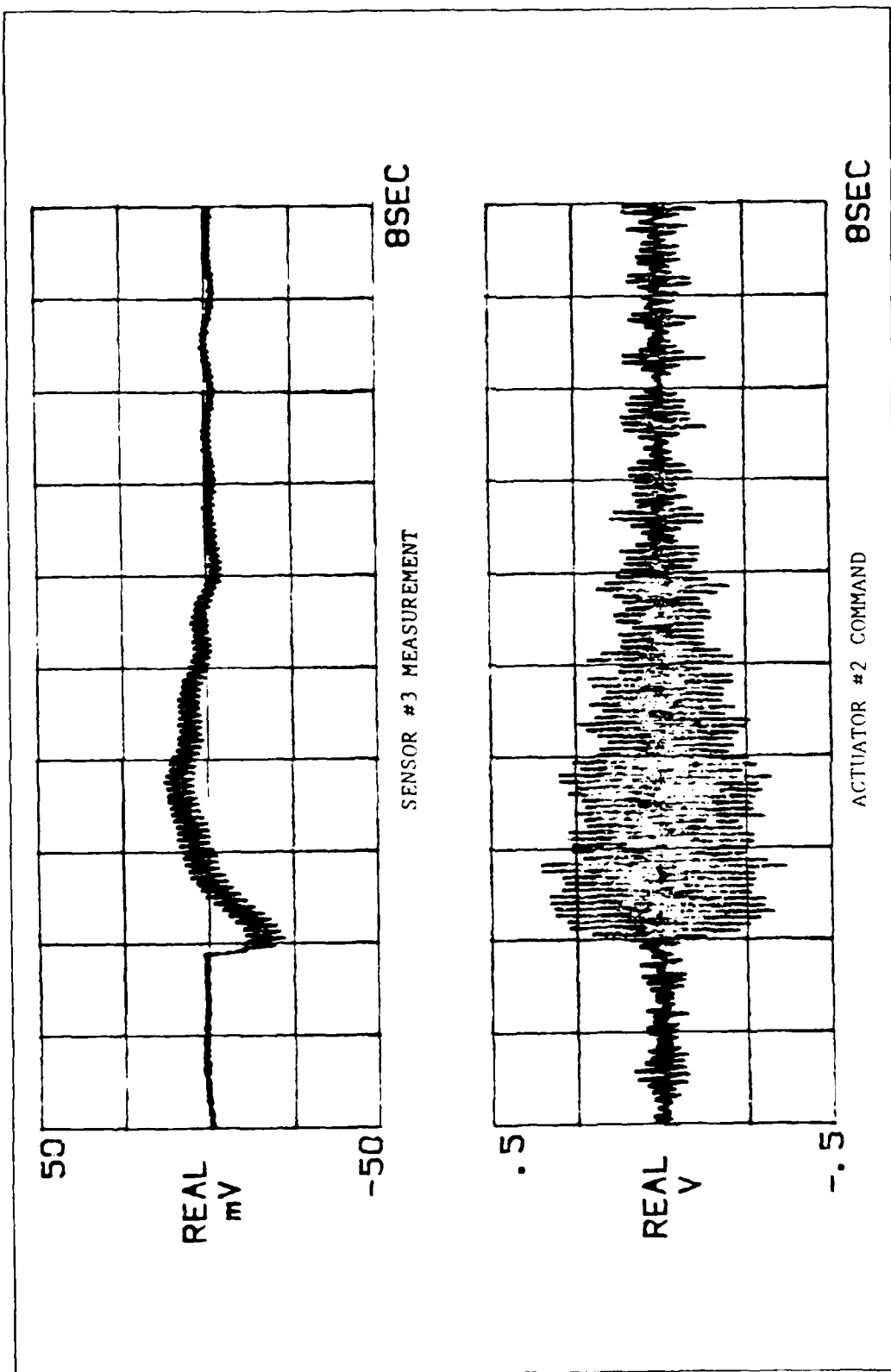
Figure 7.3. Sensor Input vs Command Output - Second Z Bending
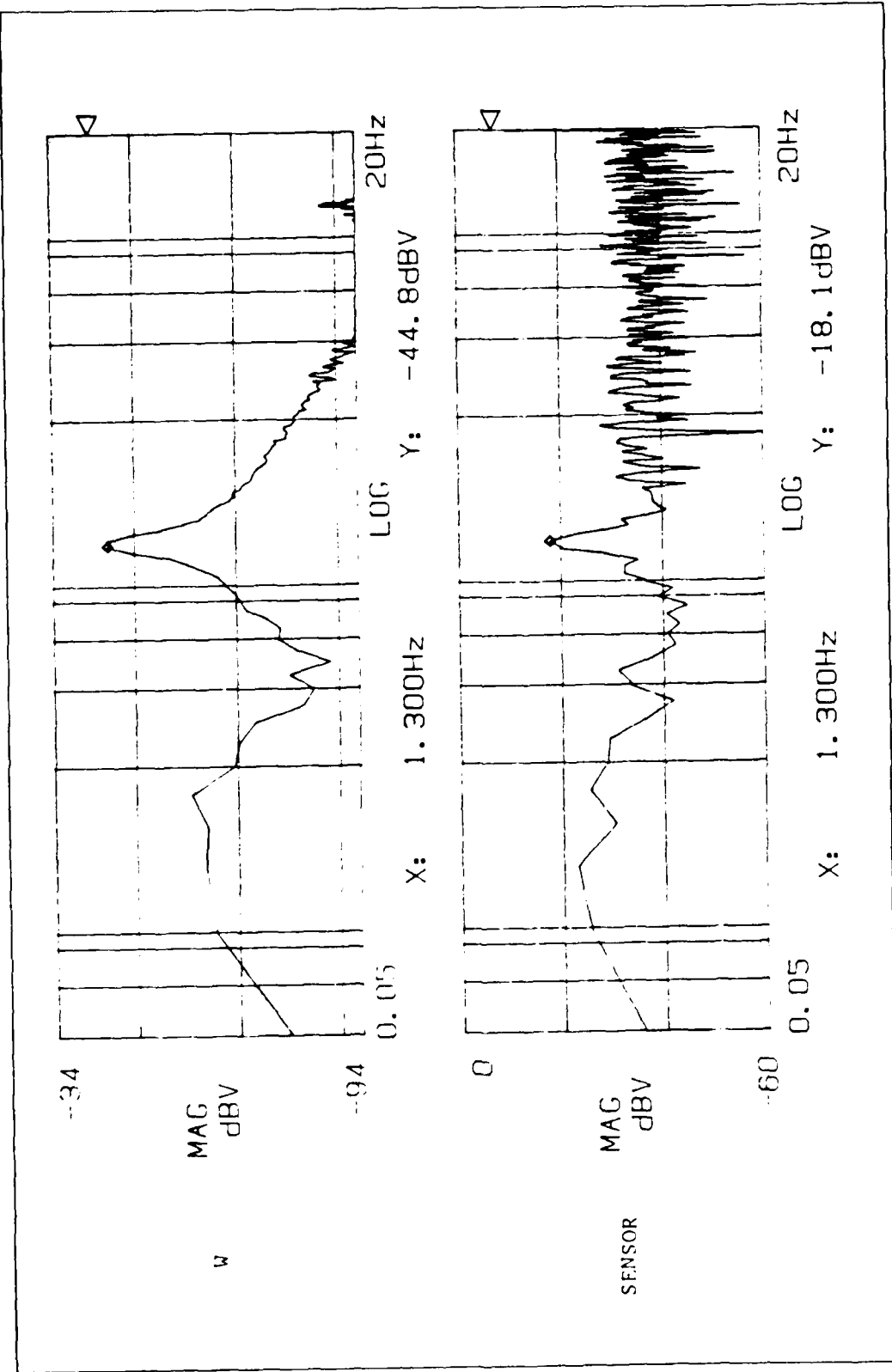
Figure 7.4. Sensor vs Suppressed Measurement Spectral Response

7 - 12

VIII. Conclusions and Recommendations

Conclusions

Several issues important to future design and testing in the area
of large space structure control have been raised in this experiment.
First, if linear proof mass actuators are to be used in controlling
lightweight, flexible structures, care should be taken to ensure that
not only are they not placed at or near nodes on the structure, but that
they don't create a node at the control point by their mere presence.
Colocation of these actuators should be avoided to the extent possible.
The second problem associated with the actuators is the placement of
their dynamics. To reduce the computational burden on the control
system, it is always desirable to have a flat response from the actuator
over the control bandwidth. To accomplish this, along with the
desirable characteristics of maintaining a free floating and centered
proof mass, dictates moving the low order poles of the system to very
low frequency. This has the undesirable effect of making the actuator
very responsive to drift and bias shift. Using the actuators in this
configuration requires highly accurate instrumentation and excellent
signal conditioning to filter out all signals outside the control
bandwidth.

This sensitivity obviously makes sensors an important issue.
Integrating accelerometer data to generate a velocity measurement will
continually generate problems with low frequency signals unless an
accelerometer capable of accurately sensing acceleration frequencies
below 1 Hz and amplitudes to less than a tenth percent of scale is used.
None of the piezoelectric accelerometers evaluated for use in this

experiment were truely adequate for the task. While the fundamental frequency in this experiment was still above 1 Hz, a large structure on orbit may have many modes at or below this frequency. The only accelerometers capable of adequately performing in this regime may be the PIGA (Pendulous Integrating Gyroscopic Accelerometer) type widely used in inertial navigation platforms or others of similar capability. Position sensors are also possibilities for use in the control design. While no position sensors were used or evaluated for this experiment, development of an accurate position sensor for use on a large space structure control would expand the options available to the control designer. Benefits of a particular sensor or sensor type would be dependent on the specific experiment or vehicle to be controlled.

With the number of problems seen with noise in this experiment, both high and low frequency, a deterministic observer may not be the best algorithm with which to approach the problem. While some of the difficulties could be reduced by better signal conditioning and more accurate instrumentation, the less costly solution may be to implement some form of a stochastic estimator in the controller.

Lastly, while the demonstration of reduced order controllers was only partially successful, all indications from the experiment were that it is a viable technique given adequate observability and controlability of the modes in question.

Recommendations for Future Work

A number of improvements could be made to increase the accuracy of the experiment and perhaps make it a better test bed for evaluating control methodologies. Several improvements in the area of the actuators could be readily made. The actuator shafts should be replaced

with ones which have a much harder surface. Scoring of the current shafts from the proof mass bearings was becoming significant even before closed loop testing of the beam was started. Additionally, the lag prefilter should be removed from the compensator circuit and the actuator response verified. Model predictions indicate the phase and magnitude deviations of the actuator transfer function at the low end of the control bandwidth were due to this prefilter and not the actuator dynamics. As a third step, a thorough review of the compensator circuit for ways to increase the accuracy and reduce the noise in the system would be profitable. Initially, isolation of the power inputs to the operational amplifiers may be helpful.

In the area of sensing, substantially better low frequency signal conditioning will be required to be able to operate a deterministic estimator with a damping ratio higher than about 0.25.

The bias observed in the input channels of the PC-1000 should be isolated and removed. While the problem can be worked around, it degrades the performance and dynamic range of the experiment. For some of the higher gain controllers applied to the higher modes the output bias was observed to be as much as 7 volts. With a maximum output of 10 volts, the dynamic range of the control signal has been significantly reduced.

Enhancing the controlability of the higher bending modes is needed to adequately demonstrate modal suppression, but this may be difficult to accomplish for this structure. If the actuators controlling one axis are removed, the finite element model predicts only a few percent increase in the relative amplitude between the first and second bending modes. A more viable approach to being able to demonstrate suppression of coupled modes may be to place an asymmetric mass on the base plate large enough to significantly couple the bending fundamental modes.

Bibliography

1. Martin, Joseph W., III, "A Free-Free Beam for the Study of Spacecraft Control," MS Thesis, Department of Electrical Engineering, The Ohio State University Graduate School, Columbus, Ohio, 1987.

2. Balas, M.J., "Active Control of Flexible Systems," AIAA Symposium on Dynamics and Control of Large Flexible Spacecraft, Blacksburg, Virginia, June 14, 1977.

3. Coradetti, T., "Orthogonal Subspace Reduction of Optimal Regulator Order," Proceedings of the AIAA Guidance and Control Conference, Boulder, Colorado, August 6-8, 1979.

4. Calico, Robert A., Jr, and A.M. Janiszewski, "Control of a Flexible Satellite via Elimination of Observation Spillover," Proceedings of the Third VPI&SU/AIAA Symposium on the Dynamics and Control of Large Flexible Spacecraft, Blackburg, Virginia, June, 1981.

5. Wright, Richard L., Jr, "Experimental Control of Simultaneously Excited Structural Modes," MS Thesis GAE/AA/85D-19, School of Engineering, Air Force Institute of Technology, Wright-Patterson AFB, Ohio, December, 1985.

6. MSC·PAL Users Manual, MacNeal-Schwendler Corporation, 815 Colorado Boulevard, Los Angeles, Calfornia 90041, October, 1984.

7. Craig, Roy R., Jr, Structural Dynamics: An Introduction to Computer Methods. John Wiley & Sons, New York, 1981.

8. Roark, R.J., and W.C. Young, Formulas for Stress and Strain (Fifth Edition). McGraw-Hill, New York, 1975.

9. Meirovitch, L., Analytical Methods in Vibrations. McMillan Publishing Co., New York, 1967.

10. Cook, Robert D., Concepts and Applications of Finite Element Analysis (Second Edition). John Wiley & Sons, New York, 1981.

11. Franklin, G.F., et al., Feedback Control of Dynamic Systems.
     Addison-Wesley Publishing Co., Reading, Massachusetts, 1986.

12. PC-1000 Systolic Array Processor Operations Manual, Systolic
     Systems Inc., 1550 La Pradera Drive, Campbell, California 95008,
     Second Edition, 1985.

13. Aldridge, E.S., "Decentralized Control of a Large Space Structure
     as Applied to the CSDL 2 Model," MS Thesis GA/AA/82D-1, School of
     Engineering, Air Force Institute of Technology, Wright-Patterson
     AFB, Ohio, December, 1982.

LINEAR MOTORS

**KAISER
ELECTROPRECISION**

DEFINITIONS (Continued)

CONTINUOUS RMS CURRENT – Using maximum power dissipation and 60Hz impedance (since it is essentially resistive) a maximum current rating can be calculated from $P = i^2 R$. However the resistance used in this calculation is at maximum temperature, not the room temperature value given on the data sheet.

The resistances of both the coil and the secondary increase at 0.4% per degree Celsius, and the typical temperature rise of the secondary is about 2/3 that of the coil. RMS current rating is calculated from this information, or measured experimentally.

RMS current rating multiplied by force constant gives RMS force rating. This is a useful number of comparing capabilities of motors and is similar to rated torque of a rotary motor.

PULSE CURRENT – Three factors limit the maximum current pulse that may be applied to the motor

- Demagnetization
- Heating damage to the coil connectors
- Physical strength of the armature assembly

Armatures are normally tested for strength at high temperature so that this failure mode should not be the limiting one. The other two processes depend on current pulse width as well as amplitude. Demagnetization only becomes a problem after secondary current, whose flux opposes armature flux, decays. Damage to connections only occurs if the current pulse is long enough to heat them excessively. The value given on the data sheet is a conservative one based on tests and experience.

MODEL 512 LINEAR MOTOR

The Model 512 is for use in disc recording systems, and other applications requiring servo-controlled linear motion. Constant force range is 0.9 inches. Total stroke is 1 inch.

**Special units can be built with force constant up to 2.5 lb/amp.**

DIMENSIONS (inches)

MOTOR CHARACTERISTICS AT 25°C

Force Constant	= 1.0 lb/amp
Coil DC Resistance	= 6 ohms
Coil Inductance (in air)	= 1.52 mH @ 1 kHz
Coil Mass	= 22.5 gm
Total Motor Weight	= 795 gm (1.75 lb)

MAXIMUM RATINGS AT 25°C AMBIENT

Coil Temperature	= 130°C
Power Dissipation	= 34 watts
Continuous RMS Current (dissipation limited)	= 2 amps
Pulse Current	= 10 amps 10 msec

MODEL 517 LINEAR MOTOR

The Model 517 is a permanent-magnet moving-coil DC linear motor designed for positioning heads on floppy disc drives and for other applications requiring a compact linear driver. The constant force stroke length of the standard unit is 1.6 inches. Special motors of the same diameter but greater length can be designed for stroke requirements up to 3 inches without loss of efficiency. Customer-specified coil resistances and mounting interfaces can be provided. Single and bifilar wound coils are available.

DIMENSIONS (inches)

MOTOR CHARACTERISTICS AT 25°C
Bifilar Winding – electrical characteristics for one half of winding

Force Constant	9.5 lb/amp
Coil DC Resistance	11.5 ohms
Coil Inductance, fully retracted	2.0 mH at 1 kHz
1.6, extended	3.4 mH at 1 kHz
Thermal Resistance, coil to air	7 °C/watt
Coil Mass	0.6 lb
Total Motor Weight	3.1 lb

MAXIMUM RATINGS AT 25°C AMBIENT

|	
Coil Temperature	135°C
Power Dissipation	16 watts
Continuous RMS Current (dissipation limited)	1.4 amps
Pulse Current	10 amps 10 msec

Figure A.1. Linear Motor Specifications
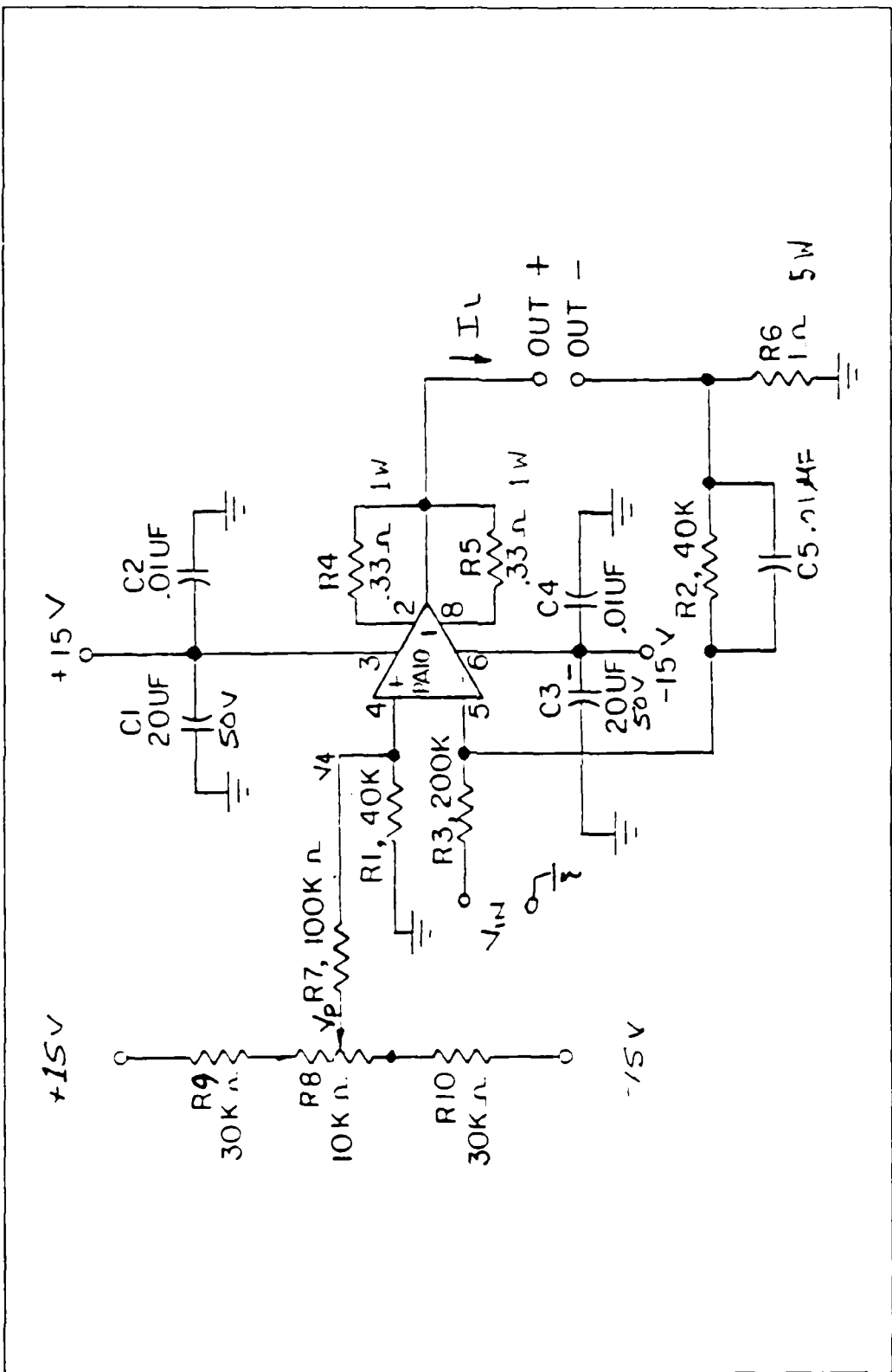
Figure A.2. Actuator Power Amplifier Circuit Diagram

ENDEVCO® MODELS 2262-25/2262C-25
## LOW g (DAMPED) PIEZORESISTIVE ACCELEROMETERS
±25 g

The Models 2262-25 and 2262C-25 Accelerometers are designed to measure a broad variety of long duration, low level acceleration phenomena. ENDEVCO's PIEZITE® Type P-11 elements are employed in a bridge circuit to obtain a high level output at ±25 g full scale. This output is high enough to drive most tape recorders and low frequency galvanometers directly, without amplification. The Model 2262C is a six-wire device that uses a pair of fixed resistors in half the bridge to present a fixed resistance to the extra pair of leads for shunt calibration techniques.

Although the rated range of these transducers is ±25 g, they may be used to ±50 g. A unique system of overrange stops limits the movement of the seismic element allowing the units to withstand shock up to 80 times their rated range without calibration shift. Viscous damping extends their useful frequency range and reduces the effect of spurious high frequency vibrations.

Typical applications for these accelerometers include transportation environment testing, transient accelerations on large structural members, and combined environments of steady state acceleration plus transient inputs.

(All values are typical at +75°F (+24°C) unless otherwise specified.)

		MODEL 2262-25	MODEL 2262C-25
PERFORMANCE			
RANGE	g	±25	±25
SENSITIVITY			
(at 10 Vdc excitation, ref 100 Hz)			
Typical/Minimum	mV/g	20/16	10/8
NON-LINEARITY & HYSTERESIS			
(% of reading, max to full range)	%	±1	±1
FREQUENCY RESPONSE			
(±5% max, ref 100 Hz)	Hz	0 to 650	0 to 650
MOUNTED RESONANT FREQ	Hz	2500	2500
DAMPING RATIO		0.7 -0.15/-0.10	0.7 -0.15/-0.10
TRANSVERSE SENSITIVITY (max)	%	3	3
THERMAL SENSITIVITY SHIFT			
(ref +75°F (+24°C))	%	-5/-2/0/-2/-5	-5/-2/0/-2/-5
	°F	0/+25/+75/+150/+200	0/+25/+75/+150/+200
	°C	-18/-4/+24/+66/+93	-18/-4/+24/+66/+93
ZERO MEASURAND OUTPUT (max)	mV	±25	±25
THERMAL ZERO SHIFT (max)	mV	±20	±20
BASE STRAIN SENSITIVITY			
(at 250 µstrain)	EQ g	0.005	0.005
ELECTRICAL			
EXCITATION	Vdc	10.0	10.0
INPUT RESISTANCE	Ω	1800	1000
OUTPUT RESISTANCE	Ω	1400	1000
INSULATION RESISTANCE			
(minimum at 100 Vdc)	MΩ	100 leads to case	100 leads to case
GROUNDING		Cable shield common to case	Cable shield common to case
		Case isolated from sensors	Case isolated from sensors
PHYSICAL			
WEIGHT (excluding cable)	oz (gm)	1 (28)	1 (28)
CASE MATERIAL		Stainless steel type 416	Stainless steel type 416
ELECTRICAL CONNECTIONS		Integral six-pin connector	Integral six-pin connector
MOUNTING TORQUE		Hole for 10-32 mounting stud	Hole for 10-32 mounting stud
		18 lbf-in (2 Nm)	18 lbf-in (2 Nm)
ENVIRONMENTAL			
ACCELERATION LIMITS			
(in any direction)			
Static	g	250	250
Sinusoidal	g	250	250
Shock	g	2000	2000
TEMPERATURE			
Operating	°F (°C)	0 to +200 (-18 to -93)	0 to +200 (-18 to -93)
Non-Operating	°F (°C)	-20 to +220 (-29 to +104)	-20 to -220 (-29 to +104)
HUMIDITY		Hermetically sealed by welding and glass-to-metal fusion	Hermetically sealed by welding and glass-to-metal fusion

NOTES

1. Non-linearity above 25 g is ±3% of reading, maximum to 50 g.
2. Frequency response at a damping ratio of 0.7 is -35% to -10% typical at 0° -200°F (-18° -93°C) and 2000 Hz.
3. Thermal Zero Shift millivolts specified are at 0° -200°F -18° -93°C, reference +75°F -24°C.
4. Rated excitation is 10.0 Vdc. The strain gage elements have a positive temperature coefficient of resistance of approximately 0.5% per °F.
5. Other excitation voltages may be used to 15.0 Vdc but should be specified at time of order to obtain a more accurate calibration. Warmup time to meet all specifications is two minutes maximum. Endevco Model 4423 Signal Conditioner is recommended as the excitation source.
6. Measurand at approximately 1 Vdc. Bridge resistance increases with applied voltage.

CALIBRATION DATA SUPPLIED
(at 75°F -24°C, and 10.00 Vdc excitation)

FREQUENCY RESPONSE RANGE	Range in Hz
SENSITIVITY at 100 Hz	mV/g
ZERO MEASURAND OUTPUT	mV
MAXIMUM TRANSVERSE SENSITIVITY	% of calibrated sensitivity
MOUNTED RESONANT FREQUENCY	Hz
DAMPING RATIO	Ratio of critical damping
INPUT AND OUTPUT RESISTANCE	Ω

ACCESSORIES INCLUDED
Model 2981-3 (10-32) or Model 2981-4 M5 metric mounting stud.
2262-25: Model 3022B-30 Cable Assembly, 4-conductor, shielded, 30 in (76 cm) long.
2262C-25: Model 3023B-30 Cable Assembly, 6-conductor, shielded, 30 in (76 cm) long.
U.S. Patent Nos. 3,336,...

Continued product improvement necessitates that Endevco reserve the right to modify these specifications without notice. Endevco maintains a program of constant surveillance over all products to ensure a high level of reliability. This program includes attention to reliability factors during product design, the support of stringent Quality Control requirements, and compulsory corrective action procedures. These measures together with conservative specifications have made the name Endevco synonymous with reliability.

ENDEVCO Σ

Figure A.3. Endevco Accelerometer Specifications

HPD SERIES—HERMETICALLY SEALED (PIN TERMINATION)

- HERMETICALLY SEALED BY TIG AND EB WELDING

- IMPERVIOUS TO HOSTILE ENVIRONMENTS

- THROUGH-BORE CONSTRUCTION

HPD Series units are similar to the DC-D and HCD Series. Tungsten inert gas (TIG) and electron beam (EB) welding provide hermetic sealing that is free from oxidation-producing faults that may cause leakage. For this reason, HPD Series LVDT's are impervious to dirt, water, steam spray, and most corrosives. They have been qualified at pressures up to 1000 psig (70 bars) and are suitable for numerous high-pressure applications. HPD units employ a glass-sealed, pin-terminal header that allows the core and core rod to pass through the unit. HPD units have double magnetic shielding that makes them insensitive to external magnetic influences.

GENERAL SPECIFICATIONS

Input: ±15 V DC (nominal), ±20 mA

Operating Temperature Range ... 0°F to +160°F (-18°C to +70°C)

Surviva Temperature Range ... -65°F to +200°F (-55°C to +95°C)

Null Voltage ... 0 V DC

Ripple ... Less than 25 mV rms

Linearity ... ±0.25% full range

Stability ... 0.125% full scale

Temperature Coefficient of Scale Factor .... 0.04%/°F (0.08%/°C)

Shock Survival ..... 250 g for 11 milliseconds

Vibration Tolerance . 10 g up to 2 kHz

Coil Form Material .. High density, glass-filled polymer

Housing Material ... AISI 400 series stainless steel

Electrical

Termination .... 6-pin terminal header

Output Impedance .. Less than 1 Ohm

PERFORMANCE SPECIFICATIONS AND DIMENSIONS

LVDT MODEL NUMBER	NOMINAL LINEAR RANGE	SCALE FACTOR	RESPONSE -3dB	WEIGHT Grams		A (Body)	DIMENSIONS B (Core)	P
	Inches	V/inch	Hz	Body	Core	Inches	Inches	Inches
050 HPD	±0 050	200	500	36	2	2 40	0 59	0 55
125 HPD	±0 125	80	500	45	3	3.23	1 10	0.96
250 HPD	±0 250	40	500	57	5	4 10	1 80	1.39
500 HPD	±0 500	20	200	77	8	5 79	3 00	2.23
1000 HPD	±1 000	10	200	115	10	8 05	3 80	3 32
2000 HPD	±2 000	5 0	200	169	13	11 42	5.00	5 05
3000 HPD	±3 000	3.3	200	231	14	16 62	6.20	7 59
5000 HPD	±5 000	2.0	200	284	17	20 45	6 20	9 56
10000 HPD	±10 00	1 0	200	520	24	34 57	12 00	16 61

ORDERING INFORMATION

(Fold out page 32 for instructions on how to use this chart.)

OPTION NC	METRIC THREAD CORE (NOTE 1) 005	TEFLON BORELINER 010	SMALL DIAMETER CORE (NC) (2) 020	10 FOOT (3m) LEADS 040	MILDLY RADIATION RESISTANT 060
MODEL NC					
050 HPD	A	B	B	-	X
125 HPD	A	B	B	-	X
250 HPD	A	B	B	-	X
500 HPD	A	B	B	-	X
1000 HPD	A	C	X	-	X
2000 HPD	A	C	X	-	X
3000 HPD	A	C	X	-	X
5000 HPD	A	C	X	-	X
10000 HPD	A	C	X	-	X

Note 1 See outline drawing for metric thread nuts
Note 2 Consult factory for exact dimensions and revised nuts

INPUT   OUTPUT

+15VDC

-15VDC

COMMON

±10 VDC

750 ± 010 DIA

236 ± 005 DIA

13 ± 030

P

A ± 030

6 48 UNC 28 (Standard)
M3 X 0.5 6H (Metric)

188 ± 005 DIA

B ± 030

38 Minimum Depth

P is nominal center position of core or coil
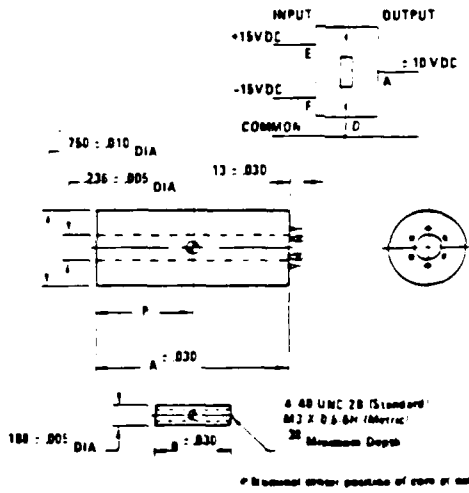
Figure A.4. LVDT Specifications

Table A.1. Actuator Configurations

Actuator #	Component	Serial #	Calibration
1	Base Assembly	1	-
	Proof Mass	1	-
	Power Amplifier	1	-
	Accelerometer	RA40	23.18 mV/g
	LVDT	5358	20.750 V/in
2	Base Assembly	2	-
	Proof Mass	2	-
	Power Amplifier	2	-
	Accelerometer	RY95	17.59 mV/g
	LVDT	5356	20.348 V/in
3	Base Assembly	3	-
	Proof Mass	3	-
	Power Amplifier	3	-
	Accelerometer	RB46	20.76mV/g
	LVDT	5359	20.295 V/in
4	Base Assembly	4	-
	Proof Mass	4	-
	Power Amplifier	4	-
	Accelerometer	RF68	17.90 mV/g
	LVDT	5364	20.216 V/in

Appendix B: Actuator Development Problems

1) Pure integrators in the either the forward or feedback paths exacerbated the low frequency problems to the point that the configuration was impossible to test. The proof mass continually wandered into the end brackets and would not maintian a stable oscillation. This effectively eliminated the option of implementing an inverse plant model to cancel the low frequency dynamics of the system.

2) High frequency noise was a problem thoughout the development. The high frequency dynamics in the open loop response proved to be a problem when the acceleration feedback loop was added, especially when the gain was turned up in that loop. High gain in the acceleration feedback loop is desireable since it has the two benefits of moving the actuator dynamics lower and increases the ability of the proof mass to float freely when uncommanded. When the gain was turned up to a high enough level to effect the system dynamics, high frequency noise would feed back into the motor and drive the system unstable. The only solution found to this problem was to low-pass filter the acceleration signal in an attempt to reduce the magnitude of this noise. This was successful to some degree, but adding enough filtering at a frequency low enough to remove the 150 hz dynamics destroyed the phase of the feedback signal in the operating bandwidth. Three low-pass filters with break points at 80 hz provided sufficient reduction in the high frequency components of the signal that the feedback gain could be increased enough to significantly affect the dynamics. Unfortunately this shifted the phase of the feedback signal 90° at the fundamental bending modes, which is effectively velocity feedback (i.e. a viscous damper). The compromise was to implement only one low-pass filter with

a break point of 50 Hz in the acceleration feedback path. With this
configuration the feedback was still effectively an acceleration signal
while the magnitude of the high frequency noise was somewhat reduced.

3)   Some high frequency oscillation is ocassionally still observed
in the system, especially when all the actuators are on the beam and
high frequency vibration of one will be measured by another. This is
not a consistent problem and usually doesn't affect the overall
experiment. The origin seems to be the actuator 150 hz bracket dynamics
still feeding back through the compensator. The oscillation is not
strongly unstable, and usually is not noticable. Occasionally, the
response gets large enough that it is audible as a low hum coming from
the actuator. When this occurs it will usually stop by holding the
offending actuator on or around the LVDT mounting bracket. The signal
can also become noticeable if the actuator proof masses are allowed to
rest against the stops when not commanding the system.

4)   The actuator proof masses will tend to drift over on a long
term basis during operation due to a very low frequency drift in the
power amplifier. The power amplifer has been observed to oscillated
with a period of approximately 40 minutes and a peak voltage of 0.15 V
after turn on. This effect damps out with time, but the actuators have
still required centering adjustment even after several hours of
operation. The cause of this oscillation was not isolated since its was
of such a low frequency relative to the time required to run a test on
the beam. Possible causes lie in the power amplifier itself and
possibly in the power supply. This problem will cause the proof masses
to drift into the stops if left unattended for several minutes. Thus,
proof mass centering be checked prior to running any tests on the beam.

5) A configuration for the compensator was found that provided acceptable freqeuncy response performance over the desired bandwidth. However, the actuator exhibited a drift with input amplitude. As the amplitude of the input command was increased, the zero reference of the power amplifier appeared to change. This caused the proof mass to shift toward one end of the travel and oscillate about that point. The effect was not noticable in low frequency response since the proof mass stroke was saturated before the amplitude was high enough to cause the problem. However, the problem was noticable at the first torsion frequency of the beam. A test run using a combined fundamental and torsion freqeuncy command determine that the maximum output force that could be applied to any two modes simultaneously was 0.1 lbf. This low level of force output was not acceptable if the closed loop control result were expected to increase the beam damping by more than a few percent. Various approaches were tried to alleviate this problem such as AC coupling the input signal to ensure it has no bias; AC coupling the command from the compensator to the power amplifier; adding another feedback loop around the power amplifier, which was found to have other benefits, but had no affect on the drift problem; and substantially increasing the position feedback gain, to the detriment of the frequency response. The only change that had any affect on the problem was the increase of the feedback gain. However, all it really did was to raise the point at which the drift became noticable, and it completely destroyed the flat frequency response in the low end of the bandwidth.

Since the problem appeared to be associated with the power amplifier circut, Mr. Ken Taylor of TRW, who did the original design of the power amplifier circuit, was consulted as to the problem. Mr. Taylor's recommendation was to check the very high frequency output of the power amplifier. He felt the amplifier may have unstable

oscillations in the kilohertz to megahertz frequency range due the high impedance of the input, and the fact that the amplifier was driving a large inductive load (the motor) through very long cables (8 to 10 ft for this experiment). He suggested adding an RC network across the amplifier output if the high freqeuncy oscillations were observed.

Since the Ono Sokki Analyzer is limited to 40 KHz, the amplifier output was checked on an oscilloscope. A ±15 V oscillation was observed at approximately 66 KHz. Applying the fix that Mr. Taylor suggested was successful in eliminating it. This modification did not change the frequency response of the actuators, and did relieve the input amplitude drift problem to some extent. The drift was still present at high input amplitudes, but the high frequency output was increased to almost 2.5 lbf from the 0.1 lbf limit previously measured. While this is still below the actuators theoretical capability, it is a much more acceptable level for this experiment. Later testing revealed in fact that this drift was not an actuator problem, but was due to a very slight shift in the input bias from the Ono Sokki. The actuators were found to respond to as little as 2 mV of bias, and 5 mV would run the proof mass to the end of its travel. This sensitivity to bias and very low frequency inputs continues to be a problem and requires very high quality input signal to keep the actuators centered.

6) The phase response of the transfer function was observed to change with input amplitude. Some variations with amplitude were also observed, however they were much smaller than the phase shifts. The initial thought would be that as the input amplitude is reduced, the force applied by the motor to the proof mass is reduced. The expected consequence would be that friction starts to become a significant portion of the force on the proof mass, and accounts for the phase

change. Unfortunately, the shift in phase is opposite to the expected
effect of friction. One would expect friction to cause a lag in the
output as it holds the proof mass back slightly at the end of each
stroke. The observed behavior however, is that the phase increases as
the input magnitude is decreased. In an attempt to determine if the
phase shift was related to friction non-linearities, the time response
was plotted to see if the output had any discontinuities. Figures B.1
through B.3 show the proof mass position as measured by the LVDT
compared with the input command. The data indicates that there is no
observable sticking of the proof mass, even at very low input levels.

This problem was not resolved, but the phase shift from zero
degrees in the final configuration is within $\pm 10^{\circ}$ for the expected input
amplitude range. Isolation of this problem would be a topic to
investigate to improve the accuracy of the experiment.

7) *Bearing and shaft friction was found to cause a problem when*
the actuators were mounted on the beam. The proof masses float to a
great extent as the beam vibrates but still add approximately 3.5%
damping to the fundamental bending modes. The displacement eventually
damps down to a small enough level that the acceleration feedback
command cannot overcome the friction between the bearings and shaft. At
this point the proof masses stop floating and become part of the
structural mass. The result is a nonlinear structure. In examining the
actuator shafts, scoring by the bearings was becoming significant. The
problem became acute enough in actuator #2 that the proof mass would
occassionally stick while being commanded and often required manually
moving the proof mass to restore free motion. At this time the problem
still exists. New actuator shafts with a much harder finish are under
manufacture. These should solve the scoring problem, and may help the
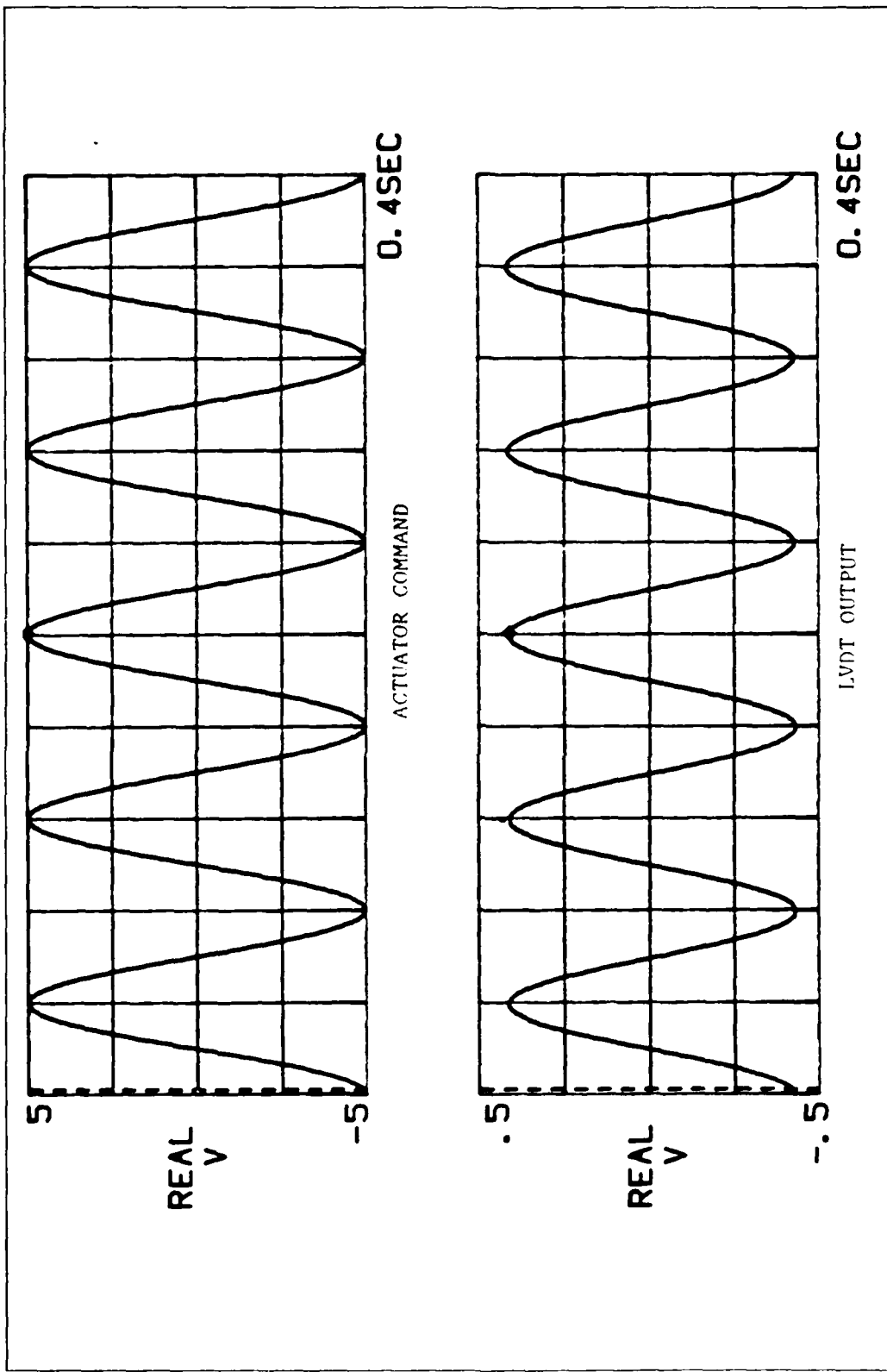
Figure B.1. Proof Mass Position Time Response - High Input Level
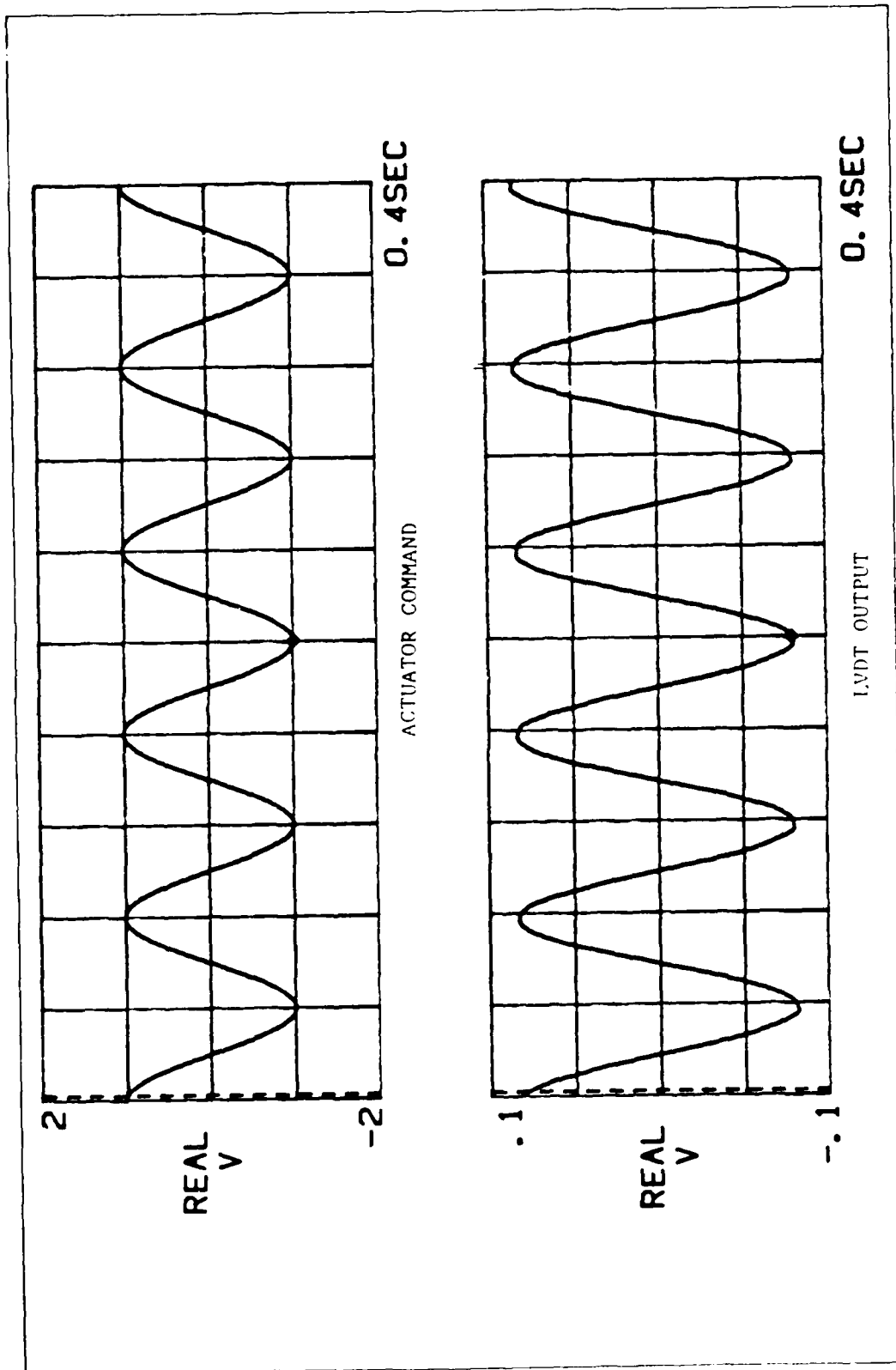
Figure B.2. Proof Mass Position Time Response - Intermediate Input Level
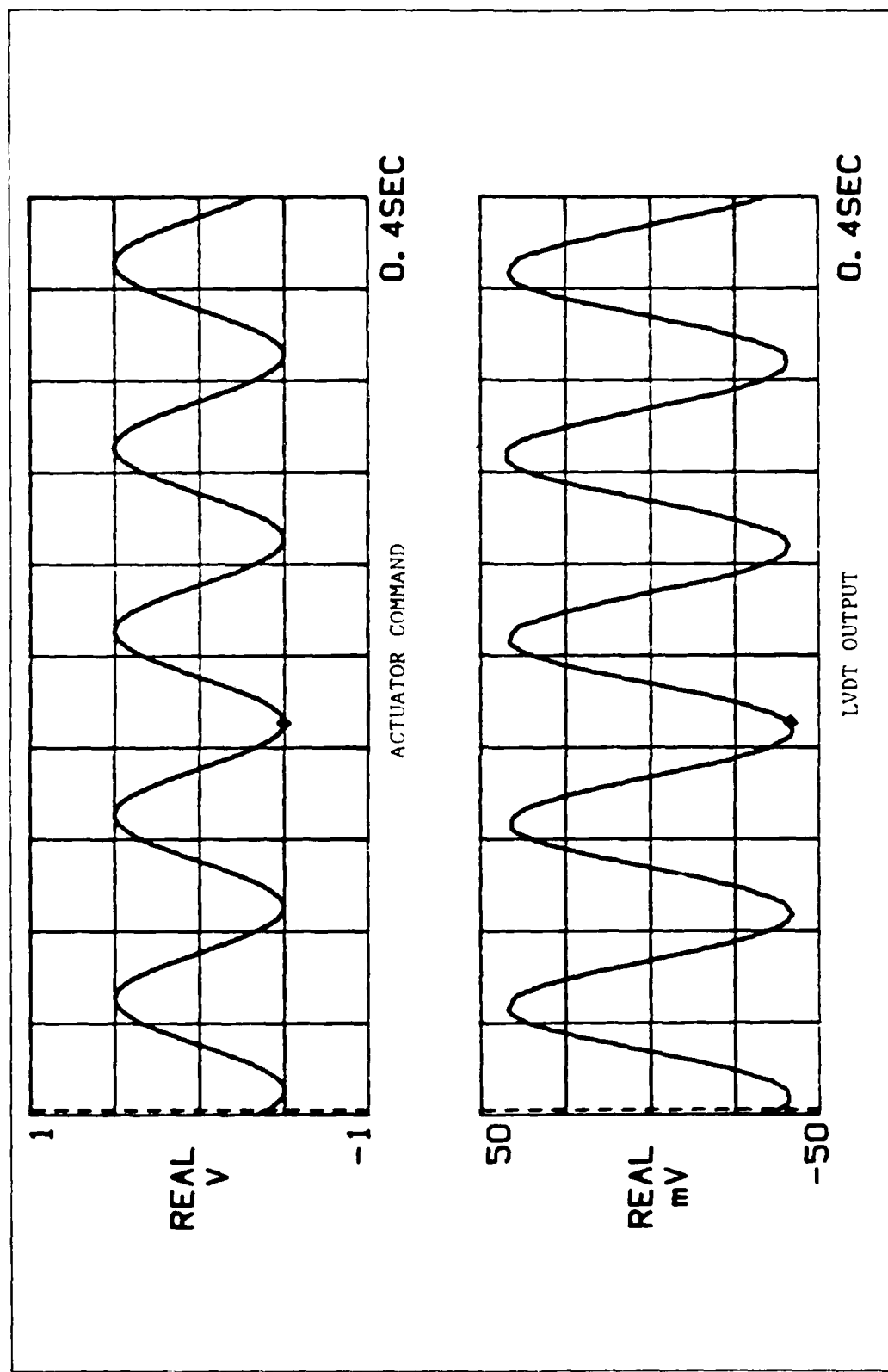
Figure B.3. Proof Mass Position Time Response - Low Input Level

low amplitude sticking. Another modification that will further reduce the amplitude at which the proof masses stop floating is to increase the acceleration feedback gain. At this time the gain is as high as is practical for this configuration. The limiting factor in the acceleration feedback has been high frequency noise. The feedback circuit currently has one low-pass filter on the accelerometer signal. More signal conditioning will be required to keep high frequency oscillations out of the actuator when the gain is increased. Increased acceleration gain will also affect the actuator dynamics, moving the complex pole pair to even lower frequency. This may actually be beneficial if the resonance can be moved below the range of any low frequency drift that might be in the command signal. If this modification is made, the acceleration feedback amplifier output should be checked to ensure the signal is not close to saturating either the feedback amplifier or the subsequent summing junction.

## Appendix C: Actuator Mass Model

To develop an accurate actuator mass model the configuration was divided into six components, each of which could be approximated by simple figures (see Figure C.1). These components include all of the major parts of the actuator system with significant mass. The mass of the remaining parts not represented directly by one of the components was applied to the nearest representative figure. A description of each component, its mass and dimensions is listed in Table C.1.

Table C.1. Actuator Mass Model Components

Part	Figure Description	Mass $\left(\dfrac{lbf \cdot sec^2}{in}\right)$	Dimensions (in)			
			Length	Width	Height	Diameter
1	Rectangular Plate	142.34E-6	1.1	0.3	1.7	-
2	Circular Cylinder	199.28E-6	4.5	-	-	0.25
3	Rectangular Plate	483.95E-6	1.1	0.3	1.7	-
4	Rectangular Plate	199.28E-6	1.1	0.3	2.125	-
5	Circular Cylinder	540.89E-6	5.5	-	-	0.75
6	Hollow Circular Cylinder	2.9324E-3	2.25	Inside Diameter = 0.25 Outside Diameter = 2.125		

The mass moments of inertia about the component's center of gravity are calculated by assuming the center of gravity lies at the center of figure then orienting parts in the global coordinate frame of the structure according to the orientation of the specific actuator. The
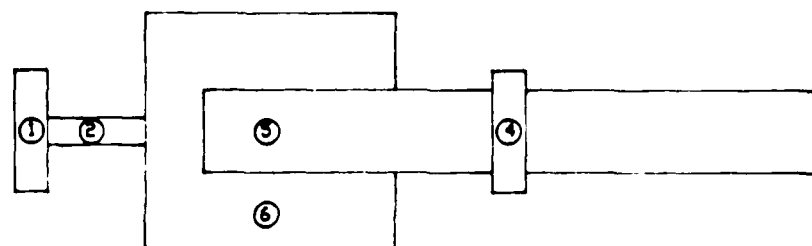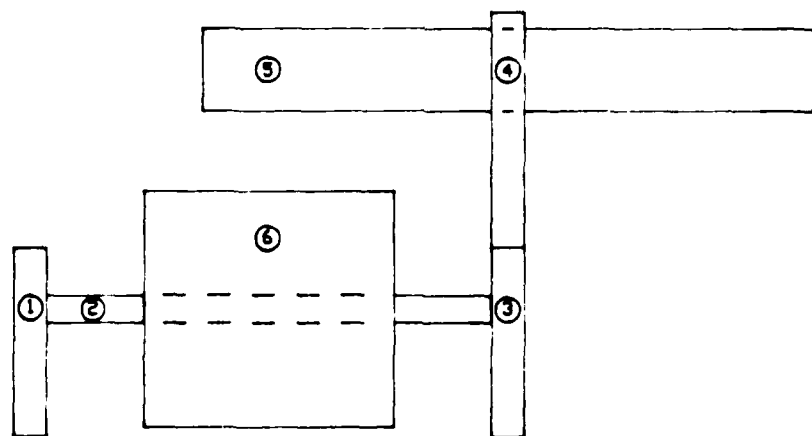
Figure C.1. Actuator Mass Model Components

resulting centers of gravity and mass moments of inertia for each
actuator are shown in Tables C.2 through C.5.

Table C.2. Actuator #1 Mass Model

Part	Center of Gravity (in)			Mass Moments of Inertia $(\text{lbf} \cdot \text{sec}^2 \cdot \text{in})$		
	$\bar{x}$	$\bar{y}$	$\bar{z}$	I_x	I_y	I_z
1	69.90	-2.25	-4.00	15.42E-6	48.63E-6	35.35E-6
2	69.60	0.00	-4.00	337.06E-6	1.56E-6	337.06E-6
3	69.90	2.25	-4.00	52.43E-6	165.35E-6	120.18E-6
4	67.99	2.25	-4.00	21.59E-6	95.08E-6	76.48E-6
5	67.45	2.44	-4.00	1.3825E-3	38.03E-6	1.3825E-3
6	69.60	0.00	-4.00	3.6280E-3	2.9324E-3	3.6280E-3

Table C.3. Actuator #2 Mass Model

Part	Center of Gravity (in)			Mass Moments of Inertia $(\text{lbf} \cdot \text{sec}^2 \cdot \text{in})$		
	$\bar{x}$	$\bar{y}$	$\bar{z}$	I_x	I_y	I_z
1	69.90	-4.00	2.25	15.42E-6	35.35E-6	48.63E-6
2	69.60	-4.00	0.00	337.06E-6	337.06E-6	1.56E-6
3	69.90	-4.00	-2.25	52.43E-6	120.18E-6	165.35E-6
4	67.99	-4.00	-2.25	21.59E-6	76.48E-6	95.08E-6
5	67.45	-4.00	-2.44	1.3825E-3	1.3825E-3	38.03E-6
6	69.60	-4.00	0.00	3.6280E-3	3.6280E-3	2.9324E-3

C - 3

Table C.4. Actuator #3 Mass Model

Part	Center of Gravity (in)			Mass Moments of Inertia $(\mathrm{lbf \cdot sec^2 \cdot in})$		
	$\bar{x}$	$\bar{y}$	$\bar{z}$	I_x	I_y	I_z
1	69.90	2.25	4.00	15.42E-6	48.63E-6	35.35E-6
2	69.60	0.00	4.00	337.06E-6	1.56E-6	337.06E-6
3	69.90	-2.25	4.00	52.43E-6	165.35E-6	120.18E-6
4	67.99	-2.25	4.00	21.59E-6	95.08E-6	76.48E-6
5	67.45	-2.34	4.00	1.3825E-3	38.03E-6	1.3825E-3
6	69.60	0.00	4.00	3.6280E-3	2.9324E-3	3.6280E-3

Table C.5. Actuator #4 Mass Model

Part	Center of Gravity (in)			Mass Moments of Inertia $(\mathrm{lbf \cdot sec^2 \cdot in})$		
	$\bar{x}$	$\bar{y}$	$\bar{z}$	I_x	I_y	I_z
1	69.90	4.00	-2.25	15.42E-6	35.35E-6	48.63E-6
2	69.90	4.00	0.00	337.06E-6	337.06E-6	1.56E-6
3	69.90	4.00	2.25	52.43E-6	120.18E-6	165.35E-6
4	67.99	4.00	2.25	21.59E-6	76.48E-6	95.08E-6
5	67.45	4.00	2.44	1.3825E-3	1.3825E-3	38.03E-6
6	69.60	4.00	0.00	3.6280E-3	3.6280E-3	2.9324E-3

Appendix D: Final Modal Test Data

The modal test of the final experiment configuration was conducted in two phases. First, the fundmental bending modes in the z-axis and y-axis were measured using a sine dwell technique. Magnets were mounted on either side of the base plate in the plane of the bending axis to be tested. Magnetic induction coils were used in conjunction with these magnets to apply a sinusoidal forcing function to the structure. The frequency and damping of the modes were determined by generating a frequency response function for the structure around the natural frequency. The beam was forced at a single frequency and the steady state acceleration of the base plate recorded. Measuring the response at intervals throughout a frequency band around the being mode natural frequency creates the response function. The peak response occurs at the modal frequency and the damping can be determined using the half-power point method (equation 8). To determine the mode shape, the structure was forced at the natural frequency and the acceleration of each of the nodal points measured. For steady state motion, the displacement is proportional to acceleration and is therefore a direct measurement of the mode shape. This mode shape can be normalized to a unit vector for comparison with the finite element data. The frequency response functions are shown in Figures D.1 and D.2, and the measured modal amplitudes are listed in Table D.1.

The second phase used the GenRad Modal Analyzer to measure the first torsion and higher bending modes. The test was conducted using the impact method. The beam is tapped with a force hammer at a selected node and the response at each node is recorded. The measured time response is transformed to the frequency domain using Fast Fourier Transforms, and a frequency response function is generated for each node

D - 1

point. The frequency and damping of the mode are found from the curve

fit parameters for the response function, and the mode shapes are

determined by the magnitude and phase of the response at each node

point. Figure D.3 shows the node point geometry used internally in the

GenRad. Figure D.4 is the first torsion mode curve fit and mode

parameters. Figures D.5 through D.8 show the higher bending mode modal

parameters and mode shapes.
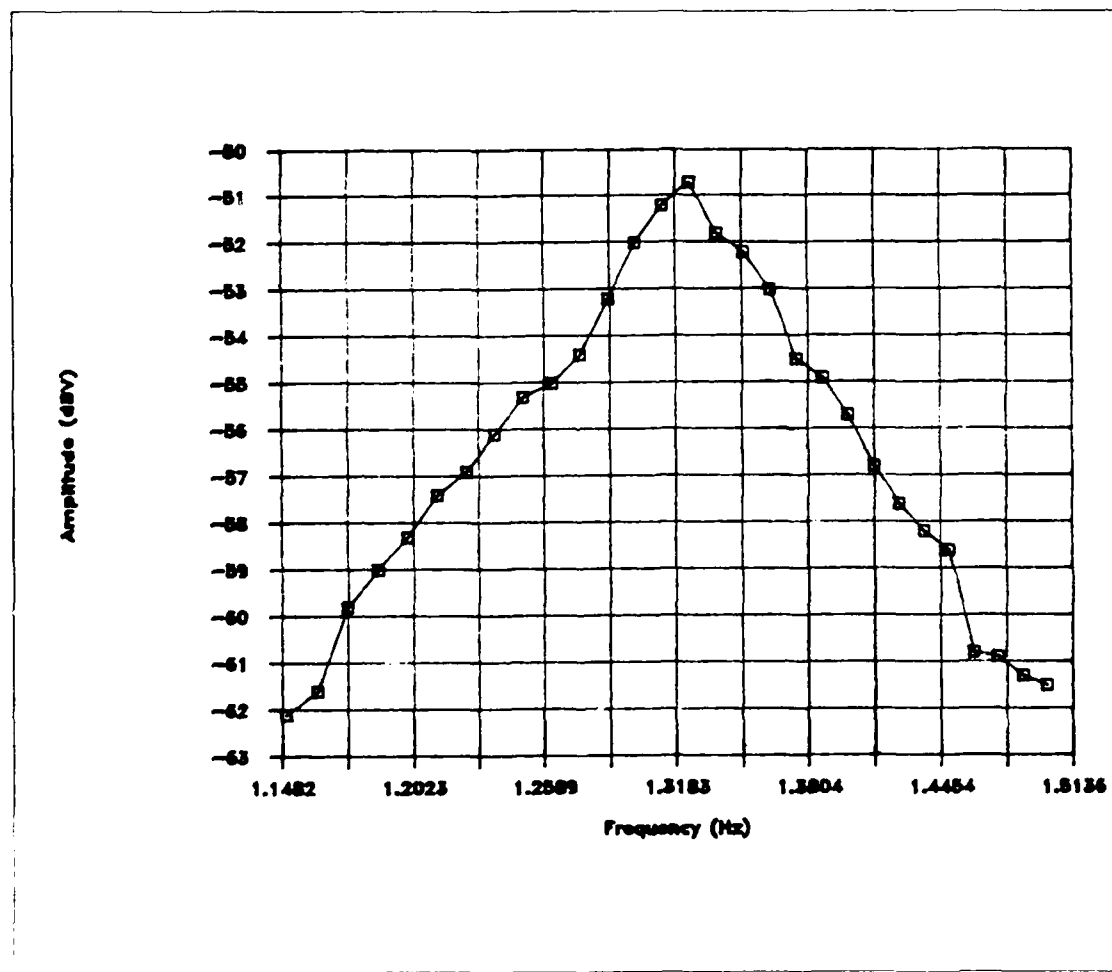
Figure D.1. Z-Axis Frequency Response Magnitude
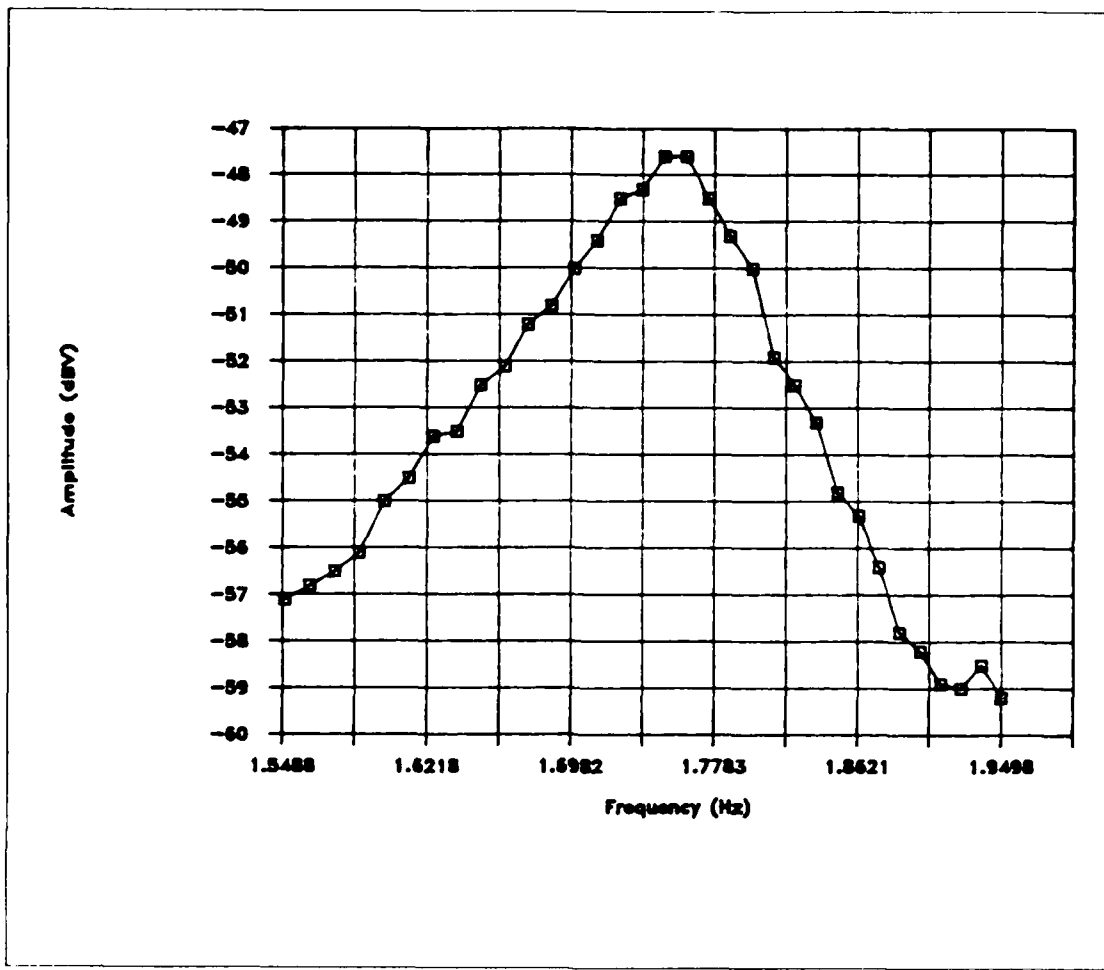
Figure D.2. Y-Axis Frequency Response Magnitude

Table D.1. Z and Y Axes First Bending Modes

Node	First Z Bending Modal Amplitudes	First Y Bending Modal Amplitudes
	Acceleration (g)	Acceleration (g)
1	0.000000	0.000000
2	0.000113	0.000073
3	0.000252	0.000674
4	0.000677	0.001836
5	0.001382	0.003171
6	0.002461	0.004519
7	0.003922	0.006179
8	0.004738	0.007805
9	0.007174	0.010108
10	0.008762	0.011995
11	0.010791	0.016117
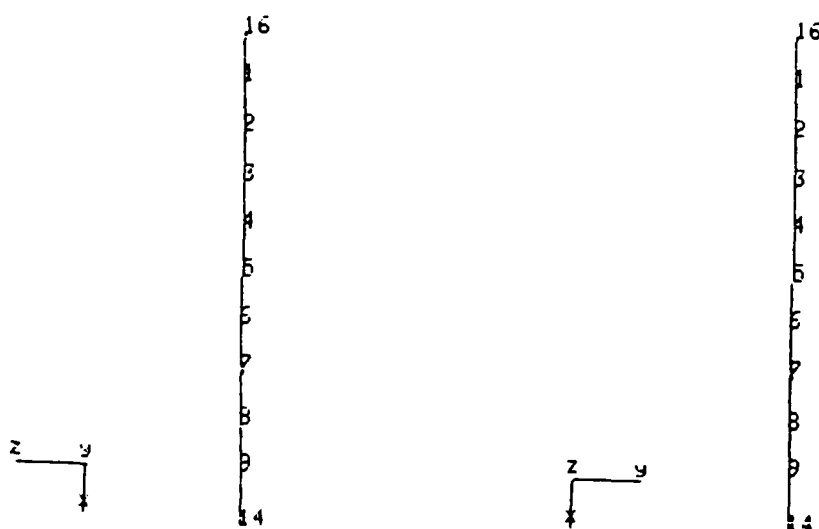
Figure D.3. Modal Test Node Point Geometry

```
                                                              ++++++++++++++++++++
                    +++++++++++++++++++++
      5.00E+01

      5.00E-03
            1.18E+01                                    1.34E+01
```
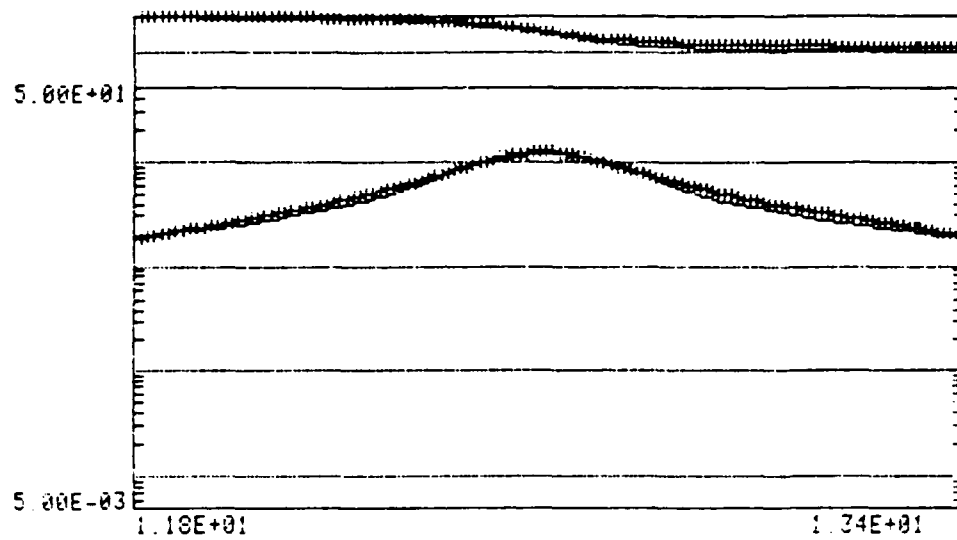
Estimated Roots (11Y-   15Y+)
Root   Frequency   Damping   Amplitude   Phase
 1   12.580   0.01268   11.543   -1.571

Figure D.4. First Torsion Frequency Response Curve Fit
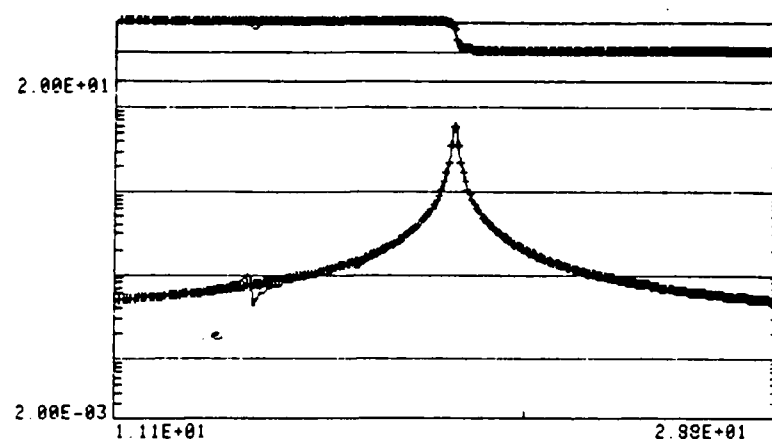
Estimated Roots (112+ 52+)

Root	Frequency	Damping	Amplitude	Phase
1	18.094	0.00291	2.1833	-1.571

Mode Shape. 2ND Z-BENDING

Loc	X Coeff	Y Coeff	Z Coeff
1	0.000E-01	0.000E-01	-4.869E-01
2	0.000E-01	0.000E-01	-1.890E+00
3	0.000E-01	0.000E-01	-3.642E+00
4	0.000E-01	0.000E-01	-5.316E+00
5	0.000E-01	0.000E-01	-6.597E+00
6	0.000E-01	0.000E-01	-7.015E+00
7	0.000E-01	0.000E-01	-5.597E+00
8	0.000E-01	0.000E-01	-5.376E+00
9	0.000E-01	0.000E-01	-3.089E+00
15	-1.713E-03	0.000E-01	9.506E-02
14	0.000E-01	0.000E-01	3.700E-01

Figure D.5. Second Z-Axis Bending Mode

Estimated Roots (11Z+   5Z+)
Root   Frequency   Damping   Amplitude   Phase
 1   43.454   0.00217   1.5613   1.571
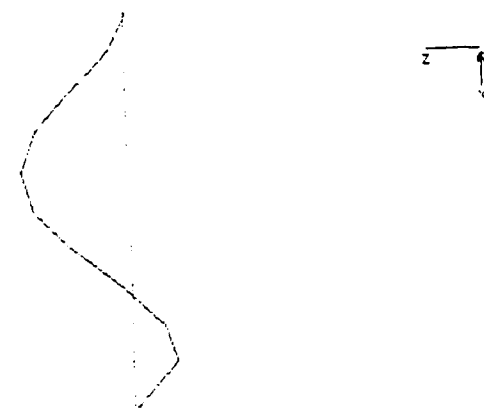
Mode Shape, 3RD Z-BENDING
Loc   X Coeff   Y Coeff   Z Coeff
  1   0.000E-01 0.000E-01 4.905E-01
  2   0.000E-01 0.000E-01 1.521E+00
  3   0.000E-01 0.000E-01 2.484E+00
  4   0.000E-01 0.000E-01 2.922E+00
  5   0.000E-01 0.000E-01 2.597E+00
  6   0.000E-01 0.000E-01 1.573E+00
  7   0.000E-01 0.000E-01 2.239E-01
  8   0.000E-01 0.000E-01 -8.664E-01
  9   0.000E-01 0.000E-01 -1.212E+00
 16   1.489E-02 0.000E-?? -6.689E-03
 14   0.000E-01 0.000E-01 -1.191E-01

Figure D.6. Third Z-Axis Bending Mode
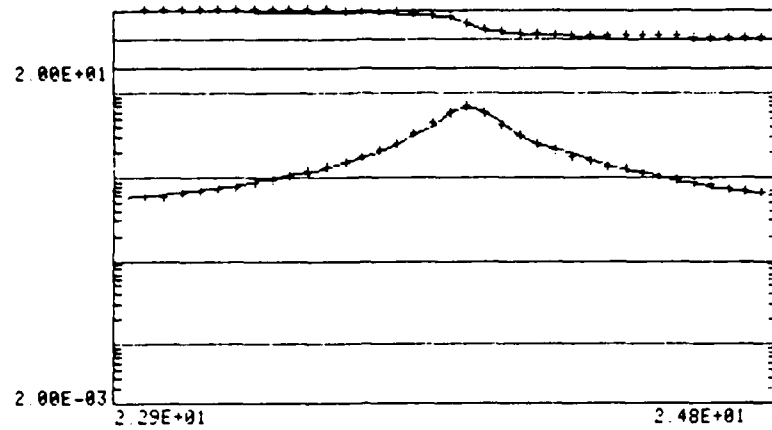
Modal Parameters: 2ND Y-BENDING
Label   Freq   Damping Amplitude   Phase   Ref   Res
  1   23.397 0.00319 3.209   -1.571   11Y+   5Y+

2ND Y-BENDING
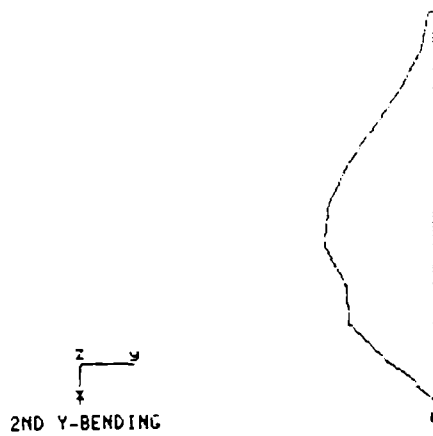
Mode Shape, 2ND Y-BENDING
Loc   X Coeff   Y Coeff   Z Coeff
 1   0.000E-01 -6.969E-01   0.000E-01
 2   0.000E-01 -2.127E+00   0.000E-01
 3   0.000E-01 -3.829E+00   0.000E-01
 4   0.000E-01 -5.524E+00   0.000E-01
 5   0.000E-01 -6.684E+00   0.000E-01
 6   0.000E-01 -7.003E+00   0.000E-01
 7   0.000E-01 -5.637E+00   0.000E-01
 8   0.000E-01 -5.391E+00   0.000E-01
 9   0.000E-01 -3.090E+00   0.000E-01
16   7.694E-03 -1.094E-01   0.000E-01
14   0.000E-01   3.990E-01   0.000E-01

Figure D.7. Second Y-Axis Bending Mode
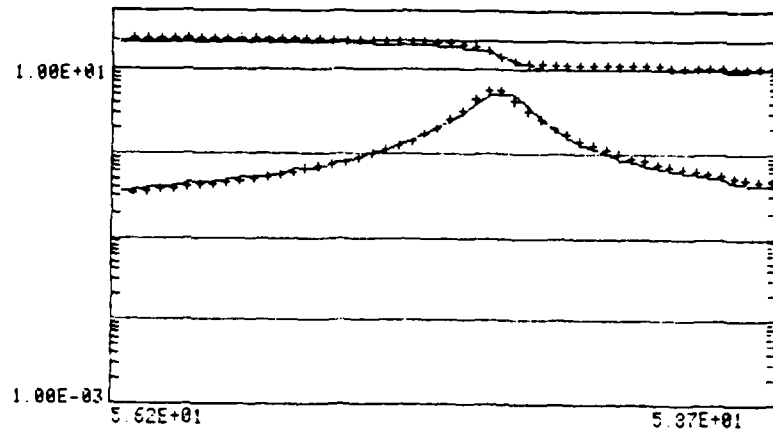
Estimated Roots (11Y+   4Y+)

Root	Frequency	Damping	Amplitude	Phase
1	57.624	0.00138	2.7957	1.571
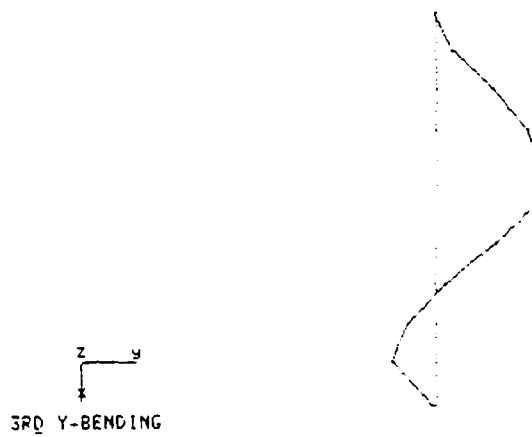
3RD Y-BENDING

Mode Shape, 3RD Y-BENDING

Loc	X Coeff	Y Coeff	Z Coeff
1	0.000E-01	9.028E-01	0.000E-01
2	0.000E-01	2.809E+00	0.000E-01
3	0.000E-01	4.491E+00	0.000E-01
4	0.000E-01	5.298E+00	0.000E-01
5	0.000E-01	4.707E+00	0.000E-01
6	0.000E-01	2.884E+00	0.000E-01
7	0.000E-01	4.330E-01	0.000E-01
8	0.000E-01	-1.510E+00	0.000E-01
9	0.000E-01	-2.193E+00	0.000E-01
16	-1.563E-02	-1.391E-02	0.000E-01
14	0.000E-01	-2.215E-01	0.000E-01

Figure D.8. Third Y-Axis Bending Mode

D - 10

SPECIFICATIONS		8628A50 8628A5 8630A50 ✳8630A5 8692A50 8692A5	
Acceleration range	g	±50	±5
Acceleration limit	g	±80	±8
Sensitivity,±5% at 100 Hz, 3 g rms	mV/g	100	1000
Threshold	µV rms	50	100
	µg rms	500	100
Shock (0.2ms pulse width), max.	g	5000	5000
Amplitude Linearity, nom.	%	±1	±1
Time Constant, nom.	s	0.5	0.5
Resonant Frequency, mounted, nom.	kHz	9	9
Frequency Response,±5% points	Hz	1...2k	1...2k
Phase Shift, 1...2k Hz	°	<5	<5
Transverse Sensitivity	%	<3	<3
Strain Sensitivity @ 250u in/in	g/µ in/in	<.001	<.001
Temperature Range, operating	°F	+32...150	
Temperature Range, storage	°F	-10...200	
Temperature Coefficient of Sensitivity	%/°F	-.04	-.04
Supply Current	mA	2...18	2...18
Source Voltage	VDC	20...30	20...30
Source Impedance	kΩ	100	100
Output Bias, nominal	VDC	11	11
Output Impedance	Ω	<100	<100
Output Current	mA	2	2
Output Voltage, F.S., nominal	V	±5	±5
Ground Isolation	MΩ	10	10
Material Housing and Base		Aluminum Alloy	
Seal Case and Connector		Environmental Epoxy	

MODEL 8628   MODEL 8630   MODEL 8692
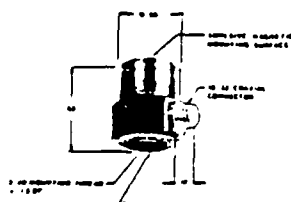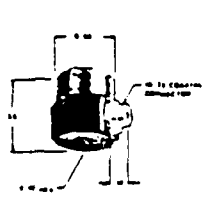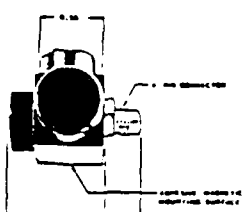
Weight   gr 6.7   4.5   14.5
Mounting Torque in-lbf 8

Figure E.1. Kistler Accelerometer Specifications

Appendix F: Advanced Beam State Space Formulation

Using the final modal test data, the **A** matrix for the first five modes of the structure is

$$
A = \begin{bmatrix}
0 & 0 & 0 & 0 & 0 & 1 & 0 & 0 & 0 & 0 \\
0 & 0 & 0 & 0 & 0 & 0 & 1 & 0 & 0 & 0 \\
0 & 0 & 0 & 0 & 0 & 0 & 0 & 1 & 0 & 0 \\
0 & 0 & 0 & 0 & 0 & 0 & 0 & 0 & 1 & 0 \\
0 & 0 & 0 & 0 & 0 & 0 & 0 & 0 & 0 & 1 \\
-69.83 & 0 & 0 & 0 & 0 & -0.630 & 0 & 0 & 0 & 0 \\
0 & -120.9 & 0 & 0 & 0 & 0 & -0.770 & 0 & 0 & 0 \\
0 & 0 & -6247 & 0 & 0 & 0 & 0 & -2.008 & 0 & 0 \\
0 & 0 & 0 & -12925 & 0 & 0 & 0 & 0 & -0.660 & 0 \\
0 & 0 & 0 & 0 & -22545 & 0 & 0 & 0 & 0 & -0.9610
\end{bmatrix}
$$

Applying the transfer function of the actuator, the $\Phi^T B$ matrix takes the form

$$
\Phi^T B = \begin{bmatrix}
0 & 0 & 0 & 0 \\
0 & 0 & 0 & 0 \\
0 & 0 & 0 & 0 \\
0 & 0 & 0 & 0 \\
0 & 0 & 0 & 0 \\
0 & 2.747 & 0 & -2.747 \\
-2.323 & 0 & -2.323 & 0 \\
0.484 & 0.484 & 0.496 & 0.471 \\
0 & -0.215 & 0 & 0.215 \\
0.243 & 0 & -0.243 & 0
\end{bmatrix}
$$

Since the sensor scale factors have been adjusted to unity in the input to the PC-1000, the C matrix partitions are just $C_p = 0$, a 4x5 zero matrix and C_v has the form

$$C_v \Phi = \begin{bmatrix} 0 & -4.943 & 1.240 & 0 & 0.608 \\ 4.905 & 0 & 1.240 & -0.573 & 0 \\ 0 & 4.943 & 1.240 & 0 & -0.608 \\ -4.905 & 0 & 1.240 & 0.573 & 0 \end{bmatrix}$$

These matrices can be partitioned to form any subset of modes for inclusion in the controller. Examples of two z-axis controllers are shown in Figures F.1 and F.2. These configurations include the first three modes, but apply control gain only to the first z bending mode. Estimator and controller eigenvalues differ for the two formulations for comparison of feedback gains.

EIGENVALUES OF AC + BCB SYSTEM :

8.35919	0.152724
8.35919	0.152724
79.0425	1.20013e-02
79.0425	1.20013e-02
10.9956	3.53201e-02
10.9956	3.53201e-02

EIGENVALUES OF AC + KCC SYSTEM :

8.69709	0.200668
8.69709	0.200668
79.8805	0.102854
79.8805	0.102854
11.7257	0.248876
11.7257	0.248876

Figure F.1. Z-Axis Controller Example 1

F - 3

```
8.36112  0.199335              9.21896  0.302894
8.36112  0.197335              9.21890  0.302894
79.0425  1.20012e-02          79.8805  0.102852
79.0425  1.20012e-02          79.8805  0.102852
10.9956  3.53201e-02          11.7257  0.248876
10.9956  3.53201e-02          11.7257  0.248876
```

$$
A = \begin{bmatrix}
0.0000e+00 & 0.0000e+00 & 0.0000e+00 & 0.1000e+01 & 0.0000e+00 & 0.0000e+00 \\
0.0000e+00 & 0.0000e+00 & 0.0000e+00 & 0.0000e+00 & 0.1000e+01 & 0.0000e+00 \\
0.0000e+00 & 0.0000e+00 & 0.0000e+00 & 0.0000e+00 & 0.0000e+00 & 0.1000e+01 \\
-0.6985e+02 & 0.0000e+00 & 0.0000e+00 & -0.1301e+03 & 0.0000e+00 & 0.0000e+00 \\
0.0000e+00 & -0.1209e+02 & 0.0000e+00 & 0.0000e+00 & -0.7697e+02 & 0.0000e+00 \\
0.0000e+00 & 0.0000e+00 & -0.6248e+04 & 0.0000e+00 & 0.0000e+00 & -0.1897e+01
\end{bmatrix}
$$

$$
B = \begin{bmatrix}
0.0000e+00 & 0.0000e+00 & 0.0000e+00 & 0.0000e+00 \\
0.0000e+00 & 0.0000e+00 & 0.0000e+00 & 0.0000e+00 \\
0.0000e+00 & 0.0000e+00 & 0.0000e+00 & 0.0000e+00 \\
0.0000e+00 & 0.2747e+01 & 0.0000e+00 & -0.2747e+01 \\
-0.2323e-01 & 0.0000e+00 & 0.2323e+01 & 0.0000e+00 \\
0.4836e+00 & 0.4836e+00 & 0.4960e+00 & 0.4712e+00
\end{bmatrix}
$$

$$
C = \begin{bmatrix}
0.0000e+00 & 0.0000e+00 & 0.0000e+00 & 0.0000e+00 & -0.4943e-01 & 0.1240e-01 \\
0.0000e+00 & 0.0000e+00 & 0.0000e+00 & 0.4905e+01 & 0.0000e+00 & 0.1240e-01 \\
0.0000e+00 & 0.0000e+00 & 0.0000e+00 & 0.0000e+00 & 0.4947e-01 & 0.1240e-01 \\
0.0000e+01 & 0.0000e+00 & 0.0000e+00 & -0.4905e+01 & 0.0000e+00 & 0.1240e-01
\end{bmatrix}
$$

$$
K = \begin{bmatrix}
0.0000e+01 & 0.2212e-01 & 0.0000e+00 & -0.2212e-01 \\
-0.1768e-01 & 0.0000e+00 & 0.1758e-01 & 0.0000e+00 \\
0.1439e-01 & 0.1439e-01 & 0.1439e-01 & 0.1439e-01 \\
0.0000e+01 & -0.1515e+00 & 0.0000e+00 & 0.5051e+00 \\
0.5125e+00 & \text{---} & -0.5135e+00 & 0.0000e+00 \\
-0.2929e-01 & -0.2929e+01 & -0.2929e+01 & -0.2929e+01
\end{bmatrix}
$$

$$
G = \begin{bmatrix}
0.5777e-08 & 0.9603e-05 & -0.5916e-07 & 0.4224e-09 & 0.1515e-03 & -0.1275e-01 \\
-0.1376e-01 & 0.4723e-10 & -0.4506e-05 & -0.4921e+00 & 0.3079e-10 & -0.1275e-02 \\
0.9002e-05 & -0.9606e-05 & -0.6392e-07 & 0.4333e-09 & -0.1515e-03 & -0.1305e-02 \\
0.1376e-01 & 0.4802e-10 & 0.4406e-05 & 0.4921e+00 & 0.3272e-10 & -0.1242e-01
\end{bmatrix}
$$

$$
F_{22} = \begin{bmatrix}
9.9983d-01 & 1.9513d-21 & 0.1509d-11 & 0.4138d-07 & 0.9140d-19 & -0.1699d-11 \\
-4.6872d-19 & 9.9973d-01 & 7.1599d-11 & 6.9772d-17 & 0.2610d-03 & -0.2142d-11 \\
0.2902d-10 & 2.8145d-12 & 9.8740d-01 & -0.2235d-08 & -3.7726d-11 & 0.0099d-03 \\
-0.1386d-01 & -2.4166d-17 & 6.2839d-08 & 9.8099d-01 & 0.3363d-16 & -0.7660d-05 \\
-0.7165d-15 & -2.4037d-01 & 9.4065d-05 & 9.1470d-16 & 9.8911d-01 & -0.4529d-05 \\
5.0215d-07 & 4.2325d-09 & -0.2241d+01 & -0.1855d-05 & -0.6586d-08 & 9.6500d-01
\end{bmatrix}
$$

$$
F_{21} = \begin{bmatrix}
4.2585d-14 & 4.3015d-05 & 4.2585d-14 & -1.0015d-05 \\
-2.6596d-05 & 3.3780d-14 & 2.6596d-05 & 3.3780d-14 \\
2.6505d-06 & 2.6505d-06 & 2.6505d-06 & 2.6505d-06 \\
5.2332d-11 & -1.0049d-03 & 5.2332d-11 & 1.0049d-03 \\
1.0233d-07 & 4.4421d-11 & -1.0233d-07 & 4.4421d-11 \\
-5.7913d-03 & -5.7913d-03 & -5.7913d-03 & -5.7913d-03
\end{bmatrix}
$$

Figure F.2. Z-Axis Controller Example.

MICROCOPY RESOLUTION TEST CHART

NATIONAL BUREAU OF STANDARDS

Vita

Thomas Alan Cristler was born on 20 July 1960 in Eugene, Oregon. At one year of age he moved with his parents to Pendleton, Oregon, where he remained until graduation from Pendleton High School in May, 1978. Following his high school graduation he entered the United States Air Force Academy, and in June, 1982, received a regular commission as a Second Lieutenant and the degree of Bachelor of Science of Astronautical Engineering. After graduation he was assigned to the 6595th Aerospace Test Group, Vandenberg AFB, California, where he was an analyst with the Antisatellite Responsible Test Organiztion and participated in the first space testing of the Antisatellite weapon system. After completion of this assignment he entered the School of Engineering, Air Force Institute of Technology, in May, 1986.

Permanent Address: 17 N.E. Mt. Hebron Dr.

Pendleton, OR 97801

REPORT DOCUMENTATION PAGE

Form Approved
OMB No. 0704-0188

1a. REPORT SECURITY CLASSIFICATION	1b. RESTRICTIVE MARKINGS
UNCLASSIFIED	

2a. SECURITY CLASSIFICATION AUTHORITY	3. DISTRIBUTION/AVAILABILITY OF REPORT
	Approved for public release; distribution unlimited
2b. DECLASSIFICATION/DOWNGRADING SCHEDULE	

4. PERFORMING ORGANIZATION REPORT NUMBER(S)	5. MONITORING ORGANIZATION REPORT NUMBER(S)
AFIT/GA/AA/87D-1	

6a. NAME OF PERFORMING ORGANIZATION	6b. OFFICE SYMBOL (If applicable)	7a. NAME OF MONITORING ORGANIZATION
School of Engineering	AFIT/ENG	

6c. ADDRESS (City, State, and ZIP Code)	7b. ADDRESS (City, State, and ZIP Code)
Air Force Institute of Technology Wright-Patterson AFB, Ohio 45433	

8a. NAME OF FUNDING/SPONSORING ORGANIZATION	8b. OFFICE SYMBOL (If applicable)	9. PROCUREMENT INSTRUMENT IDENTIFICATION NUMBER
Flight Dynamics Laboratory	AFWAL/FIBG	

8c. ADDRESS (City, State, and ZIP Code)	10. SOURCE OF FUNDING NUMBERS			
	PROGRAM ELEMENT NO.	PROJECT NO.	TASK NO	WORK UNIT ACCESSION NO.
AFWAL/FIBG Wright-Patterson AFB, Ohio 45433				

11. TITLE (Include Security Classification)
ACTIVE VIBRATION CONTROL OF A CANTILEVERED BEAM WITH THREE ELASTIC COORDINATES

12. PERSONAL AUTHOR(S)
Thomas A. Cristler, B.S., Capt, USAF

13a. TYPE OF REPORT	13b. TIME COVERED	14. DATE OF REPORT (Year, Month, Day)	15. PAGE COUNT
MS Thesis	FROM _____ TO _____	1987 December	191

16. SUPPLEMENTARY NOTATION

17. COSATI CODES			18. SUBJECT TERMS (Continue on reverse if necessary and identify by block number)
FIELD	GROUP	SUB-GROUP	
20	11		Vibration, Controls

19. ABSTRACT (Continue on reverse if necessary and identify by block number)

Thesis Chairman: Dr. Robert A. Calico

20. DISTRIBUTION/AVAILABILITY OF ABSTRACT	21. ABSTRACT SECURITY CLASSIFICATION
☐ UNCLASSIFIED/UNLIMITED ☐ SAME AS RPT ☐ DTIC USERS	UNCLASSIFIED

22a. NAME OF RESPONSIBLE INDIVIDUAL	22b. TELEPHONE (Include Area Code)	22c. OFFICE SYMBOL
Dr. Robert A. Calico Prof. of Aerospace Engineering	(513) 255-3517	AFIT/ENY

DD Form 1473, JUN 86   Previous editions are obsolete.

UNCLASSIFIED

Many control methods have been proposed for dealing with the
large space structure vibration control problem. To experimentally
evaluate these various approaches in a way which will allow
consistent comparison of results requires a baseline experiment in
which all variables are understood and controlled. From this base-
line, the various aspects of each control scheme can be implemented
and their relative merits compared on a consistent basis. This
experiment was implemented using a vertically suspended cantilever
beam with rectangular cross section. Proof mass actuators were
developed to provide control force inputs to the structure. Closed
loop control was formulated using linear quadratic regulator theory
and results are compared with simulation and eigenvalue predictions
to establish baseline performance. Modal suppression techniques
were implemented to demonstrate control of selected modes while main-
taining overall system stability. Results applicable to future
testing and development in the large space structure control area
are identified.

END

FILMED

MARCH, 1988

DTIC